CHALMERS
UNIVERSITY OF TECHNOLOGY

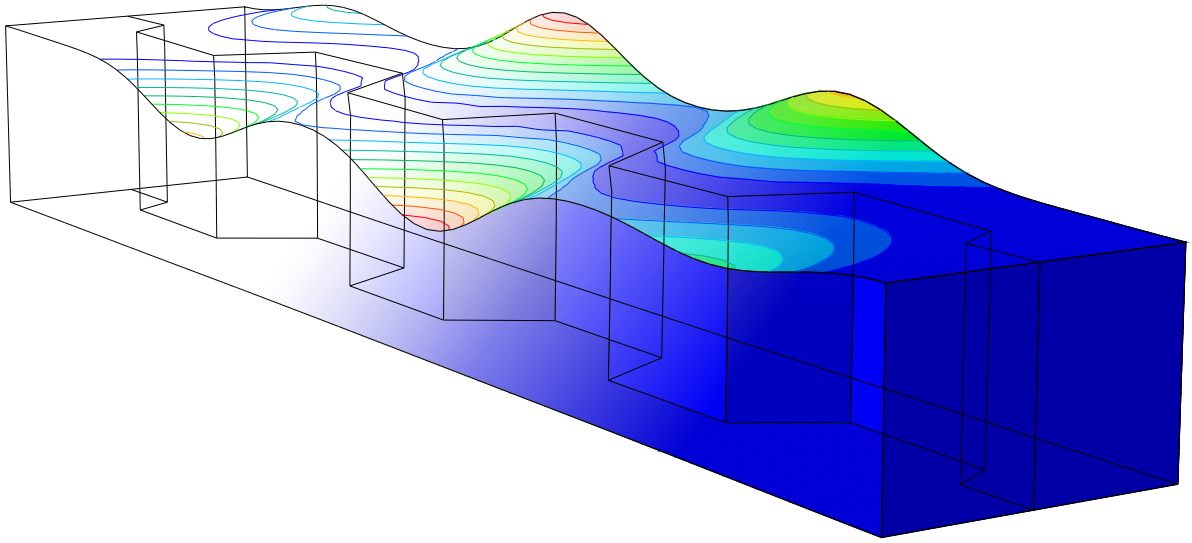

Flange Buckling Behavior of Stainless Steel Girders with Trapezoidally Corrugated Webs

A parametric numerical study

Master's thesis in the Master's Programme Structural Engineering and Building Technology

ALAA ACHOUR
ZIAD MLLI

DEPARTMENT OF ARCHITECTURE AND CIVIL ENGINEERING
CHALMERS UNIVERSITY OF TECHNOLOGY
Gothenburg, Sweden 2022
www.chalmers.se

Master's thesis 2022

Flange Buckling Behavior of Stainless Steel Girders with Trapezoidally Corrugated Webs

A parametric numerical study

Master's thesis in the Master's Programme Structural Engineering and Building Technology

ALAA ACHOUR
ZIAD MLLI

CHALMERS
UNIVERSITY OF TECHNOLOGY

Department of Architecture and Civil Engineering
Division of Structural Engineering
Research Group, Lightweight Structures
Chalmers University of Technology
Gothenburg, Sweden 2022

Flange Buckling Behavior of Stainless Steel Girders with Trapezoidally Corrugated Webs
A parametric numerical study
Master's thesis in the Master's Programme Structural Engineering and Building Technology
ALAA ACHOUR
ZIAD MLLI

Supervisors:
Andreas Wallin, Structural engineer, Norconsult
Doctoral student Fatima Hlal, Department of Architecture and Civil Engineering, Chalmers

Examiner:
Professor Mohammad al-Emrani, Department of Architecture and Civil Engineering, Chalmers

Master's Thesis 2022
Department of Architecture and Civil Engineering
Division of Structural Engineering
Research Group, Lightweight Structures
Chalmers University of Technology
SE-412 96 Gothenburg
Telephone +46 31 772 1000

Cover: A perspective view of the first eigenmode shape of specimen ID-811.

Printed by Chalmers Reproservice
Gothenburg, Sweden 2022

Flange Buckling Behavior of Stainless Steel Girders with Trapezoidally Corrugated Webs
A parametric numerical study
Master's thesis in the Master's Programme Structural Engineering and Building Technology
ALAA ACHOUR
ZIAD MLLI
Department of Architecture and Civil Engineering
Chalmers University of Technology

Abstract

The replacement of a flat web with a corrugated one in steel girders is a way of increasing the shear buckling capacity, without the need of additional vertical stiffeners. But, except for that, the corrugation of the web changes the bending behavior, more specifically the normal stress buckling behavior of the flange plate. Numerous investigations have been conducted on this subject for trapezoidally corrugated web I-girders in carbon steel, with the one by Jáger et al. being the most extensive one, comprising both experimental and numerical investigations. But, no design models for trapezoidally corrugated web I-girders in stainless steel are available.

The current study aims at investigating the normal stress flange buckling of trapezoidally corrugated web I-girders in stainless steel in terms of the elastic buckling coefficient and required reduction factor. The analyses are performed in the analysis software ABAQUS. The results of the parametric numerical studies are compared to the existing models for carbon steel girders suggested by Eurocode 3 (EN1993-1-5), the DASt Richtlinie 015 and Jáger et al. In case these prove to be inaccurate, a design model is developed.

The results of the comparisons generally showed that the method of approximating the buckling coefficient and required reduction factor developed by Jáger et al. is an improvement compared to Eurocode 3. The DASt Richtlinie 015 leads to the most inaccurate approximations of the reduction factor.

The suggested buckling curve of Eurocode 3, originally developed for flat web girders, has a too high relative slenderness limit of $\bar{\lambda}_p = 0,748$, which, according to the obtained results, should be $\bar{\lambda}_p = 0,4$. This is the main reason behind the Eurocode model resulting in over-estimations for almost all analysed girders. The improvement in the accuracy of estimations demonstrated by the design models of Jáger et al. are concluded to be the result of considering several parameters related to corrugation geometry. This insight is applied in the development of a new model to approximate the buckling coefficient, consequently used as input parameter in the expression of the relative slenderness ratio $\bar{\lambda}_p$. A buckling curve is then designed as a function of this parameter.

Keywords: corrugated web, stainless steel, Duplex, normal stress, flange buckling, parametric study, numerical study.

Beteendet av flänsbuckling hos stålbalkar i rostfritt stål med trapetsprofilerade liv
En parametrisk numerisk studie
Examensarbete inom masterprogrammet konstruktionsteknik och byggnadsteknologi
ALAA ACHOUR
ZIAD MLLI
Institutionen för arkitektur och samhällsbyggnadsteknik
Chalmers tekniska högskola

Sammanfattning

Ersättningen av en platt livplåt med en korrugerad hos stålbalkar är ett sätt att öka sjuvbucklingskapaciteten, utan behovet av vertikala avstyvningar. Utöver detta förändrar livplåtens korrugering beteendet i böjning, mer specifikt normalspänningsbucklingen av flänsen. Flera studier har utförts på stålbalkar med korrugerade liv i kolstål, där forskningen av Jáger et al. är den mest omfattande, med både fysiska och numeriska studier. Dock, finns det inga modeller för balkar med korrugerade liv i rostfritt stål.

Denna studie har som huvudsyfte att undersöka beteendet av flänsbuckling hos stålbalkar i rostfritt stål med trapetsprofilerade liv i termer av den elastiska bucklingskoefficienten och reduktionsfaktorn. Analyserna körs i programvaran ABAQUS. Resultaten av de parametriska numeriska studierna jämförs med de befintliga modellerna för balkar i kolstål som föreslås av Eurokod 3 (EN1993-1-5), DASt Richtlinie 015 och Jáger et al. Om dessa inte leder till bra approximationer utvecklas en ny beräkningsmodell.

Resultaten av jämförelserna visade generellt att beräkningsmodellerna för att approximera bucklingskoefficienten och reduktionsfaktorn, utvecklade av Jáger et al., är bättre än Eurokod 3. DASt Richtlinie 015 leder till de mest inexakta approximationerna av reduktionsfaktorn.

Den föreslagna knäckningskurvan av Eurokod 3, ursprungligen utvecklad för balkar med platta livplåtar, har en för hög gräns på den relativa slankheten $\bar{\lambda}_p = 0,748$, som i enlighet med dem erhållna resultaten borde vara $\bar{\lambda}_p = 0,4$. Detta är huvudorsaken bakom att Eurokodmodellen resulterar i överskattningar för nästan alla analyserade balkar. Förbättringen av noggrannheten som demonstreras av beräkningsmodellen utvecklad av Jáger et al. tros vara resultatet av övervägandet av flera parametrar relaterade till korrugeringsgeometrin. Denna insikt tillämpas i utvecklingen av en ny modell för att approximera bucklingskoefficienten, som sedan används som indataparameter i uttrycket av den relativa slankheten $\bar{\lambda}_p$. En knäckningskurva tas sedan fram som funktion av denna parameter.

Nyckelord: korrugerat liv, rostfritt stål, Duplex, normalspänning, flänsbuckling, parametrisk studie, numerisk studie.

Preface

The current master's thesis is part of a research program at the Department of Architecture and Civil Engineering at Chalmers University of Technology. The project was carried out in collaboration with the building construction department at Norconsult in Gothenburg, between January and June 2022.

We are grateful for the continuous assistance and genuine engagement in the project of our supervisor Doctoral student Fatima Hlal and supervisor and examiner Professor Mohammad al-Emrani. They have been of essential aid throughout the thesis, always having a kind and joyful attitude.

Further, we would also like to thank the team at the building construction department of Norconsult for providing a welcoming and including atmosphere at their office. Special thanks to our supervisor Andreas Wallin, who has consistently provided us with all needed aids and taken the time to support us with his experience and feedback.

Lastly, we would also like to thank our opponent group, Sarah Aref and Mahdi Mahdi for their continuous interest in the project and valuable feedback.

Alaa Achour & Ziad Mlli, Gothenburg, June 2022

Contents

List of Figures

List of Tables

List of Acronyms

Below is the list of acronyms that have been used throughout this thesis listed in alphabetical order:

CWIG	Corrugated Web I-Girders
FE	Finite Element
FEA	Finite Element Analysis

Nomenclature

Below is the nomenclature of variables that have been used throughout this thesis.

Variables - Lowercase Roman letters

a_1	Length of longitudinal fold
a_2	Length of inclined fold
a_3	Depth of corrugation
a_4	Length of inclined fold projection on longitudinal axis
b	Reference plate width for the determination of elastic critical stress
$\bar{b}$	Reference plate width for determination of relative slenderness
b_f	Flange width
$b_{f.eff}$	Effective flange width
$b_{f.t(c)}$	Width of tension (compression) flange
c_f	Flange outstand width in the case of flat web girders, large flange outstand in the case of corrugated web girders
$f_{y(f)}$	Yield strength of steel (flange plate)
f_T	Reduction factor for the calculation of moment resistance of corrugated web I-girders, according to the EN1993-1-5
f_u	Ultimate strength of steel
h_{lever}	Lever arm distance between centers of gravity of the flanges
h_w	Web height
m	Constant for the determination of the engineering strain relation of stainless steels according to the EN1993-1-4
m_{wav}	Number of half-sine waves in the longitudinal direction of the buckled plate
n	Constant for the determination of the engineering strain relation of stainless steels according to the EN1993-1-4
n_{wav}	Number of half-sine waves in the transverse direction of the buckled plate

q	Transverse, uniform load
t_f	Flange plate thickness
$t_{f.t(c)}$	Thickness of tension (compression) flange
t_p	Plate thickness
t_w	Web plate thickness
$t_{w.eff}$	Effective web thickness with respect to axial load-carrying contribution of corrugated web I-girders
z_{top}	Vertical distance from neutral plane to outermost compression fibre

Variables - Uppercase Roman letters

D	Plate bending stiffness
E	Young's modulus
E_y	Tangent modulus of elasticity at yielding
I_i	Second moment of area of a cross-section around axis i
$I_{i.eff}$	Second moment of area of the effective cross-section around axis i
M	Bending moment around the strong axis
$M_{cr.num}$	Critical bending moment around the strong axis, as obtained from a numerical analysis
M_{Exp}	Ultimate bending moment from physical experiment around the strong axis
M_i	Bending moment around axis i
$M_{i.Rd}$	Design bending moment around axis i in the ultimate limit state, according to the EN1993-1-5
M_{pl}	Plastic moment capacity around the strong axis
$M_{ult.approx}$	Approximate ultimate bending moment capacity around the strong axis, based on the model developed in the current study
$M_{ult.DASt}$	Ultimate moment capacity around the strong axis, according to the DASt-Richtlinie 015
$M_{ult.EC}$	Ultimate moment capacity around the strong axis, according to the EN1993-1-5
$M_{ult.Jager}$	Ultimate bending moment around the strong axis, according to Jáger et al.
$M_{ult.num}$	Ultimate bending moment around the strong axis, obtained from a numerical analysis

$M_{ult.num.geo}$	Ultimate bending moment around the strong axis, obtained from a numerical analysis, considering geometric imperfections only
M_{yield}	Yield moment capacity around the strong axis
N	Axial force
$N_{ult.num}$	Ultimate normal force based on a numerical analysis
P	Transverse point load
R	Enclosing effect of corrugation configuration
V_i	Shear force in the i-direction
$W_{i.eff}$	Section modulus of the effective cross-section around axis i

Variables - Lowercase Greek letters

α	Corrugation angle
β	Callibrated, adjusting index derived by Jáger et al. taking into account girder geometry in the reduction factor expression
γ_{M0}	Partial coefficient from the EN1993-1-1
γ_{M1}	Partial coefficient from the EN1993-1-1
δ	Out-of-plane deflection
ϵ	Material parameter for carbon steel, according to the EN1993-1-5
$\epsilon_{ss(f,w)}$	Material parameter for stainless steel (flange, web plate), according to the EN1993-1-4
ε	Engineering strain
ε_{el}	Elastic strain at yielding
ε_{pl}	Plastic strain
ε_u	Ultimate strain
η	Coefficient used in the adjusting index β by Jáger et al.
κ_σ	Elastic buckling coefficient of a plate
$\kappa_{\sigma.approx}$	Approximate elastic buckling coefficient, based on the model developed in the current study
$\kappa_{\sigma.EC}$	Elastic buckling coefficient according to the EN1993-1-5
$\kappa_{\sigma.Jager}$	Elastic buckling coefficient according to Jáger et al.
$\kappa_{\sigma.num}$	Elastic buckling coefficient as obtained from a numerical analysis
$\bar{\lambda_p}$	Relative slenderness ratio of a plate
$\bar{\lambda}_{p.lim}$	Limit relative slenderness ratio of a plate for class 4 classification
ν	Poisson ratio
ρ	Reduction factor of plate width
ρ_{approx}	Approximate reduction factor of flange plate, based on the model developed in the current study
ρ_{num}	Reduction factor of flange plate, based on a numerical analysis
σ	Engineering stress
$\sigma_{cr.num}$	Critical normal stress based on a numerical analysis
$\sigma_{cr(p)}$	Elastic critical stress of a plate
σ_i	Normal stress in the direction i
σ_{true}	True stress

ϕ	Developed factor used to determine whether normal stress web buckling is current as first eigenmode
χ	Reduction factor related to the lateral instability of corrugated web I-girders, according to the EN1993-1-5
ψ	Stress ratio of a plate

1
Introduction

The concept of corrugated web I-girders has emerged as a way to increase structural efficiency, in terms of material usage [1]. The idea is built upon the use of a corrugated web plate welded to two flange plates. There is a variety of corrugation types, including sinusoidal and the trapezoidal, with the latter being the most widely used [2]. The efficiency of such members can be further expanded by using stainless steel, reducing maintenance costs. In the following sub-chapter a brief history and a more comprehensive background connected to the concept is presented.

1.1 Background

Beginning in 1956, corrugated web I-girders (CWIG) were initially a subject of interest within the aeronautics industry and the area of application was in the airplane wings. Due to the efficiency of such structural members, the concept was adopted within the field of civil engineering [3]. Applications in buildings can be dated back to the beginning of the 1960s in Europe, and the 1980s in highway bridges in both Europe and Japan [2]. The main efficiency is coming from saving material due to a significantly high shear buckling strength of the corrugated web. Consequently, reduced fabrication costs and fatigue performance are achieved through the use of thinner web plates and no vertical stiffeners [1, 4].

Despite the recognized advantages of CWIG, there is very limited research done on their behavior with respect to load-carrying capacity in bending and with respect to flange buckling [3]. But, it has been shown that classical beam theory cannot be utilized to analyze CWIG [2]. Further, current design methods and research are focused on corrugated web I-girders in carbon steel, and no regulations are available for stainless steel.

CWIG are characterized by a different stress distribution, compared to flat web girders. More specifically, there is a deviation from uniform normal stresses in the flanges, with the first research on the topic being performed by Lindner in 1992 [3].

Additionally, there is no commonly accepted procedure to calculate the flange buckling resistance in CWIG in carbon steel. There are several suggestions for the choice of the buckling coefficient κ_σ, to implement in the calculation of the relative plate slenderness $\bar{\lambda}_p$ in the EN1993-1-5 [5, 6]. There is no agreement in the different methods and the suggested buckling curve given in the EN1993-1-5 [5, 6] often leads

to over-estimations of buckling capacities, especially in the case of flange plates in cross-section class 4. A background to this is its failure to consider weighing parameters regarding flange buckling resistance of trapezoidally CWIG. Experimental research has shown that the main affecting parameters are the flange-to-web thickness ratio (t_f/t_w) and the corrugation geometry (enclosing effect R) [7].

The most extensive research on the topic of flexural strength of CWIG in carbon steel is made by Jáger et al. (2017) [8], comprising 16 physical tests and large-scale numerical study with varying geometries [8]. For now, the design proposal of Jáger et al., for the flexural resistance of CWIG, is the one with the most satisfactory accuracy.

As the name suggests, stainless steels have an increased corrosion resistance, which implies reduced costs during the service life of the structure. Apart from that, the use of stainless steel has numerous advantages, ranging from high strength-to-weight ratio to improved performance in extreme heat. [9].

The inconsistencies and unsatisfactory precision of the suggested calculation procedure in the EN1993-1-5 [5, 6], on local flange buckling of plates in cross-section class 4 advocate further investigations on the topic. Additionally, there is a lack of design methods for slender flanges of CWIG in stainless steel, which supports research to be conducted on the behavior, buckling coefficient and buckling curves needed for the design of such members.

1.2 Objectives

The objectives of the study are summarized as:

- To perform a parametric study and investigate the buckling coefficient κ_σ and the correlation between the relative slenderness ratio $\bar{\lambda}_p$ and the reduction factor ρ with regard to the thin flange buckling subjected to bending moment.

- To establish the relevancy of current models, such as the one proposed by Jáger et al. (2017) [7], on stainless steel and, in the event of that not being the case, develop a relevant model.

1.3 Methods

The methods adopted in the current thesis comprise an initial and preparatory literature study, and with the gathered insight, an FE model is constructed and verified. This model then serves as a base for the parametric modelling for the purpose of conducting a large-scale test based on FE models. The output is then compared with models in design standards (EN1993-1-5 [5, 6] & DASt-Richtlinie 015 [10]), or proposed in previous studies (Jáger et al. (2017) [7]). The mentioned method steps

are discretized and presented below:

- As a first step, a literature study is performed, in order to gather relevant and preparatory information connected to the flange buckling behavior of steel girders with trapezoidally corrugated webs.

- The second step is building and verifying an initial FE model in the analysis software ABAQUS to determine a suitable mesh size and boundary and loading conditions. Verification is made by comparing the results from the numerical study with a chosen experiment from the literature.

- Further, the verified models are used to study the corresponding behavior of the chosen stainless steel grade. This step is concluded with an imperfection sensitivity analysis, to determine a suitable equivalent geometric imperfection.

- The next step is to construct a parametric model to study the effect of different corrugation profiles and girder geometries on the buckling coefficient κ_σ and subsequent capacity reduction ρ of slender flanges in trapezoidally CWIG.

- Lastly, a comparison between the obtained results and the design models provided in the EN1993-1-5 [5, 6], the DASt-Richtlinie 015 [10] and as proposed by Jáger et al. (2017) [7] is conducted. A suitable design method is then suggested (or the current methods are accepted).

1.4 Limitations

The scope is defined by the following limitations:

- The study focuses on girder dimensions applicable for bridge girders (see Chapter 5.1)

- Only the stainless steel grade of Duplex 1.4162 is to be considered.

- The corrugation of the web plate is limited to trapezoidal.

- No physical tests will be performed in the current study.

- The post-failure behavior will not be studied to deep extent.

1.5 Outline

- Chapter 2 presents the conducted literature study on the flexural resistance of trapezoidally CWIG.

- Chapter 3 introduces the construction and validation of the FE model in the analysis software ABAQUS, against experimental specimens in carbon steel.

- In Chapter 4, the adopted material model of the treated stainless steel grade Duplex 1.4168 is presented. Further, the behavior of the constructed beams in Chapter 3 is compared when applying carbon steel and stainless steel properties. The chapter is concluded with an imperfection sensitivity study of the stainless steel beams.

- Proceeding, in Chapter 5, the results of the linear buckling analyses of the parametric study are presented. These include obtained first eigenmodes and the relevancy of existing models for calculating the buckling coefficient κ_σ. Finally, the developed approximating model is also presented.

- Chapter 6 focuses on the observation of ultimate failure modes from the non-linear analyses, and what characterizes them.

- Chapter 7 concludes the parametric study through the comparison of existing calculation models for determining the ultimate moment capacity M_{ult} with the FEA results. A developed buckling curve expression is finally presented.

- Chapter 8 summarizes the gained insights of the project.

- In Chapter 9 further studies on the subject are suggested.

2

Literature review

This chapter presents a brief introduction to normal stress buckling theory of plates and normal stress buckling resistance of flat web I-girders, according to the Eurocode. Further, the geometry and major effects that characterize trapezoidally CWIG are introduced, and proceeded by design models on their normal stress buckling resistance according to the EN1993-1-5 [5, 6], Jáger et al. [7] and the DASt Richtlinie 015 [10]. Further, affecting parameters on the normal stress buckling resistance are presented and, finally, a short description of different types of stainless steels and their mechanical properties.

2.1 Normal stress buckling theory

As an introduction to the subject of plate buckling, the current sub-chapter presents a brief theory background relating to the elastic critical stress σ_{cr} and buckling coefficient κ_σ of plates. Further, the concept of cross-section classes suggested in the EN1993-1-1 [11] is also presented.

2.1.1 Elastic critical stress and buckling coefficient of plates

In the context of plate buckling due to axial loading, the concept of the elastic critical stress σ_{cr} and the elastic buckling coefficient κ_σ are essential. To determine whether a plate, under a certain axial loading condition, is susceptible to elastic buckling, the elastic critical stress σ_{cr} needs to be determined. Consequently the square root of the yield strength-to-critical stress ratio, $\sqrt{f_y/\sigma_{cr}}$, can be determined, which describes the relative slenderness of the plate $\bar{\lambda}_p$. The relative slenderness $\bar{\lambda}_p$ which determines if the current situation of plate geometry, boundary and loading conditions would lead to elastic buckling (plate with class 4 classification) [5].

To consider the current boundary and loading conditions of a plate, a corresponding elastic buckling coefficient κ_σ can be derived. This procedure is built upon the differential equation describing the relation between the out-of-plane deflection δ and the in-plane loading σ_x, as in Equation 2.1*:

*Here, the demonstrated case is the one of a rectangular plate, simply supported on the 4 edges and axially loaded with a uniform load σ_x along the short edge.

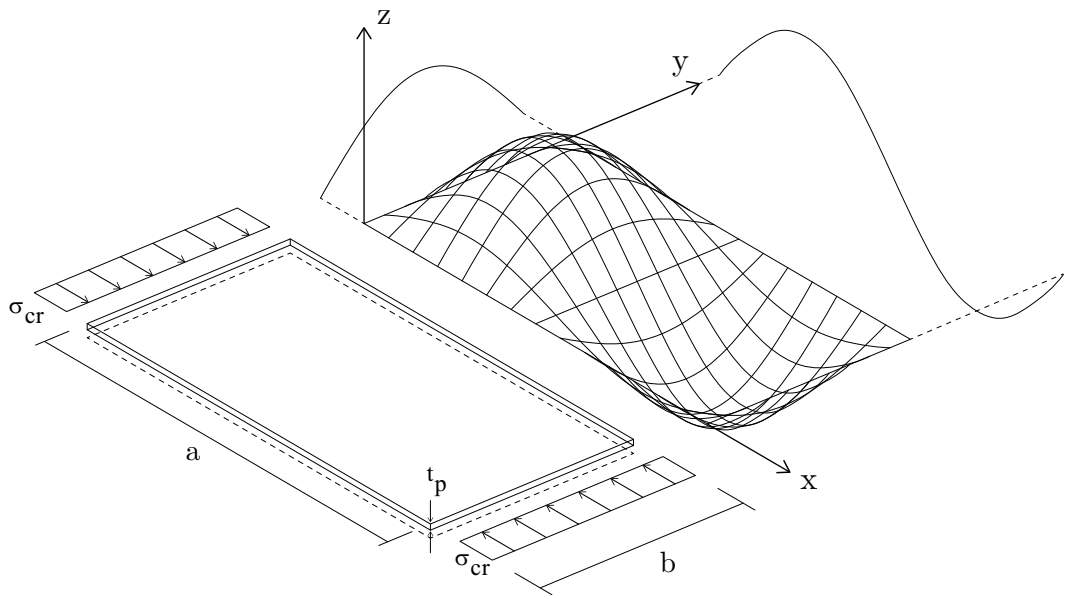

Figure 2.1: Illustration of a possible buckling mode of a plate simply supported on all edges, with the critical axial load σ_{cr}. In this case, $m_{wav} = 2$ and $n_{wav} = 1$.

$$D \cdot \left[\frac{\partial^4 \delta}{\partial x^4} + 2 \cdot \frac{\partial^4 \delta}{\partial x^2 \partial y^2} + \frac{\partial^4 \delta}{\partial y^4} \right] = -\sigma_{cr} \cdot t_p \cdot \frac{\partial^2 \delta}{\partial x^2} \tag{2.1}$$

With the general solution presented in Equation 2.2:

$$\delta = A \cdot sin(\frac{m_{wav} \cdot \pi \cdot x}{a}) \cdot sin(\frac{n_{wav} \cdot \pi \cdot y}{b}) \quad [m] \tag{2.2}$$

Where D is the bending stiffness of the plate, determined as in Equation 2.3:

$$D = \frac{E \cdot t_p^3}{12 \cdot (1 - \nu^2)} \quad [Nm^2/m] \tag{2.3}$$

Here, the x- and y-directions refer to the longitudinal and transverse directions and t_p is the plate thickness. A corresponds to a constant, m_{wav} and n_{wav} are the numbers of half-sine waves in the x- and y-directions, respectively. The plate is assumed to be loaded along the short edge with dimension b, and a is the length of the plate. An illustration of the above is in Figure 2.1.

Deriving the expressions of the differentials in Equation 2.1 with the aid of the general solution in Equation 2.2 leads to the expression presented in Equation 2.4 for

the elastic critical stress σ_{cr}, assuming the lowest possible number of n_{wav}=1 *:

$$\sigma_{cr} = \kappa_\sigma \cdot \frac{\pi^2 \cdot E}{12 \cdot (1 - \nu^2) \cdot (\frac{b}{t_p})^2} \quad [MPa] \tag{2.4}$$

Where E is the material's Young's modulus and ν is the Poisson ratio.

In the case of a rectangular plate, simply supported on the 4 edges and axially loaded with a uniform load along the short edge b, the expression for κ_σ is derived as in Equation 2.5:

$$\kappa_\sigma = \left[\frac{m_{wav} \cdot b}{a} + \frac{a}{m_{wav} \cdot b} \right]^2 \tag{2.5}$$

To obtain the lowest critical stress σ_{cr}, the buckling coefficient κ_σ needs to have the lowest possible value, which is always 4 in the current case of loading and boundary conditions. Different buckling coefficients can be derived for any combination of loading and boundary conditions, examples of various κ_σ are presented in Figure 2.2 [12].

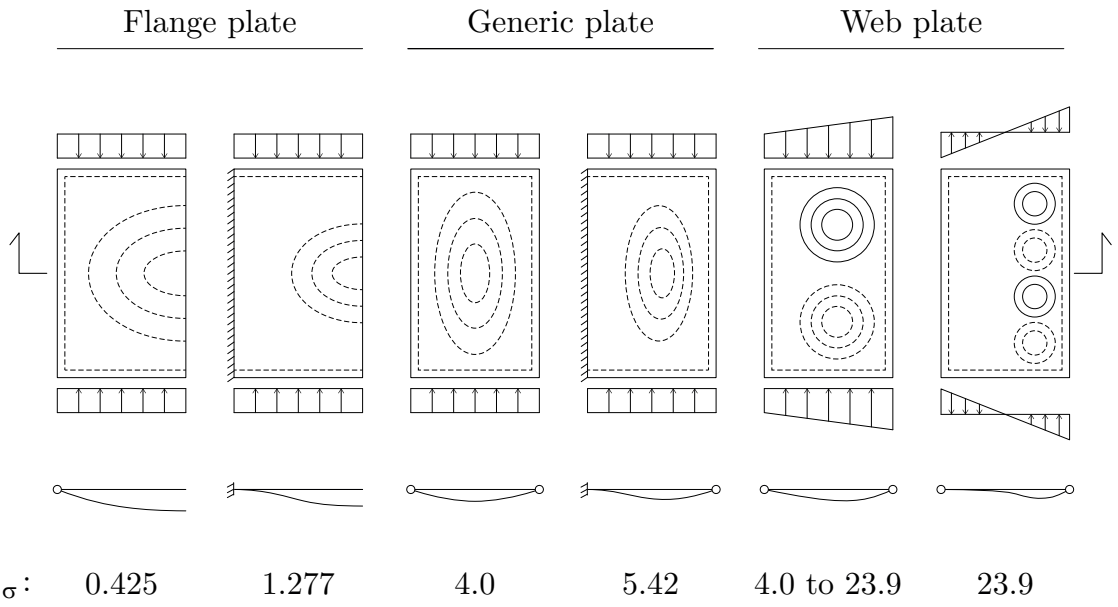

Figure 2.2: Demonstration of different buckling modes of plates, corresponding to different buckling coefficients κ_σ, relevant for different types of plate members. Adaptation from Al-Emrani & Åkesson (2020) [12].

*The only relevant value of n_{wav} is 1, since a higher number of transverse waves could not occur in this case.

2.1.2 Cross-section classes of plates

To expand on the presented theory of the elastic buckling from Chapter 2.1.1, the concept of cross-section classes according to the EN1993-1-1 [11] is reviewed in this section. The determination of cross-section classes for plates is relevant in the design of steel members in flexure, or pure compression, and there are 4 separate classes, characterized by varying slenderness. The differences among the classes lies in their capacity of elongation/compression on the edges before failure through buckling occurs.

The classes are numbered in such a way that the lower the class, the lower is the slenderness (stockier) and, thereby, the higher is the rotational capacity, see Figure 2.3. Members corresponding to classes 1 and 2 are expected to develop a fully plastic flexural capacity, and the difference lies in the additional rotational capacity of class 1 members, allowing them to work as mechanisms in statically indeterminate structures. One step down are the class 3 members, with the possibility to develop the full elastic capacity, with the yield stress occurring in the fibres with maximum strain.

The last, and weakest, slenderness class is cross-section class 4, classifying members with the inability to develop the full elastic capacity before local buckling occurs. To take the elastic buckling into account in the design of such members, the area that is expected to buckle is discarded in the calculations of the cross-sectional properties, and an effective cross-section is considered instead (Figure 2.3). Reference is also made to Figure 2.2, where the elastic buckling mode of a web plate in pure bending is illustrated.

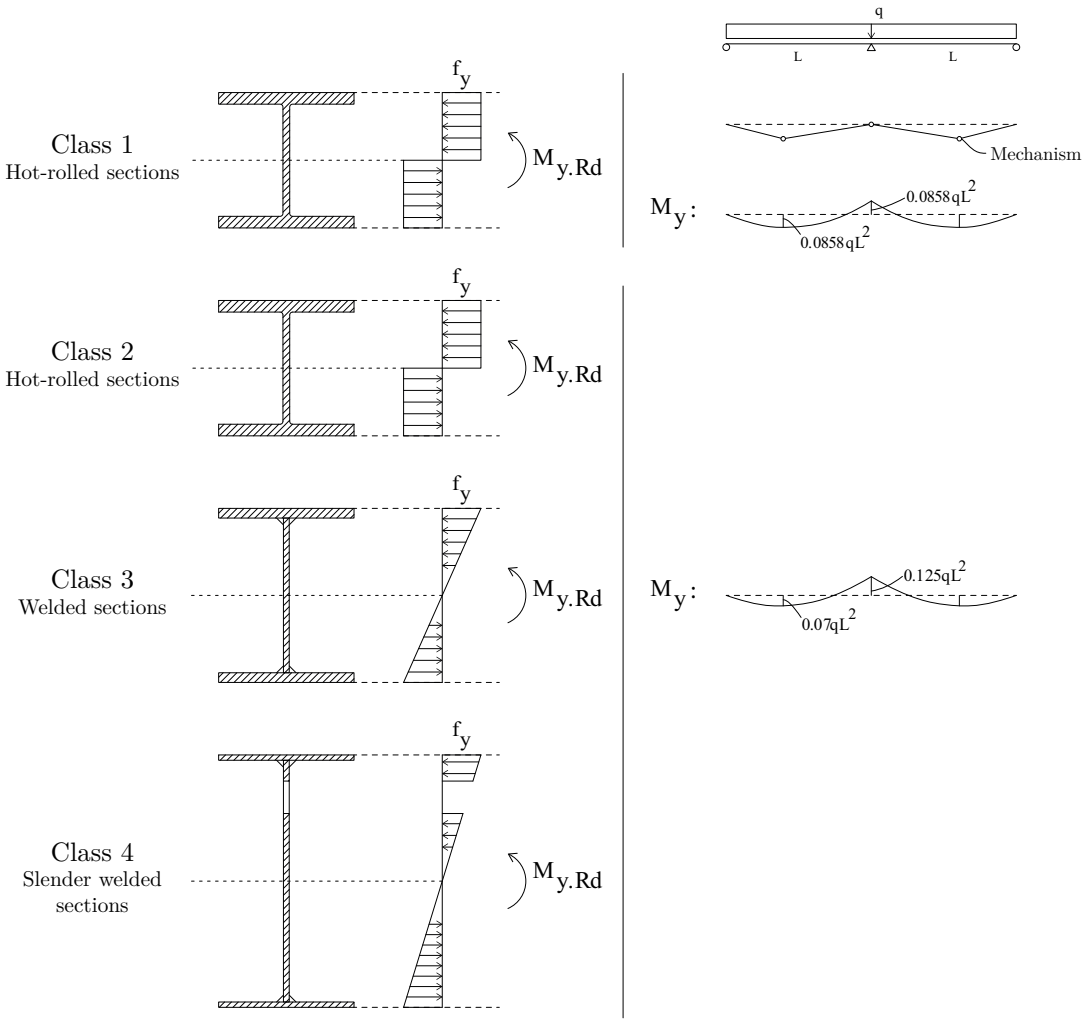

Figure 2.3: Examples of cross-sections belonging to the 4 different cross-section classes. Also, the moment distributions in a statically indeterminate structure are demonstrated. Adaption from Al-Emrani & Åkesson (2020) [12].

2.2 Normal stress buckling for flat web I-girders, according to the Eurocode

Contrary to web plates in flexure, the flanges exhibit a constant stress state ($\psi = 1$) and the EN1993-1-1 [11] considers such members as outstands *. The current EN1993-1-1 (2005) [11] provides limitations for the 4 cross-section classes for members in carbon steel, and the EN1993-1-4 (2006) [13, 14] for stainless steel. The latest draft of the EN1993-1-4 (2020) [15] provides slightly different limitations for stainless steel, as shown below:

*Only recommendations regarding welded members are treated

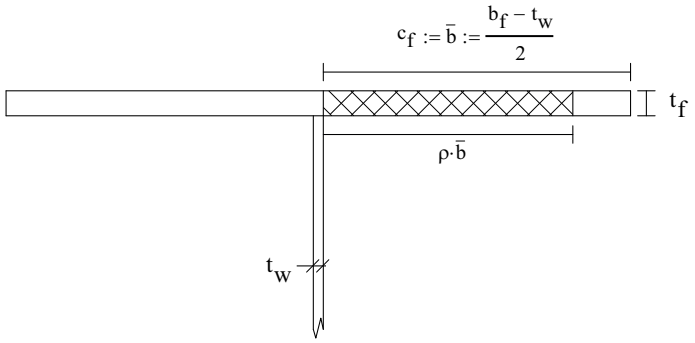

Figure 2.4: Illustration of flange outstand c_f, reference plate width $\bar{b}$, flange thickness t_f and reduced flange width $\rho \cdot \bar{b}$ for class 4 flange plates in flat web girders according to the EN1993-1-5 [5, 6].

	Carbon steel	Stainless steel (current version)	Stainless steel (new draft)	Class
$c_f/t_f \leq$	9ϵ	$9\epsilon_{ss}$	9ϵ	1
$c_f/t_f \leq$	10ϵ	$10\epsilon_{ss}$	10ϵ	2
$c_f/t_f \leq$	14ϵ	$14\epsilon_{ss}$	14ϵ	3

Where c_f is the dimension of the flange outstand (discarding the welds) and t_f is the flange plate thickness (Figure 2.4). A differentiation is made in the material parameter ϵ and ϵ_{ss} as presented in Equations 2.6 and 2.7:

$$\epsilon = \sqrt{235/f_y} \quad \text{for carbon and stainless steel} \tag{2.6}$$

$$\epsilon_{ss} = \left[\frac{235}{f_y} \cdot \frac{E}{210000} \right]^{0.5} \quad \text{for stainless steel in EN1993-1-4 (2006) [13]} \tag{2.7}$$

Where $f_y\,[MPa]$ is the yield strength and $E\,[MPa]$ is Young's modulus and, in the current case of Equation 2.7, $E = 200000\,[MPa]$.

The same expression for the relative slenderness ratio $\bar{\lambda_p}$ is provided for carbon and stainless steel in the EN1993-1-5 [5, 6] and EN1993-1-4 [13, 15] correspondingly, as in Equation 2.8:

$$\bar{\lambda}_p = \sqrt{\frac{f_y}{\sigma_{cr.p}}} = \frac{\bar{b}/t_f}{28,4\epsilon\sqrt{\kappa_\sigma}} \tag{2.8}$$

$$\kappa_\sigma = 0,43 \text{ in all cases}$$

Where $\sigma_{cr.p}$ refers to the critical stress, and the definition of the plate width $\bar{b}$ corresponds to the size of the flange outstand c_f (Figure 2.4). It is to be noted that the material parameter ϵ depends on which version of the Eurocode is applied (see Equations 2.6 and 2.7)

Further, the consequent reduction factor ρ for the outstands is obtained with the buckling curve defined by Equation 2.9:

$$\rho = \frac{\bar{\lambda_p} - 0,188}{\bar{\lambda_p}^2} \qquad \text{in all Eurocode versions} \tag{2.9}$$

Lastly, the effective flange width of one outstand is $b_{f.eff} = \rho \cdot c_f$, see Figure 2.4.

Flexural resistance
The effective cross-section of the web is determined through a similar procedure as presented above for the flanges, and the final flexural resistance $M_{y.Rd}$ around the major axis y (Figure 2.6) of the member can be determined as shown in Equation 2.10:

$$M_{y.Rd} = W_{y.eff} \cdot \frac{f_y}{\gamma_{M0}} \quad [kNm] \tag{2.10}$$

Here, γ_{M0} is a partial factor suggested in the EN1993-1-1 [11] and $W_{y,eff}$ is the section modulus of the effective section defined as in Equation 2.11:

$$W_{y.eff} = \frac{I_{y.eff}}{z_{top}} \quad [m^3] \tag{2.11}$$

Where $z_{top}\,[m]$ is the vertical distance from the neutral plane of the effective cross-section to the compression fibre and $I_{y.eff}\,[m^4]$ is the second moment of area of the effective cross-section.

2.3 Design models on normal stress buckling for trapezoidally CWIG in carbon steel

This section presents the relevant geometric parameters related to trapezoidally CWIG. To further deepen the understanding of these members, the section introduces two of the major effects, the "accordion effect" and flange transverse bending,

that characterize and differentiate CWIG from regular, flat web I-girders. The section is concluded with the suggested calculation procedures of the EN1993-1-5 [5, 6], Jáger et al. [7] and the DASt-Richtlinie 015 [10] relating to the normal stress buckling resistance of trapezoidally CWIG in carbon steel.

2.3.1 Geometry

As mentioned in the introduction of Chapter 1, the trapezoidal configuration is the most commonly used for webs in corrugated web I-girders (CWIG). The corrugated web consists of longitudinal and inclined folds, with the longitudinal being the segments that are parallel with the axial direction of the beam and the inclined the ones having an angle with the axial direction. The geometry of the mentioned configuration can be described with the aid of 5 parameters, 4 of them being dimensions (a_1, a_2, a_3 and a_4) and one being the corrugation angle (α) [16]. All geometric parameters are as denoted in Figure 2.5.

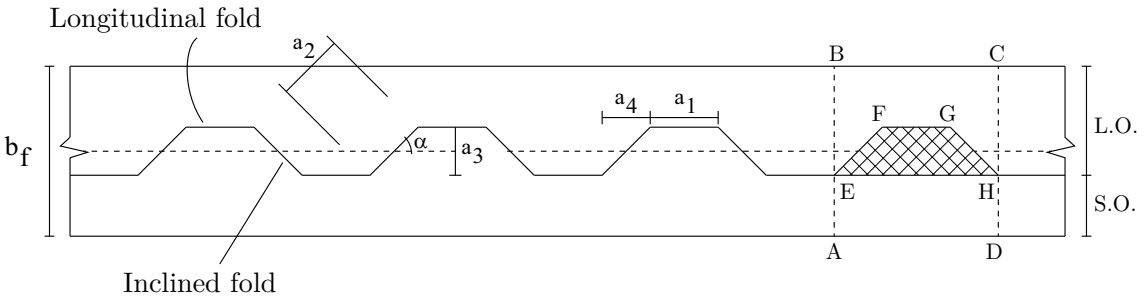

Figure 2.5: Illustration of geometric parameters related to trapezoidally corrugated web I-girders. The notations L.O and S.O refer to the large and small flange outstands, respectively.

For the purpose of characterizing the corrugation geometry related to the flange width, a parameter called the *enclosing effect* (R) has been defined in the scope of research related to trapezoidally CWIG. The enclosing effect R describes the ratio of the area enclosed by two adjacent inclined folds (EFGH in Figure 2.5) and the total flange area (ABCD in Figure 2.5). The expression is as presented in Equation 2.12:

$$R = \frac{(\alpha_1 + \alpha_4)\alpha_3}{(\alpha_1 + 2\alpha_4)b_f} \tag{2.12}$$

Where b_f is the flange width, as indicated in Figure 2.5.

In the context of describing the plate slenderness of the compression flange, the small and large flange outstand are defined, as in Figure 2.5, with the sizing (small - large) referring to the widths of the small and large flange plate segments on either

side of the longitudinal fold [16].

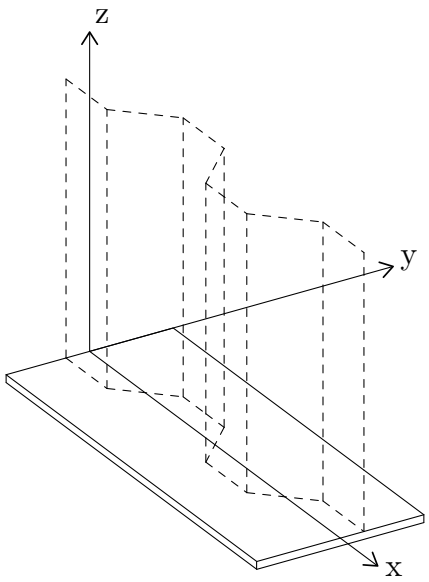

Figure 2.6: Used coordinate system.

In order to maintain a consistency throughout the report, the used coordinate system is defined as in Figure 2.6, with the coordinate x describing the axial direction of the beam, y the transverse and z the vertical direction.

2.3.2 The accordion effect

Transitioning to the behavior of CWIG, which despite their improved resistance against shear buckling (compared with flat web I-girders), are affected by low axial stiffness as a result of the corrugation. The mentioned phenomenon is often referred to as the *accordion effect*, referring to the high axial flexibility. The significantly low axial stiffness of the corrugated web has led researchers treating the flexural capacity of CWIG to neglect the contribution of the web, and only considering the flange contribution [16]. More detailed studies, as the one by Elgaaly et al. (1997) [1] on the bending resistance of CWIG, have proven that indeed the majority of the web shows negligible normal stresses, except for the parts close to, and constrained by the flange plates [1].

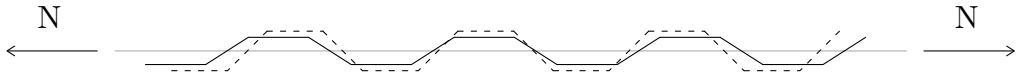

Figure 2.7: Intuitive illustration of the accordion effect.

A study concentrated on quantifying the contribution of the web in CWIG in carrying axial stresses by Inaam & Upadhyay (2022) [16] differentiates between the

longitudinal and inclined folds with respect to their contributions to the axial stiffness. More specifically, the longitudinal folds are only loaded in the global axial direction and therefore deform less and demonstrate a higher axial rigidity compared to the inclined folds, which are additionally loaded with in-plane bending and deform to a higher degree (Figure 2.7). This would suggest that corrugations with higher length of longitudinal folds per corrugation should have higher axial stiffness, and thereby reduced accordion effect.

Inaam & Upadhyay [16] concluded the study by defining a *web participation factor*, which indicates the degree of web contribution in flexural resistance, represented as a corresponding web plate with a fictitious thickness $t_{w.eff}$, as shown in Equation 2.13:

$$t_{w.eff} = (participation\ factor) \cdot t_w \tag{2.13}$$

Where $t_{w.eff}$ and t_w are the fictitious web thickness and the actual web thickness, respectively. Important to mention is that two prerequisites need to be satisfied for the justification of applying the proposed model: (i) the flange plates need to be compact (non-slender) and (ii) laterally restrained [16].

2.3.3 Flange transverse bending

The corrugation of the web in CWIG causes a transverse bending of the flanges, which, in turn, causes torsion of the section. The development of transverse bending in the flanges is a result of the transverse eccentricity of the longitudinal folds (compared to the x-axis, see Figure 2.6). This means that the shear flow at the flange-to-web intersection causes an additional loading of the flanges in the form of transverse bending (around the strong axis of the flange). With this as a background, it is deduced that classical beam theory cannot be exclusively used to study the flexural behavior of CWIG.

A tested method to analyze the out-of-plane behavior of CWIG in bending is to translate the components of the shear flow at the flange-to-web intersection as external loads acting on the flange. A derivation of the transverse shear force V_y in the flanges, based on equilibrium of an infinitesimal beam segment, implies a decoupling of the flange transverse bending and the in-plane bending behaviors. As a conclusion, Abbas et al. [2] suggested that the normal stresses σ_x in the flanges can be obtained by a superposition of the resulting stresses from the in-plane and transverse flexure actions (around the y- and z-axes, respectively), as shown in Equation 2.14:

$$\sigma_x = \frac{M_y \cdot z}{I_y} + \frac{M_z \cdot y}{I_z} \quad [MPa] \tag{2.14}$$

Where z and y refer to distances in the vertical and transverse directions, respectively, from the axes of symmetry. M_y, I_y and M_z, I_z refer to bending moments and second moments of area around the y- and z-axes, respectively (see Figure 2.6) [2].

2.3.4 Normal stress buckling resistance of trapezoidally CWIG, in carbon steel, according to the Eurocode

For the case of trapezoidally CWIG, the Eurocode only provides a design procedure for girders in carbon steel.

The elastic buckling coefficient κ_σ of the flange outstand of CWIG is not constant as for flat web I-girders (Chapter 2.2). This implies that there is no direct way of determining if the flange outstand is slender by only considering the c_f/t_f ratio. Instead, the relative slenderness ratio $\bar{\lambda_p}$ needs to be determined first, and compared to the limit value of $0,748$. A prerequisite for that is, as already discussed, the determination of the buckling coefficient κ_σ.

The EN1993-1-5 [5, 6] provides the calculation formula of the buckling coefficient $\kappa_{\sigma.EC}$ as shown in Equation 2.15:

$$\kappa_{\sigma.EC} = min(0,43 + \left(\frac{c_f}{a_1 + 2a_4}\right)^2; \quad 0,6) \tag{2.15}$$

The relative slenderness ratio $\bar{\lambda_p}$ is determined as introduced for flat web I-girders in Equation 2.8, where the definition of the plate width $\bar{b}$ (see Figure 2.8) depends on the version of the EN1993-1-5:

$$\bar{b} = \frac{b_f - t_w}{2} \qquad \text{in the current EN1993-1-5 [5]}$$

$$\bar{b} = c_f = \frac{b_f + a_3 - t_w}{2} \qquad \text{in the new draft of EN1993-1-5 [6]}$$

Further, the consequent reduction factor ρ for the flange width b_f is obtained with the buckling curves defined by Equation 2.9, for flat web I-girders. The reduction factor ρ is then applied on the complete flange width b_f to obtain the effective width $b_{f.eff} = \rho \cdot b_f$ for the resistance, as indicated in Figure 2.8.

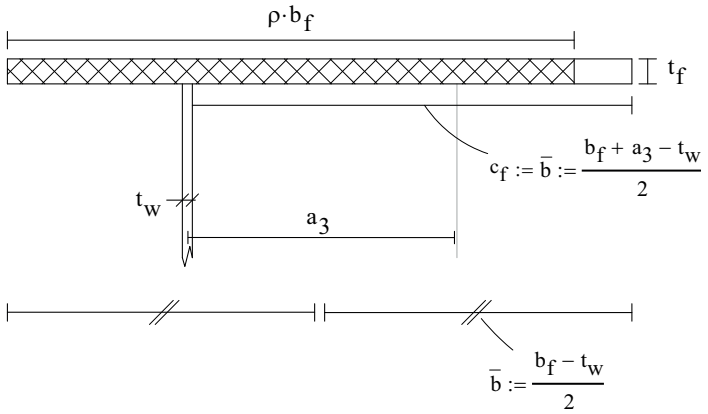

Figure 2.8: Illustration of relevant parameters in the determination of effective flange area of class 4 flange plates in CWIG according to the EN1993-1-5 [5, 6].

Flexural resistance
Both versions of the EN1993-1-5 (2006 & 2019) [5, 6] neglect the web contribution in the flexural capacity $M_{y,Rd}$ around the major axis y (Figure 2.6). The current version [5] suggests a capacity defined as the *minimum* of the capacities in Equations 2.16 a, b, c:

$$M_{y.Rd.1} = \frac{b_{f.t} \cdot t_{f.t} \cdot f_T \cdot f_y}{\gamma_{M0}} \cdot h_{lever} \quad [kNm] \tag{2.16a}$$

$$M_{y.Rd.2} = \frac{b_{f.c} \cdot t_{f.c} \cdot f_T \cdot f_y}{\gamma_{M0}} \cdot h_{lever} \quad [kNm] \tag{2.16b}$$

$$M_{y.Rd.3} = \frac{b_{f.c} \cdot t_{f.c} \cdot \chi \cdot f_y}{\gamma_{M1}} \cdot h_{lever} \quad [kNm] \tag{2.16c}$$

Where $h_{lever} = h_w + (t_{f.t} + t_{f.c})/2$ is the lever arm between the centers of gravity of the flanges. The subscript f refers to "flange" and the subscripts t and c refer to the tension and compression flange, respectively. γ_{M0} and γ_{M1} are partial factors suggested in the EN1993-1-1 [11].

$M_{y.Rd.1}$ corresponds to the capacity restricted by the yielding of the tension flange. $M_{y.Rd.2}$ describes the capacity of the section, being restricted by the yielding of the compression flange, with the flange width $b_{f.c}$ being the effective flange width $b_{f.eff}$ with respect to elastic buckling, as discussed above. The factor f_T is a reduction factor taking into account the additional stresses from the transverse bending of the flanges in trapezoidally CWIG. The expression for f_T is given in Equation 2.17:

$$f_{y.r} = f_y \cdot f_T \quad [MPa] \tag{2.17}$$

Where the reduction factor f_T is determined as in Equation 2.18:

$$f_T = 1 - 0,4 \cdot \sqrt{\frac{\sigma_x(M_z)}{\frac{f_y}{\gamma_{M0}}}} \tag{2.18}$$

The third mentioned capacity denoted as $M_{y.Rd.3}$ refers to the capacity of the girder limited by the global out-of-plane buckling of the compression flange. χ in the expression 2.16 c is a reduction factor related to instability.

The new draft of the EN1993-1-5 (2019) [6] suggests the same calculation procedure of the flexural resistance $M_{y.Rd}$, with the only difference lying in the elimination of the reduction factor f_T.

2.3.5 Normal stress buckling resistance of trapezoidally CWIG, in carbon steel, according to Jáger et al.

Buckling coefficient
In the current formulation of the EN1993-1-5 [5] (Equation 2.15), the constant term of the expression, $0,43$, is replaced by Jáger et al. [7] in order to consider the supporting effect of the web. The suggested replacement is as in Equation 2.19:

$$\kappa_{\sigma.Jager} = 0,43 \cdot \left(25,5 \cdot \frac{b_f/2}{h_w} \cdot \frac{t_w}{t_f}\right)^{0,6} + \left(\frac{c_f}{a_1 + 2 \cdot a_4}\right)^2 \tag{2.19}$$

Where h_w is the web height, and for the rest of the indications, reference is made to Figures 2.5 and 2.8. Further, there was an observation of a shift in failure modes of the flange plates at $t_f/t_w = 2,5$, marking the change in the rigidity of the support in the flange-to-web intersection. This is reflected in Equation 2.19 by replacing the term $25.5\, b_f/2/h_w$ with 2,5 as in Equation 2.20:

$$\kappa_{\sigma.Jager} = 0,43 \cdot \left(2,5 \cdot \frac{t_w}{t_f}\right)^{0,6} + \left(\frac{c_f}{a_1 + 2 \cdot a_4}\right)^2 \tag{2.20}$$

As can be seen, for $t_f/t_w = 2,5$ the first term in the expression becomes 0,43 (as in the EN1993-1-5 [5]), representing a plate simply supported on three edges (Figure 2.2). Further, the results of the numerical analyses have indicated a power relation between the buckling coefficient κ_σ and the inverse of t_f/t_w, related with the enclosing effect R as the exponent. This inclusion of R by Jáger et al. results in the final expression of $\kappa_{\sigma.Jager}$ according to Equation 2.21:

$$\kappa_{\sigma.Jager} = 0,43 \cdot \left(2,5 \cdot \frac{t_w}{t_f}\right)^{0,6+R} + \left(\frac{c_f}{a_1 + 2 \cdot a_4}\right)^2 \leq 1,3 \tag{2.21}$$

Buckling curve
Jáger et al. [7] concluded that the class 4 classification of $c_f/t_f > 14\epsilon$ proposed by the EN1993-1-5 [5] is appropriate for the large flange outstands of CWIG. Though, it was noted that the relative slenderness limit defining the transition between compact and slender (class 4) flange sub-plates needs to depend on the buckling coefficient κ_σ as well.

So, inserting the slenderness limit of:

$$c_f/t_f = 14\epsilon \implies c_f/t_f/\epsilon = 14$$

into the expression of the relative slenderness $\bar{\lambda}_p$ in Equation 2.8, the expression in Equation 2.22 is obtained:

$$\bar{\lambda}_{p.lim} = \frac{0,493}{\sqrt{\kappa_\sigma}} \tag{2.22}$$

Where $\bar{\lambda}_{p.lim}$ symbolizes the current slenderness limit for cross-section class 4.

So, an expression as in Equation 2.23 was formulated:

$$\rho = \left(\frac{\bar{\lambda}_{p.lim}}{\bar{\lambda}_p}\right)^\beta = \left(\frac{0,493}{\sqrt{\kappa_\sigma} \cdot \bar{\lambda}_p}\right)^\beta = ... = \left(14 \cdot \epsilon \cdot \frac{t_f}{c_f}\right)^\beta \leq 1,0 \tag{2.23}$$

Worth mentioning is that the reduction factor ρ was developed to be applied on the large flange outstand c_f, and not the whole flange width b_f.

The factor β is an index that was calibrated based on parametric studies to obtain a better fit of the obtained buckling curve in Equation 2.23 and the test results. The expression of β was developed to take into account the flange-to-web thickness ratio t_f/t_w, corrugation angle α and enclosing effect R, which were found to be weighing factors as discussed in Table 2.2. The calibration resulted in the following expression of β in Equation 2.24:

$$\beta = 5 \cdot \eta \cdot R \cdot \left(\frac{1}{\tan(\alpha)}\right)^\eta = 5 \cdot \eta \cdot R \cdot \left(\frac{a_4}{a_3}\right)^\eta \quad 0,5 < \beta < 1,0 \tag{2.24}$$

With the exponent η being as in Equation 2.25:

$$\eta = 0,45 + 0,06 \cdot \frac{t_f}{t_w} \tag{2.25}$$

The lower limitation of the index β to 0,5 is due to the irrelevancy of lower values, since they have been shown to lead to over-estimations of capacities [7].

2.3.6 Normal stress buckling resistance of trapezoidally CWIG, in carbon steel, according to the DASt-Richtlinie 015

The method proposed in the DASt-Richtlinie 015 [10] suggests the reduction of the compression flange as an effective width, $b_{f.eff}$, calculated as in Equation 2.26:

$$b_{f.eff} = 30,7 \cdot t_f \cdot \sqrt{\frac{240}{f_{yf}}} \leq b_f \tag{2.26}$$

2.4 Affecting parameters on normal stress buckling of trapezoidally CWIG in carbon steel

The following presented parameters affecting the normal stress buckling behavior of trapezoidally CWIG are based on the results of the experiments conducted by Jáger et al. (2017) [3, 7] on carbon steel specimens.

2.4.1 Flange-to-web thickness ratio

The flange-to-web thickness ratio t_f/t_w has been observed to heavily affect the rigidity of the support in the flange-to-web intersection. More specifically, at the lower range of the $t_f/t_w < 2,5$, the web can be seen as providing a rigid support, resulting in a separated buckling of the flange plate sub-panels. At higher $t_f/t_w > 2,5$, the stiffness of the support at the flange-to-web intersection transfers to a pinned support, and an unrestricted rotation of the flange plate is current as flange buckling failure instead. At more extreme t_f/t_w higher than 5, the web plate may undergo a flange induced buckling, where a part of the web at its intersection with the compression flange cripples locally along a fold length. The latter is observed in the post-failure range [3].

2.4.2 Enclosing effect and corrugation angle (corrugation geometry)

As a way to consider the overall geometry of the current corrugation configuration, the enclosing effect R (see Chapter 2.3.1) has been used by researchers in the studied subject of trapezoidally CWIG. It has been observed that higher values of R result in a weaker supporting condition of the compression flange in the experiments conducted by Jáger et al. [3]. The observation was made through the decreasing buckling coefficient κ_σ for identical flange-to-web thickness ratios t_f/t_w.

But, a certain corrugation configuration cannot be entirely described by the enclosing effect alone, instead, the corrugation angle α needs to be specified along with that. Consequently, the supporting effect of the corrugation, with respect to the corrugation geometry, needs to include the corrugation angle α. Corrugation angles approaching 0 have been shown to increase the web contribution in the flexural resistance. This is a result of higher web contribution in the axial load-carrying capacity, being increasingly similar to the behavior of flat web I-girders.

2.4.3 Summary of affecting parameters on normal stress buckling capacity

To summarize, the main affecting parameters on the normal stress buckling resistance of trapezoidally CWIG are presented below in Table 2.1.

Table 2.1: Overview of the affecting parameters on the normal stress buckling of flange plates in trapezoidally CWIG in carbon steel.

Parameter	Method	Observed effect	Buckling capacity
t_f/t_w	FE & experimental	Direct effect on the failure mode. At $t_f/t_w < 2,5$: separated buckling of flange subplates. At $t_f/t_w > 2,5$: unrestricted rotation of flange plate. Additionally, if $t_f/t_w > 5$: flange induced buckling of the web.	Higher $t_f/t_w \rightarrow$ Lower capacity
R	FE	Affecting the supporting effect of the web on the compression flange.	Higher $R \rightarrow$ Lower capacity
α	FE	Corrugation angles approaching 45^o lead to decreasing supporting effect of the flange.	$\alpha = 45^o \rightarrow$ Lowest capacity $\alpha < 45^o \rightarrow$ Among highest capacities $\alpha > 45^o \rightarrow$ Intermediate capacities

2.5 Stainless steel

This sub-chapter introduces the different types of stainless steels, and highlights the 3 relevant stainless steel groups used in building construction. Further, an overview of the mechanical properties of stainless steels is presented.

2.5.1 Types of stainless steels

According to [9], a common point for materials referred to as stainless steels is their chromium content, with the minimum value of 10,5% and their distinct resistance against corrosion and heat. In order to fit different applications, there are different sub-categories of stainless steels, characterized by varying alloying properties. There are 5 recognized groupings, with the 3 major ones in the context of building construction, and their primary properties listed in Table 2.2.

Table 2.2: Overview of general properties of the 3 most common stainless steel groups in building construction.

Type	Contents	Distinct properties	Compared with carbon steel	Applications
Austenitic	17-18% chromium 8-11% nickel	High ductility, adaptable to cold forming and welding	Superior toughness in a range of temperatures	Most commonly used in building construction
Ferritic	10,5-18% chromium ∼0% nickel	Reasonable resistance against stress corrosion cracking Lower weldability and ductility compared to Austenitic grades	Comparable with grade S355 steel, in machining and forming	Usually indoor applications and less harsh environments
Duplex	20-26% chromium 1-8% nickel	Superior strength, and resistance to stress corrosion cracking Adaptable to welding but less forming possibilities	Higher strength	Lightweight structures

There are further 2 groups of stainless steels, the *martensitic* and *precipitation hardening* stainless steels [9].

2.5.2 Mechanical properties of stainless steel

Stress-strain relationship

A major difference between stainless steels and ordinary carbon steels is the stress-strain behavior. A typical stress-strain curve for carbon steels demonstrates a clear distinction between the linear-elastic range and the initiation of plasticity at the yield stress f_y. The curve then exhibits a plateau, and strain hardening until failure. Stainless steels do not demonstrate the same behavior, since no clear yield limit can be distinguished. In order to define a corresponding yield strength for stainless steels, a definition of a so-called proof strength is used. It describes the stress that corresponds to a 0,2% plastic strain upon unloading, as shown in Figure 2.9 [9].

Comparing the different stainless steel grades (Figure 2.10), it can be observed that the strongest one is the duplex, with a highly nonlinear stress strain behavior. The ferritic grade exhibits lower strengths compared to duplex stainless steels, but still higher than carbon steels [9].

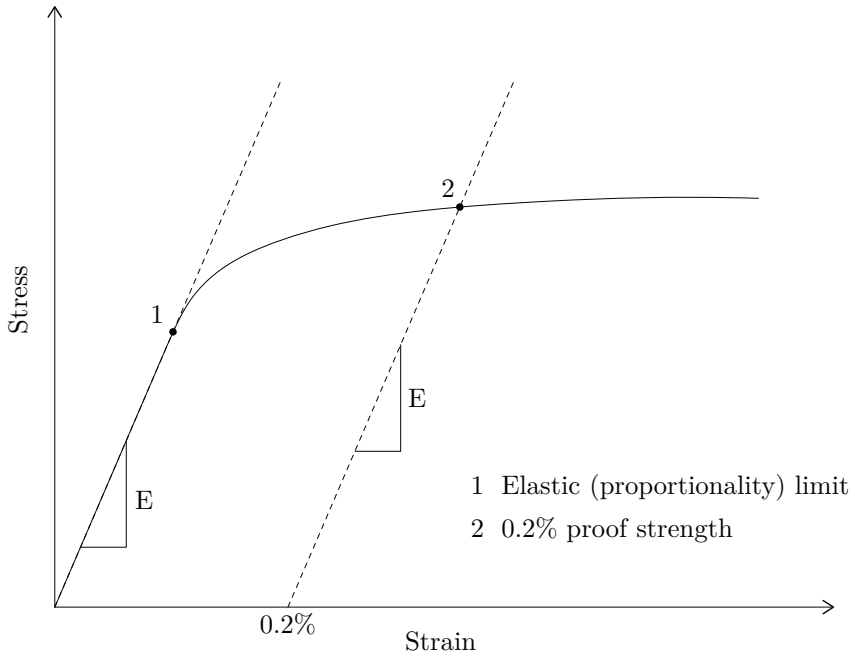

Figure 2.9: Illustration of the definition of proof strength. Adaptation from [9].

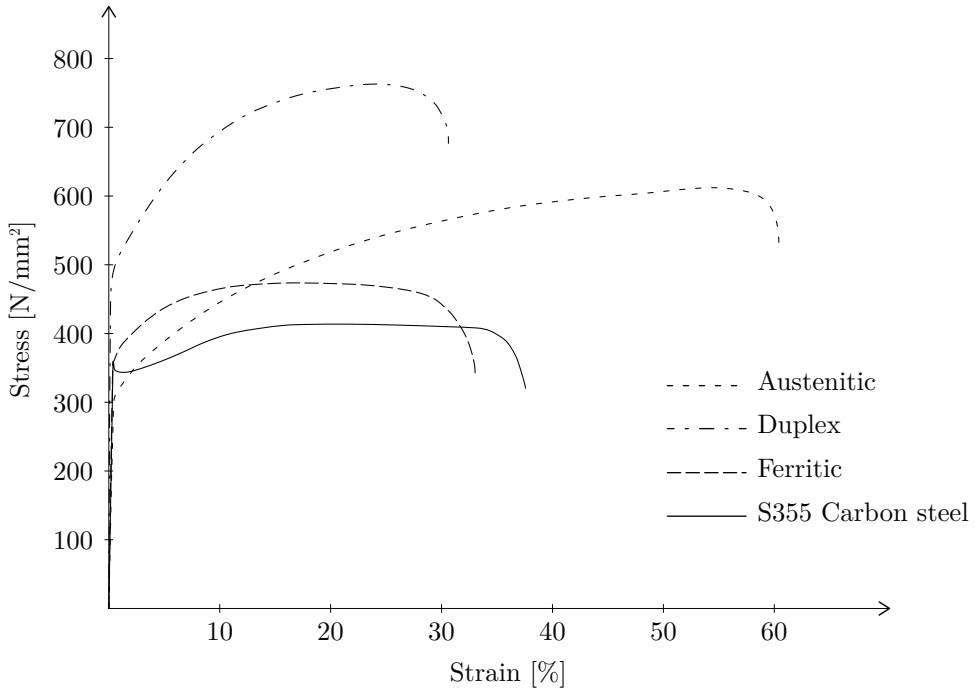

Figure 2.10: Full range stress-strain relations for stainless steel and carbon steel. Adaptation from [9].

Affecting factors on the stress-strain behavior

A way to increase the strength of steel materials is through *cold working*, with the downside of a minor reduction in ductility. This slightly negative effect is compensated by the highly increased initial ductility from the annealing. It needs to be

noted that the process of cold working leads to an anisotropy in the mechanical properties of the material. Further, a distinction needs to be made between the lower axial compressive strength and the tensile strength in both directions [9].

An additional increase in strength capacity of stainless steels can be obtained in higher *strain rates*, in comparison with carbon steel members [9].

3

Construction and validation of the FE model

The current chapter presents the construction and validation of the FE model used in the numerical study conducted in this thesis. The verification was made based on 4 out of the 16 experimental tests conducted by Jáger et al. (2017) [3], where each specimen was modelled and a suitable mesh size determined. The choice of 4 specimens covers all the observed failure modes of normal stress buckling. The core objects of the validation were the comparisons of ultimate moment capacities and failure modes.

3.1 The software

In all the FE models constructed in the current study, the analysis software ABAQUS CAE 2020 was implemented. It provides the necessary types of analyses of, among others, linear buckling and material and geometric nonlinear analysis. The software is also compatible with the Python programming language, making it suitable for parametric studies.

3.2 Mesh setting

The structural shell elements were deemed suitable for modelling the studied trapezoidally CWIG. These are appropriate to use in the context of thin-walled elements, and to describe both in-plane and out-of-plane bending as well as larger deformations. The two used elements in ABAQUS were the 4-noded, linear S4R and 8-noded, quadratic S8R shell elements. Both element types have 6 degrees-of-freedom at each node, 3 translational and 3 rotational.

3.3 Loading and boundary conditions

The applied boundary conditions in the models were a pinned and a roller in the axial direction (x). Both ends have a rotational restraint around the vertical (z) and longitudinal (x) directions. These two restraints ensure that the beam only bends around its major axis (y). Additionally, to ensure that the outer sections respect the condition of 'a plane section remaining plane', the shell edges of the web and flanges on both ends were tied to their corresponding section master middle points,

see Figure 3.1.

Proceeding to the loading condition, a moment around the major axis y was applied at the master middle points on either side.

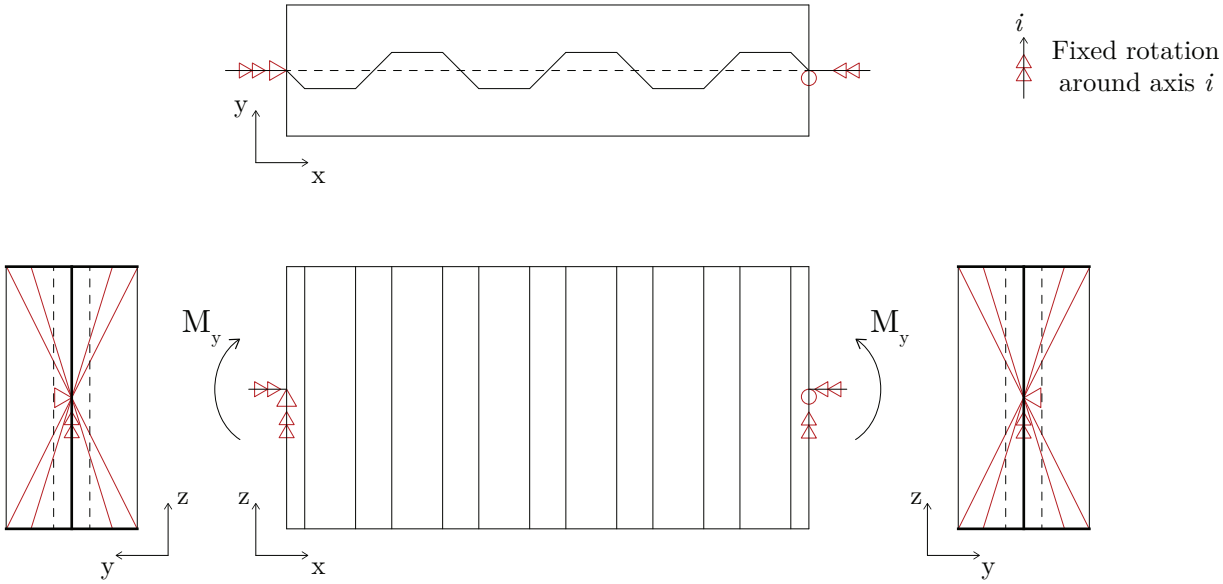

Figure 3.1: Illustration of the boundary and loading conditions used in all the studied models.

3.4 Material model of carbon steel

For the validation study conducted by Jáger et al. [3], after the failure of the specimens undamaged parts were collected from the flange and web plates and their yield f_y and ultimate f_u strengths were determined. In their model build and validation, a linear elastic - hardening plastic material model was implemented, as illustrated in Figure 3.2 was used [7]. The elastic stiffness was defined by a Young's modulus $E = 210000\,MPa$. The yield plateau starts at the end of the linear elastic part, defined by the strain $\varepsilon_{el} = f_y/E$, and the strain of $\varepsilon_{pl1} = 0,01$. The ultimate strength is assumed to be reached at the strain of $\varepsilon_{pl2} = 0,15$ [7].

The validation study in the current thesis is based on the same material model presented in Figure 3.2.

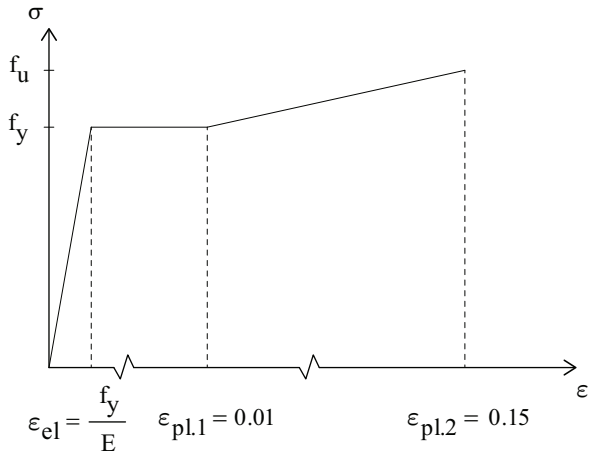

Figure 3.2: Used material model for carbon steel. Adaptation from Jáger et al. (2017) [7].

The Poisson ratio is taken as $\nu = 0,3$ in all cases for carbon steel.

3.5 Modelling of initial imperfections

In the current study, in order to reach a similar failure mode and ultimate capacity as the tested girders, the shape of the first eigenmode for each case was utilized. The latter was obtained through the linear buckling analysis and the magnitudes scaled with the measured initial geometric imperfections and introduced as the initial shapes of the FE models in the nonlinear analyses.

3.6 Validation of the FE model

This sub-chapter presents the experiments by Jáger et al. [3] used as reference to verify the constructed models. In total, four beams were modelled and verified, them being 2TP1-1, 7TP1, 9TP3 and 3TP1-1.

3.6.1 Description of the experimental setup of Jáger et al.

A four-point bending test arrangement was utilized by Jáger et al. [3] (Figure 3.3), with a total span length of $8\,m$ and the point loads applied $3,475\,m$ from each support. The central part of the beam consists of a $1,050\,m$ long, interchangeable corrugated test specimen, subjected to pure bending. The central part is attached to the external girder parts through an bolted connection with exaggerated dimensions, to provide a fixed connection. The beam is supported in the lateral direction at the points of load introduction to eliminate the possibility of lateral torsional buckling. The external girder parts are also overly stiffened.

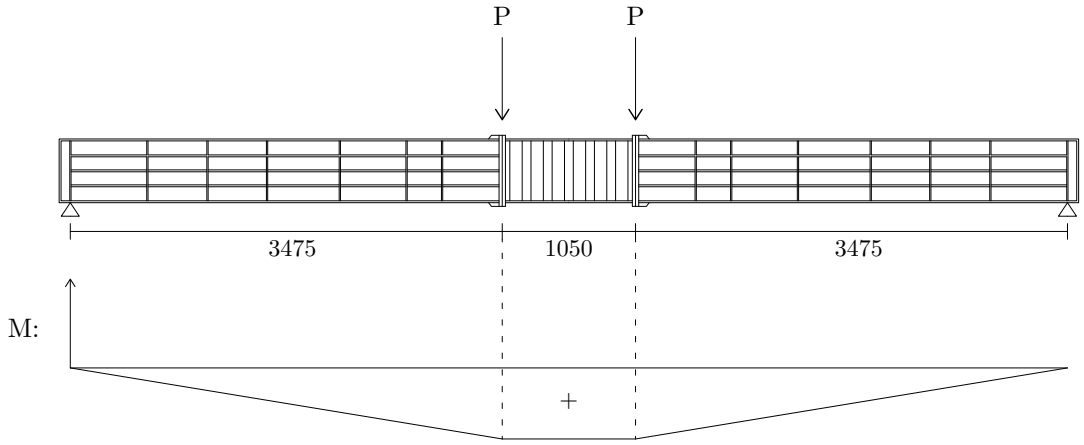

Figure 3.3: Illustration of the used four-point bending test in the experiments conducted by Jáger et al. (2017) [3].

To gather data on strains/stresses and displacements, strain gauges and displacement transducers were placed at different points in the flanges. The instruments were placed at the sections of the longitudinal folds closest to the middle and of the middle inclined fold. Focusing on the displacement transducers, there were two of them, where one was placed at the edge of the bottom flange at the mid-span section, and the second one at the opposite edge of the top flange at the section of one of the two adjacent longitudinal folds. Apart from measuring global displacements, these were used to collect data on the relative displacement of the top and bottom flange.

3.6.2 Geometries and material parameters

The chosen girders in the current validation process are 4, and have two different corrugation geometries, types TP1 and TP3. The former has a corrugation angle of 45 deg and the latter 30 deg, an overview of the geometric parameters of the girders is also presented in Table 3.1. There is a variation in flange and web thicknesses, but all specimens have the same web height of $h_w = 500\,mm$, and nominal flange width of $b_f = 250\,mm$.

No data on the thickness of the vertical stiffeners at the points of load application are presented in Jáger (2017) [3], but, in order to ensure a sufficiently high stiffness, these were modelled as 16 mm thick plates.

Table 3.1: Overview of the geometric parameters corresponding to each considered specimen of Jáger et al. [3].

Geometry						
Beam 2TP1-1						
a_1 [mm]	a_3 [mm]	$\alpha[^o]$	t_f [mm]	b_f [mm]	t_w [mm]	t_f/t_w
97	69	45	7,9	250	5,97	1,32
Beam 7TP1						
a_1 [mm]	a_3 [mm]	$\alpha[^o]$	t_f [mm]	b_f [mm]	t_w [mm]	t_f/t_w
97	69	45	12,2	250	3,84	3,18
Beam 9TP3						
a_1 [mm]	a_3 [mm]	$\alpha[^o]$	t_f [mm]	b_f [mm]	t_w [mm]	t_f/t_w
88	44	30	12,16	247	4,04	3,01
Beam 3TP1-1						
a_1 [mm]	a_3 [mm]	$\alpha[^o]$	t_f [mm]	b_f [mm]	t_w [mm]	t_f/t_w
97	69	45	14,59	250	3,01	4,85

As previously mentioned, all specimens from the experiment have been tested with regard to their yield and ultimate capacities, f_y and f_u, respectively. These are presented in Table 3.2, along with the corresponding ultimate elastic strain ε_{el}, based on the Young's modulus of $E = 210000\,MPa$.

As in the case of the geometry of the vertical stiffeners bounding the middle region, no data is provided on the material parameters of these members. In the current study, the same material parameters as for the flange plates was applied.

Table 3.2: Overview of the material parameters corresponding to each considered specimen of Jáger et al. [3].

Material parameters		
Beam 2TP1-1		
Flange		
f_y [MPa]	f_u [MPa]	ε_{el}
452	548	2,15e-03
Web		
f_y [MPa]	f_u [MPa]	ε_{el}
406	530	1,93e-03
Beam 7TP1		
Flange		
f_y [MPa]	f_u [MPa]	ε_{el}
364	496	1,73e-03
Web		
f_y [MPa]	f_u [MPa]	ε_{el}
474	584	2,26e-03
Beam 9TP3		
Flange		
f_y [MPa]	f_u [MPa]	ε_{el}
365	500	1,74e-03
Web		
f_y [MPa]	f_u [MPa]	ε_{el}
457	584	2,18e-03
Beam 3TP1-1		
Flange		
f_y [MPa]	f_u [MPa]	ϵ_{el}
387	516	1,84e-03
Web		
f_y [MPa]	f_u [MPa]	ϵ_{el}
363	514	1,73e-03

3.6.3 Girder 2TP1-1 of Jáger et al.

The first studied girder has a corrugation profile of type TP1, having a corrugation angle of 45 *deg*. The flange-to-web thickness ratio is 1,32 and, according to the results of the experiment, a separated flange buckling should be expected. The flange of the current specimen is the most slender one among the studied specimens.

3.6.3.1 Mesh convergence

The mesh sensitivity analysis was applied with respect to the first eigenvalue in the linear buckling analysis. The element sizes were determined based on even number of elements per longitudinal fold, starting with the most coarse mesh with 2 elements/fold, to the most dense with 10 elements/fold. The sensitivity analysis

was applied on the two considered element types of S4R and S8R. The results are presented in a diagram in Figure 3.4, and in Table 3.3 for S8R and Table 3.4 for S4R.

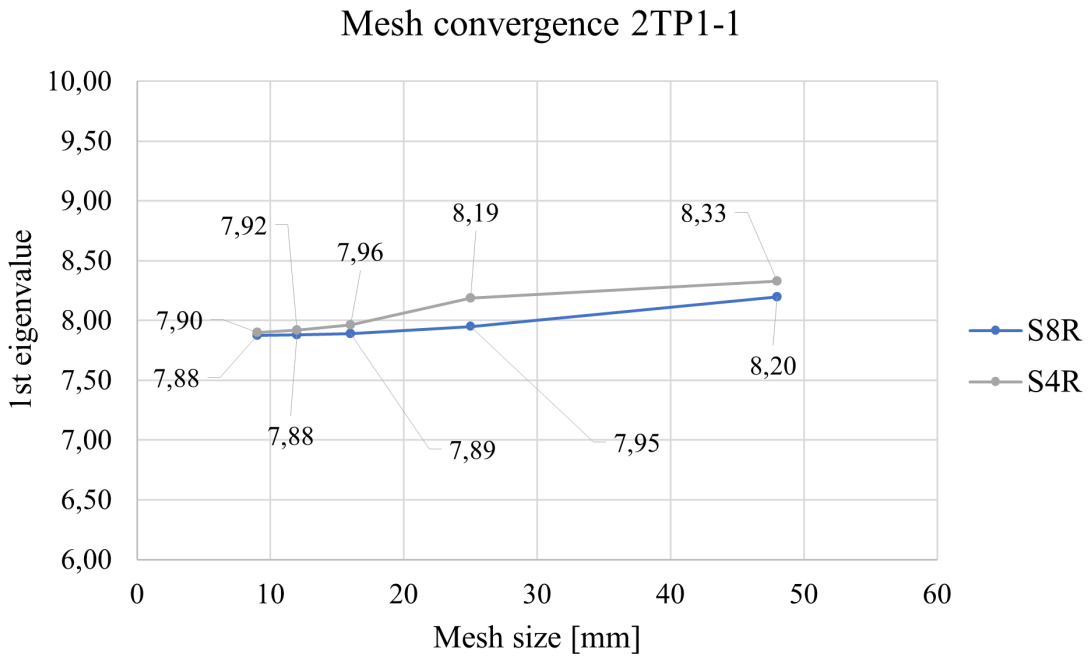

Figure 3.4: Plot of the mesh convergence study for specimen 2TP1-1.

Table 3.3: Mesh convergence study for 2TP1-1, type S8R.

S8R			
Mesh size [mm]	Per longitudinal fold	Eigenvalue	Relative diff
48	**2**	**8,20**	**1,041**
25	4	7,95	1,009
16	6	7,89	1,002
12	8	7,88	1,001
9	10	7,88	1

Table 3.4: Mesh convergence study for 2TP1-1, type S4R.

S4R			
Mesh size [mm]	Per longitudinal fold	Eigenvalue	Relative diff
48	2	8,33	1,054
25	**4**	**8,19**	**1,037**
16	6	7,96	1,008
12	8	7,92	1,003
9	10	7,90	1

As can be observed from the tables above, the S8R elements can be considered as converged already at 2 elements per longitudinal fold, since a relative difference of

diff $\approx$ 4% is obtained. For the linear S4R elements a finer mesh was required to obtain a convergence, with 4 elements per longitudinal fold. The element type S8R was chosen to proceed with, with a mesh density corresponding to 4 elements per longitudinal fold.

3.6.3.2 Linear buckling analysis

The linear buckling analysis on specimen 2TP1-1 resulted in a critical moment of $M_{cr.num} = 796\ kNm$ for the first eigenmode. The resulting shape is presented in Figure 3.5, where a separated flange buckling is observed, see Chapter 2.4.1.

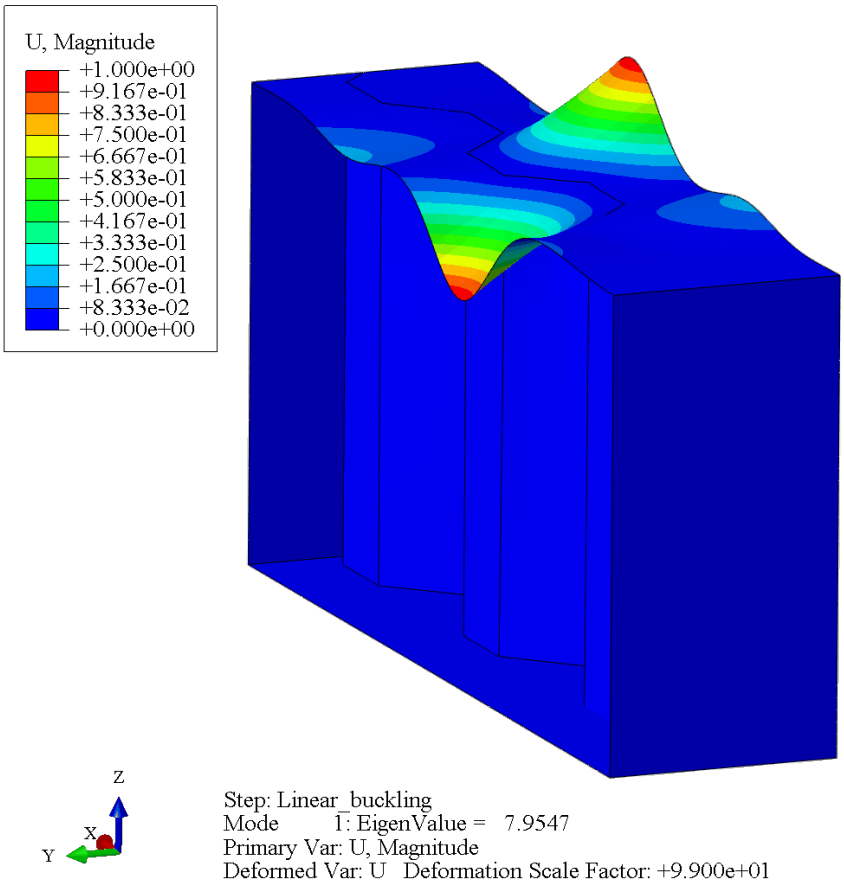

Figure 3.5: First obtained eigenmode for specimen 2TP1-1. U represents combined displacement magnitude.

3.6.3.3 Ultimate capacity from the nonlinear analysis

Applying the initial geometric imperfection amplitude on the first eigenmode (Figure 3.5) and conducting a material and geometric nonlinear analysis, result in what is shown in Table 3.5, where the initial geometric imperfection is also presented. The ultimate moment capacity of $M_{ult.num.geo} = 408\ kNm$ was obtained in the FE analysis, compared to the experimental result of $M_{exp} = 369\ kNm$ leading to an overestimation of 11%. This can be explained by the major difference in the applied

first eigenmode shape and the actual measured distribution of initial imperfections of the specimen (Figure 3.6).

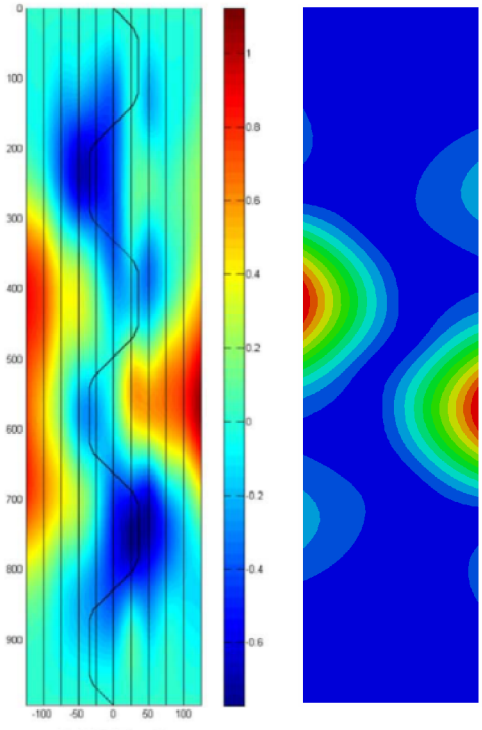

Figure 3.6: Comparison of the measured initial geometric imperfections of specimen 2TP1-1 (left) and the obtained first eigenmode shape (right).

Comparing the failure modes (Figure 3.7), it is visible that they correspond to the first eigenmode shape, where a separated buckling is noted. The limit value of $t_f/t_w < 2,5$ for separated buckling, suggested in the literature (see Chapter 2.4.1), is also respected since the current ratio is $t_f/t_w = 1,32$ (Table 3.1). This adds to the reliability of the model in the current state, since the first of the three distinguished failure modes is successfully described.

Table 3.5: Initial geometric imperfection, and ultimate moment capacities for specimen 2TP1-1.

2TP1-1	
Initial imperfection [mm]	1,1
$M_{ult.num.geo}$ [kNm]	408
M_{exp} [kNm]	369
Relative diff.	1,11

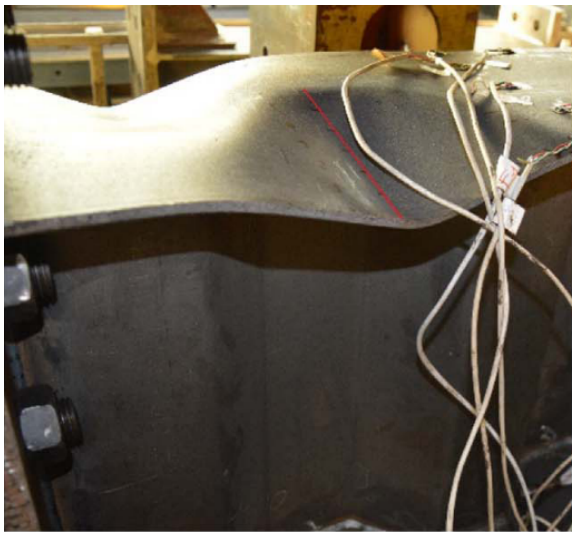

(a) Failure mode of specimen

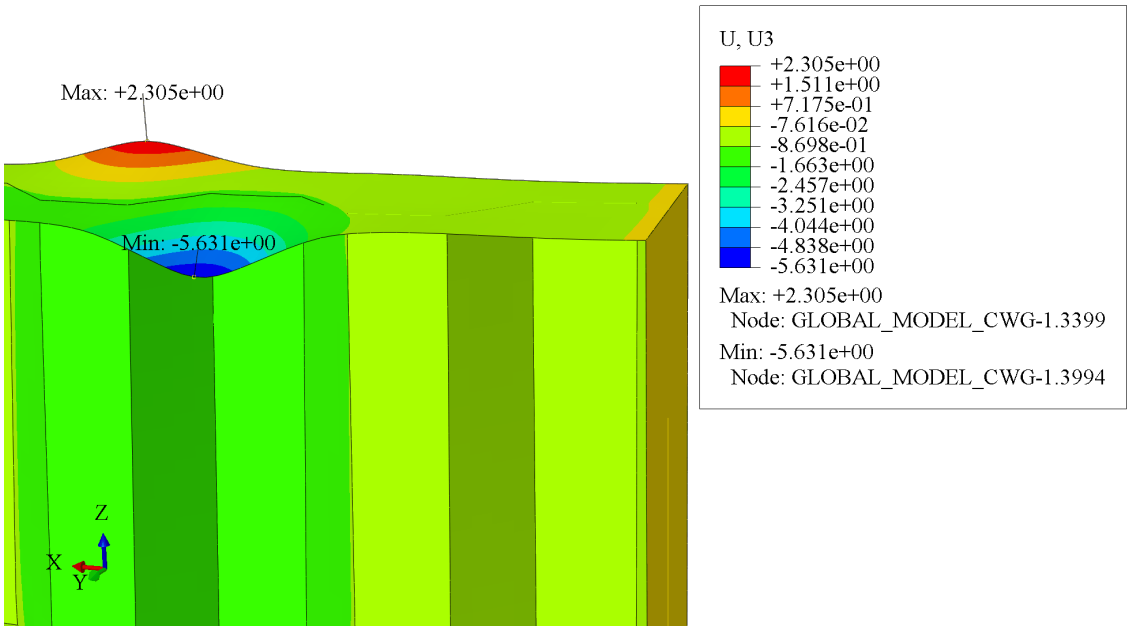

(b) Failure mode of FE model

Figure 3.7: Comparison of the failure modes of specimen 2TP1-1 in the physical experiment by Jáger et al. [3] (a) and the nonlinear FE analysis at the occurrence of flange buckling (b). Vertical displacement *U3* in *mm*.

3.6.4 Girder 7TP1 of Jáger et al.

Specimen 7TP1 has also a corrugation angle of 45 *deg* and the flange-to-thickness ratio of 3,18, implying an unrestricted rotation of the compression flange in the ultimate state, according to the results of the experiments.

3.6.4.1 Mesh convergence

For the FE model of specimen 7TP1, a convergence was observed at 4 elements per longitudinal fold, as shown in Tables 3.6 and 3.7 for elements S8R and S4R, respectively. A drastic drop in relative difference was observed between the mesh sizes corresponding to 2 and 4 elements/fold for type S8R as seen in Figure 3.8, dropping from a relative difference of 5,1% to 1,2%. On the other hand, for type S4R, the corresponding difference is negligible, more specifically 4,4% to 4,1%. In the following, the element type S8R was implemented with 4 elements per longitudinal fold.

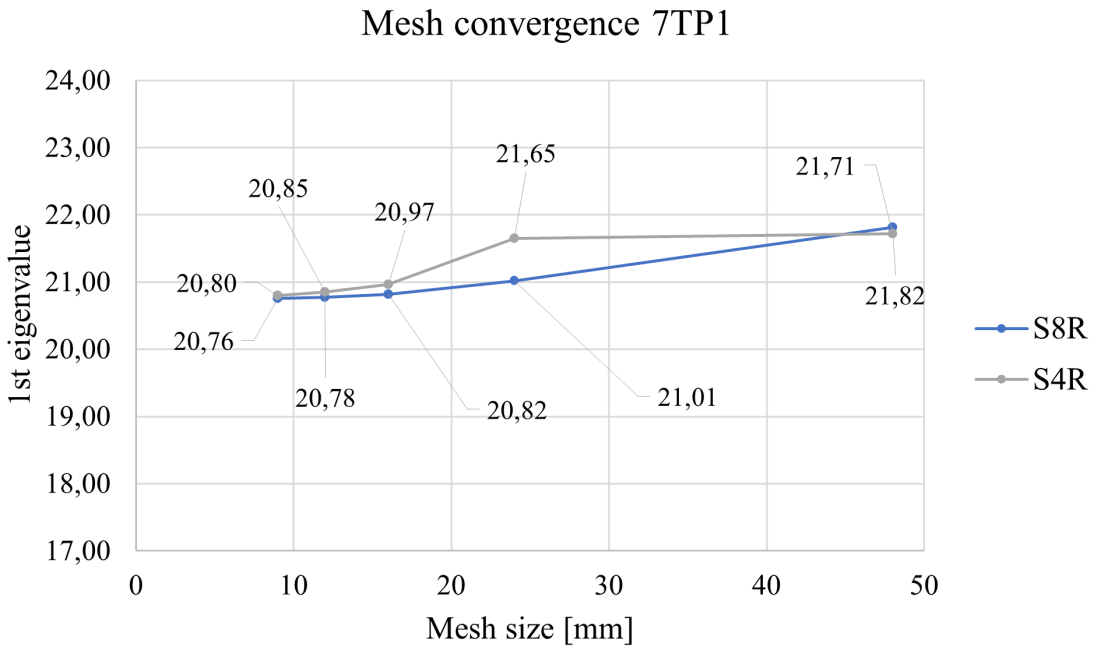

Figure 3.8: Plot of the mesh convergence study for specimen 7TP1.

Table 3.6: Mesh convergence study for 7TP1, type S8R.

S8R			
Mesh size [mm]	Per longitudinal fold	Eigenvalue	Relative diff
48	2	21,82	1,051
24	**4**	**21,01**	**1,012**
16	6	20,82	1,003
12	8	20,78	1,001
9	10	20,76	1

Table 3.7: Mesh convergence study for 7TP1, type S4R.

S4R			
Mesh size [mm]	Per longitudinal fold	Eigenvalue	Relative diff
48	2	21,71	1,044
24	**4**	**21,65**	**1,041**
16	6	20,97	1,008
12	8	20,85	1,002
9	10	20,80	1

3.6.4.2 Linear buckling analysis

The first eigenmode from the linear buckling analysis for the model of specimen 7TP1 is shown in Figure 3.9, with a critical moment of $M_{cr.num} = 2101\ kNm$. Contrary to specimen 2TP1-1, an unrestricted flange rotation can be noted in this eigenmode.

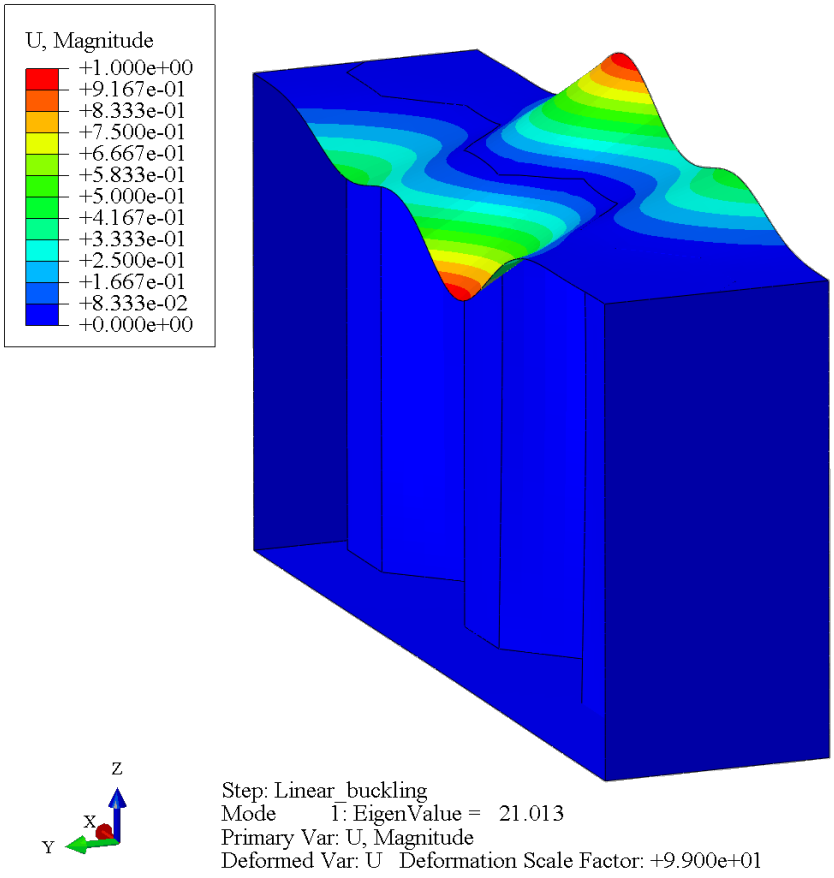

Figure 3.9: First obtained eigenmode for specimen 7TP1. U represents combined displacement magnitude.

3.6.4.3 Ultimate capacity from the nonlinear analysis

The nonlinear analysis resulted in an ultimate moment capacity of $M_{ult.num.geo} = 553\,kNm$ compared to the actual capacity of $M_{exp} = 588\,kNm$ with an underestimation of 6% (Table 3.8). The difference is negligible and the results are considered being in good correspondence. The observed failure modes follow the first eigenmode (Figure 3.9), demonstrating an unrestricted rotation of the flange plate. The literature suggests the expectancy of unrestricted flange rotation at $t_f/t_w > 2,5$ (see Chapter 2.4.1), which is the current case with $t_f/t_w = 3,18$, and the actual failure mode.

Table 3.8: Initial geometric imperfection, and ultimate moment capacities for specimen 7TP1.

7TP1	
Initial imperfection [mm]	1,22
$M_{ult.num.geo}$ [kNm]	553
M_{exp} [kNm]	588
Relative diff.	0,94

(a) Failure mode of specimen

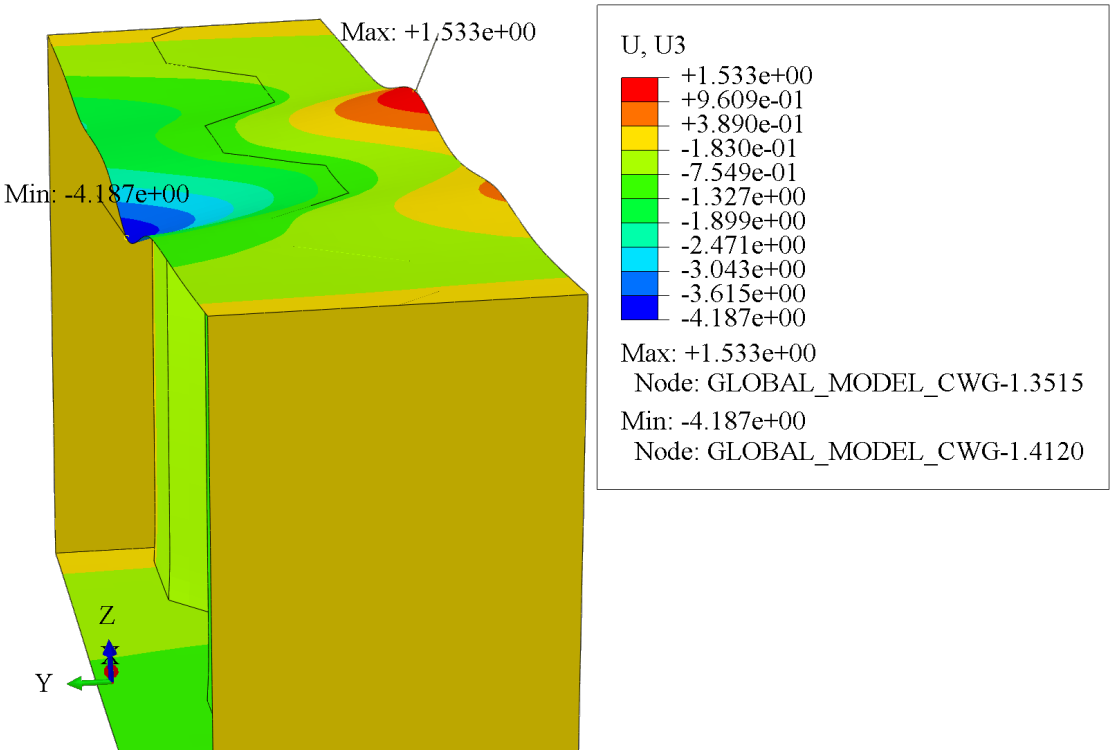

(b) Failure mode of FE model

Figure 3.10: Comparison of the failure modes of specimen 7TP1 in the physical experiment by Jáger et al. [3] (a) and the nonlinear FE analysis at the occurrence of flange buckling (b). Vertical displacement *U3* in *mm*.

3.6.5 Girder 9TP3 of Jáger et al.

The corrugation profile of the current specimen is TP3, having the lower corrugation angle $\alpha = 30\,deg$. The flange-to-web thickness ratio is 3,01, meaning that an unrestricted rotation of the compression flange is to be expected, according to the results of the experiments.

3.6.5.1 Mesh convergence

In the current model of specimen 9TP3, the allowance of a coarse mesh was implied for both element types of S8R and S4R, as seen in Figure 3.12 and Tables 3.9 and 3.10. For S8R, the relative difference between the coarse (2 elements/longitudinal fold) and the finest (10 elements/longitudinal fold) meshes is only 2,2%. Correspondingly, for S4R, the difference is 4%. Despite the mentioned, the same mesh density as for the previous models was applied, with 4 elements per longitudinal fold and S8R.

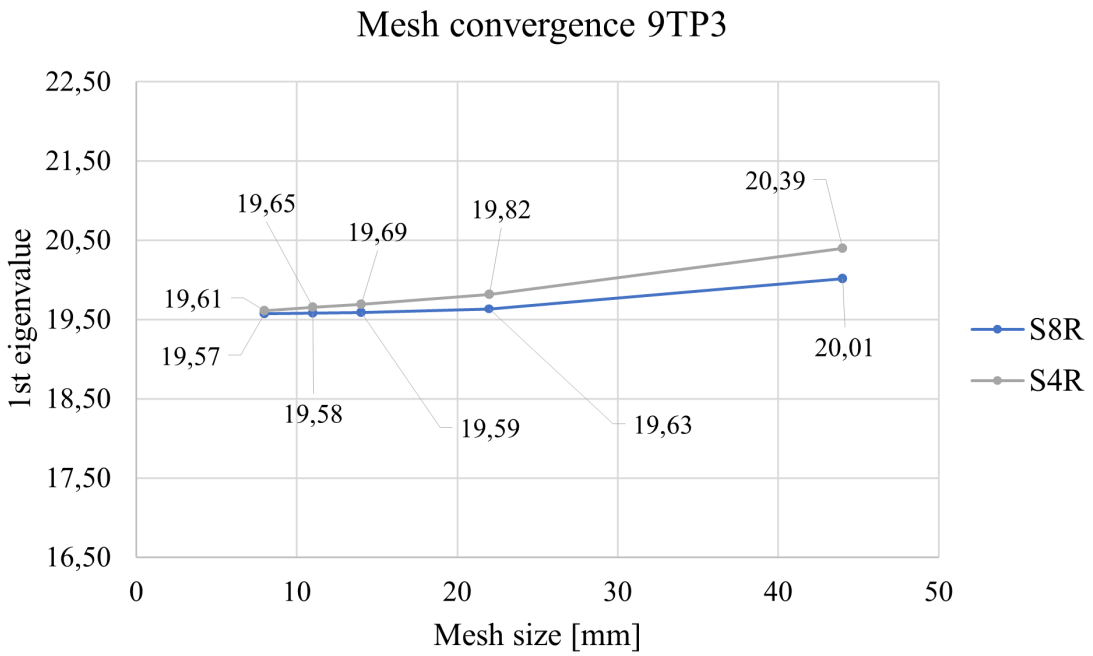

Figure 3.11: Plot of the mesh convergence study for specimen 9TP3.

Table 3.9: Mesh convergence study for 9TP3, type S8R.

S8R			
Mesh size [mm]	Per longitudinal fold	Eigenvalue	Relative diff
44	**2**	**20,01**	**1,022**
22	4	19,63	1,003
14	6	19,59	1,001
11	8	19,58	1,000
8	10	19,57	1

Table 3.10: Mesh convergence study for 9TP3, type S4R.

S4R			
Mesh size [mm]	Per longitudinal fold	Eigenvalue	Relative diff
44	**2**	**20,39**	**1,040**
22	4	19,82	1,011
14	6	19,69	1,004
11	8	19,65	1,002
8	10	19,61	1

3.6.5.2 Linear buckling analysis

The linear buckling analysis resulted in a critical moment of $M_{cr.num} = 1963\ kNm$ for the model of specimen 9TP3 and a first eigenmode demonstrating an unrestricted rotation of the flange (Figure 3.12). Comparing with the previous specimen, 7TP1, the similar mode was observed with the unrestrained rotation of the flange. The major difference lies in the larger buckling length in the current case of 9TP3, possibly owing to the lower corrugation angle α.

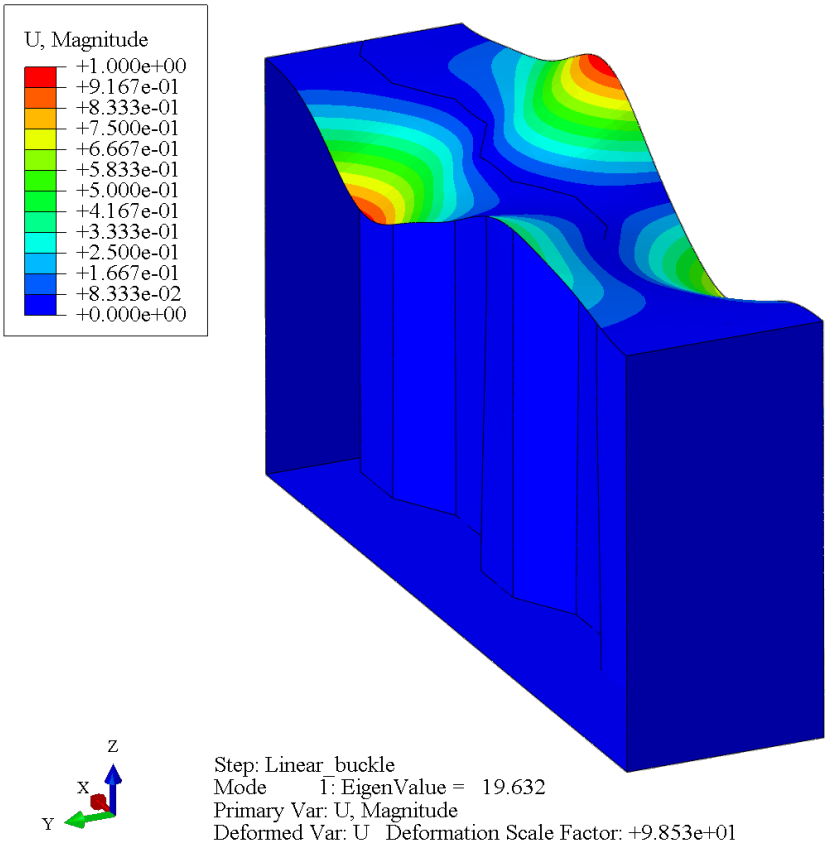

Figure 3.12: First obtained eigenmode for specimen 9TP3. U represents combined displacement magnitude.

3.6.5.3 Ultimate capacity from the nonlinear analysis

The ultimate capacity from the nonlinear analysis of the current specimen resulted in $M_{ult.num.geo} = 558\,kNm$, compared to the actual measured capacity of $M_{exp} = 585\,kNm$ (Table 3.11). The underestimation is 5%, which is within an acceptable range. The same buckling behavior or unrestricted flange rotation is noted here, as demonstrated in Figure 3.13. Similar to specimen 7TP1, the $t_f/t_w = 3,01 > 2,5$, implying an unrestricted flange rotation, according to the literature (see Chapter 2.4.1).

Table 3.11: Initial geometric imperfection, and ultimate moment capacities for specimen 9TP3.

9TP3	
Initial imperfection [mm]	1,42
$M_{ult.num.geo}$ [kNm]	558
M_{exp} [kNm]	585
Relative diff.	0,95

As a further step in verifying the FE model, the available data on relative flange displacement of 9TP3 was used. The comparison made is presented in Figure 3.14. What can be observed is that the initial stiffnesses are aligning to a satisfactory degree.

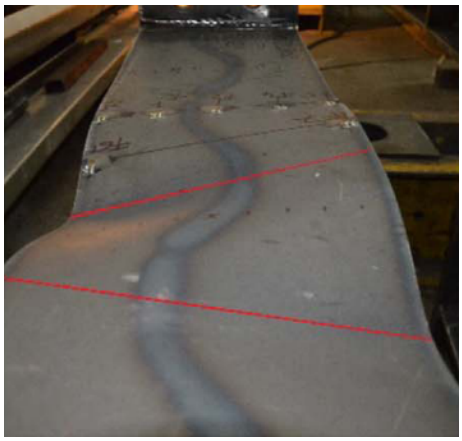

(a) Failure mode of specimen

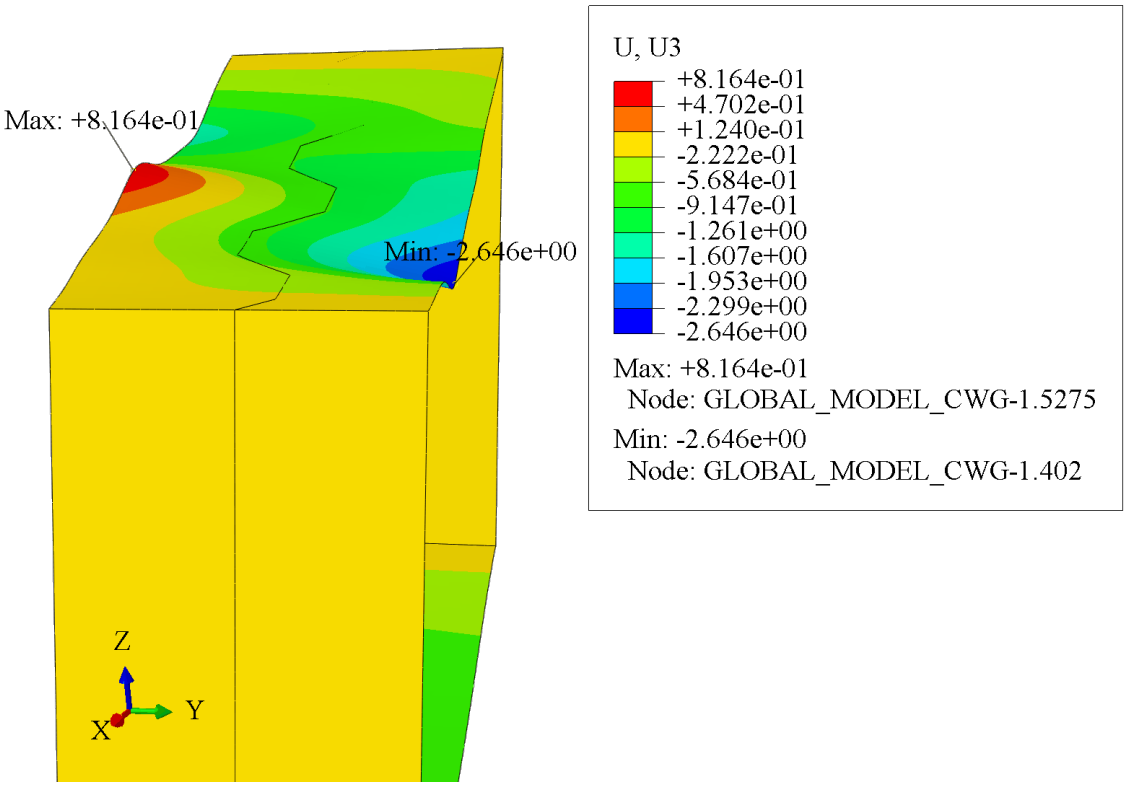

(b) Failure mode of FE model

Figure 3.13: Comparison of the failure modes of specimen 9TP3 in the physical experiment by Jáger et al. [3] (a) and the nonlinear FE analysis at the occurrence of flange buckling (b). Vertical displacement *U3* in *mm*.

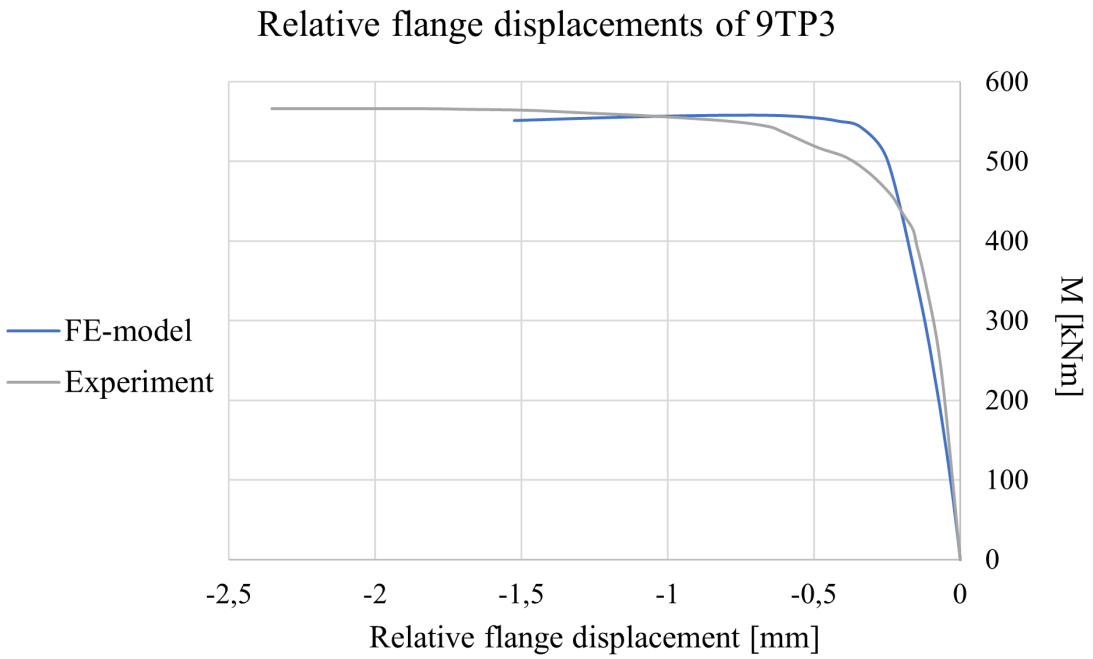

Figure 3.14: Comparison of the relative flange displacements between the FE-model and the experiment for specimen 9TP3.

3.6.6 Girder 3TP1-1 of Jáger et al.

The last studied specimen is 3TP1-1, having a corrugation profile of type TP1 with a corrugation angle $\alpha = 45\,deg$. The flange-to-web thickness ratio is the highest among the studied specimens, having a magnitude of 4,85. The experimental results showed that a flange induced buckling of the web should be expected at this level of magnitude.

3.6.6.1 Linear buckling analysis

The results of the mesh convergence analyses was utilized in the current model, that being the use of S8R elements, with 4 elements per longitudinal fold. The linear buckling analysis on the model of specimen 3TP1-1 also resulted in a first eigenmode with an unrestricted rotation of the flange plate. The critical moment in the current case is $M_{cr.num} = 3150\,kNm$.

What is a novelty in this case is that an area in an inclined fold of the web plate close to the compression flange is affected (Figure 3.15). This is demonstrated by a displacement in that area, which is non-zero, contrary to the case in the specimens discussed earlier, where all displacements in the web were 0.

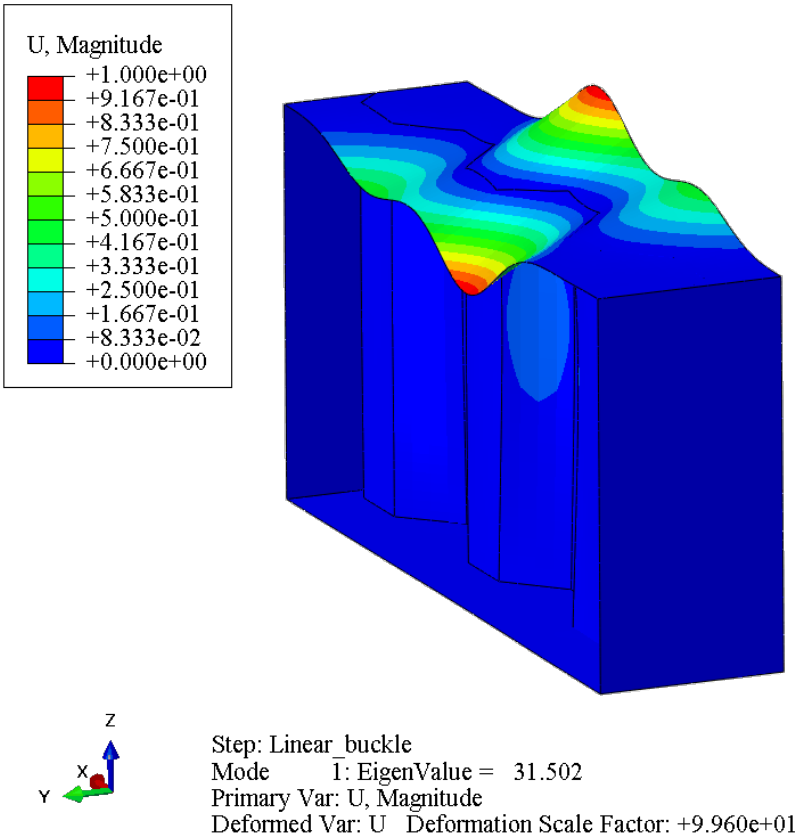

(a) First eigenmode of the specimen

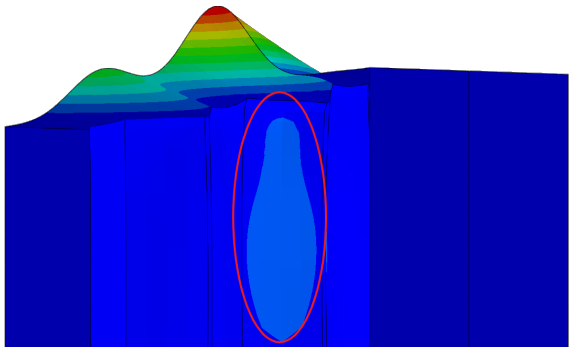

(b) A closeup, indicating the affected web

Figure 3.15: First obtained eigenmode for specimen 3TP1-1, indicating the affected web. U represents combined displacement magnitude.

3.6.6.2 Ultimate capacity from the nonlinear analysis

The model of specimen 3TP1-1 demonstrated an ultimate capacity of $M_{ult.num.geo} = 713\,kNm$, being 4% lower compared to the measured moment of $M_{exp} = 743\,kNm$, as presented in Table 3.12. Of interest in the case of the studied model is in the post-failure range, where a so-called flange induced buckling of the web was observed in the experiment (Figure 3.16a). The literature suggests the expectancy of this mode in girders with $t_f/t_w \approx 5$ or higher (see Chapter 2.4.1), with the current girder

having a $t_f/t_w = 4,85$. As can be seen in Figure 3.16 b, the mentioned mode is clearly visible in the last studied load step.

Table 3.12: Initial geometric imperfection, and ultimate moment capacities for specimen 3TP1-1.

3TP1-1	
Initial imperfection [mm]	1,2
$M_{ult.num.geo}$ [kNm]	713
M_{exp} [kNm]	743
Relative diff.	0,96

(a) Failure mode of specimen

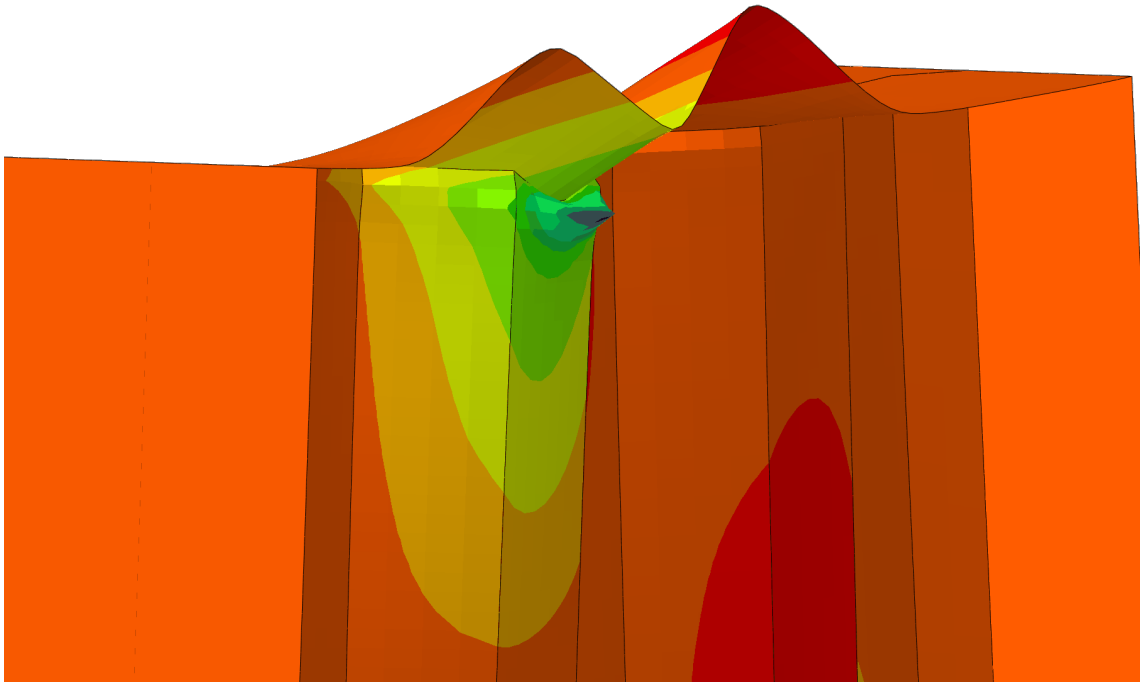

(b) Failure mode of FE model

Figure 3.16: Comparison of the failure modes of specimen 3TP1-1 in the physical experiment by Jáger et al. [3] (a) and the nonlinear FE analysis at the last studied increment in post-failure (b).

3.7 Discussion

The validation process presented in this chapter has revealed that the constructed model is able to describe all the observed failure modes of normal stress buckling of the compression flange in trapezoidally CWIG, as obtained by Jáger et al. [3].

The first mode is relevant in the lower range of flange-to-web thickness ratios t_f/t_w (lower than 2,5), which is the separated buckling of the subplates in the flange. The relevant specimen for this mode was the 2TP1-1, where the model had a clear resemblance to the tested girder. The second mode is the unrestricted rotation of the

flange plate, relevant for higher t_f/t_w (higher than 2,5), and in the current study, it was specimens 7TP1 and 9TP3. The analyses conducted on these models also provided similar failure modes, further increasing the credibility of the constructed models. Lastly, at more extreme t_f/t_w approaching 5, a third and last mode has been observed in the physical experiments, visible in the post-failure range. The mentioned mode is the flange induced buckling of the web, which was also reflected in the conducted nonlinear analysis of the specimen.

Apart from the modes, the ultimate capacities of the studied specimens corresponded to a satisfactory degree, ranging from underestimations of 4% to an overestimation of 11%. The pattern that was observed was that specimen 2TP1-1 with the more slender flange, and lower t_f/t_w demonstrated the largest deviation in ultimate moment capacities (11%). In the constructed model, the initial distribution of geometric imperfections was assumed to correspond to the first eigenmode shape, which was not the case in reality. The latter could be the a major influencing factor in the comparatively larger overestimation of 11%.

The chosen element type for the meshes was the quadratic S8R element, with a mesh density corresponding to 4 elements per longitudinal fold, since all models showed a clear convergence at this level of accuracy.

4

Model extension to Duplex 1.4162 stainless steel

This chapter describes the used material model for the current stainless steel grade of Duplex 1.4162, used in the following analyses. Further, the material of the studied specimens in Chapter 3 was replaced with the Duplex 1.4162, being the most commonly used grade in bridge girders. The general observed behavior is presented here, followed by a comparison with their carbon counterparts. The chapter is concluded with the determination of a suitable equivalent geometric imperfection, through a simplified imperfection sensitivity analysis, for the used stainless steel grade.

4.1 Material model for Duplex 1.4162

The adopted method for modelling the material behavior for Duplex 1.4162 in the current study is the one suggested in the EN1993-1-4 [13]. The stress-strain behavior of stainless steel is characterized by strong nonlinearity, and the expressions for the engineering strain ε are as shown in Equation 4.1:

$$\varepsilon = \begin{cases} \frac{\sigma}{E} + 0,002 \left(\frac{\sigma}{f_y}\right)^n & \text{for } \sigma \leq f_y \\ 0,002 + \frac{f_y}{E} + \frac{\sigma - f_y}{E_y} + \varepsilon_u \left(\frac{\sigma - f_y}{f_u - f_y}\right)^m & \text{for } f_y < \sigma \leq f_u \end{cases} \tag{4.1}$$

Where:
σ is the engineering stress.
f_y and f_u are the material yield (proof) and ultimate strength, respectively.
E is Young's modulus for the material.
The value for the coefficient n is suggested as 5 for the current Duplex grade.
The coefficient m is as presented in Equation 4.2:

$$m = 1 + 3,5\frac{f_y}{f_u} \tag{4.2}$$

The ultimate strain ε_u is determined as in Equation 4.3:

$$\varepsilon_u = 1 - \frac{f_y}{f_u} \tag{4.3}$$

E_y corresponds to the tangent modulus of elasticity of the stress-strain relationship, at the yield strength, calculated as in Equation 4.4:

$$E_y = \frac{E}{1 + 0,002n\frac{E}{f_y}} \tag{4.4}$$

In the implementation of the stress-strain values in the modelling software ABAQUS, it is the true stress, σ_{true}, and true plastic strain, $\varepsilon_{true.plastic}$ that were used. These are determined as shown in Equations 4.5 and 4.6:

$$\sigma_{true} = \sigma\,(1 + \varepsilon) \tag{4.5}$$

$$\varepsilon_{true.plastic} = \varepsilon_{true} - \frac{\sigma_{true}}{E} \tag{4.6}$$

Where the expression for the true strain ε_{true} is in Equation 4.7:

$$\varepsilon_{true} = \ln\,(1 + \varepsilon) \tag{4.7}$$

The current stainless steel grade is the Duplex 1.4162, and the relevant material parameters used in the current study are in accordance with the 2015 amendment of the EN1993-1-4 [14]. Young's modulus E is suggested as $200000\,MPa$, and Poisson's ratio as $\nu = 0,3$ and the used stress-strain parameters for different plate thicknesses in the FE analyses are presented in Table 4.1.

Table 4.1: The true stress σ_{true} and corresponding true, plastic strain $\varepsilon_{true.plastic}$ for Duplex 1.4162 and different relevant plate thicknesses.

Duplex 1.4162					
t≤6,4 mm		6,4<t≤10 mm		10<t≤75 mm	
σ_{true}	$\varepsilon_{true.plastic}$	σ_{true}	$\varepsilon_{true.plastic}$	σ_{true}	$\varepsilon_{true.plastic}$
532	0	482	0	452	0
543	0,00217	492	0,00219	462	0,00409
563	0,00296	503	0,00249	483	0,00573
585	0,00567	523	0,00389	504	0,01187
610	0,01267	570	0,01567	586	0,04299
699	0,0694	655	0,06784	703	0,13794
876	0,22	887	0,26076	856	0,40498

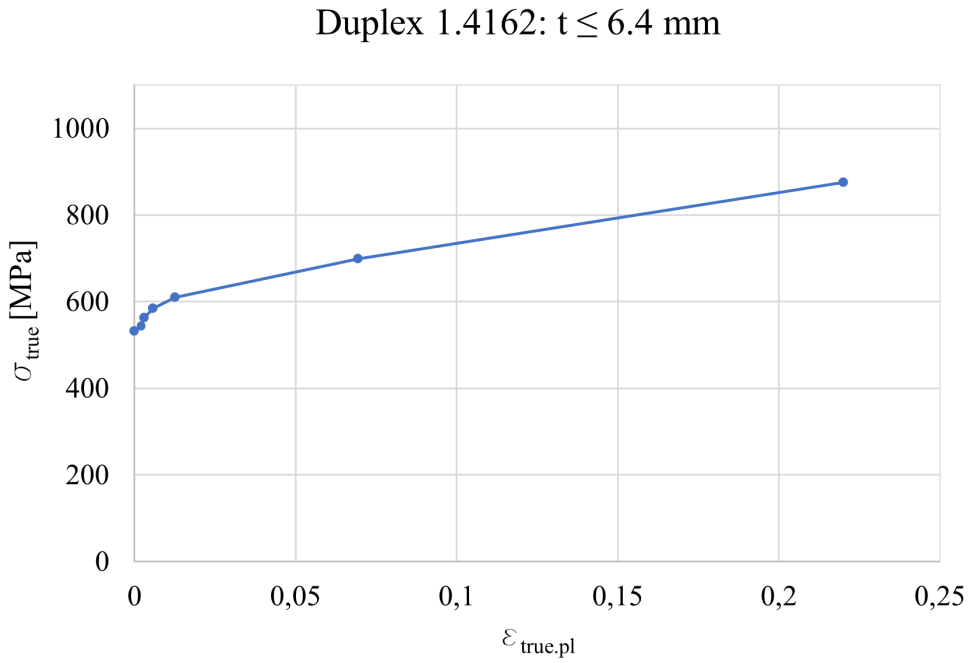

Figure 4.1: True stress σ_{true} against true plastic strain $\varepsilon_{true.plastic}$, for plates with $t \leq 6{,}4\ mm$ in Duplex 1.4162.

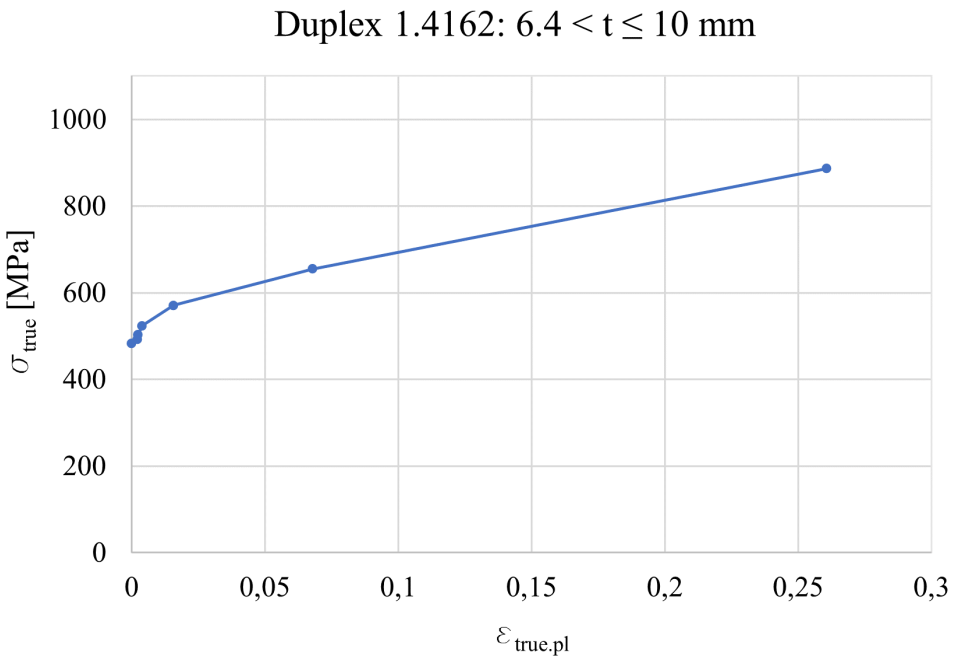

Figure 4.2: True stress σ_{true} against true plastic strain $\varepsilon_{true.plastic}$, for plates with $6,4 < t \leq 10$ mm in Duplex 1.4162.

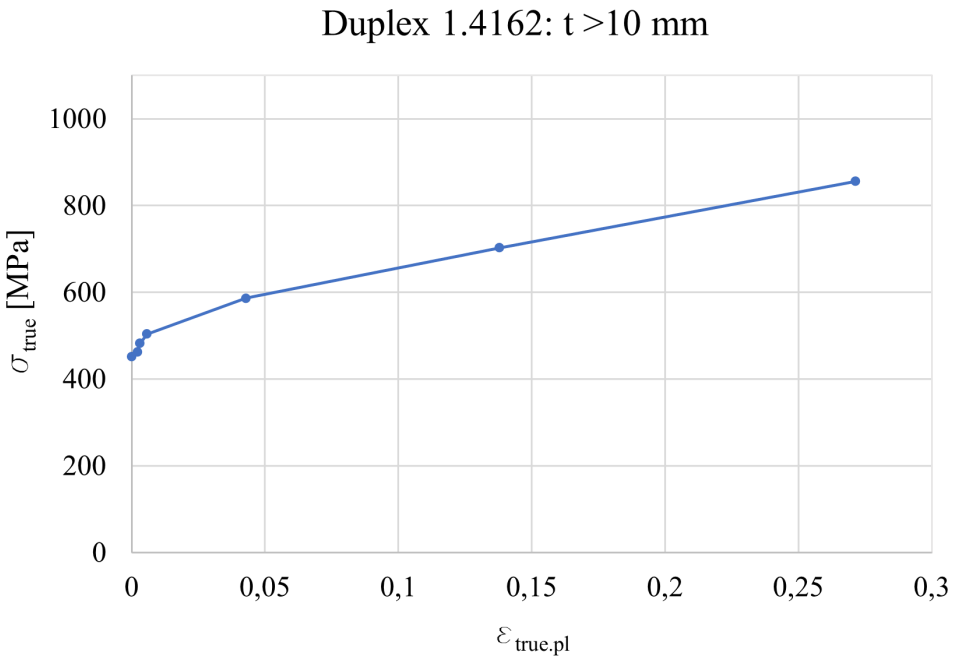

Figure 4.3: True stress σ_{true} against true plastic strain $\varepsilon_{true.plastic}$, for plates with $t > 10$ mm in Duplex 1.4162.

4.2 Behavior of test specimens with Duplex 1.4162 material model

In the current sub-chapter, the observed behavior of the specimens modelled and used for the verification in Chapter 3 is presented, replacing the material properties to the ones corresponding to Duplex 1.4162 (see Table 4.1). A distinction in behavior was made between specimens 2TP1-1 & 7TP1 and 9TP3 & 3TP1-1, where the former demonstrated elastic buckling and did not reach their yield capacities M_{yield}.

In Figure 4.4, the obtained load-displacement relation for the modelled specimen 2TP1-1 is illustrated, with 3 points of interest being marked, where 1: point of yield initiation; 2: ultimate capacity; 3: further into the post-failure range. For the current specimen 2TP1, yielding was initiated in the middle region of the compression flange only. Upon reaching the ultimate capacity, the model demonstrated two distinct yielding strips across the compression flange, with no yielding in the tension flange, suggesting elastic buckling of the compression flange. In post-failure, the compression flange has a concentrated yielding region in the area of observed normal stress buckling. A similar behavior was noted for specimen 7TP1, which is therefore not treated here.

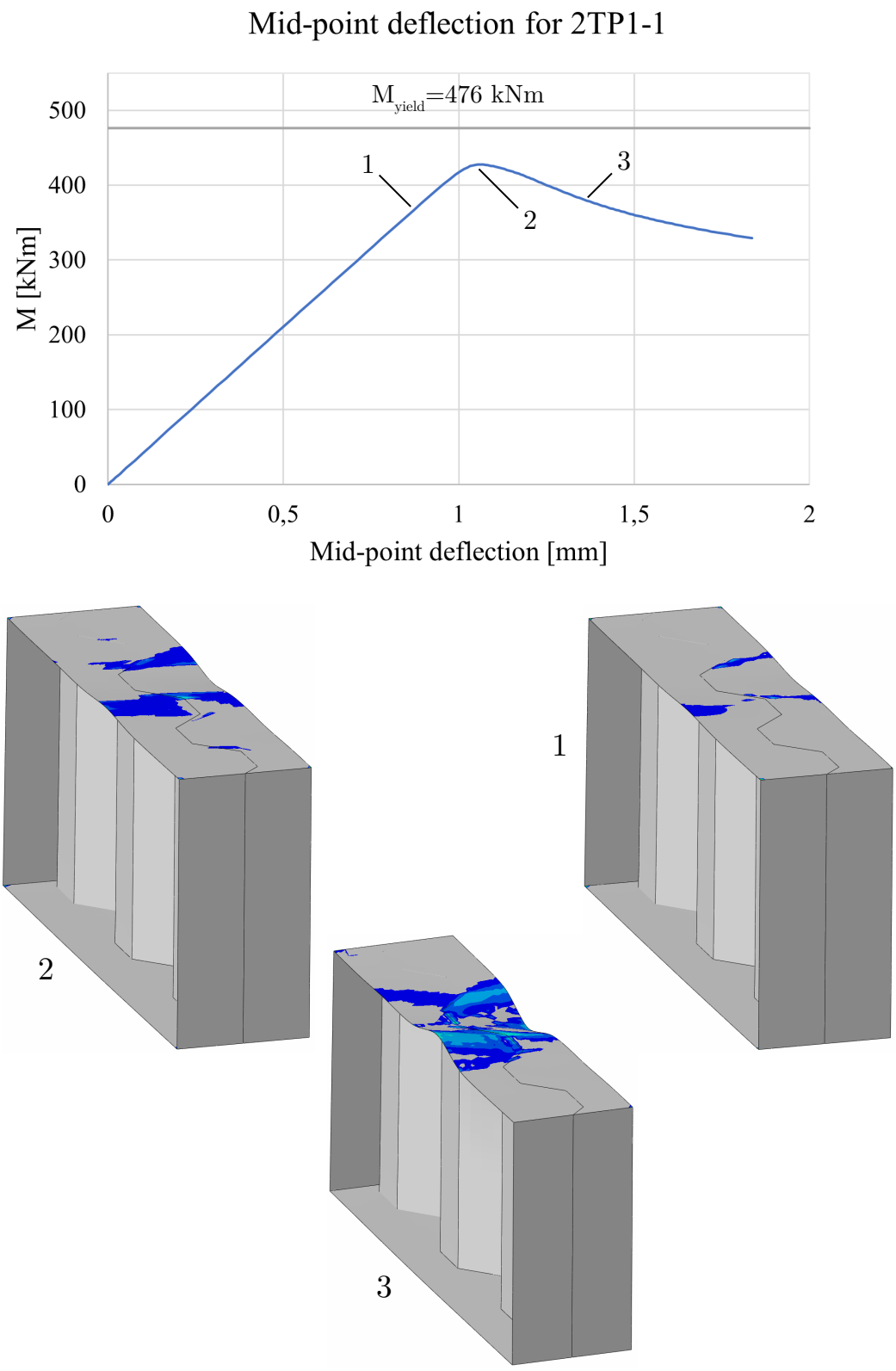

Figure 4.4: Overview of the noted behavior for specimen 2TP1-1 with Duplex 1.4162 properties.

In Figure 4.5, an overview of the observed behavior of 9TP3 with Duplex properties is presented. Yielding is initiated at the compression flange, as three distinct yielding spots, and upon reaching the ultimate capacity, they evolved into three distinct yielding strips across the compression flange. Since the current specimen did not fail in elastic buckling, the tension flange also started to yield at the ultimate capacity. Further into the post-failure range, there was an almost complete yielding of the compression flange.

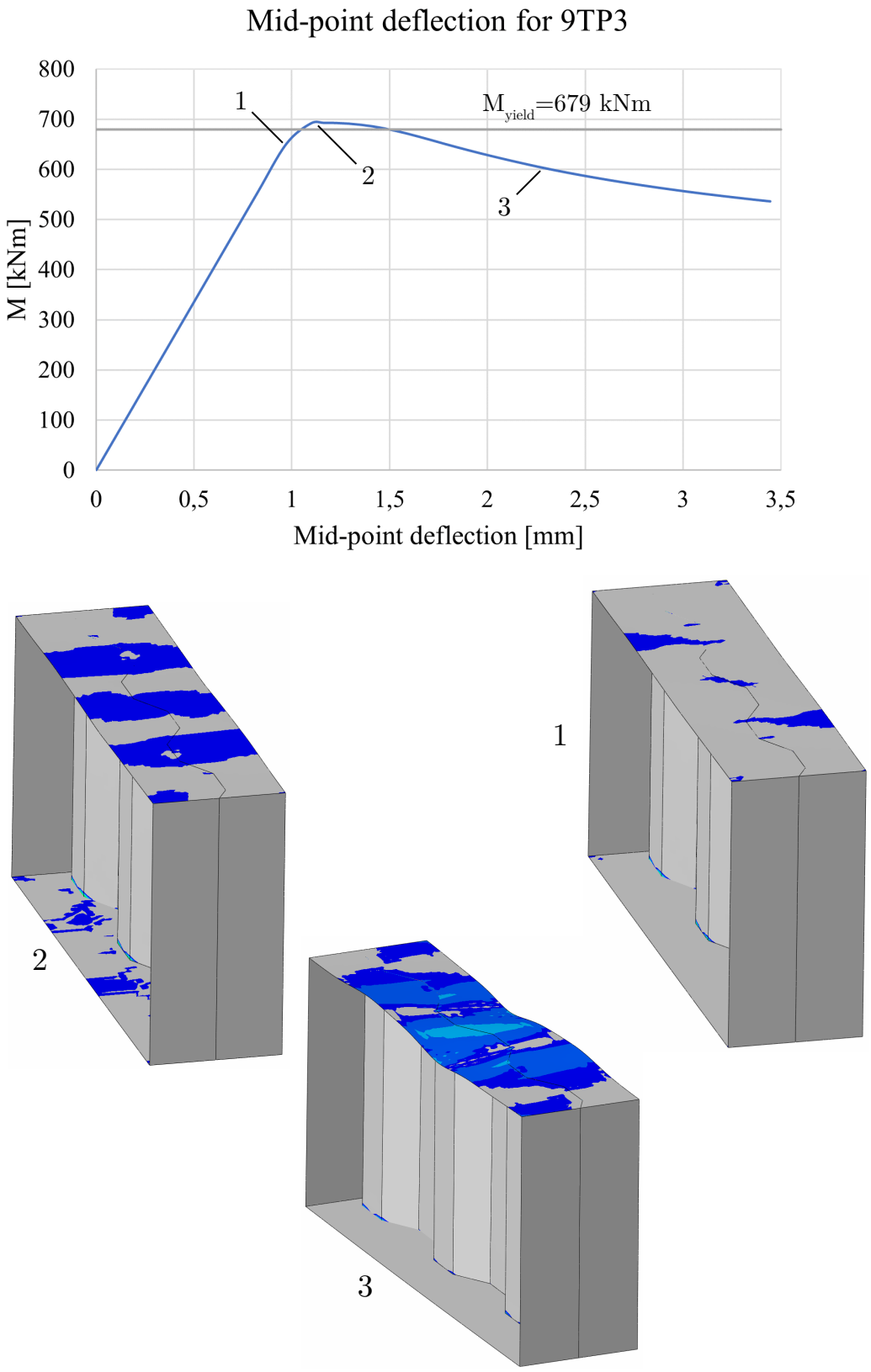

Figure 4.5: Overview of the noted behavior for specimen 9TP3 with Duplex 1.4162 properties.

4.3 Comparison of test specimens with the studied materials

The comparison of the behaviors of the studied specimens with material parameters corresponding to carbon steel and Duplex 1.4162 stainless steel, is presented through the load-displacement graphs in Figures 4.6-4.9. In each graph, the point of first noted yielding is marked, where a pattern of comparatively earlier yielding of the Duplex specimens was observed. This is thought to be the result of the more pronounced strain hardening of the Duplex material (see Chapter 2.5.2).

Commenting on the overall observed behaviors, the models with Duplex material parameters demonstrate similar, but up-scaled tendencies as their carbon steel counterparts. Owing to the lower Young's modulus of $E = 200000\ MPa$ of the Duplex grade, compared to $E = 210000\ MPa$ for carbon steel, a lower initial stiffness is obtained for the former in all the studied models.

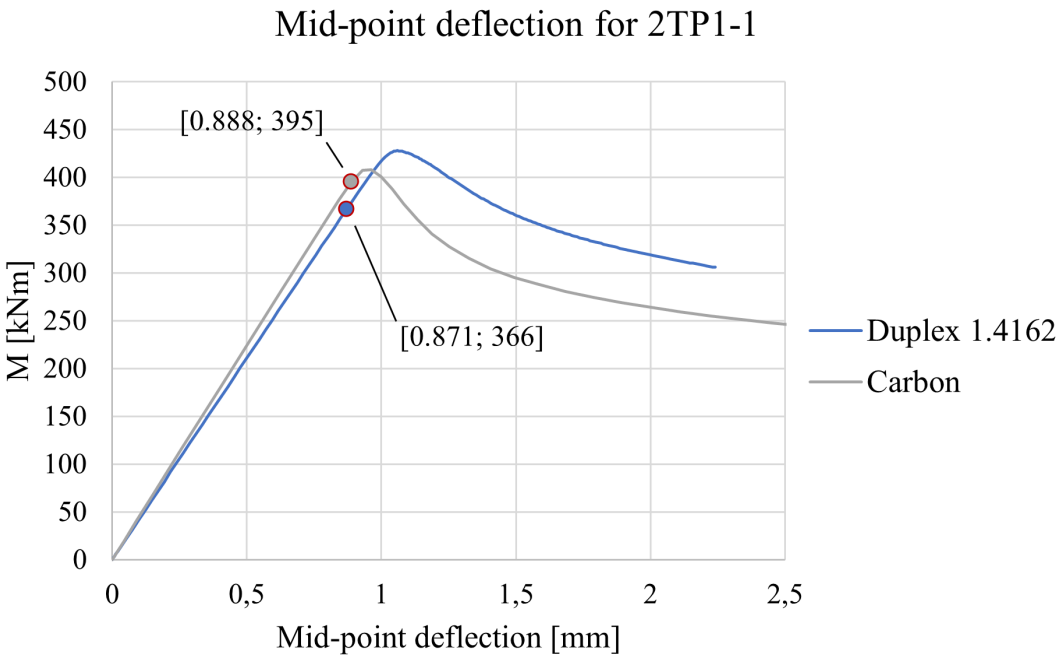

Figure 4.6: Comparison of load vs mid-point displacement behaviors for specimen 2TP1-1. The marked points indicate the first occurrence of yielding for each case.

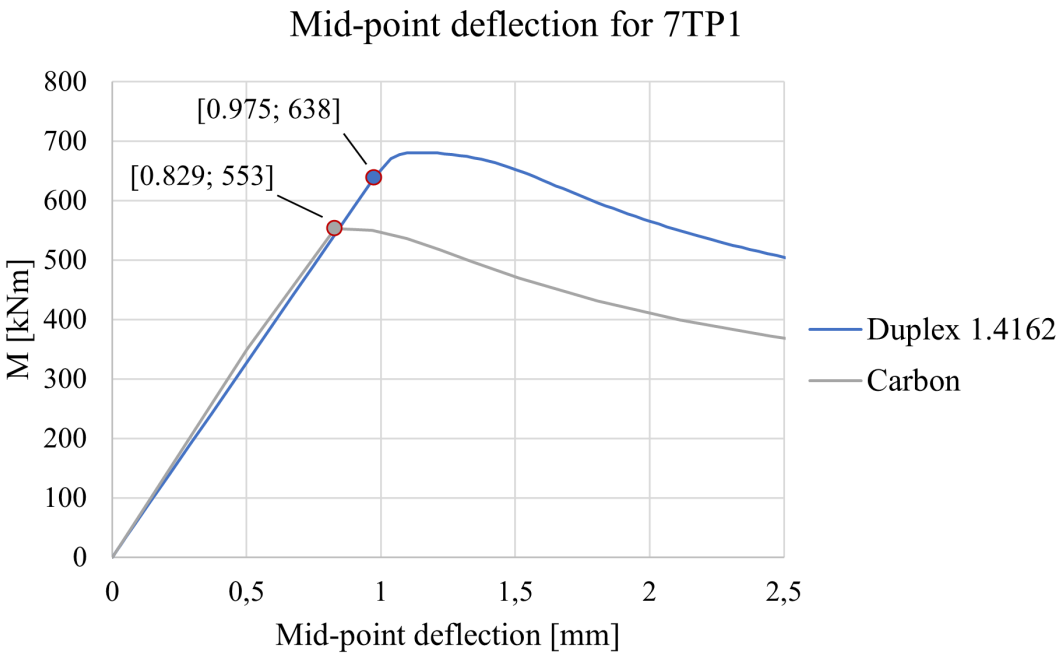

Figure 4.7: Comparison of load vs mid-point displacement behaviors for specimen 7TP1. The marked points indicate the first occurrence of yielding for each case.

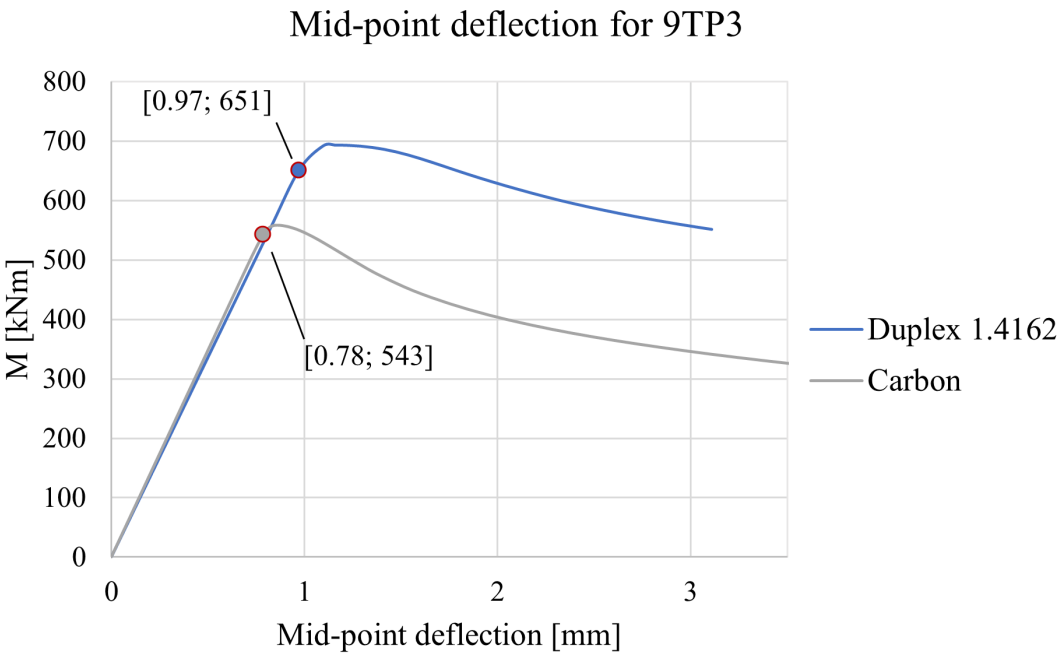

Figure 4.8: Comparison of load vs mid-point displacement behaviors for specimen 9TP3. The marked points indicate the first occurrence of yielding for each case.

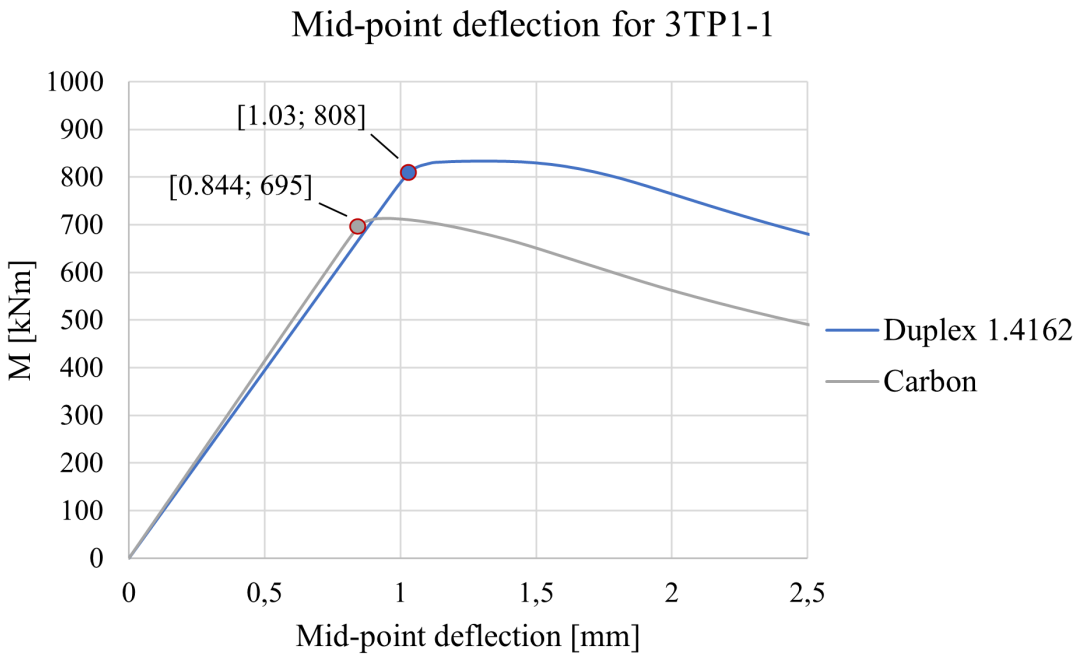

Figure 4.9: Comparison of load vs mid-point displacement behaviors for specimen 3TP1-1. The marked points indicate the first occurrence of yielding for each case.

4.4 Imperfection sensitivity of test specimens made of Duplex 1.4162

In order to take into account both mechanical and geometric imperfections for the beams in Duplex 1.4162, an amplified, equivalent geometric imperfection was determined based on the first eigenmode shape. Due to the lack of test data on the ultimate capacities of CWIG in stainless steel, a comparison was made with the imperfection sensitivity curves constructed by Jáger et al. (2017) [7] on carbon steel beams. In their conducted studies, the authors concluded that an equivalent geometric imperfection equaling $c_f/50$ is suitable for class 4 flanges, and is overly conservative for more compact flange plates [7].

In the current study, the comparisons were made on specimens 2TP1-1, 9TP3 and 3TP1-1 as presented in Figures 4.10-4.12, respectively. For the curves corresponding to Duplex 1.4162, the plotted points correspond to imperfection magnitudes of $c_f/100$, $c_f/50$ and $c_f/25$. Specimen 2TP1-1 has the most slender flange plate among the studied specimens, and is the only one demonstrating elastic buckling of the flange plate. This results in an only slightly increased moment capacity of the Duplex beam, compared to carbon. The remaining two specimens 9TP3 and 3TP1-1 reach close to, or exceed, the plastic moment capacities, implying a higher utilization of the higher yield strength of the Duplex grade, which is reflected in the graphs.

The drop in moment capacity between imperfection magnitudes of 0 and $c_f/50$ is equivalent in the cases of girders 2TP1-1 and 9TP3 (Figures 4.10 and 4.11, respec-

tively). So, with the similar observed behaviors between the two materials, the application of an equivalent geometric imperfection of the magnitude $c_f/50$ is justified for Duplex girders.

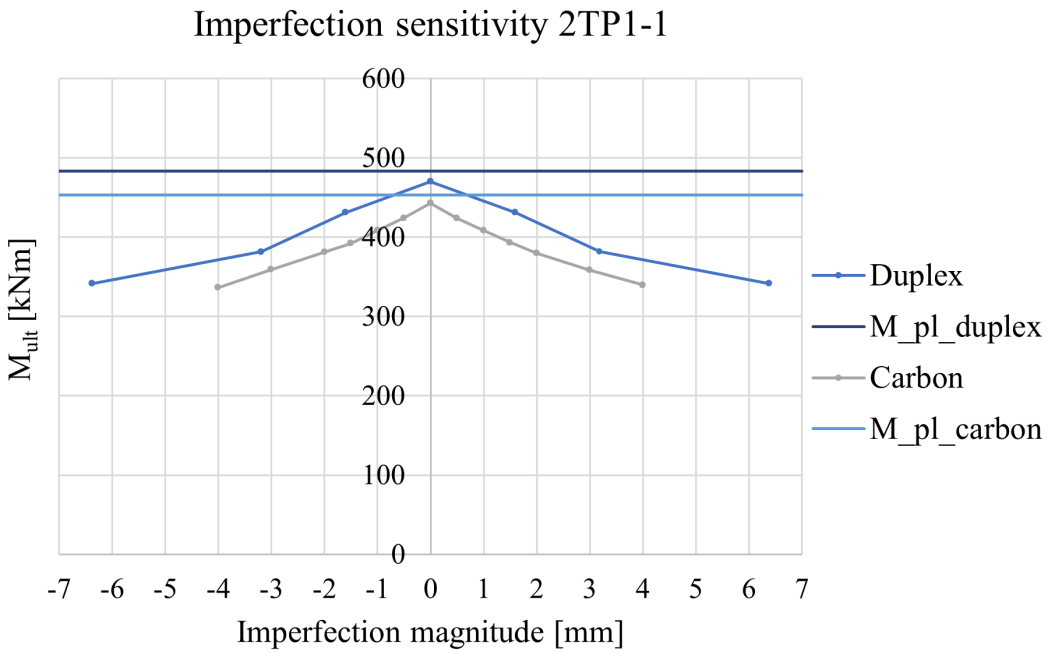

Figure 4.10: Imperfection sensitivity curves for specimen 2TP1-1 for the Duplex 1.4162 grade and carbon steel. The latter is obtained by Jáger et al. (2017) [7].

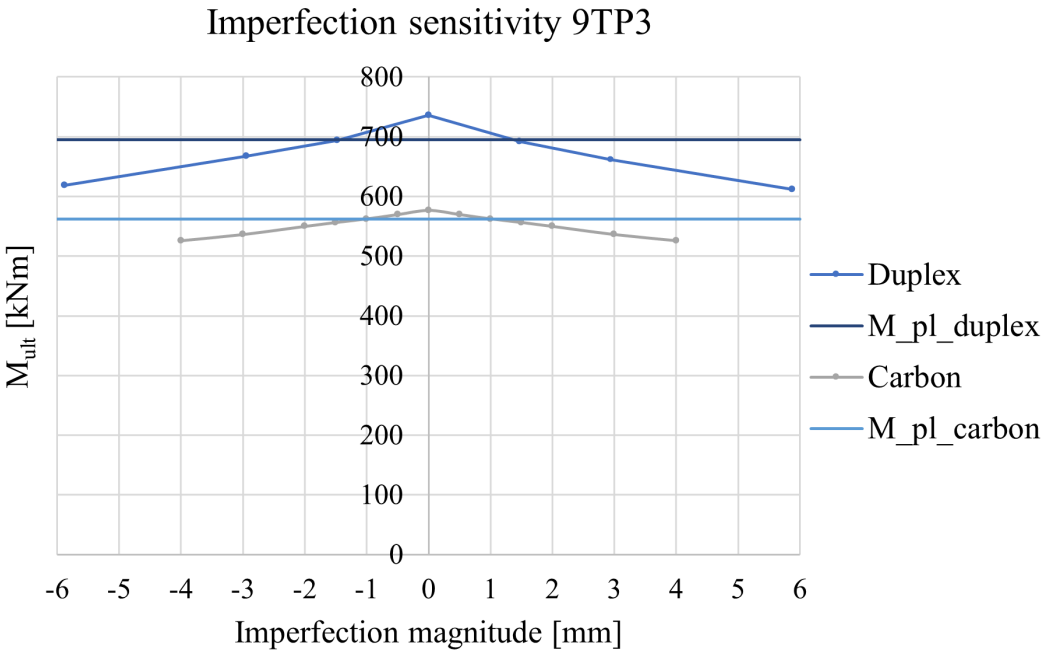

Figure 4.11: Imperfection sensitivity curves for specimen 9TP3 for the Duplex 1.4162 grade and carbon steel. The latter is obtained by Jáger et al. (2017) [7].

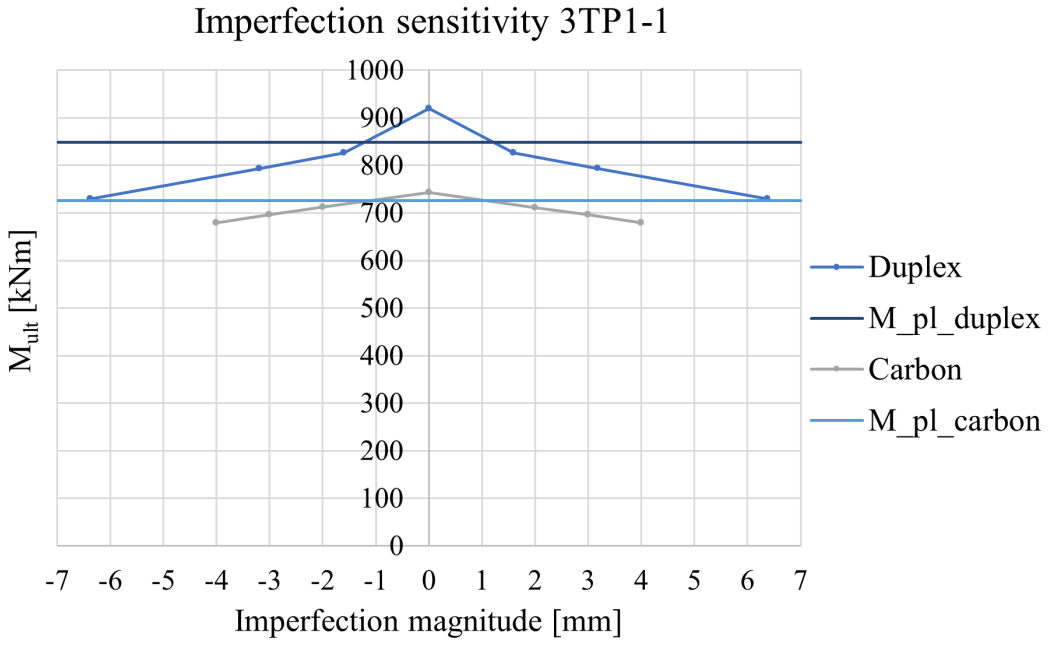

Figure 4.12: Imperfection sensitivity curves for specimen 3TP1-1 for the Duplex 1.4162 grade and carbon steel. The latter is obtained by Jáger et al. (2017) [7].

5

Parametric study: linear buckling analyses

This chapter presents the applied setup and parameter range of the linear buckling analyses, along with the corresponding results in the form of first eigenmodes and buckling coefficients $\kappa_{\sigma.num}$. Additionally, comparisons were made with the proposed methods of the EN1993-1-5 [6] and Jáger et al. [7]. The chapter is concluded with a presentation of the developed model to calculate $\kappa_{\sigma.approx}$, approximating the buckling coefficient.

The used Python script for the parametric analyses in ABAQUS is presented in Appendix A.

5.1 Setup and parameter range

The parametric study is based on the model built in Chapter 3, with the only difference being the addition of two longitudinal folds on either end of the beam. These segments each have a length corresponding to $a_1/2$, see Figure 5.1.

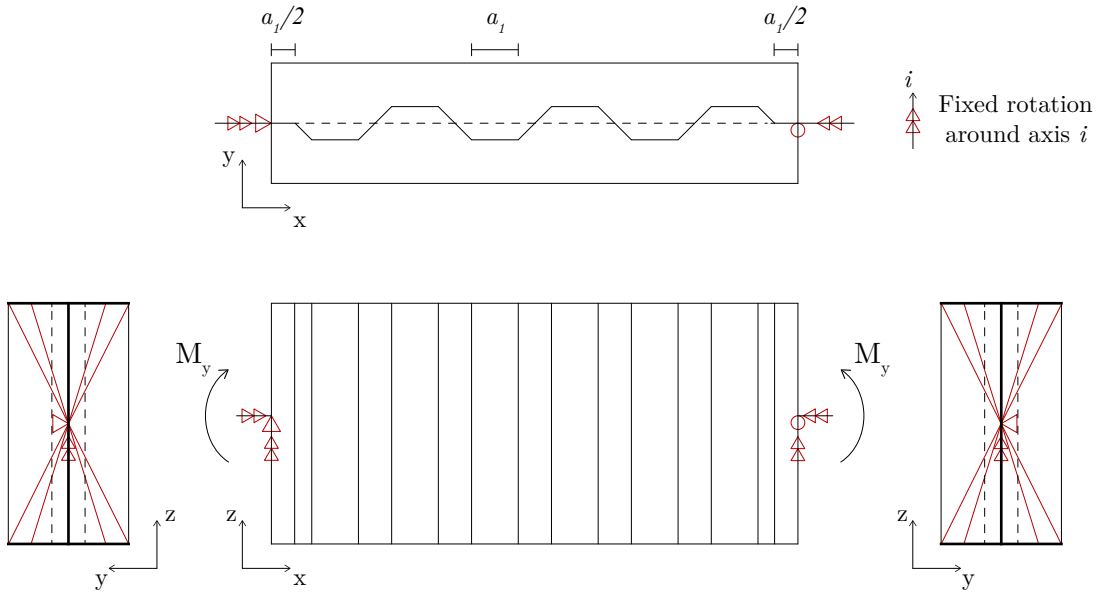

Figure 5.1: Illustration of the configuration, boundary and loading conditions applied in the linear buckling analyses.

The applied parameter range was chosen to reflect the corrugations of trapezoidally CWIG used in practice, and are as summarized below:

α	30 - 45 - 60 [deg]
b_f/a_3	2 - 2,4 - 2,7 - 3 - 3,2 - 3,3 - 4 - 5 - 6 - 6,7 - 8
$c_f/t_f/\epsilon_{ss.f}$	7,1 - 37
a_1/a_3	2 - 3 - 4
t_f/t_w	2,5 - 3,5 - 4,17 - 5 - 5,83 - 6,25 - 8,33 - 8,75 - 12,5
b_f	400 - 600 - 800 - 1000 [mm]
h_w	500 [mm]
R	0,0854 - 0,444
f_{yf}	452 [MPa]

For the meaning of the different geometric parameters, reference is made to Chapter 2.3.1 and Figure 2.8. The total number of analysed girders was 450. The mesh density applied is the one determined in Chapter 3, with S8R elements and 4 elements per longitudinal fold. The only addition is that the mesh size should fit at least 4 elements along the web height.

5.2 Buckling modes

The observed buckling modes were primarily the unrestricted rotation of the compression flange, with a few exceptions of normal stress web buckling. The following two sub-sections present some of these eigenmodes.

5.2.1 Unrestricted rotation of the compression flange

In Figures 5.2-5.4, the top views of different buckling modes are shown, for varying a_1/a_2 (see Figure 2.5). In each case, 3-4 corrugations are presented.

The general pattern noted was that at enclosing effects $R > 0,17$ the buckling length is almost, or equal to the distance between two adjacent inclined folds $a_1 + 2a_4$, as in Figures 5.2 a,b, 5.3 a,b and 5.4 a,b. This is a result of the inclined folds being able to provide enough support to confine the buckle. At $R < 0,17$ the buckling length becomes larger than $a_1 + 2a_4$, for instance as in Figure 5.2 c,d.

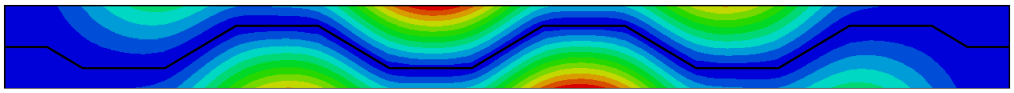

(a) Buckling mode of ID-457: $b_f/a_3 = 2 \quad R = 0,34 \quad \kappa_{\sigma.num} = 0,341$

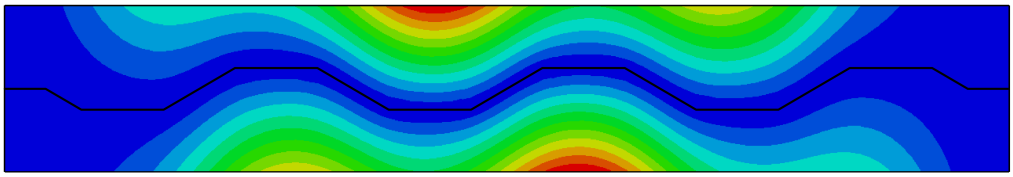

(b) Buckling mode of ID-4: $b_f/a_3 = 4 \quad R = 0,171 \quad \kappa_{\sigma.num} = 0,666$

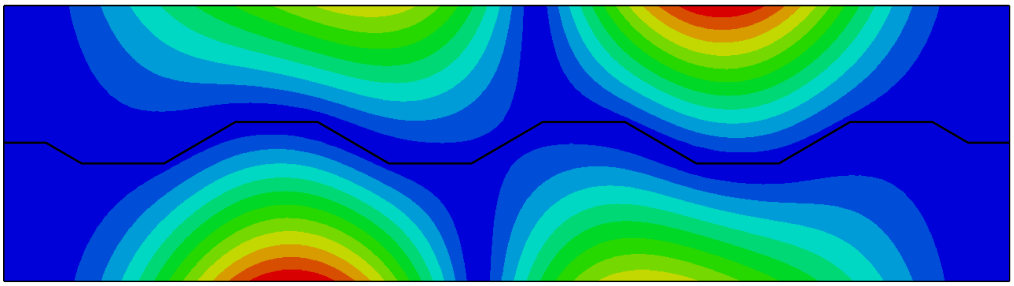

(c) Buckling mode of ID-913: $b_f/a_3 = 6,7 \quad R = 0,10 \quad \kappa_{\sigma.num} = 0,839$

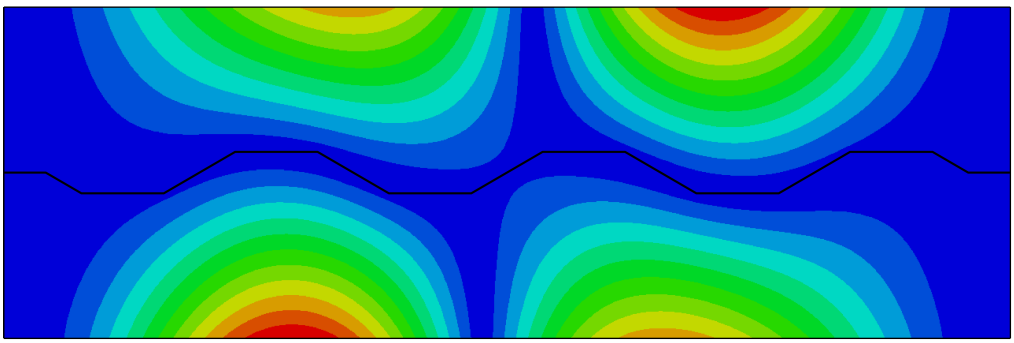

(d) Buckling mode of ID-958: $b_f/a_3 = 8 \quad R = 0,085 \quad \kappa_{\sigma.num} = 0,860$

Figure 5.2: Unrestricted flange rotation buckling modes for $a_1/a_2 = 1$.

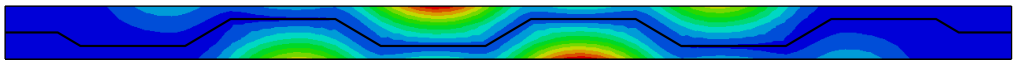

(a) Buckling mode of ID-136: $b_f/a_3 = 2 \quad R = 0,384 \quad \kappa_{\sigma.num} = 0,593$

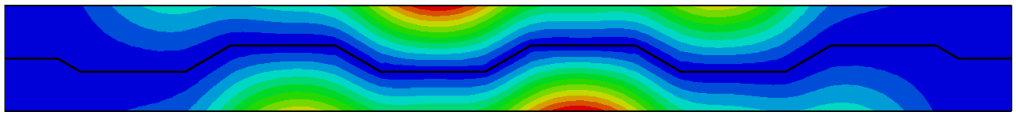

(b) Buckling mode of ID-88: $b_f/a_3 = 4 \quad R = 0,192 \quad \kappa_{\sigma.num} = 0,720$

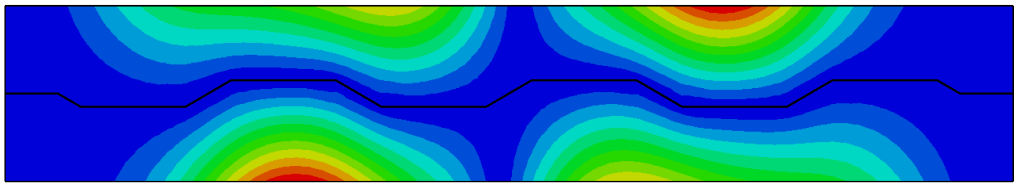

(c) Buckling mode of ID-547: $b_f/a_3 = 6,7 \quad R = 0,115 \quad \kappa_{\sigma.num} = 0,813$

Figure 5.3: Unrestricted flange rotation buckling modes for $a_1/a_2 = 2$.

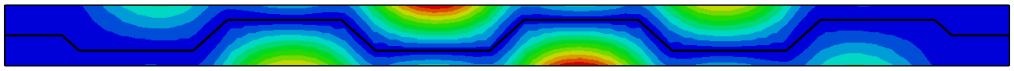

(a) Buckling mode of ID-691: $b_f/a_3 = 2 \quad R = 0,417 \quad \kappa_{\sigma.num} = 0,527$

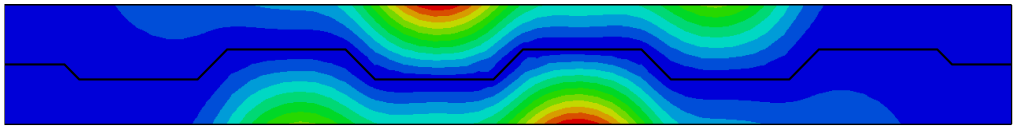

(b) Buckling mode of ID-649: $b_f/a_3 = 4 \quad R = 0,208 \quad \kappa_{\sigma.num} = 0,814$

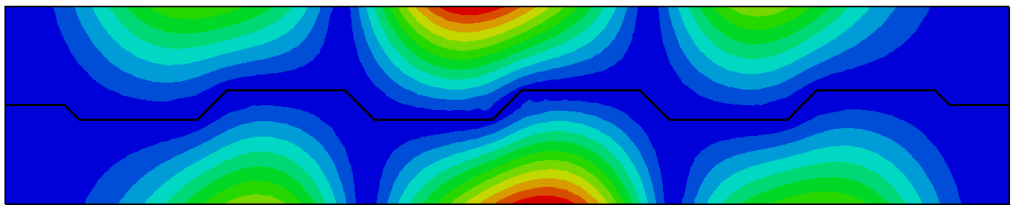

(c) Buckling mode of ID-697: $b_f/a_3 = 6,7 \quad R = 0,125 \quad \kappa_{\sigma.num} = 0,979$

Figure 5.4: Unrestricted flange rotation buckling modes for $a_1/a_2 = 2,83$.

In total, 386 cases of normal stress flange buckling as first eigenmode were observed. All corrugation properties and FEA results for these girders are given in Tables B.1-B.8 in Appendix B.

5.2.2 Normal stress web buckling

In some cases, the lowest eigenmode has been normal stress buckling of the web (Figures 5.5 a,b,c), or normal stress flange buckling, with a 'distorted' web (Figures

5.6). In an attempt to separate when either buckling mode is current, a factor ϕ corresponding to Equation 5.1 is suggested:

$$\phi = (a_1/a_4) \cdot (h_w/t_w/\epsilon_{ss.w})/(c_f/t_f/\epsilon_{ss.f}) \tag{5.1}$$

Where a distinction between the material parameter ϵ_{ss} (see Equation 2.7) of the web and flange plates is made.

The first term of a_1/a_4 (see Figure 2.5) considers the higher web contribution in the longitudinal load-carrying as suggested by Inaam & Upadhyay (2022) [16], a higher value means higher contribution. Further, the two terms $h_w/t_w/\epsilon_{ss.w}$ and $c_f/t_f/\epsilon_{ss.f}$ describe the web and flange slenderness, respectively. A higher web slenderness should lead to higher risk of web buckling and, conversely, a higher flange slenderness should result in a lower risk of web buckling.

In Figure 5.7, the presented factor (Equation 5.1) for all the specimens is plotted against the a_1/a_4, and an approximate separating line can be drawn. The grey points lying above the line are such beams that demonstrated normal stress flange buckling with a distorted web, as shown in Figure 5.6. This means that there is no well-defined limit, rather a transition from pure flange to pure web buckling. A method to separate the occurrence of these buckling modes is presented in Equation 5.2:

$$\text{If } \phi > 6,28 \cdot \frac{a_1}{a_4} + 18,5 \rightarrow \text{Web buckling} \tag{5.2}$$

There were 64 cases of normal stress web buckling, and corrugation properties and FEA results for these girders are given in Tables B.9 & B.10 in Appendix B.

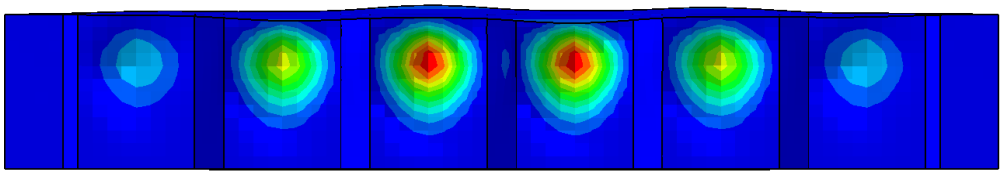

(a) Buckling mode of ID-184

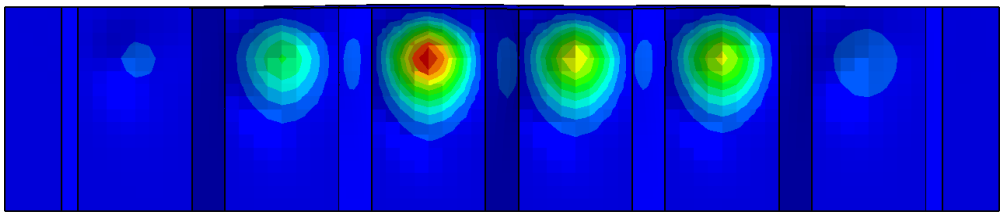

(b) Buckling mode of ID-754

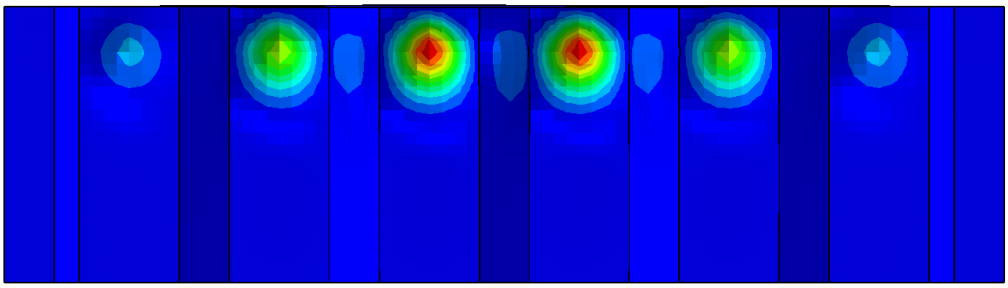

(c) Buckling mode of ID-1051

Figure 5.5: Three normal stress web buckling modes.

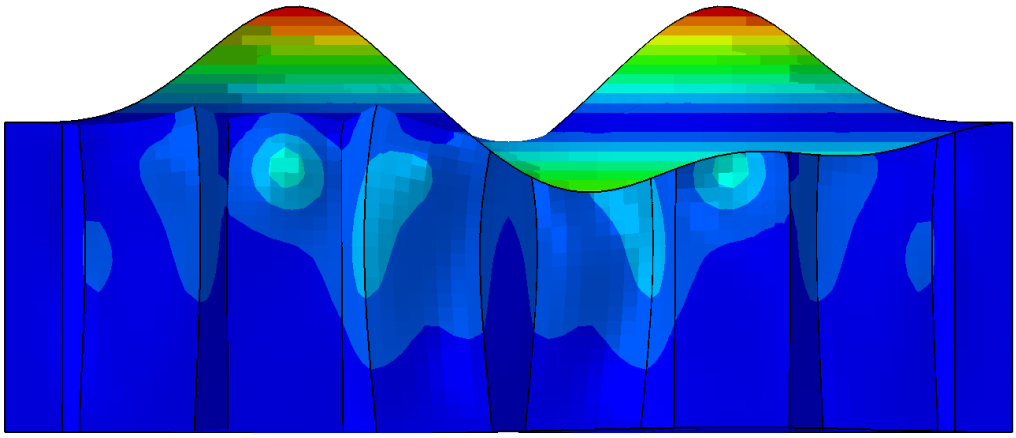

Figure 5.6: Normal stress flange buckling, with a distorted web, of ID-751.

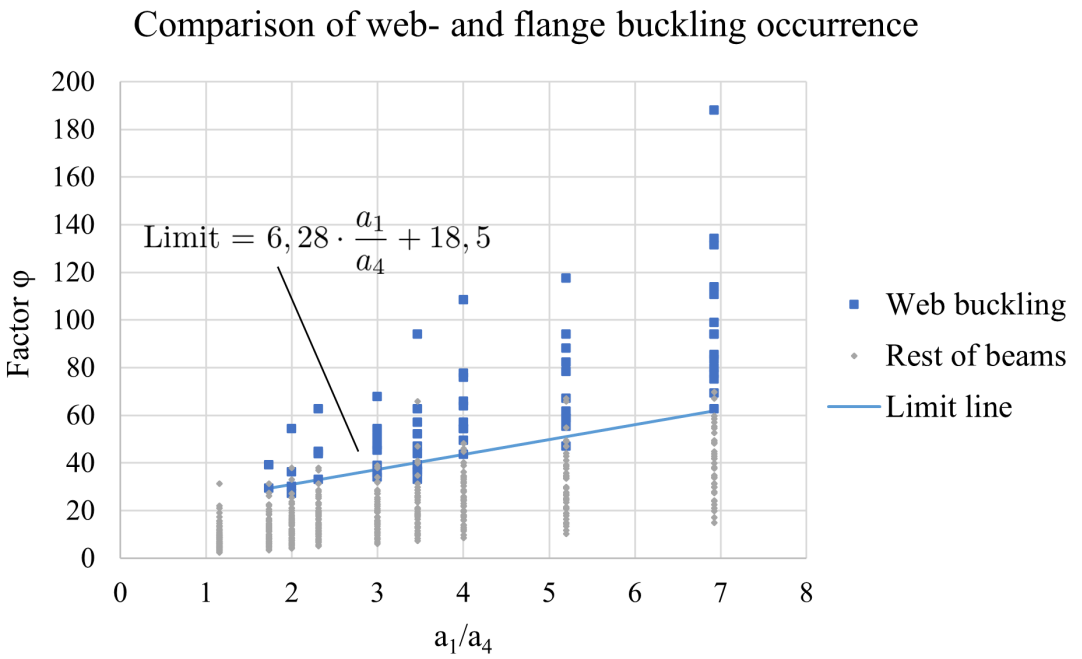

Figure 5.7: Comparison of web- and flange buckling occurrence.

5.3 The elastic buckling coefficient κ_σ

The buckling coefficient was investigated for girders demonstrating normal stress flange buckling as lowest eigenmode, which, as mentioned in Chapter 5.2.1, are 386. The buckling analyses resulted in a critical moment $M_{cr.num}$ that needed to be translated into a corresponding critical stress $\sigma_{cr.num}$ and thereby buckling coefficient $\kappa_{\sigma.num}$. This was performed through the procedure presented in Equations 5.3 a,b,c:

$$N_{ult.num} = \frac{M_{cr.num}}{h_w + t_f} \quad [N] \tag{5.3a}$$

$$\sigma_{cr.num} = \frac{N_{ult.num}}{b_f \cdot t_f} \quad [MPa] \tag{5.3b}$$

$$\kappa_{\sigma.num} = \frac{\sigma_{cr.num} \cdot 12 \cdot (1-\nu^2) \cdot (c_f/t_f)^2}{\pi^2 \cdot E} \tag{5.3c}$$

Where $E = 200000\,MPa$ for stainless steel, $M_{cr.num}$ is in Nm and all length dimensions are in mm. The adopted derivation of $\kappa_{\sigma.num}$ presented in Equation 5.3 c is based on the large outstand-to-thickness ratio c_f/t_f as governing slenderness.

The corrugation properties and FEA results for all the studied beams where normal stress flange buckling was noted are given in Tables B.1-B.8 in Appendix B.

The following sub-sections present the comparisons of the obtained buckling coefficients $\kappa_{\sigma.num}$ with the suggestions of the EN1993-1-5 [6] and Jáger et al. [7]. Proceeding, the developed expression for κ_σ is presented, and also compared with the FEA results.

5.3.1 Comparison of the FEA results with the EN1993-1-5

The suggested expression of the buckling coefficient $\kappa_{\sigma.EC}$ of the EN1993-1-5 [6], as presented in Equation 2.15, leads to a majority of safe results, but with many overly unsafe capacities. This is clearly seen in Figure 5.8, where the ratio $\kappa_{\sigma.EC}/\kappa_{\sigma.num}$ is plotted against the outstand slenderness $c_f/t_f/\epsilon_{ss.f}$. The slenderness limit for cross-section class 3 suggested in the EN1993-1-4 [14] of $c_f/t_f/\epsilon_{ss.f} > 14$ is also plotted.

The large scatter observed could be the result of the EN1993-1-5 lacking consideration of important parameters such as the flange-to-web thickness ratio t_f/t_w and the enclosing effect R.

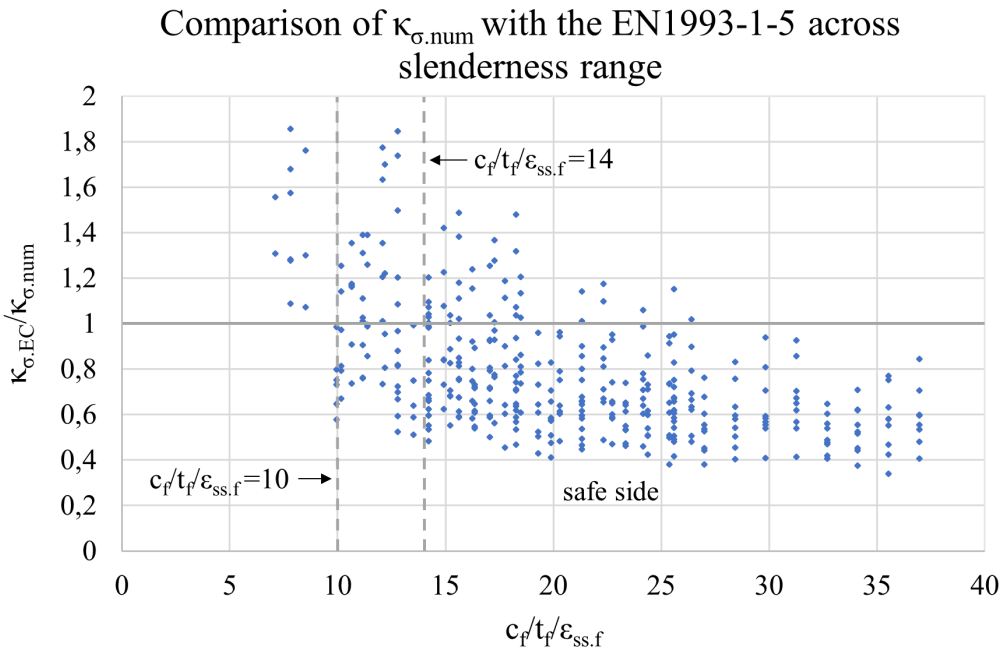

Figure 5.8: Comparison of the FEA results of $\kappa_{\sigma.num}$ with the EN1993-1-5 [6] $\kappa_{\sigma.EC}$ across the slenderness range.

Table 5.1 shows the statistical evaluation of the comparison of $\kappa_{\sigma.EC}$ and $\kappa_{\sigma.num}$ from FEA. What can be concluded is that the upper limitation of $\kappa_{\sigma.EC} = 0,6$ could be the background to the high average underestimation of 28,6%, in the range of

$c_f/t_f/\epsilon_{ss.f} > 14$.

The comparisons with the model of the EN1993-1-5 [6] are presented for each girder in Tables C.1-C.5 in Appendix C.

Table 5.1: Statistical evaluation on the comparison of the FEA results $\kappa_{\sigma.num}$ with $\kappa_{\sigma.EC}$ [6].

Statistical evaluation for κ_σ: EN1993-1-5 [6]				
	Average	**Standard deviation**	**Min**	**Max**
All	0,780	0,285	0,339	1,857
$\boldsymbol{c_f/t_f/\epsilon_{ss.f} > 14}$	0,714	0,285	0,339	1,486

5.3.2 Comparison of the FEA results with Jáger et al.

In Figure 5.9 the proposal of Jáger et al. [7] (see Equation 2.21) is compared with the FEA results plotted as $\kappa_{\sigma.Jager}/\kappa_{\sigma.num}$ against the slenderness range on the x-axis. The graph is complemented with Table 5.2, presenting the statistical evaluation of the comparison. Contrary to the buckling coefficient suggested in the EN1993-1-5 [6], the results are more concentrated on the safe side, with an average underestimation of 36,9% in the slenderness range $c_f/t_f/\epsilon_{ss.f} > 14$, suggested as slenderness limit for cross-section class 3 in the EN1993-1-4 [14].

The standard deviation of the results is lower compared to the EN1993-1-5 [6], with a value of 0,159 in contrast to Eurocode's 0,285 in the high slenderness range $c_f/t_f/\epsilon_{ss.f} > 14$. The slight improvement could be attributed to the consideration of the flange-to-web thickness ratio t_f/t_w and enclosing effect R.

The comparisons with the model proposed by Jáger et al. [7] are presented for each girder in Tables C.6-C.15 in Appendix C.

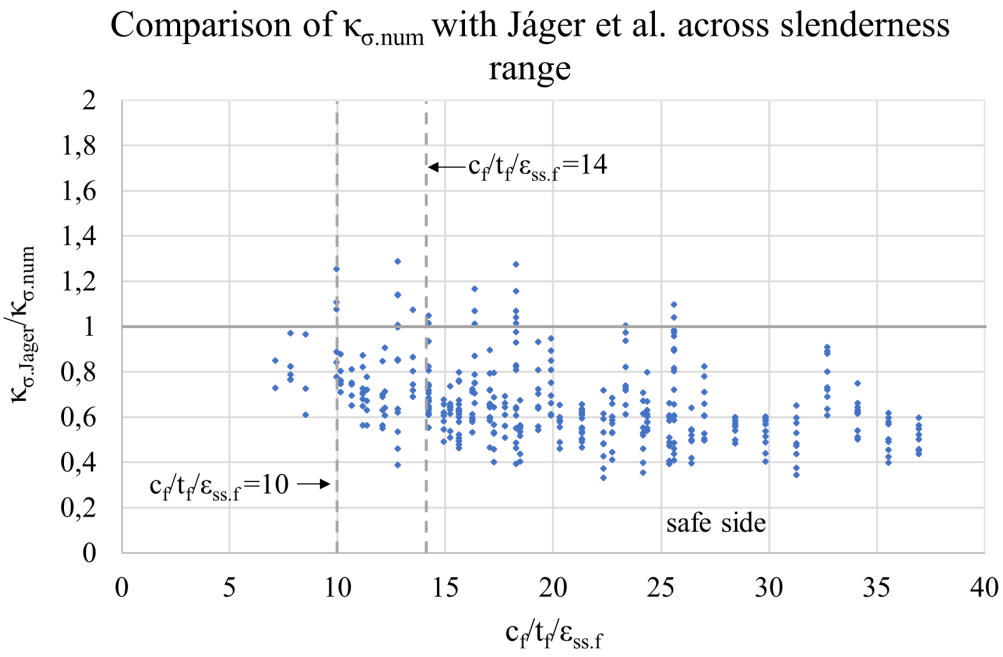

Figure 5.9: Comparison of the FEA results of $\kappa_{\sigma.num}$ with the suggestion of Jáger et al. [7] $\kappa_{\sigma.Jager}$ across the slenderness range.

Table 5.2: Statistical evaluation on the comparison of the FEA results $\kappa_{\sigma.num}$ with $\kappa_{\sigma.Jager}$ [7].

Statistical evaluation for κ_σ: Jáger et al. [7]				
	Average	**Standard deviation**	**Min**	**Max**
All	0,659	0,171	0,332	1,288
$\boldsymbol{c_f/t_f/\epsilon_{ss.f} > 14}$	0,631	0,159	0,332	1,276

5.3.3 Approximating expression of the elastic buckling coefficient $\kappa_{\sigma.num}$

This sub-section presents the effect of the two parameters R and t_f/t_w on the buckling coefficient $\kappa_{\sigma.num}$, by, to the highest possible degree, filtering out the influence of other parameters in each case. The sub-section is concluded with the development of a new model for $\kappa_{\sigma.approx}$ suggested in this thesis.

5.3.3.1 Effect of enclosing effect R

The buckling coefficient $\kappa_{\sigma.num}$ demonstrates a positive, linear dependency with respect to the enclosing effect R, as seen in Figure 5.10. In the current case, each line in the graph corresponds to three beams, each having the same flange plate and corrugation dimensions, except for the corrugation angle α and inclined fold length a_2. So, what increases the enclosing effect R are the increasing corrugation angles α

which somewhat reduce the buckling length. This is illustrated for the three beams having $t_f/t_w = 5,83$ and $c_f/t_f = 15$ in Figures 5.11 a,b,c.

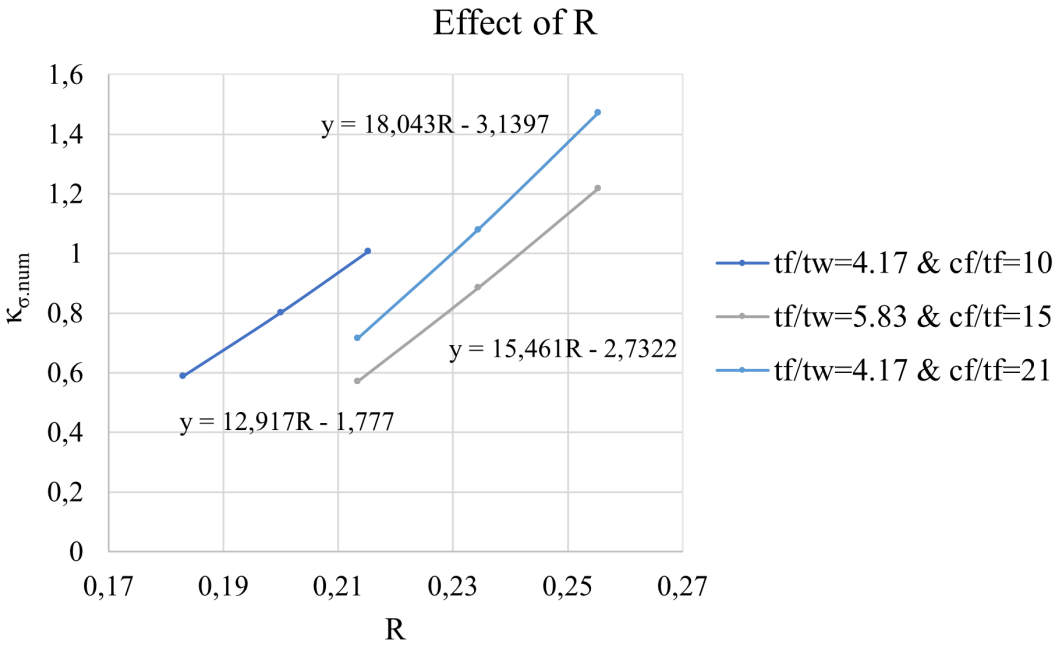

Figure 5.10: The effect of the enclosing effect R.

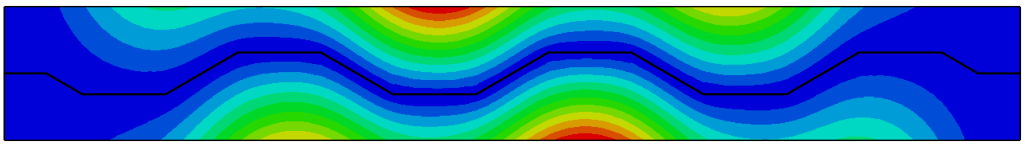

(a) Buckling mode of ID-511 with $R = 0,213$ & $\alpha = 30\,deg$

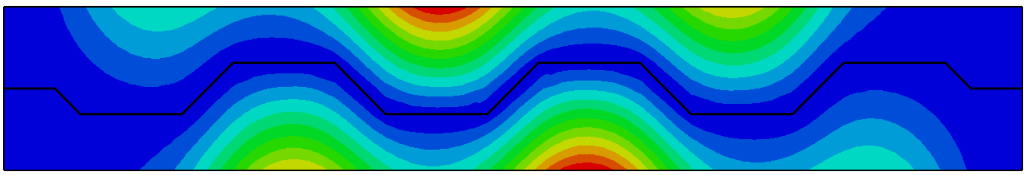

(b) Buckling mode of ID-661 with $R = 0,234$ & $\alpha = 45\,deg$

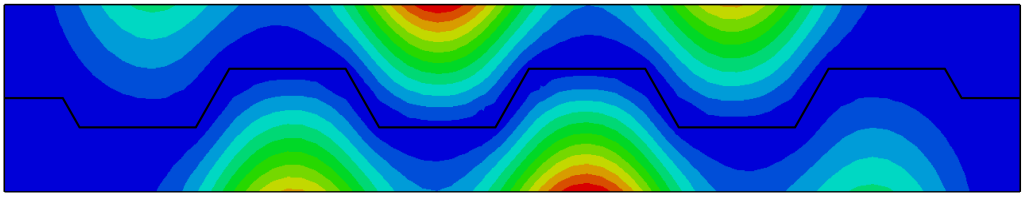

(c) Buckling mode of ID-811 with $R = 0,255$ & $\alpha = 60\,deg$

Figure 5.11: Three beams with the same overall dimensions, but varying corrugation angles α and enclosing effects R. Here, $t_f/t_w = 5,83$ and $c_f/t_f = 15$.

5.3.3.2 Effect of flange-to-web thickness ratio t_f/t_w

A negative power relation was observed between the buckling coefficient $\kappa_{\sigma.num}$ and the flange-to-web thickness ratio t_f/t_w, implying a decrease of capacity, as seen in Figure 5.12. This could be due to the decreasing supporting effect of the web plate for higher t_f/t_w. Overall, two different tendencies were observed. One for the lower and one for the higher range of enclosing effects R, so a separation was made at an enclosing effect of $R = 0,17$. This value was observed to define a limit of whether the flange buckling occurs between two adjacent inclined folds or has a higher buckling length, see Chapter 5.2.1.

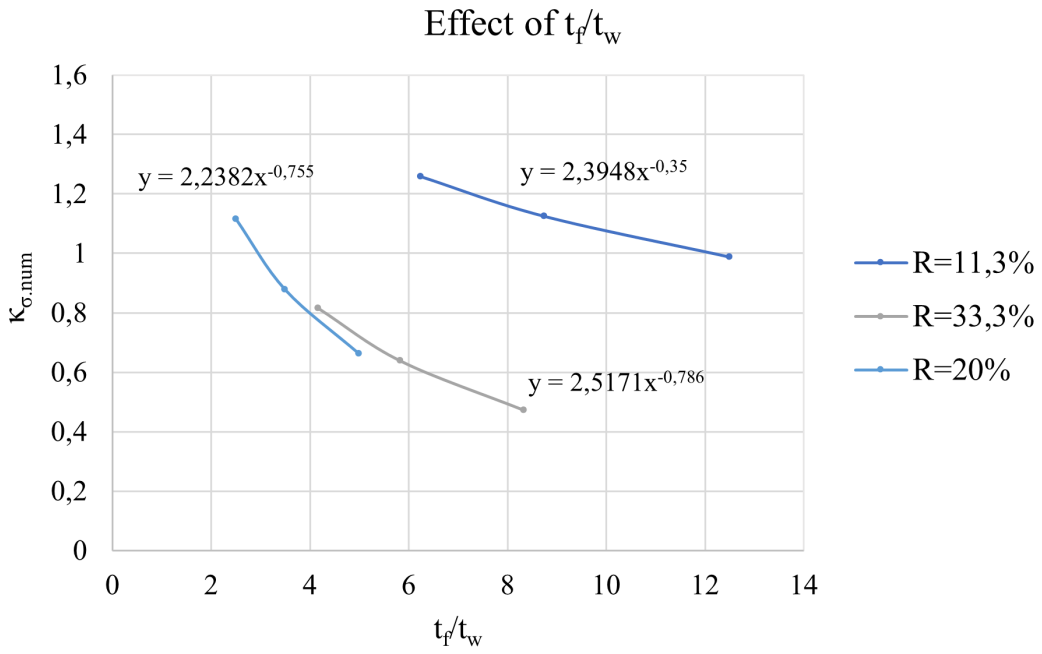

Figure 5.12: The effect of flange-to-web thickness ratio t_f/t_w.

5.3.3.3 Expressions for $\kappa_{\sigma.approx}$

Worth mentioning at this stage is that the effort of determining an approximating model for the buckling coefficient κ_σ did not aim at obtaining safe-side approximations. It is rather approximating the actual buckling coefficient in the most accurate way possible.

In the development of an approximating expression for $\kappa_{\sigma.num}$ a choice of separating beams with $R < 0,17$ and $R > 0,17$ was made. The background to this is what has been discussed in Chapters 5.2.1, where a buckling length almost or equal to $a_1 + 2a_4$ (distance between two adjacent inclined folds) was observed for $R > 0,17$, and higher otherwise. Additionally, different tendencies were noted in the relation of $\kappa_{\sigma.num}$ against t_f/t_w in Chapter 5.3.3.2, for R higher or lower than 0,17. Thereby, two separate expressions for the approximate $\kappa_{\sigma.approx}$ were developed, as discussed in the continuation.

For $R < 0,17$, a linear relation between $\kappa_{\sigma.num}$ and the R was chosen, based on the results presented in Chapter 5.3.3.1. As for the t_f/t_w, given the observations made in Chapter 5.3.3.2, a factor $12t_w/t_f$ raised to the power of $0,24+R$ was derived and deemed relevant in the regression analysis. Additional terms of $[c_f/(a_1+2a_4)]^{-2}$, flange outstand-to-thickness ratio c_f/t_f, and flange width-to-corrugation depth ratio b_f/a_3, enhanced the accuracy of the results.

The resulting expression for $R < 0,17$ is $\kappa_{\sigma.approx.R<0.17}$ presented in Equation 5.4:

$$\kappa_{\sigma.approx.R<0.17} = 0,29\left[12\frac{t_w}{t_f}\right]^{0,24+R} + 3,166R - \\ - 0,134\left[\frac{c_f}{a_1+2a_4}\right]^{-2} + 0,0205\frac{c_f}{t_f} + 0,0086\frac{b_f}{a_3} + 0,156 \quad (5.4)$$

A comparison of the approximating $\kappa_{\sigma.approx.R<0.17}$ and the $\kappa_{\sigma.num}$ from FEA is shown in Figure 5.13.

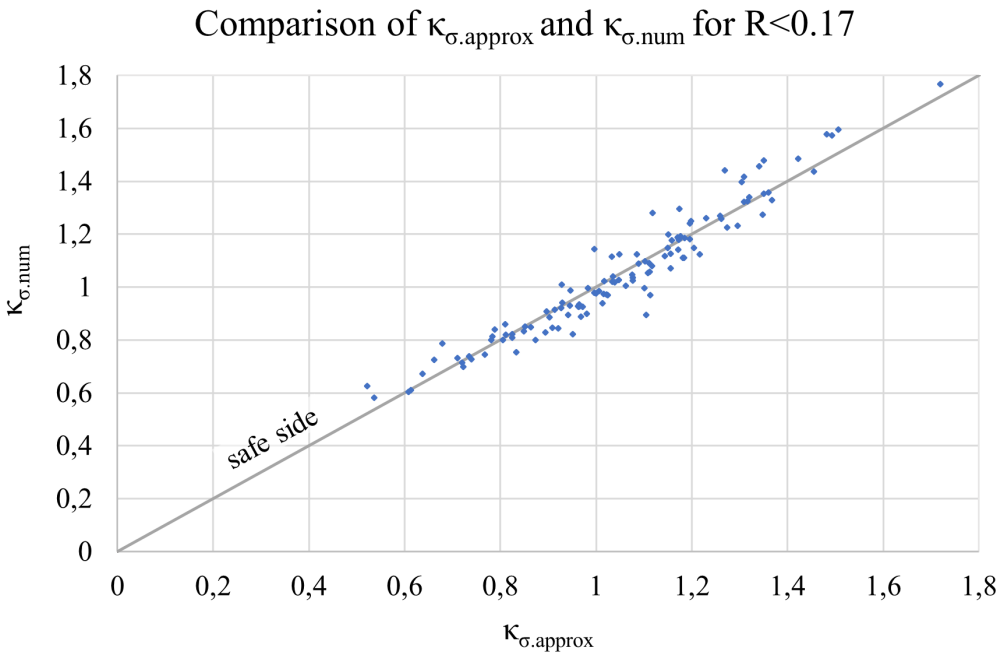

Figure 5.13: Comparison of $\kappa_{\sigma.approx}$ and $\kappa_{\sigma.num}$ for enclosing effects $R < 0,17$.

For $R > 0,17$ a similar approach was adopted as for $R < 0,17$, the major difference is in the terms related to t_f/t_w and $[c_f/(a_1+2a_4)]$. In the case of t_f/t_w, a term of $2,9t_w/t_f$ raised to the power of $0,5+R$ was applied, based on Figure 5.12. As for the term $[c_f/(a_1+2a_4)]$, the most accurate results were obtained when it is raised

to the power of 1.

The obtained expression for $\kappa_{\sigma.approx.R>0.17}$ is presented in Equation 5.5:

$$\kappa_{\sigma.approx.R>0.17} = 0,29\left[2,9\frac{t_w}{t_f}\right]^{0,5+R} + 1,73R + \\ + 1,575\left[\frac{c_f}{a_1+2a_4}\right] + 0,022\frac{c_f}{t_f} + 0,102\frac{b_f}{a_3} - 1,173 \quad (5.5)$$

A comparison of the approximating $\kappa_{\sigma.approx.R>0.17}$ and the $\kappa_{\sigma.num}$ from FEA is shown in Figure 5.14.

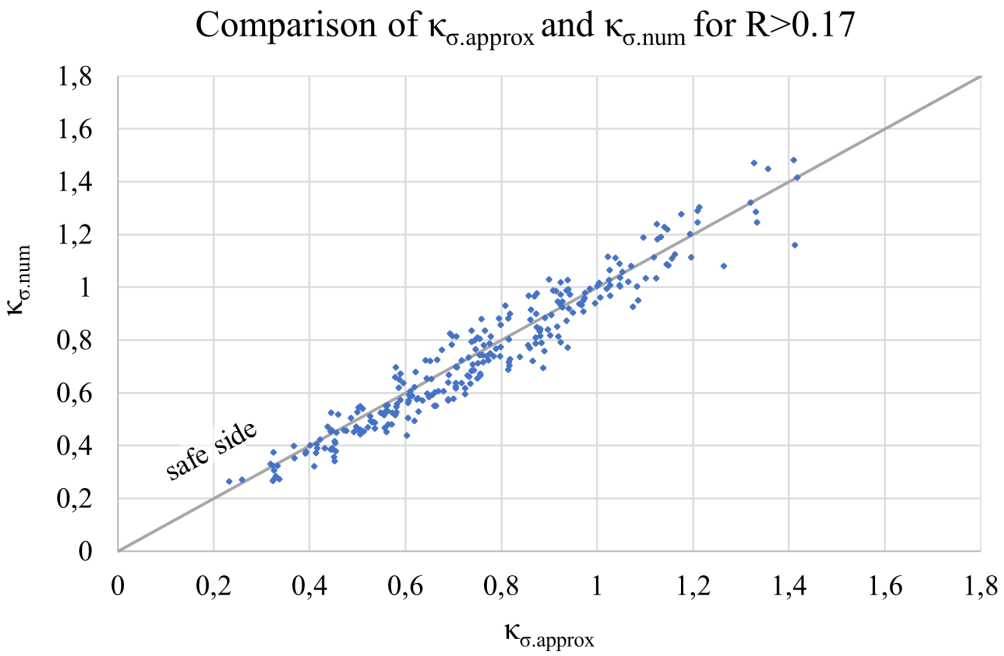

Figure 5.14: Comparison of $\kappa_{\sigma.approx}$ and $\kappa_{\sigma.num}$ for enclosing effects $R > 0.17$.

Applying the expressions in Equations 5.4 and 5.5 on all the studied beams where normal stress flange buckling was observed, the comparison graphs in Figures 5.15 and 5.16 were obtained.

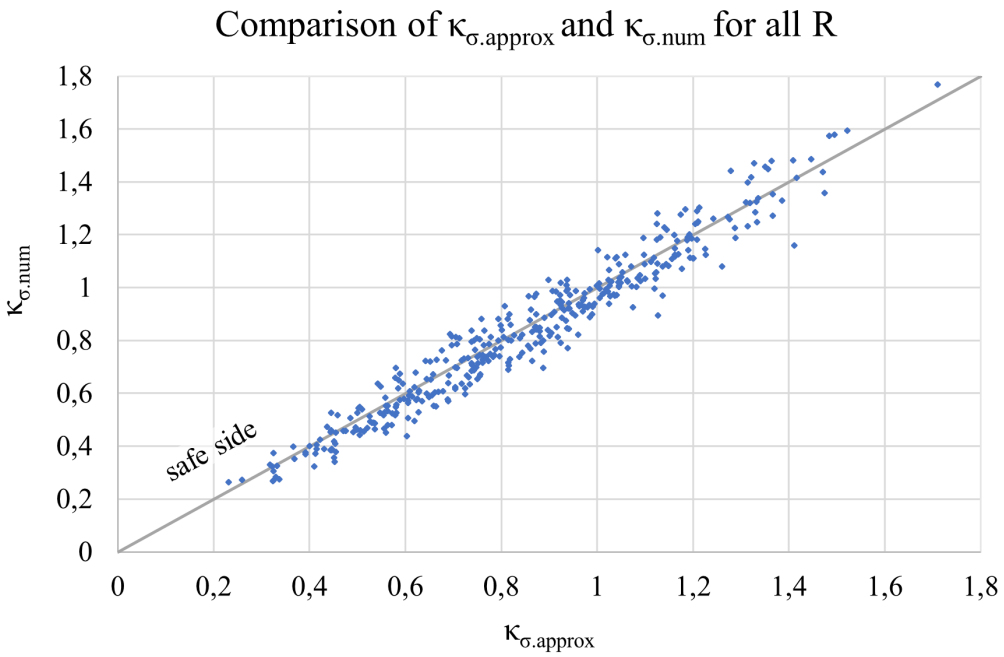

Figure 5.15: Comparison of $\kappa_{\sigma.approx}$ and $\kappa_{\sigma.num}$ for all beams.

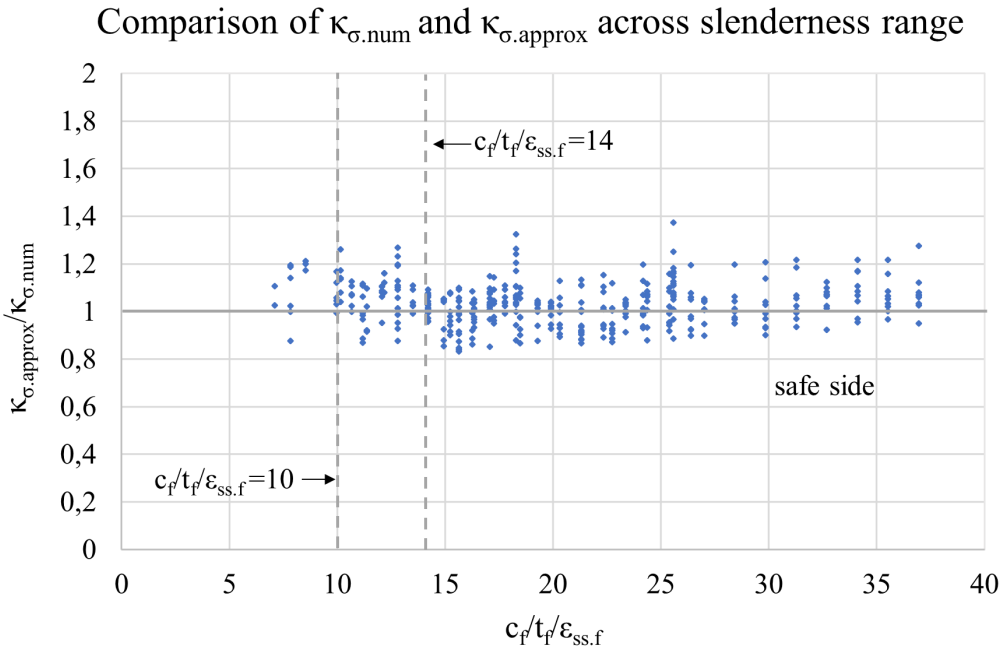

Figure 5.16: Comparison of the FEA results of $\kappa_{\sigma.num}$ with the approximate $\kappa_{\sigma.approx}$ across the slenderness range.

A statistical evaluation of the FEA results compared to the developed approximation $\kappa_{\sigma.approx}$ is presented in Table 5.3. The model approximates the buckling coefficient to a satisfactory degree in the majority of the cases, and the mean value lies at approximately 1 with an improved standard deviation of 0,09 compared to around

0,16 obtained when using the proposal of Jáger et al. [7] in Table 5.2.

The comparisons with the model developed in the current thesis are presented for each girder in Tables C.19-C.22 in Appendix C.

Table 5.3: Statistical evaluation on the comparison of the FEA results of $\kappa_{\sigma.num}$ with the developed approximation $\kappa_{\sigma.approx}$.

Statistical evaluation: $\kappa_{\sigma.approx}$			
Average	**Standard deviation**	**Min**	**Max**
1,031	0,090	0,832	1,374

6

Parametric study: Ultimate failure modes

As mentioned in Chapter 5.2 the only flange buckling modes obtained in the parametric study were the unrestricted rotation of the compression flange (386 girders), apart from some cases of normal stress web buckling (64 girders). A further distinction of the specimens demonstrating unrestricted rotation of the compression flange (as first eigenmode) is the occurrence of flange induced buckling of the web in the post-failure range. So, relevant failure modes in the current study are: (i) the failure mode can occur as pure unrestricted flange rotation or (ii) accompanied by flange induced web buckling in post-failure.

These two failure modes are presented in the current chapter, along with their relation to the corresponding first eigenmodes.

The used Python script for the parametric analyses in ABAQUS is presented in Appendix A.

6.1 Pure unrestricted rotation of the flange

Pure unrestricted rotation of the flange as ultimate failure mode was only observed in beams having the lowest studied $t_f/t_w = 2,5$, as for specimens ID-208 and ID-448 in Figures 6.1 and 6.2, respectively.

Attempting to find a pattern between the first eigenmode and the ultimate failure mode, the mode of the web was focused on. A way to distinguish whether pure unrestricted rotation of the flange, or flange induced buckling of the web is current, was thought to lie in the web having a noticeable out-of-plane deformation in the first eigenmode. This was not the case, since this was noted for specimens ID-139 and ID-448 in Figures 6.3 a,c, indicated by the lighter shade of some areas in the web, despite undergoing pure unrestricted rotation of the flange as ultimate failure mode.

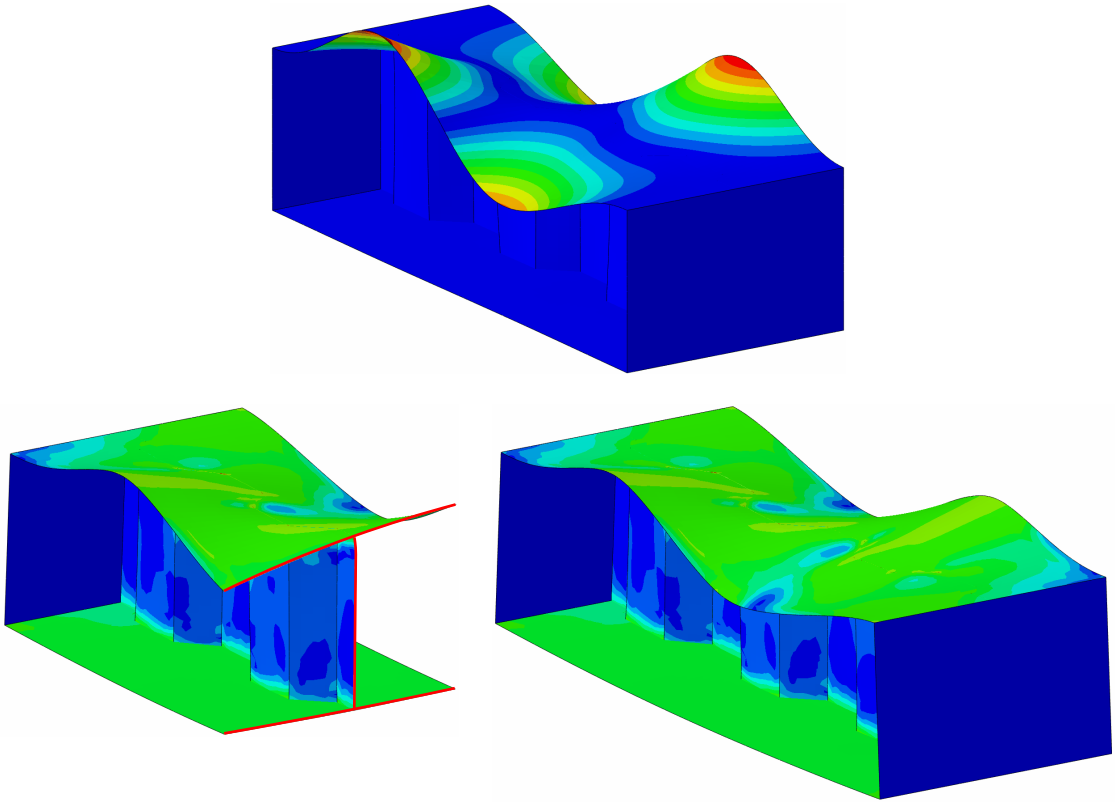

Figure 6.1: Comparison of first eigenmode (top) and ultimate failure mode (bottom) of ID-208, with $t_f/t_w = 2,5$.

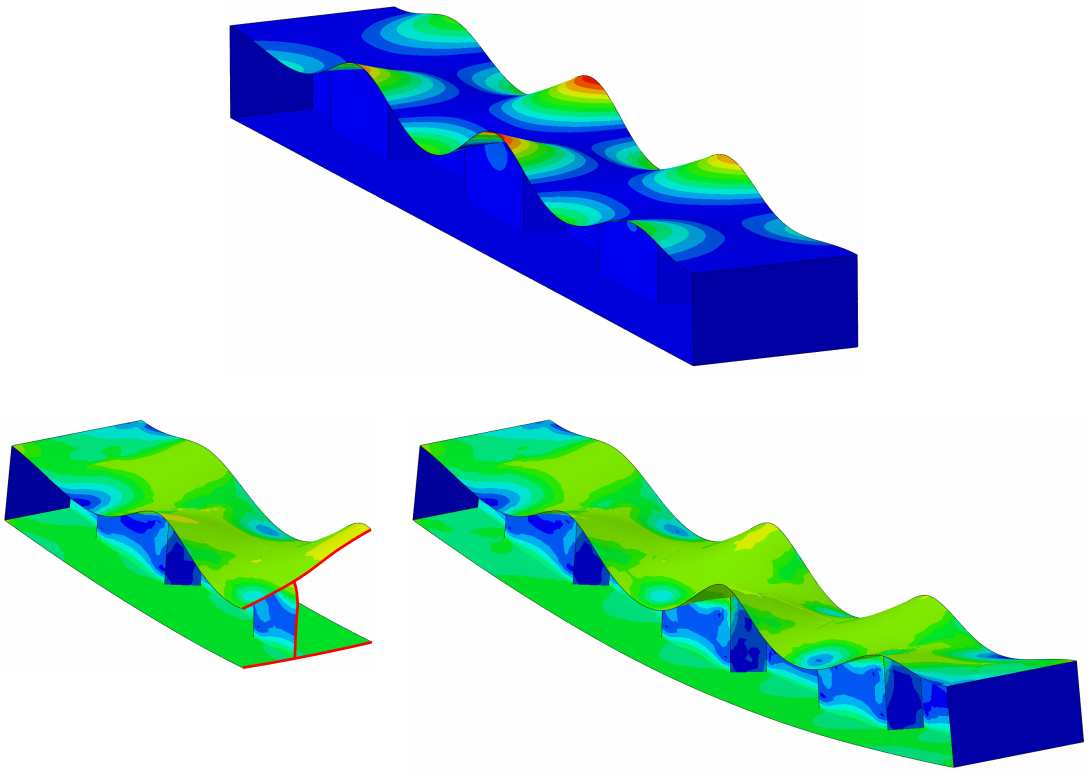

Figure 6.2: Comparison of first eigenmode (top) and ultimate failure mode (bottom) of ID-448, with $t_f/t_w = 2,5$.

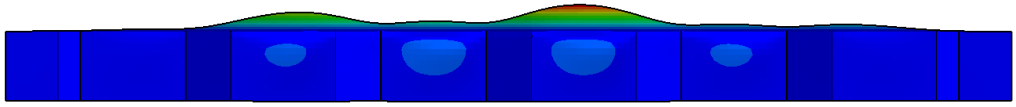

(a) Buckling mode of ID-139: $t_f/t_w = 2,5$

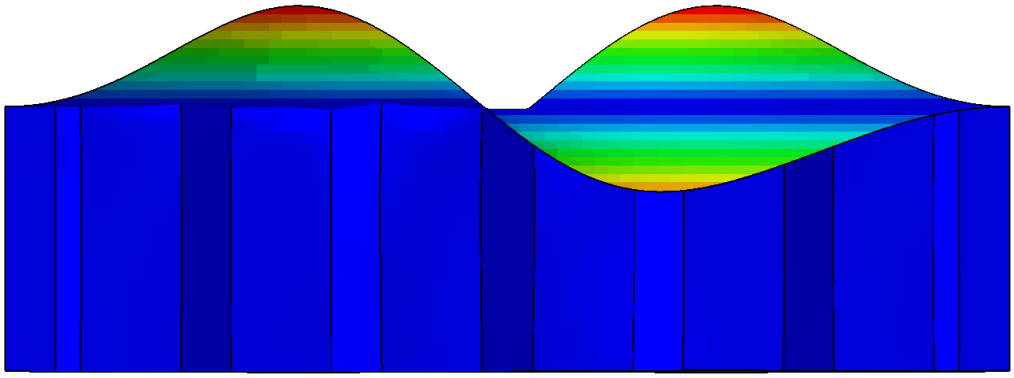

(b) Buckling mode of ID-208: $t_f/t_w = 2,5$

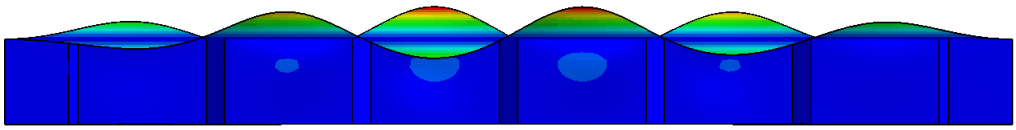

(c) Buckling mode of ID-448: $t_f/t_w = 2,5$

Figure 6.3: First eigenmodes of three beams that demonstrated pure unrestricted rotation of the flange in the nonlinear analysis.

Figure 6.4 illustrates the typical observed behavior of beams that demonstrated pure unrestricted rotation of the flange, which in the current case is for ID-208. Prior to failure, yielding of the web plate at the flange-to-web intersection in some areas could be seen (stage 2 in Figure 6.4). Reaching the ultimate capacity, the yielding in the flange-to-web intersection expanded in both longitudinal and vertical directions, still as distinct lines (stage 3). Further into the post-failure range, the same tendency can be seen (stage 4).

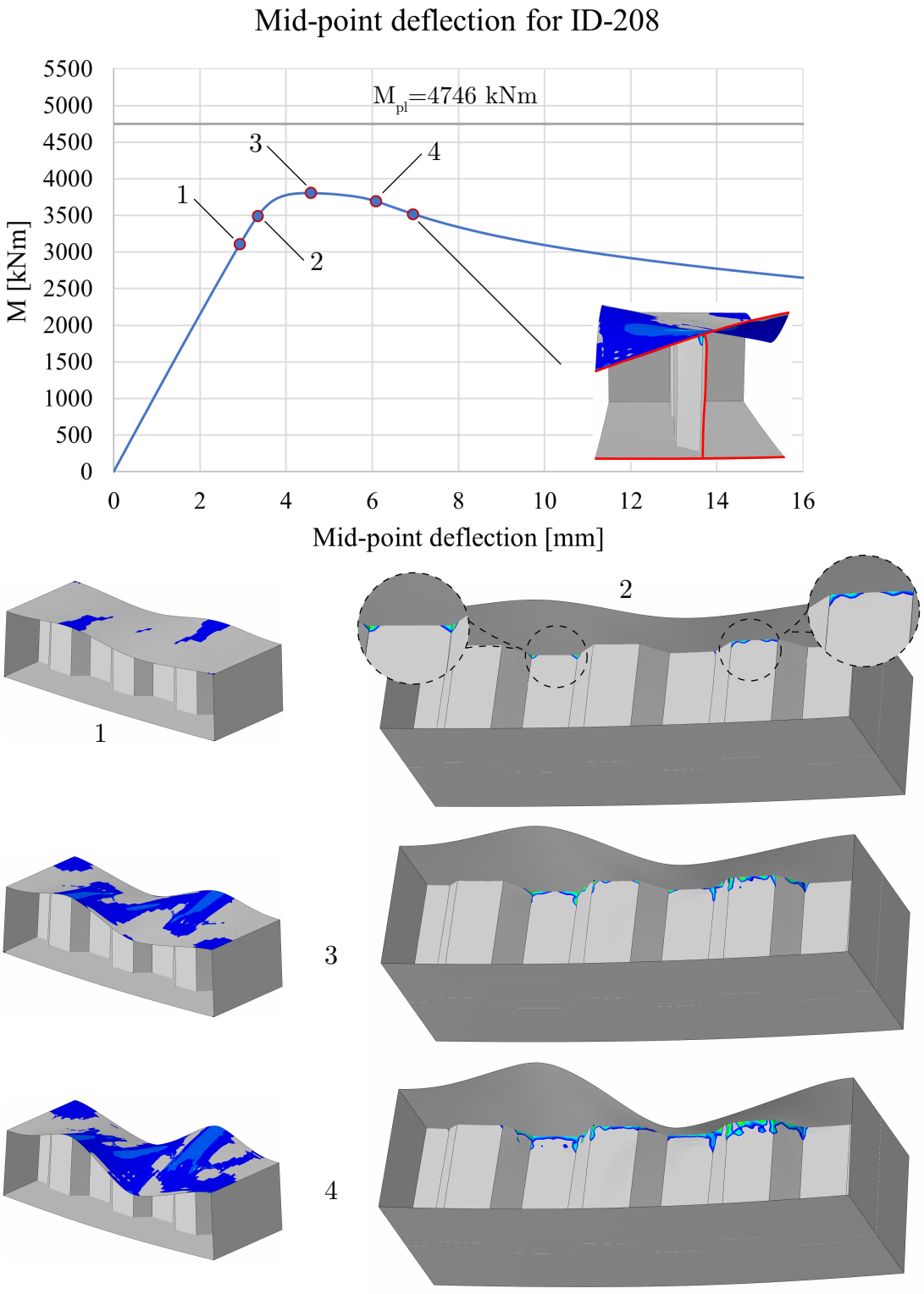

Figure 6.4: Overview of the behavior of ID-208 in the nonlinear analysis, demonstrating a pure unrestricted rotation of the flange.

6.2 Flange induced buckling of the web

Referring to the findings of Jáger et al. [3], presented in Chapter 2.4.1, flange induced buckling of the web is observed in the post-failure range, as a developing mechanism. Further, flange induced buckling of the web was noted for carbon steel beams having $t_f/t_w >\approx 5$. In the current study, the limit was $t_f/t_w \approx 3,5$.

The ultimate failure modes of some specimens demonstrating flange induced buckling of the web in post-failure are shown in Figures 6.5, 6.6 and 6.7. The first eigenmodes of a few beams, undergoing flange induced buckling of the web, are shown in Figures 6.8 a,b,c,d.

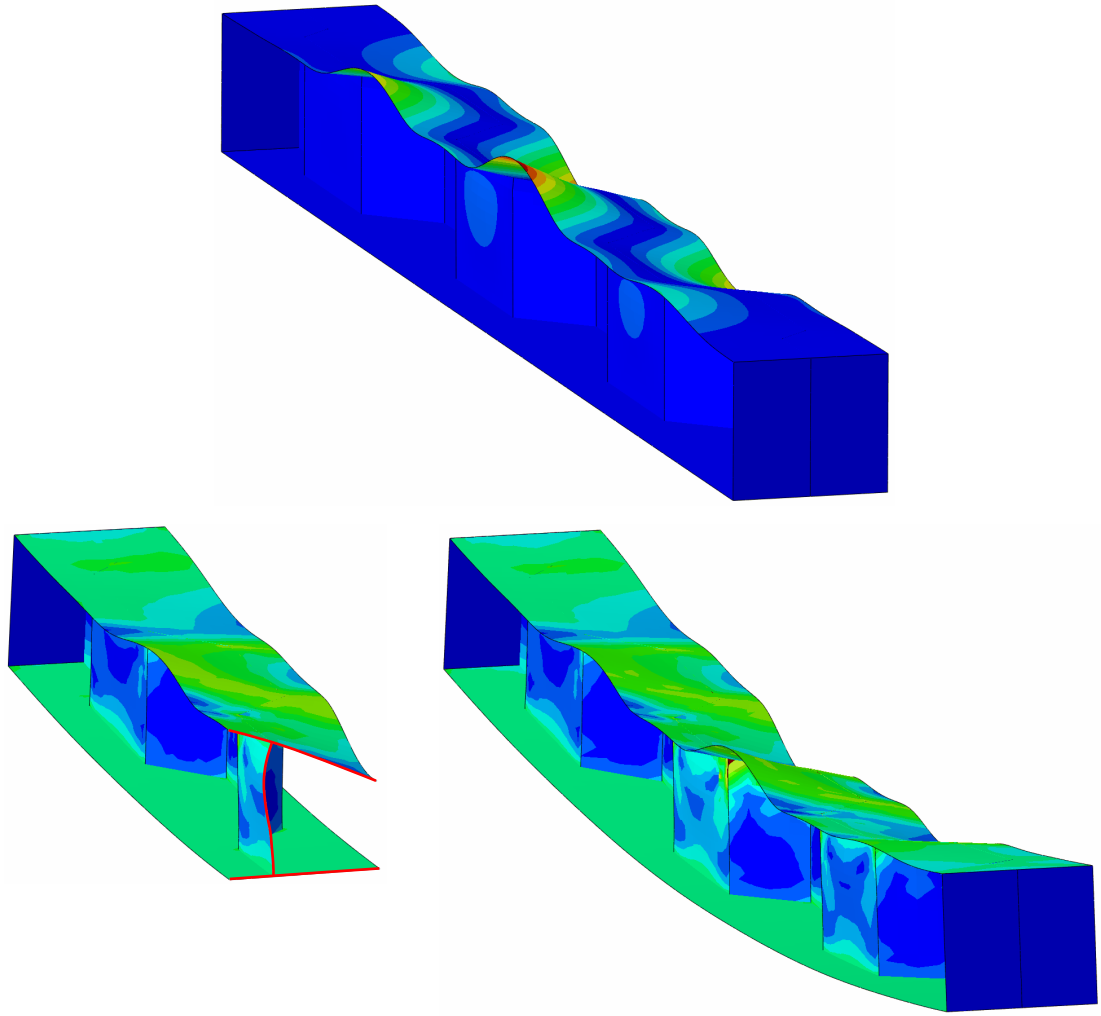

Figure 6.5: Comparison of first eigenmode (top) and ultimate failure mode (bottom) of ID-223, with $t_f/t_w = 4,17$.

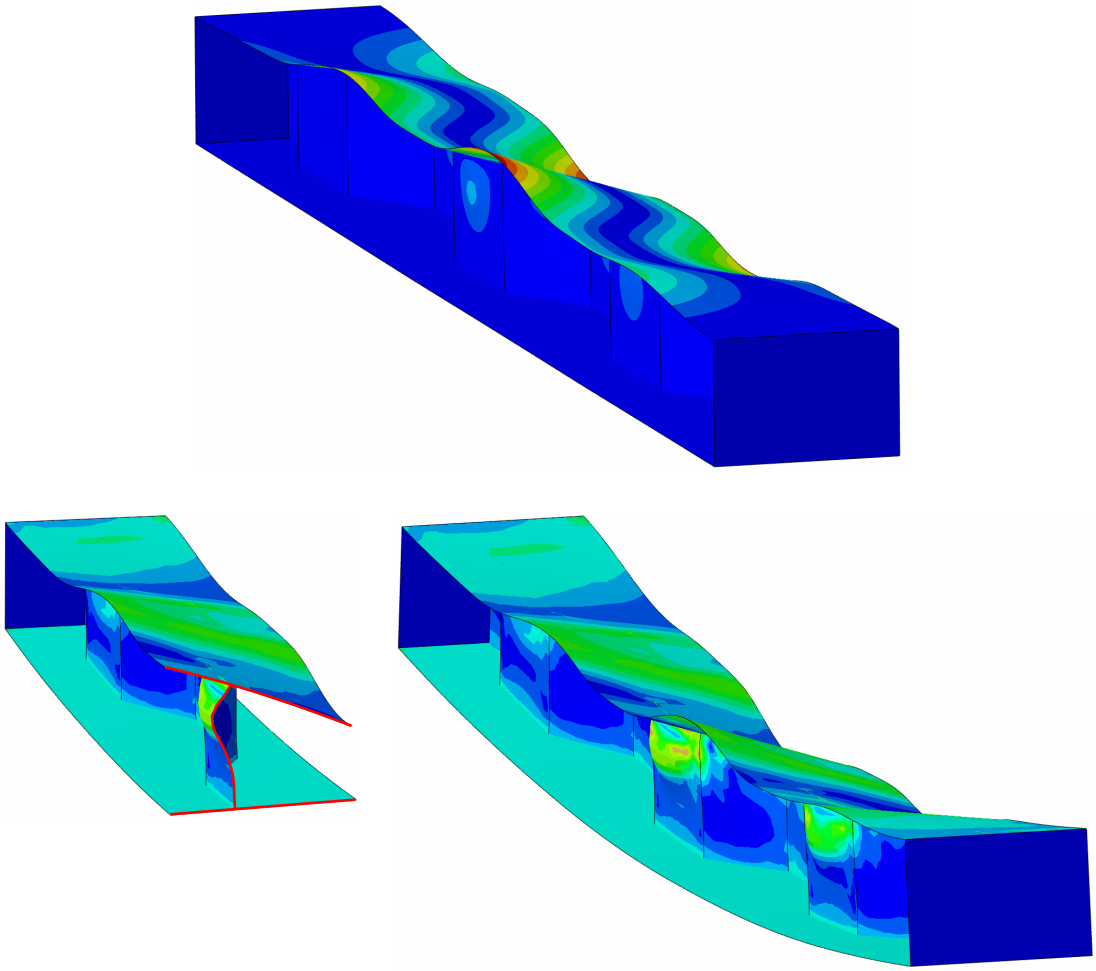

Figure 6.6: Comparison of first eigenmode (top) and ultimate failure mode (bottom) of ID-478, with $t_f/t_w = 8,75$.

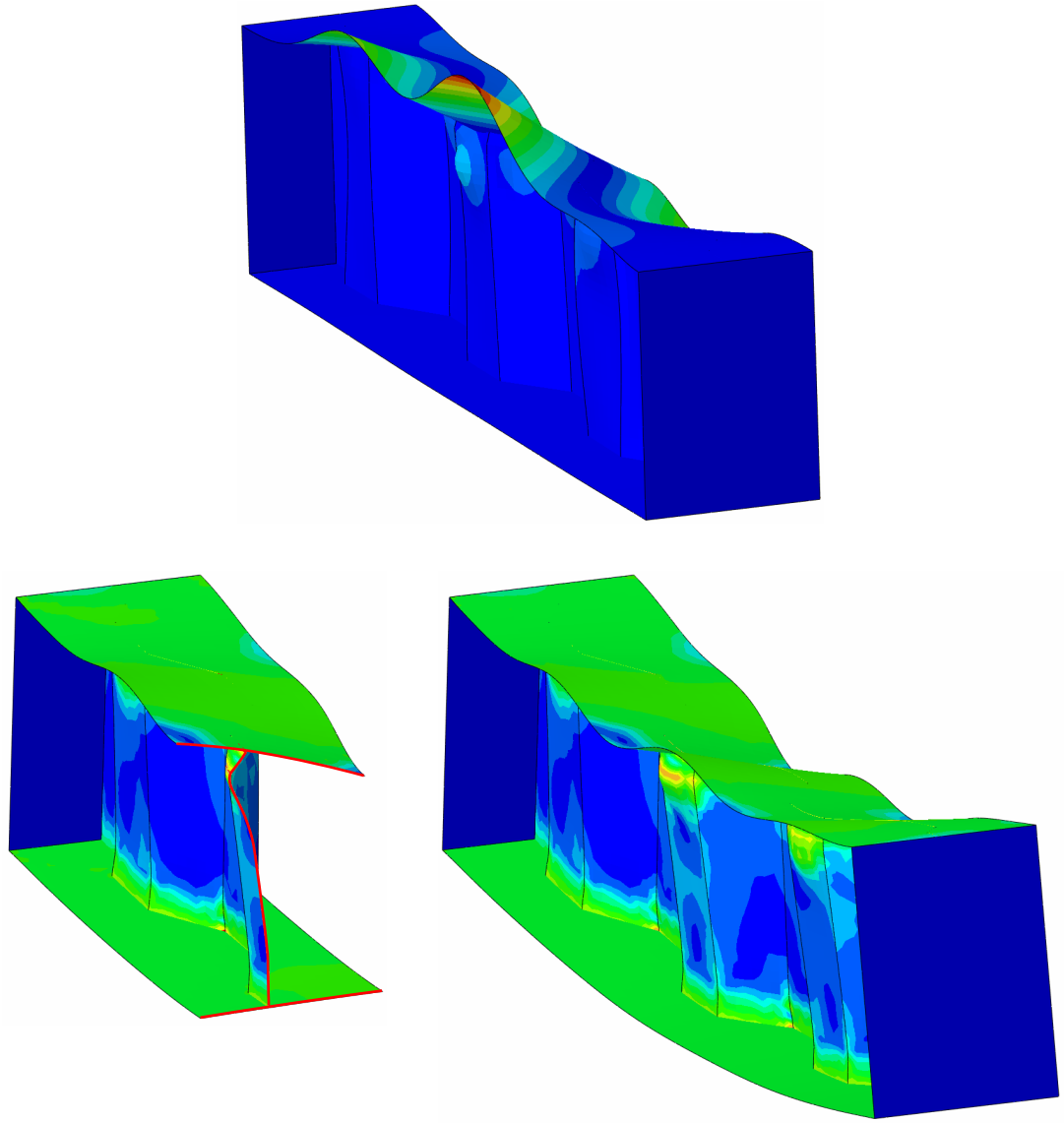

Figure 6.7: Comparison of first eigenmode (top) and ultimate failure mode (bottom) of ID-901, with $t_f/t_w = 12,5$.

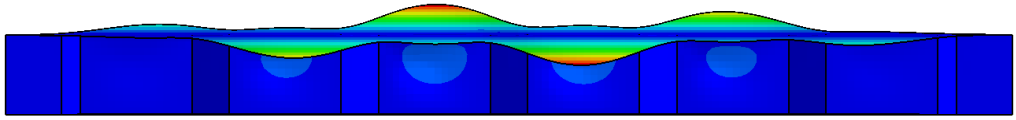

(a) Buckling mode of ID-223: $t_f/t_w = 4,17$

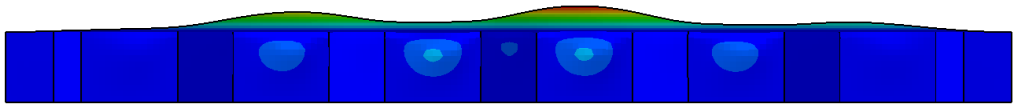

(b) Buckling mode of ID-478: $t_f/t_w = 3,5$

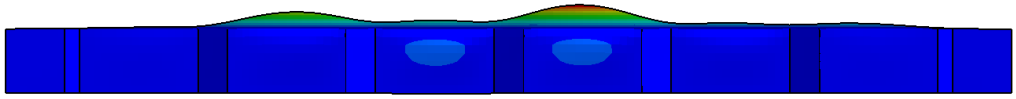

(c) Buckling mode of ID-745: $t_f/t_w = 8,75$

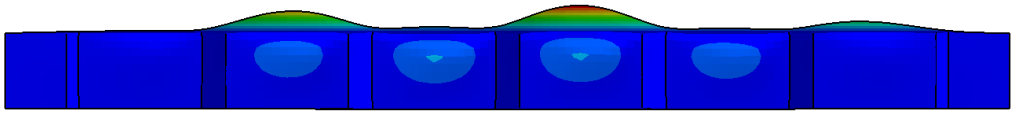

(d) Buckling mode of ID-1324: $t_f/t_w = 5$

Figure 6.8: First eigenmodes of four beams that demonstrated flange induced buckling of the web in the nonlinear analysis.

The overall behavior of beams undergoing flange induced buckling of the web in post-failure is represented by beam ID-223 in Figure 6.9. In this specific case, yielding in the web is initiated at failure (stage 1), as distinct spots in the flange-to-web intersection, which are more prominent in stage 2. In post-failure (stage 3) yielding in the flange-to-web intersection is developed to continuous lines. Apart from that, what characterizes the development of the failure mechanism, related to flange induced web buckling, is an additional yielding strip a small distance below the compression flange. This yielding strip is thought to weaken the web in the vertical direction, allowing the flange plate to buckle into the web.

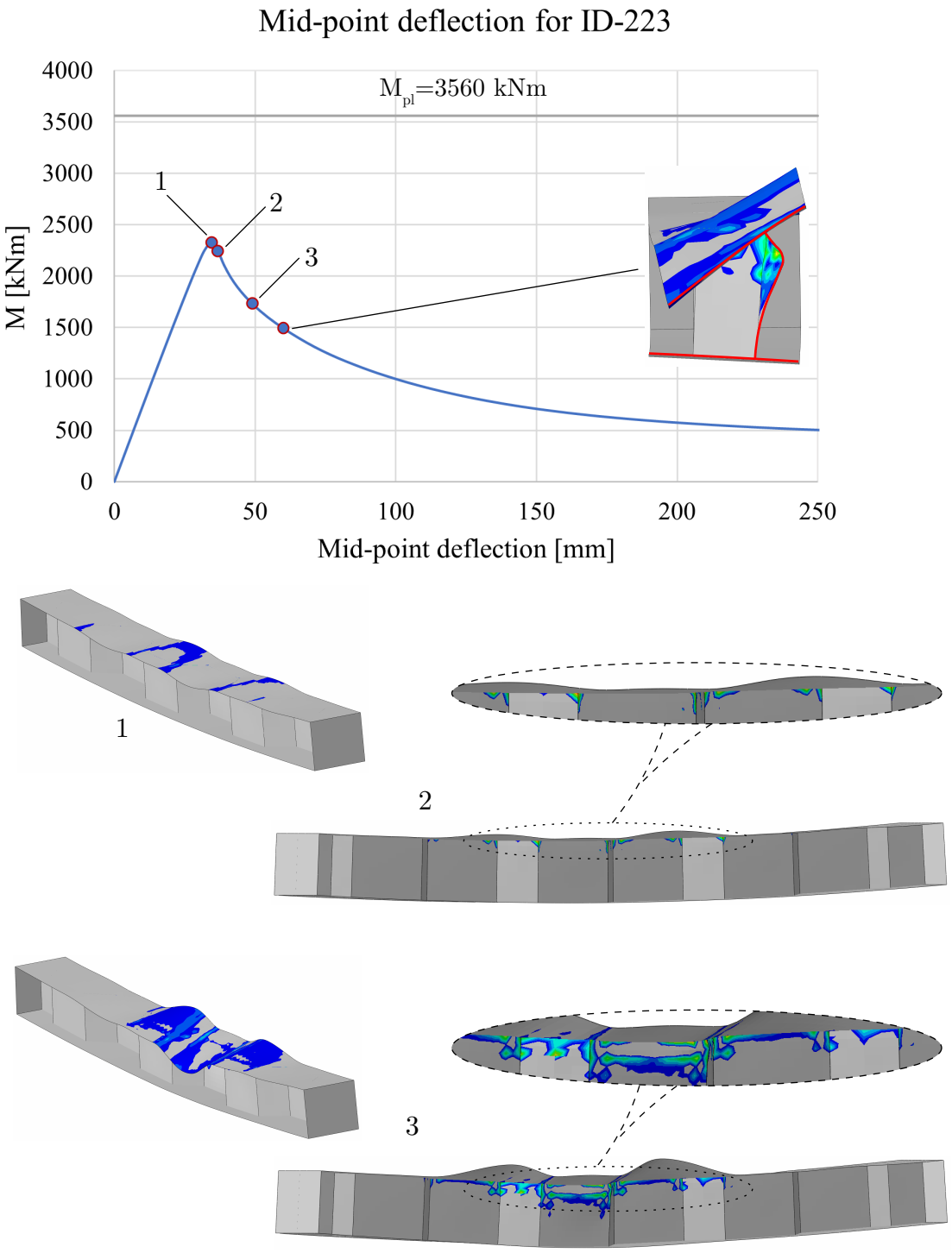

Figure 6.9: Overview of the behavior of ID-223 in the nonlinear analysis, demonstrating a flange induced web buckling.

7

Parametric study: nonlinear analyses

This chapter presents the results of the study on the parametric nonlinear analyses, where the ultimate moment capacities $M_{ult.num}$ were compared with the models suggested by the EN1993-1-5 [6], Jáger et al. [7] and the DASt-Richtlinie 015 [10]. A buckling curve was also designed and is presented as a concluding component.

The studied girders are the ones demonstrating normal stress flange buckling as first eigenmode (see Chapter 5.2). Girders where normal stress web buckling occurred as first eigenmode required no reduction, with the exception of some few cases, where minor reduction was needed. Despite that, only girders with normal stress flange buckling as lowest eigenmode are treated in the current chapter. Among the treated girders, 346 out of the 386 required a capacity reduction.

The used Python script for the parametric analyses in ABAQUS is presented in Appendix A.

7.1 Determination of ρ_{num}

The required reduction factor ρ_{num}, based on the FEA results, was calculated as in Equation 7.1, assuming no web contribution:

$$\rho_{num} = \frac{M_{ult.num}}{b_f \cdot t_f \cdot h_{lever} \cdot f_{yf}} \tag{7.1}$$

Where $M_{ult.num}$ is the ultimate moment capacity obtained in the numerical analysis. The calculated reduction factor ρ_{num} is assumed to be applied on the whole flange width b_f, see Figure 2.8.

7.2 Comparison of the FEA results with the EN1993-1-5

The reduction ρ of the flange width b_f in the EN1993-1-5 [6] is obtained through a direct relation with the relative slenderness ratio $\bar{\lambda}_p$ (see Equation 2.9). The relative slenderness ratio $\bar{\lambda}_p$ is defined as:

$$\bar{\lambda}_p(\sigma_{cr}) = \sqrt{f_y/\sigma_{cr}}$$

Which, by using the expression of σ_{cr} in Equation 2.4, can also be expressed as a function of κ_σ:

$$\bar{\lambda}_p(\kappa_\sigma) = \frac{\bar{b}/t_f}{28,4\epsilon\sqrt{\kappa_\sigma}} \qquad \text{see Equation 2.8}$$

The two versions of the relative slenderness, $\bar{\lambda}_p(\kappa_\sigma)$ & $\bar{\lambda}_p(\sigma_{cr})$, were investigated:

- For $\bar{\lambda}_p(\kappa_\sigma)$, the buckling coefficient $\kappa_{\sigma.EC}$ (Equation 2.15) suggested in the EN1993-1-5 [6] was used. Additionally, the large outstand c_f was used as reference plate width $\bar{b}$.

- For $\bar{\lambda}_p(\sigma_{cr})$, the critical normal stresses $\sigma_{cr.num}$ from the linear buckling analyses, presented in Chapter 5, were used.

The required reduction factor ρ_{num} is plotted against $\bar{\lambda}_p(\kappa_{\sigma.EC})$ in Figure 7.1. The buckling curve of the Eurocode for flat web girders (Equation 2.9) is also shown for comparison. It is obvious that there is a significant scatter in the results, especially in the higher slenderness range ($\bar{\lambda}_p(\kappa_{\sigma.EC}) > 0,85$), and that almost all results are on the unsafe side.

Figure 7.1 demonstrates that the limiting value of $\bar{\lambda}_p(\kappa_{\sigma.EC}) = 0,748$ is not relevant, and a lower limit closer to $\bar{\lambda}_p(\kappa_{\sigma.EC}) = 0,4$ should be considered. This is a major reason for the over-estimations obtained by Eurocode's method.

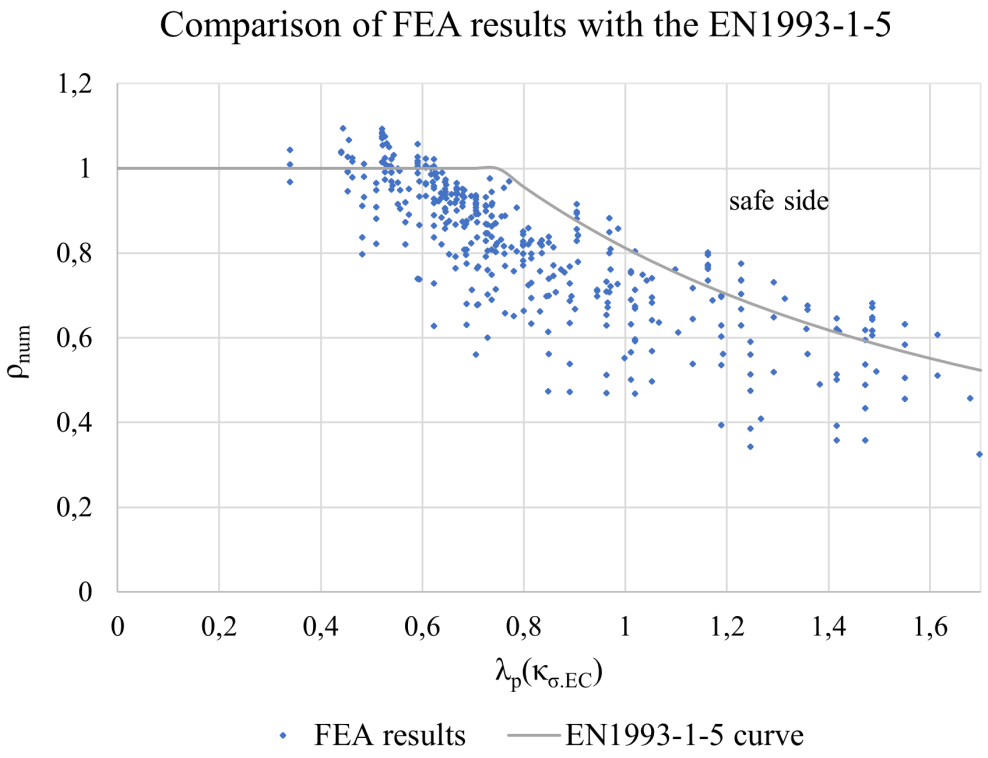

Figure 7.1: Comparison of the FEA results related to the buckling curve of the EN1993-1-5 [6], using the large outstand c_f and $\kappa_{\sigma.EC}$ for the determination of $\bar{\lambda}_p(\kappa_{\sigma.EC})$.

Plotting the required reduction factor ρ_{num} against $\bar{\lambda}_p(\sigma_{cr.num})$ in Figure 7.2 a very strong correlation can be observed. Despite that, almost all results with $\rho_{num} < 1$ are, again, below the buckling curve (for flat web girders) which is unsafe. The reason is the too high slenderness limit of 0,748, which in the current case can be distinguished to $\bar{\lambda}_p(\sigma_{cr.num}) \approx 0,45$.

Additionally, in reference to defining a slenderness limit relevant for Duplex 1.4162, a limit of $c_f/t_f/\epsilon_{ss.f} = 10$ has also been noted.

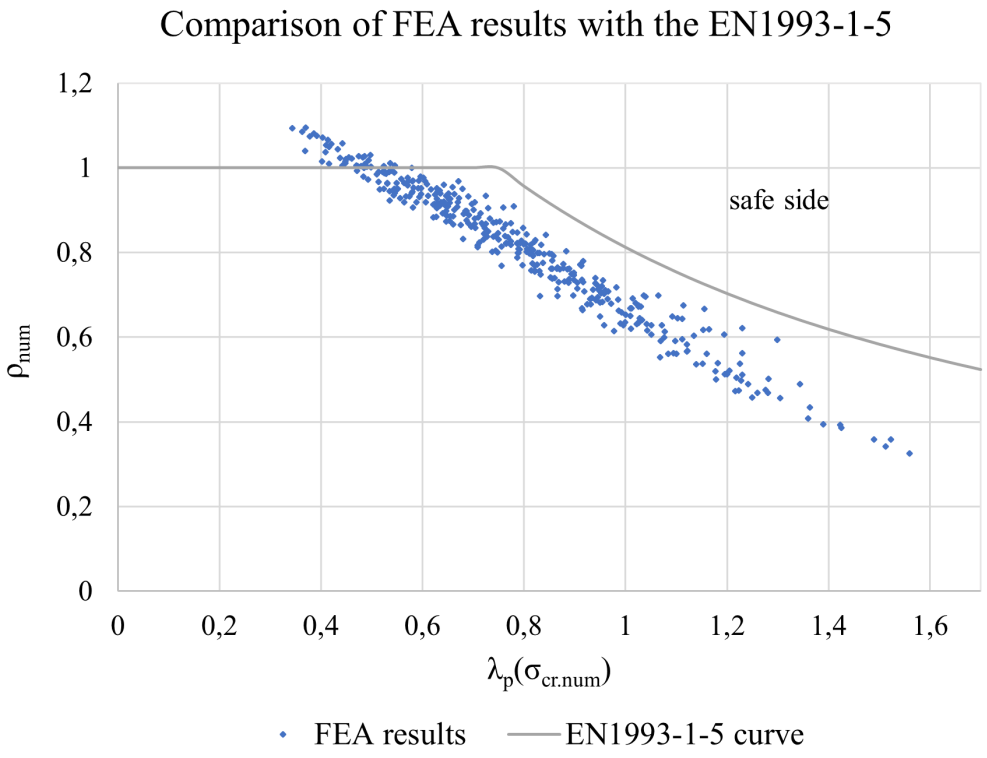

Figure 7.2: Comparison of the FEA results related to the buckling curve of the EN1993-1-5 [6], using $\bar{\lambda}_p(\sigma_{cr.num}) = \sqrt{f_{yf}/\sigma_{cr.num}}$.

The ultimate moment capacities $M_{ult.EC}$ based on the buckling curve in Equation 2.9 using $\bar{\lambda}_p(\sigma_{cr.num})$ are compared to the FEA results in Figures 7.3 and 7.4. Given the results in Figure 7.2, all the points are on the unsafe side. Table 7.1 presents the statistical evaluation of the comparison of $M_{ult.num}$ and $M_{ult.EC}$, using $\bar{\lambda}_p(\kappa_{\sigma.EC})$ & $\bar{\lambda}_p(\sigma_{cr.num})$ for the reduction factor ρ. The average over-estimations are 17% (for $\bar{\lambda}_p(\kappa_{\sigma.EC})$) and 18,2% (for $\bar{\lambda}_p(\sigma_{cr.num})$).

The comparisons with the model of the EN1993-1-5 [6] are presented for each girder in Tables C.1-C.5 in Appendix C.

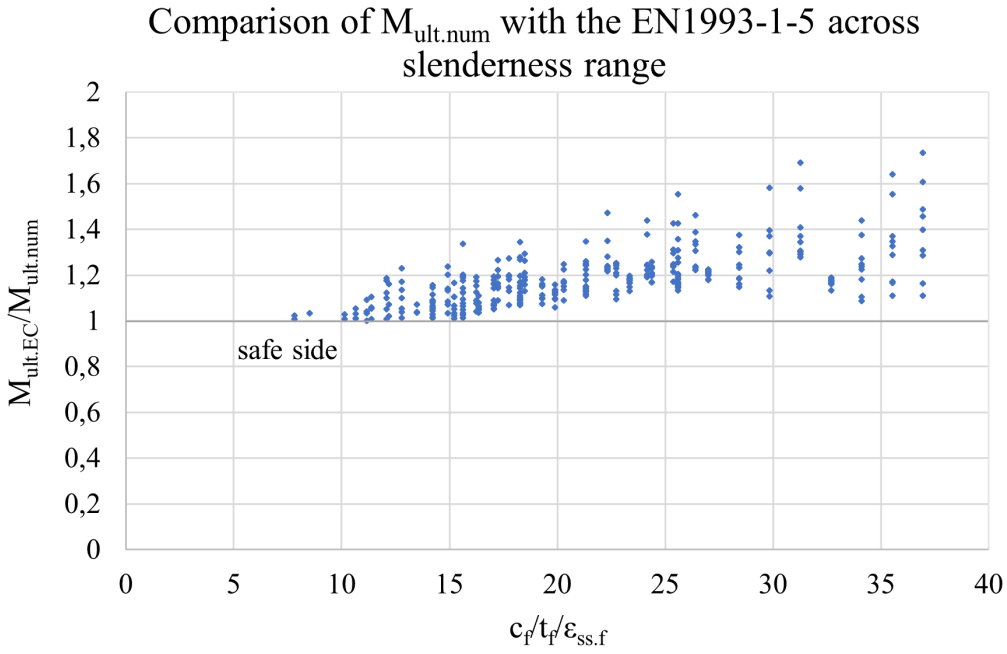

Figure 7.3: Comparison of the FEA results of $M_{ult.num}$ with the suggestion of the EN1993-1-5 [6] $M_{ult.EC}$, using $\bar{\lambda}_p(\sigma_{cr.num})$, across the slenderness range.

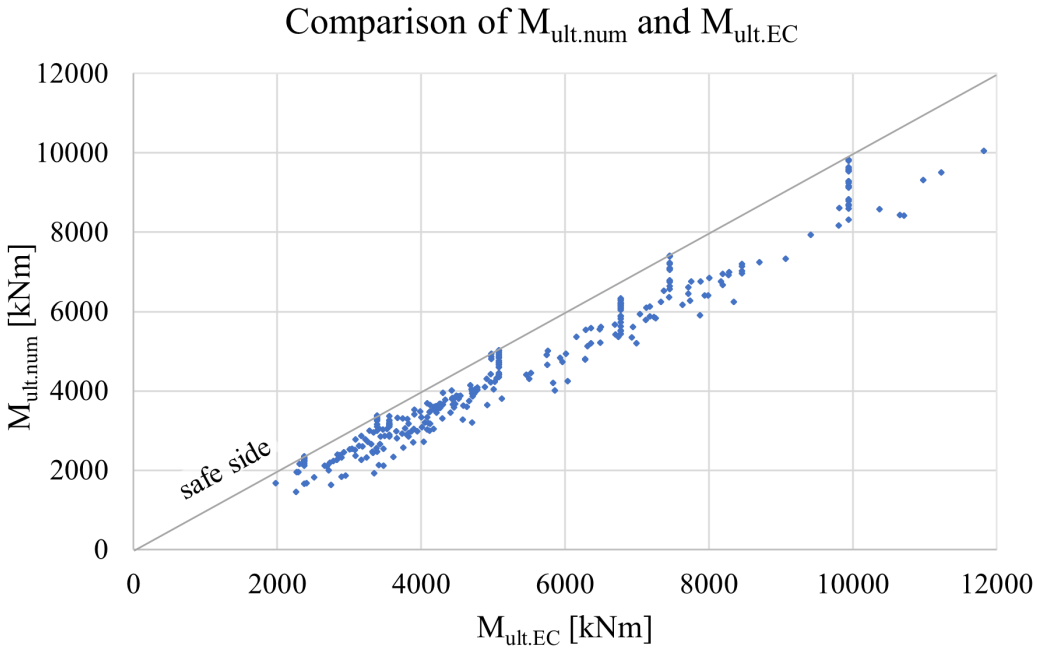

Figure 7.4: Comparison of $M_{ult.num}$ and $M_{ult.EC}$ [6], using $\bar{\lambda}_p(\sigma_{cr.num})$.

Table 7.1: Statistical evaluation on the comparison of the FEA results $M_{ult.num}$ with $M_{ult.EC}$ [6].

Statistical evaluation for M_{ult}: EN1993-1-5 [6]				
	Average	**Standard deviation**	**Min**	**Max**
Using $\bar{\lambda}_p(\kappa_{\sigma.EC})$	1,170	0,187	0,863	1,991
Using $\bar{\lambda}_p(\sigma_{cr.num})$	1,182	0,120	1,001	1,735

7.3 Comparison of the FEA results with Jáger et al.

The proposal of Jáger et al. [7], presented in Chapter 2.3.5 leads to more relevant results in the lower slenderness range, compared to the Eurocode. This is illustrated in Figures 7.5 and 7.6, where the ultimate moment capacities, $M_{ult.num}$, from FEA are compared to the capacities $M_{ult.Jager}$ according to the method of Jáger et al.

Since a lower slenderness limit was suggested according to Chapter 7.2, additional comparisons were made by exchanging the value of 14 with 10 in the expression of ρ in Equation 2.23. Additionally, the reduction factor ρ was applied on the large outstand c_f, as suggested by Jáger et al. [7], and on the whole flange width b_f. The results of these comparisons are presented in Table 7.2.

According to Table 7.2, the suggested method of calculating the reduction of the flange, with the slenderness limit of $c_f/t_f/\epsilon_{ss.f} = 14$, results in an average over-estimation of 10,9%, and a standard deviation of 0,147, which is an improvement in comparison with the over-estimation of 17% and standard deviation of 0,187 of the EN1993-1-5 [6] (Table 7.1). Applying the reduction on the whole flange width b_f, and reducing the slenderness limit to $c_f/t_f/\epsilon_{ss.f} = 10$, leads to more conservative results, with an average underestimation of 23,8% and a standard deviation of 0,095.

The comparisons with the model proposed by Jáger et al. [7] are presented for each girder in Tables C.6-C.15 in Appendix C.

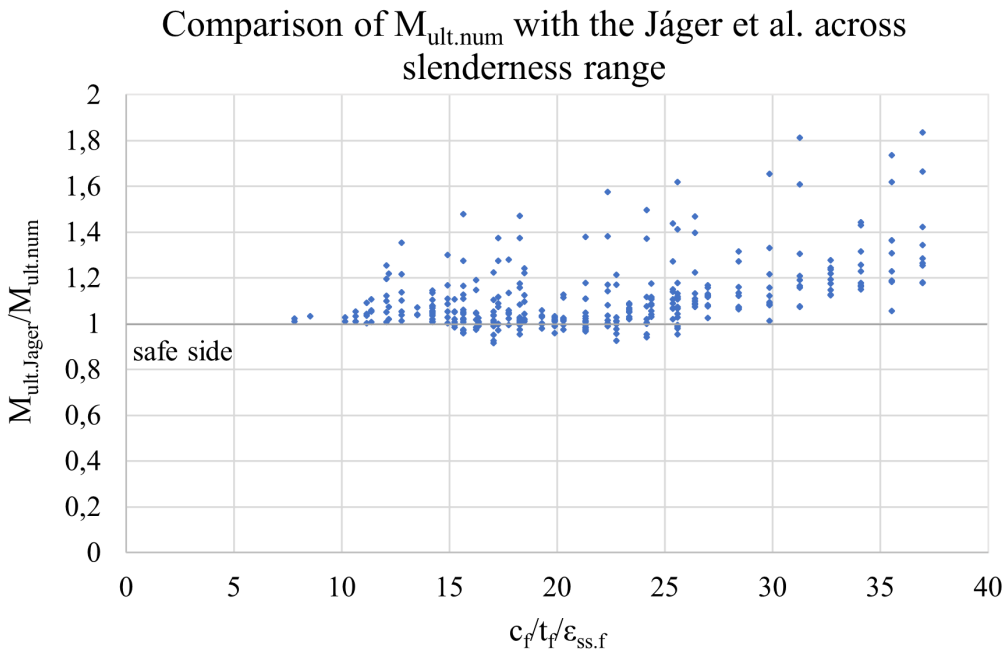

Figure 7.5: Comparison of the FEA results of $M_{ult.num}$ with the suggestion of Jáger et al. [7] $M_{ult.Jager}$ across the slenderness range.

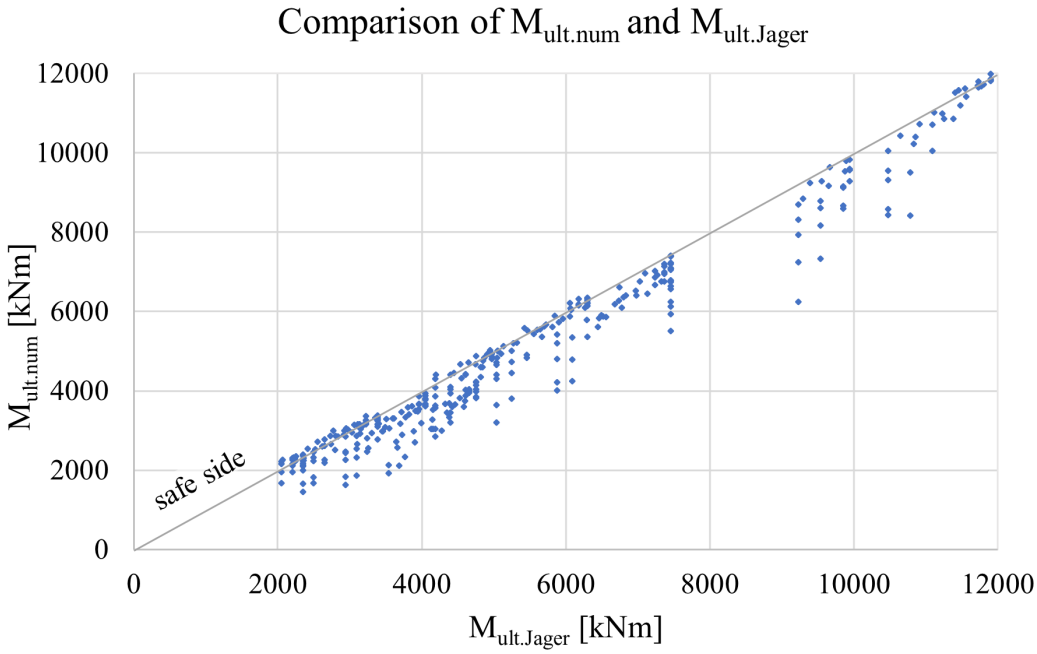

Figure 7.6: Comparison of $M_{ult.num}$ and $M_{ult.Jager}$ [7].

Table 7.2: Statistical evaluation on the comparison of the FEA results $M_{ult.num}$ with $M_{ult.Jager}$ [7].

Statistical evaluation for M_{ult}: Jáger et al. [7]					
		Average	**Standard deviation**	**Min**	**Max**
$\boldsymbol{\rho = (14\epsilon_{ss.f} \cdot c_f/t_f)^{\beta}}$	ρ applied on b_f	0,978	0,105	0,777	1,427
	ρ applied on c_f	1,109	0,147	0,916	1,834
$\boldsymbol{\rho = (10\epsilon_{ss.f} \cdot c_f/t_f)^{\beta}}$	ρ applied on b_f	0,762	0,095	0,555	1,057
	ρ applied on c_f	0,969	0,130	0,736	1,618

7.4 Comparison of the FEA results with DASt-Richtlinie 015

The method suggested in the DASt-Richtlinie 015 [10] is presented in Chapter 2.3.6, using only the flange thickness t_f as input parameter. Figures 7.7 and 7.8 show the comparison of the ultimate capacities $M_{ult.num}$ from FEA and $M_{ult.DASt}$ [10]. This method resulted in the largest scatter, especially in the slenderness range of $c_f/t_f/\epsilon_{ss.f} > 15$. The average over-estimation is 15,6% and the standard deviation is 0,224, as seen in Table 7.3. The reason behind the large scatter could be the model's lack of consideration of the corrugation geometry, since it only considers the thickness of the flange plate t_f.

The comparisons with the model proposed by the DASt Richtlinie 015 [10] are presented for each girder in Tables C.16-C.18 in Appendix C.

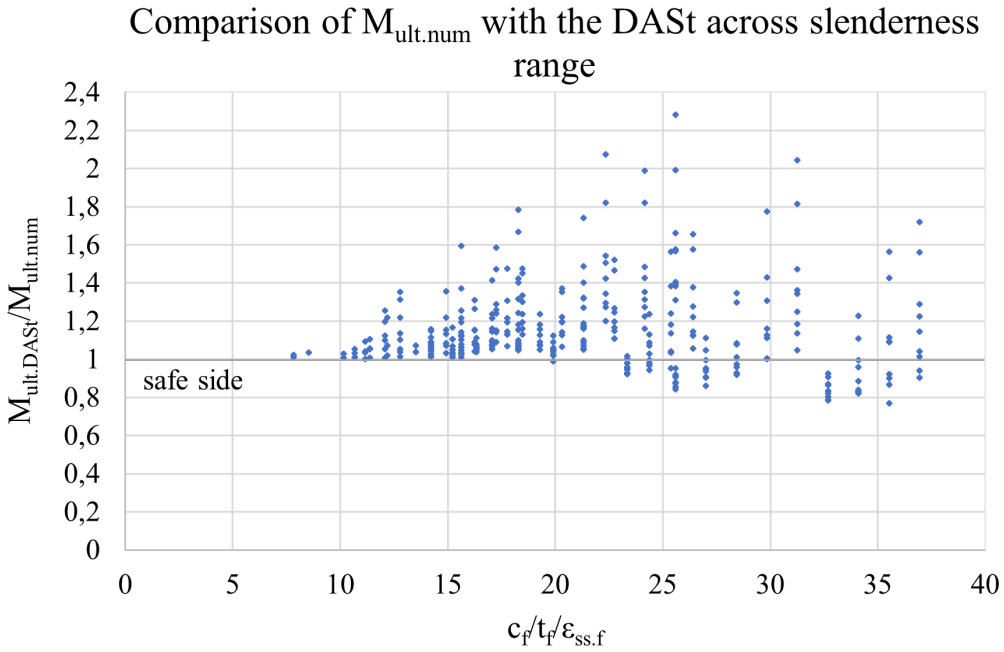

Figure 7.7: Comparison of the FEA results of $M_{ult.num}$ with the suggestion of the DASt-Richtlinie 015 [10] $M_{ult.DASt}$ across the slenderness range.

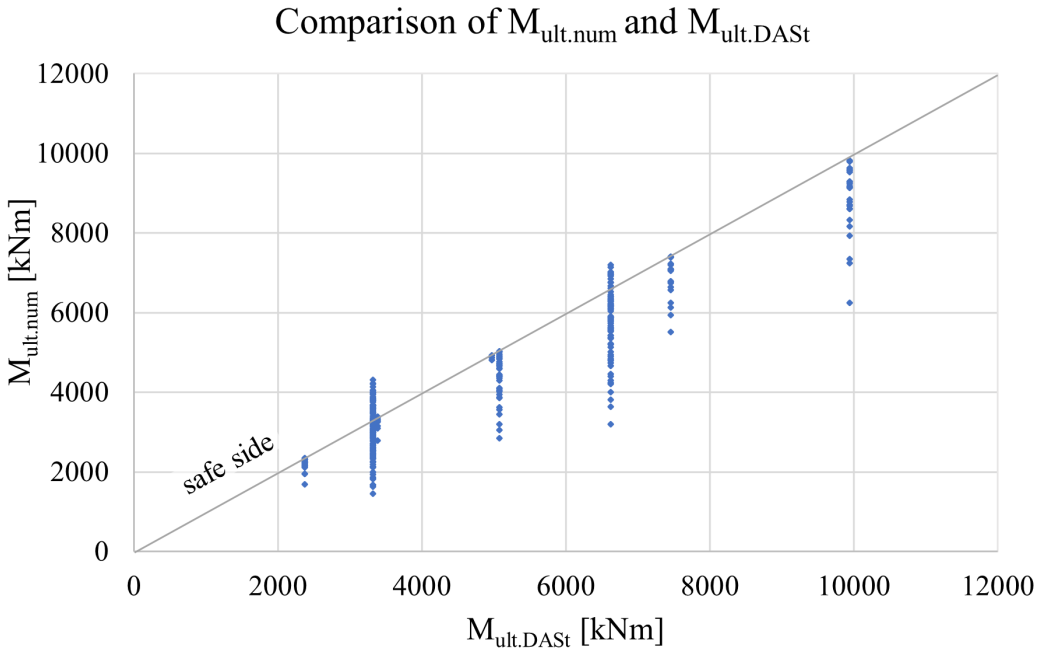

Figure 7.8: Comparison of $M_{ult.num}$ and $M_{ult.DASt}$ [10].

Table 7.3: Statistical evaluation on the comparison of the FEA results $M_{ult.num}$ with $M_{ult.DASt}$ [10].

Statistical evaluation for M_{ult}: DASt-Richtlinie 015 [10]			
Average	**Standard deviation**	**Min**	**Max**
1,156	0,224	0,769	2,283

7.5 Suggested buckling curve expression

The evaluations of the existing models presented in Chapters 7.2-7.4 led to the conclusion that they are not enough to approximate the ultimate capacity of Duplex 1.4162 beams with enough accuracy. A new model was developed, based on the relative slenderness ratio $\bar{\lambda}_p(\kappa_\sigma)$ suggested in the EN1993-1-5 [6] in Equation 2.8, using the large flange outstand c_f. The background to this choice is the satisfactory correlation, and moderate scatter, when plotting ρ_{num} against $\bar{\lambda}_p(\sigma_{cr.num})$ as shown in Figure 7.2.

Since a model for approximating κ_σ was developed in the current thesis through $\kappa_{\sigma.approx}$ according to Equations 5.4 and 5.5, the relative slenderness $\bar{\lambda}_p(\kappa_{\sigma.approx})$ was used instead. The use of $\bar{\lambda}_p(\kappa_{\sigma.approx})$ resulted in equivalent correlation as using $\bar{\lambda}_p(\sigma_{cr.num})$, but slightly increased scatter as shown in Figure 7.9. The latter is due to $\kappa_{\sigma.approx}$ only being an approximation of the actual $\kappa_{\sigma.num}$ (or, equivalently, $\sigma_{cr.num}$).

The developed buckling curve expression ρ_{approx} is presented in Equation 7.2:

$$\rho_{approx} = \frac{0,02}{\bar{\lambda}_p(\kappa_{\sigma.approx})} - 0,7 \cdot \bar{\lambda}_p(\kappa_{\sigma.approx}) + 1,227 \qquad \text{for} \quad \bar{\lambda}_p(\kappa_{\sigma.approx}) > 0,4 \quad (7.2)$$

Important to mention here is that the reduction factor ρ_{approx} is to be applied on the whole flange width b_f.

The developed buckling curve is also plotted in Figure 7.9, and it can be noted that many of the beams are well above the designed curve. This is due to the scatter mentioned, which forces some of the specimens to be further on the safe side in order to fit all of them above the curve.

The graph in Figure 7.9 is complemented with the comparison graphs in Figures 7.10 and 7.11, where the $M_{ult.num}$ from FEA and the approximate $M_{ult.approx}$ are compared. The largest underestimations of capacity are observed in the higher slenderness range of $c_f/t_f/\epsilon_{ss.f} > 27$ with underestimations exceeding 20% and reaching up to 38%.

Overall, the average underestimation of capacity of the developed model is 15,9%, as presented in Table 7.4, with a standard deviation of 0,064.

The comparisons with the model developed in the current thesis are presented for each girder in Tables C.19-C.22 in Appendix C.

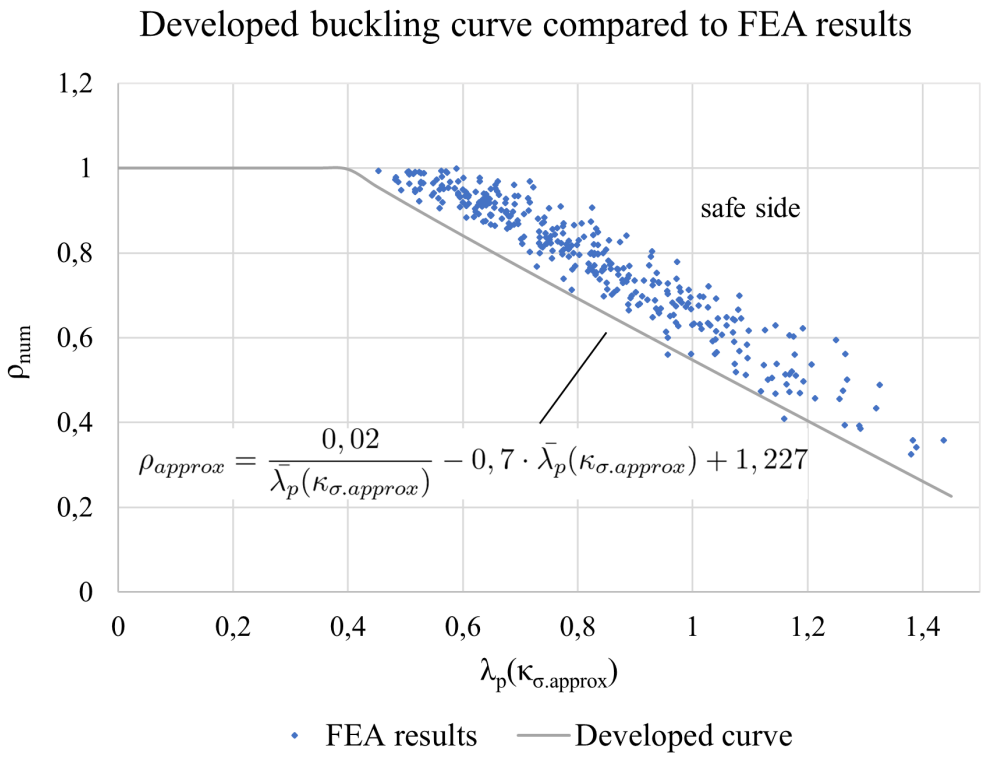

Figure 7.9: Comparison of the FEA results related to the developed buckling curve ρ_{approx}.

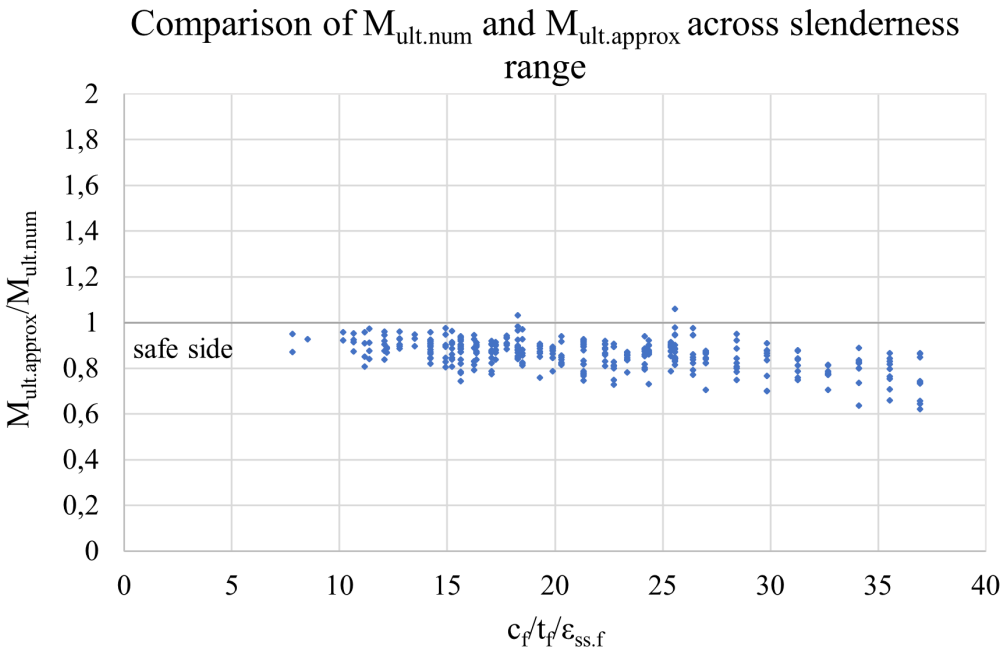

Figure 7.10: Comparison of the FEA results of $M_{ult.num}$ with the approximate $M_{ult.approx}$ across the slenderness range.

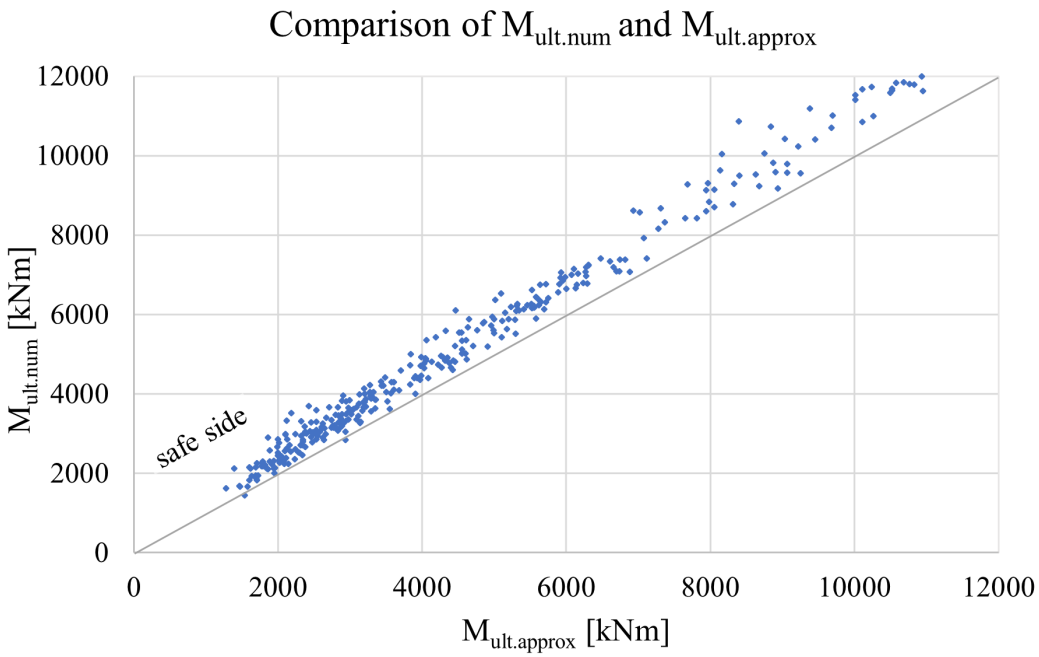

Figure 7.11: Comparison of $M_{ult.approx}$ and $M_{ult.num}$.

Table 7.4: Statistical evaluation on the comparison of the FEA results $M_{ult.num}$ with $M_{ult.approx}$.

Statistical evaluation: $M_{ult.approx}$			
Average	**Standard deviation**	**Min**	**Max**
0,861	0,064	0,620	1,059

8

Conclusion

The corrugation of the web plate in steel girders enhances the shear buckling capacity and contributes to a reduced need of material. This is achieved by the thinner web plates and no need of vertical stiffeners. However, the normal stress flange buckling behavior of such members has not been studied to any deep extent, and there are still inconsistencies in the developed models for CWIG in carbon steel. Further, there are no design models proposed on the normal stress buckling of such members in stainless steel. With this as a background, the current study has focused on investigating the buckling coefficient κ_σ and the reduction factor ρ, related to normal stress flange buckling of trapezoidally CWIG in Duplex 1.4162 stainless steel.

Comparing the buckling coefficient $\kappa_{\sigma.num}$, obtained from the numerical analyses with the suggestion of the EN1993-1-5 [6], a large scatter was observed, with many analysed girders being on the unsafe side. A corresponding comparison with the model developed by Jáger et al. [7], resulted in enhanced results with respect to scatter. Still, the scatter was considerable, leading to a number of girders ending up on the unsafe side.

The improvement noted in the model of Jáger et al. [7] is suggested to be the result of considering the parameters of flange-to-web thickness ratio t_f/t_w, and the enclosing effect R. A new model for predicting the buckling coefficient was developed in this thesis, by considering several parameters related to the corrugation geometry. A choice of developing separate expressions for girders with $R > 0,17$ and $R < 0,17$ was also made, and proved to be beneficial. The developed approximating expressions $\kappa_{\sigma.approx}$ of the buckling coefficient provided strongly improved estimations, compared to the studied models.

For the investigated parameter range, the first eigenmodes obtained were the unrestricted rotation of the compression flange and normal stress web buckling. An approximate way of distinguishing which mode is relevant has been proposed in the current thesis. The first eigenmode of girders demonstrating unrestricted rotation of the compression flange have been shown to provide no direct indication of whether flange induced buckling of the web is relevant in post-failure.

For girders with higher values of t_f/t_w, a flange induced buckling of the web was observed in post-failure, and the limit has been determined at approximately $t_f/t_w \geq 3,5$. The typical development of this failure mechanism was noted as a yielding strip along one longitudinal fold, weakening the web in the vertical direction.

With regard to the reduction factor, using the buckling curve of the EN1993-1-5 [6] led to over-estimations of capacities for almost all studied girders. This effect was pronounced in the higher slenderness range. Using the proposed model of Jáger et al. [7], resulted in some improvement in the lower slenderness range, but with considerable over-estimations for the majority of the girders. Investigating the model of the DASt Richtlinie 015 [10], the most unsafe results were obtained along with the highest scatter. Finally, the developed model of this thesis is based on the relative slenderness ratio as a function of the approximate buckling coefficient $\kappa_{\sigma.approx}$, suggested in this thesis. The capacities of all treated girders were then on the safe side, with the exception of a few, with considerably reduced scatter. The most conservative estimations were at the higher slenderness range.

The high relative slenderness limit $\bar{\lambda}_p(\kappa_{\sigma.EC}) \geq 0,748$ of the EN1993-1-5 [6] has been concluded to result in the over-estimations obtained by this model. A lowered limit of $\bar{\lambda}_p(\kappa_{\sigma.EC}) \geq 0,4$ (or $c_f/t_f/\epsilon_{ss.f} \geq 10$) is suggested as more appropriate for trapezoidally CWIG in Duplex 1.4162 stainless steel. In all studied models, a decreasing accuracy in estimating the required capacity reduction of girders with very slender flanges was noted. A possible explanation to this could be that for more slender plates, instability becomes the dominating phenomenon in failure. The latter is often challenging to predict accurately, and the consideration of several geometric (and material) parameters could be needed.

9

Further research

The study presented in this thesis has focused on only one stainless steel grade, the Duplex 1.4162. It would be valuable to conduct corresponding investigations based on varying stainless steel grades. Additionally, physical tests could provide an increased validation of the results from numerical analyses.

The developed design model to determine the reduction factor ρ could be further improved by approximating the buckling coefficient κ_σ more accurately. This would result in a less conservative model, and more efficient designs. Also, developing a new slenderness parameter (similar to $\bar{\lambda}_p$ of the Eurocode) that results in a stronger correlation with the required reduction factor can further improve the accuracy of the model.

Bibliography

[1] Elgaaly, M., Seshadri, A., Hamilton, R.W. (1997): Bending strength of steel beams with corrugated webs. *Journal of Structural Engineering*, ASCE 123, June 1997, pp. 772-782.

[2] Abbas, H.H., Driver R.G., Sauce R. (2006): Behavior of corrugated web I-girders under in-plane loads. *Journal of Engineering Mechanics*, Vol. 132, No. 8, August 2006, pp. 806-814.

[3] Dunai, L., Jáger, B., Kövesdi, B. (2017): Flange buckling behavior of girders with corrugated web Part I: Experimental study. *Thin-Walled Structures*, Vol. 118, 2017, pp. 181-195.

[4] Elgaaly, M., Seshadri, A. (1998): Depicting the behavior of girders with corrugated webs up to failure using non-linear finite element analysis. *Advances in Engineering Software*, Vol. 29, No. 3-6, 1998, pp. 195-208.

[5] CEN (2006). *Eurocode 3: Design of steel structures - Part 1-5: Plated structural elements*. Brussels.

[6] CEN (2019). *Eurocode 3: Final draft of the EN1993-1-5*. Brussels.

[7] Dunai, L., Jáger, B., Kövesdi, B. (2017): Flange buckling behavior of girders with corrugated web Part II: Numerical study and design method development. *Thin-Walled Structures*, Vol. 118, 2017, pp. 238-252.

[8] Dunai, L., Jáger, B., Kövesdi, B. (2017): Flange buckling resistance of trapezoidal web girders – Experimental and numerical study. *c/e papers*, Vol. 1, 2017, pp. 4088-4097.

[9] Steel Construction Institute (2017): *Design manual for structural stainless steel* (4th edition), SCI, SCI P413, Berkshire, UK, 2017, pp. 3-7, 15-18, p.21.

[10] DASt-Richtlinie 015 (1990): *Träger mit schlanken Stegen* (Girders with slender webs). Stahlbau-Verlagsgesellshaft, Köln, 1990.

[11] CEN (2005). *Eurocode 3: Design of steel structures - Part 1-1: General rules and rules for buildings*. Brussels.

[12] Al-Emrani, M., Åkesson, B. (2020): *Steel structures: Course literature - VSM 191*. Report. Department of Architecture and Civil Engineering. Chalmers University of Technology. Publication no. 2020:13, Gothenburg, Sweden, 2020, pp. 56-63, 82-83.

[13] CEN (2006). *Eurocode 3: Design of steel structures - Part 1-4: General rules - Supplementary rules for stainless steels*. Brussels.

[14] SIS (2015): *Eurocode 3: Design of steel structures – Part 1-4: General rules – Supplementary rules for stainless steels*. Stockholm, Sweden, 2015.

[15] CEN (2020). *Eurocode 3: Design of steel structures: Second Draft of EN1993-1-4*. Brussels.

[16] Inaam, Q., Upadhay, A. (2022): Accordion effect in bridge girders with corrugated webs. *Journal of Constructional Steel Research*, Vol. 188, 2022, pp. 1-13.

A

Appendix: Python script

```
# -*- coding: mbcs -*-
# TRANSCRIPT originated by ERIK SAVE & KARL  KERMO  and developed by:
# FATIMA HLAL & NAHEEL MOHRA and
# ALAA ACHOUR & ZIAD MLLI

from mmap import mmap
from part import *
from material import *
from section import *
from assembly import *
from step import *
from interaction import *
from load import *
from mesh import *
from optimization import *
from job import *
from sketch import *
from visualization import *
from connectorBehavior import *
from odbAccess import *
import sys
import regionToolset
import math

import shutil
import csv
import os

cwd = os.getcwd()  # Home directory
os.chdir(cwd + "/odbs")  # Work directory


csv_name = cwd + "/name of input file"  # Path of indata file

# Reading the indata file rows
with open(csv_name, 'r') as f:
    lis = [line.split() for line in f]  # Create a list of lists


# Loop for each girder ID:
for ID in range():  # Add desired range here

  line = lis[ID][0].split(';')  # Splitting the relevant row into items

  #----------------------------I N P U T   D A T A--------------------------------

  # Material parameters
  elastic_modulus = 200e3  # Elastic modulus - stainless [MPa]
  poissons_ratio = 0.3  # Poissons ratio - stainless [-]

  # Nonlinear analysis step
  Increments = 150  # Number of increments for riks analysis
  Modes = 1  # Number of modes to be considered

  # I-section
```

```
b_f = float(line[])  # Flange width [mm]
t_f = float(line[])  # Flange thickness [mm]
h_w = 500.0  # Web height [mm]
t_w = float(line[])  # Web thickness [mm]

# Corrugation geometry
corr_depth = float(line[])  # Corrugation depth [mm]
corr_ang_deg = float(line[])  # Corrugation angle in degrees
l_par_1= float(line[])  # Parallel fold length [mm]
b_edge=l_par_1/2  # Edge fold length [-]

c_f = (b_f+corr_depth)/2  # Large flange outstand [mm]

num_wavelengths = 3 # Number of total wavelengths on the girder

# Stiffeners
Stiffener_th = 16  # Stiffeners thickness [mm]

Initial_imperfection = c_f/50 # Equivalent geometric imperfection [mm]

# Angles
corr_ang = corr_ang_deg*(2*pi/360) # Corrugation angle in radians for script

# Loading
moment = 100e6  # Moment magnitude [N*mm]

# Global element size:
global_element_size = min(math.floor(l_par_1/4), math.floor(h_w/4))


#----------------------S T A R T   O F   S C R I P T--------------------------
## DEBUG MODE, when debug mode is on the analyses are not submitted
debug = 1 # 1 = debug mode on (do not submit analysis), 0 = debug mode off
#(submit analysis)

# Y - coordinates
corr_amp = corr_depth/2 # Corrugation amplitude [mm]
h_w_global = h_w+t_f # Web height used in shell model [mm]

y1 = -corr_amp
y2 = -corr_amp
y3 = -corr_amp
y4 = 0
y5 = corr_amp
y6 = corr_amp
y7 = corr_amp
y8 = 0

# X - coordinates
proj_l_inc = corr_amp/math.tan(corr_ang) # Projected length of inclined fold [mm]
l_wavelength = 4*(proj_l_inc+l_par_1/2) # Length of wavelength [mm]
L_beam = num_wavelengths*l_wavelength + 2*b_edge  # Total beam length [mm]

x1 = proj_l_inc
x2 = proj_l_inc+l_par_1/2
x3 = proj_l_inc+l_par_1
x4 = 2*proj_l_inc+l_par_1
x5 = 3*proj_l_inc+l_par_1
x6 = 3*proj_l_inc+3*l_par_1/2
x7 = 3*proj_l_inc+2*l_par_1
x8 = l_wavelength



#-----------------------------LINEAR ANALYSIS--------------------------------

#------------------------G L O B A L   M O D E L----------------------------

# Change name of global model
Model_Name_Global = 'Global Model-' + str(ID)
```

```
126
127 # Change name of model
128 mdb.Model(modelType=STANDARD_EXPLICIT, name='Model-' + str(ID))
129 mdb.models.changeKey(fromName='Model-' + str(ID), toName=Model_Name_Global)
130 global_model = mdb.models[Model_Name_Global]
131
132 # Create web - one wavelength
133 global_model.ConstrainedSketch(name='web_sketch_global', sheetSize=2000.0)
134 web_sketch_global = global_model.sketches['web_sketch_global']
135 web_sketch_global.Line(point1=(0.0, 0.0), point2=(x1, y1))
136 web_sketch_global.Line(point1=(x1, y1), point2=(x3, y3))
137 web_sketch_global.Line(point1=(x3, y3), point2=(x5, y5))
138 web_sketch_global.Line(point1=(x5, y5), point2=(x7, y7))
139 web_sketch_global.Line(point1=(x7, y7), point2=(x8, y8))
140 global_model.Part(dimensionality=THREE_D, name='web', type=DEFORMABLE_BODY)
141 global_part_web= global_model.parts['web']
142 global_part_web.BaseShellExtrude(depth=h_w_global, sketch=web_sketch_global)
143
144 del web_sketch_global
145
146 # Create edge fold
147 global_model.ConstrainedSketch(name='edge_sketch_global', sheetSize=2000.0)
148 edge_sketch_global = global_model.sketches['edge_sketch_global']
149 edge_sketch_global.Line(point1=(0.0, 0.0), point2=(b_edge,0))
150 global_model.Part(dimensionality=THREE_D, name='edge', type=DEFORMABLE_BODY)
151 global_part_edge = global_model.parts['edge']
152 global_part_edge.BaseShellExtrude(depth=h_w_global, sketch=edge_sketch_global)
153
154 del edge_sketch_global
155
156 # Create flange part above one wavelength of the web
157 global_model.ConstrainedSketch(name='__profile__', sheetSize=2000.0)
158 global_model.sketches['__profile__'].rectangle(point1=(0.0, -b_f/2), point2=(
    l_wavelength, b_f/2))
159 global_model.Part(dimensionality=THREE_D, name='flange', type=DEFORMABLE_BODY)
160 global_model.parts['flange'].BaseShell(sketch=
161 global_model.sketches['__profile__'])
162 del global_model.sketches['__profile__']
163 global_part_flange = global_model.parts['flange']
164
165 # Create flange part above edge fold
166 global_model.ConstrainedSketch(name='__profile__', sheetSize=2000.0)
167 global_model.sketches['__profile__'].rectangle(point1=(0.0, -b_f/2), point2=(
    b_edge, b_f/2))
168 global_model.Part(dimensionality=THREE_D, name='flange_edge', type=
    DEFORMABLE_BODY)
169 global_model.parts['flange_edge'].BaseShell(sketch=
170 global_model.sketches['__profile__'])
171 del global_model.sketches['__profile__']
172 global_part_flange_edge = global_model.parts['flange_edge']
173
174 # Create Stiffener
175 global_model.ConstrainedSketch(name='__profile__', sheetSize=2000.0)
176 global_model.sketches['__profile__'].rectangle(point1=(-b_f/2, 0.0), point2=(b_f
    /2,h_w_global))
177 global_model.Part(dimensionality=THREE_D, name='stiffener', type=DEFORMABLE_BODY)
178 global_model.parts['stiffener'].BaseShell(sketch=
179 global_model.sketches['__profile__'])
180 del global_model.sketches['__profile__']
181 global_part_stiffener = global_model.parts['stiffener']
182
183 # Constructing datum planes in web sketch for partitioning
184 planes_w = []  # List containing the 3 planes
185
186 plane1 = global_part_web.DatumPlaneByPrincipalPlane(principalPlane=YZPLANE,
    offset=x2)
187 plane1 = global_part_web.datums[plane1.id]
188 planes_w.append(plane1)
189
190 plane2 = global_part_web.DatumPlaneByPrincipalPlane(principalPlane=YZPLANE,
```

```
    offset=x4)
plane2 = global_part_web.datums[plane2.id]
planes_w.append(plane2)

plane3 = global_part_web.DatumPlaneByPrincipalPlane(principalPlane=YZPLANE,
    offset=x6)
plane3 = global_part_web.datums[plane3.id]
planes_w.append(plane3)


# Partitioning one wavelength of the web
global_part_web.PartitionFaceByDatumPlane(datumPlane=plane1, faces=
    global_part_web.faces.findAt((x2,y2,0),))
global_part_web.PartitionFaceByDatumPlane(datumPlane=plane2, faces=
    global_part_web.faces.findAt((x4,y4,0),))
global_part_web.PartitionFaceByDatumPlane(datumPlane=plane3, faces=
    global_part_web.faces.findAt((x6,y6,0),))


# Constructing datum planes in flange sketch for partitioning
planes_f = []  # List containing the 7 planes

plane1 = global_part_flange.DatumPlaneByPrincipalPlane(principalPlane=YZPLANE,
    offset=x1)
plane1 = global_part_flange.datums[plane1.id]
planes_f.append(plane1)

plane2 = global_part_flange.DatumPlaneByPrincipalPlane(principalPlane=YZPLANE,
    offset=x2)
plane2 = global_part_flange.datums[plane2.id]
planes_f.append(plane2)

plane3 = global_part_flange.DatumPlaneByPrincipalPlane(principalPlane=YZPLANE,
    offset=x3)
plane3 = global_part_flange.datums[plane3.id]
planes_f.append(plane3)

plane4 = global_part_flange.DatumPlaneByPrincipalPlane(principalPlane=YZPLANE,
    offset=x4)
plane4 = global_part_flange.datums[plane4.id]
planes_f.append(plane4)

plane5 = global_part_flange.DatumPlaneByPrincipalPlane(principalPlane=YZPLANE,
    offset=x5)
plane5 = global_part_flange.datums[plane5.id]
planes_f.append(plane5)

plane6 = global_part_flange.DatumPlaneByPrincipalPlane(principalPlane=YZPLANE,
    offset=x6)
plane6 = global_part_flange.datums[plane6.id]
planes_f.append(plane6)

plane7 = global_part_flange.DatumPlaneByPrincipalPlane(principalPlane=YZPLANE,
    offset=x7)
plane7 = global_part_flange.datums[plane7.id]
planes_f.append(plane7)

# Partitioning flange part above one web wavelength
for i in range(0,7):
    global_part_flange.PartitionFaceByDatumPlane(datumPlane=planes_f[i], faces=
    global_part_flange.faces.findAt((l_wavelength,0,0),))

# Create material - one model for each plate thickness range
global_model.Material(name='Stainless1')
global_model.materials['Stainless1'].Elastic(table=((elastic_modulus,
    poissons_ratio), ))
global_model.materials['Stainless1'].Plastic(table=((532.0, 0.0), (542.0,0.00217)
    , (563.0,0.00297),(585.0,0.00567),(609.0,0.0127),(699.0,0.0694),(876.0,0.2200))
    )

```

```
245 global_model.Material(name='Stainless2')
246 global_model.materials['Stainless2'].Elastic(table=((elastic_modulus,
      poissons_ratio), ))
247 global_model.materials['Stainless2'].Plastic(table=((482.0, 0.0), (492.0,0.00219)
      , (503.0,0.00249),(523.0,0.00389),(570.0,0.0157),(655.0,0.0678),(886.0,0.2607))
      )
248
249 global_model.Material(name='Stainless3')
250 global_model.materials['Stainless3'].Elastic(table=((elastic_modulus,
      poissons_ratio), ))
251 global_model.materials['Stainless3'].Plastic(table=((451.9, 0.0),
      (462.1,0.002212), (482.7,0.003104), (504.1,0.005731),(586.3,0.04299)
      ,(702.7,0.1379),(856.3,0.2714)))
252
253 # Create flange and web sections
254
255 # Flange
256 if t_f <= 6.4:
257   material_flange = str('Stainless1')
258 elif t_f > 6.4 and t_f <= 10:
259   material_flange = str('Stainless2')
260 else:
261   material_flange = str('Stainless3')
262
263 # Web
264 if t_w <= 6.4:
265   material_web = str('Stainless1')
266 elif t_w > 6.4 and t_w <= 10:
267   material_web = str('Stainless2')
268 else:
269   material_web = str('Stainless3')
270
271 # Create flange section
272 global_model.HomogeneousShellSection(idealization=NO_IDEALIZATION,
273 integrationRule=SIMPSON, material=material_flange, name='flange',
274 nodalThicknessField='', numIntPts=5, poissonDefinition=DEFAULT,
275 preIntegrate=OFF, temperature=GRADIENT, thickness=t_f, thicknessField='',
276 thicknessModulus=None, thicknessType=UNIFORM, useDensity=OFF)
277
278 # Create web section
279 global_model.HomogeneousShellSection(idealization=NO_IDEALIZATION,
280 integrationRule=SIMPSON, material=material_web, name='web', nodalThicknessField='
      ',
281 numIntPts=5, poissonDefinition=DEFAULT, preIntegrate=OFF, temperature=
282 GRADIENT, thickness=t_w, thicknessField='', thicknessModulus=None,
283 thicknessType=UNIFORM, useDensity=OFF)
284
285 # Create stiffener section
286 global_model.HomogeneousShellSection(idealization=NO_IDEALIZATION,
      integrationRule=SIMPSON, material='Stainless3', name='stiffener',
287 nodalThicknessField='', numIntPts=5, poissonDefinition=DEFAULT,
288 preIntegrate=OFF, temperature=GRADIENT, thickness=Stiffener_th, thicknessField= '
      ',
289 thicknessModulus=None, thicknessType=UNIFORM, useDensity=OFF)
290
291 # Assigning sections
292
293 # Assign section: Web
294 pw11 = (0, 0, h_w_global/2)
295 pw21 = (x1, y1, h_w_global/2)
296 pw31 = (x2-1, y2, h_w_global/2)
297 pw41 = (x3, y3, h_w_global/2)
298 pw51 = (x4-1,-tan(corr_ang), h_w_global/2)
299 pw61 = (x5, y5, h_w_global/2)
300 pw71 = (x6-1, y6, h_w_global/2)
301 pw81 = (x7, y7, h_w_global/2)
302 pw91 = (x8, y8, h_w_global/2)
303
304 global_part_web.SectionAssignment(offset=0.0, offsetField='',
305 offsetType=MIDDLE_SURFACE, region=Region(
```

```
306 faces=global_part_web.faces.findAt(((pw11),), ((pw21),), ((pw31),), ((pw41),), ((
      pw51),), ((pw61),), ((pw71),), ((pw81),), ((pw91),))),
307 sectionName='web', thicknessAssignment=FROM_SECTION)
308
309
310 # Assign section: Flange
311 pf11 = (0, 0, 0)
312 pf21 = (x1, 0, 0)
313 pf31 = (x2-1, 0, 0)
314 pf41 = (x3, 0, 0)
315 pf51 = (x4-1,0, 0)
316 pf61 = (x5, 0, 0)
317 pf71 = (x6-1, 0, 0)
318 pf81 = (x7-1, 0, 0)
319 pf91 = (x8, 0, 0)
320
321 global_part_flange.SectionAssignment(offset=0.0, offsetField='',
322 offsetType=MIDDLE_SURFACE, region=Region(
323 faces=global_part_flange.faces.findAt(((pf11),), ((pf21),), ((pf31),), ((pf41),),
       ((pf51),), ((pf61),), ((pf71),), ((pf81),), ((pf91),))),
324 sectionName='flange', thicknessAssignment=FROM_SECTION)
325
326 # Assign section: Stiffener
327 ps11 = (-b_f/2, 0, 0)
328 ps21 = (b_f/2, 0, 0)
329 ps31= (b_f/2, h_w_global, 0)
330 ps41 = (-b_f/2, h_w_global, 0)
331
332 global_part_stiffener.SectionAssignment(offset=0.0, offsetField='',
333 offsetType=MIDDLE_SURFACE, region=Region(
334 faces=global_part_stiffener.faces.findAt(((ps11),), ((ps21),),
335 ((ps31),), ((ps41),))),
336 sectionName='stiffener', thicknessAssignment=FROM_SECTION)
337
338 # Assign section: Edge fold
339 pe11 = (0, 0, 0)
340 pe21 = (b_edge, 0, 0)
341 pe31 = (b_edge, 0, h_w_global)
342 pe41 = (0, 0, h_w_global)
343
344 global_part_edge.SectionAssignment(offset=0.0, offsetField='',
345 offsetType=MIDDLE_SURFACE, region=Region(
346 faces=global_part_edge.faces.findAt(((pe11),), ((pe21),), ((pe31),), ((pe41),))),
347 sectionName='web', thicknessAssignment=FROM_SECTION)
348
349 # Assign section: Flange part above edge fold
350 pfe11 = (0, -b_f/2, 0)
351 pfe21 = (b_edge, -b_f/2, 0)
352 pfe31= (b_edge, b_f/2, 0)
353 pfe41 = (0, b_f/2, 0)
354
355 global_part_flange_edge.SectionAssignment(offset=0.0, offsetField='',
356 offsetType=MIDDLE_SURFACE, region=Region(
357 faces=global_part_flange_edge.faces.findAt(((pfe11),), ((pfe21),),
358 ((pfe31),), ((pfe41),))),
359 sectionName='flange', thicknessAssignment=FROM_SECTION)
360
361 # Creating the Assembly
362 global_model.rootAssembly.DatumCsysByDefault(CARTESIAN)
363 global_model.rootAssembly.Instance(dependent=ON, name='web',
364 part=global_part_web)
365 global_model.rootAssembly.Instance(dependent=ON, name='flange',
366 part=global_part_flange)
367 global_model.rootAssembly.Instance(dependent=ON, name='stiffener',
368 part=global_part_stiffener)
369 global_model.rootAssembly.Instance(dependent=ON, name='edge',
370 part=global_part_edge)
371 global_model.rootAssembly.Instance(dependent=ON, name='flange_edge',
372 part=global_part_flange_edge)
373
```

```
374 # Web parts array
375 global_model.rootAssembly.translate(instanceList=('web', ),
376 vector=(b_edge, 0.0, 0.0))
377
378 global_model.rootAssembly.LinearInstancePattern(direction1=(1.0,
379 0.0, 0.0), direction2=(0.0, 1.0, 0.0), instanceList=('web', ), number1=
      num_wavelengths,
380 number2=1, spacing1=l_wavelength, spacing2=1.0)
381
382 # Edge folds array
383 global_model.rootAssembly.LinearInstancePattern(direction1=(1.0,
384 0.0, 0.0), direction2=(0.0, 1.0, 0.0), instanceList=('edge', ), number1=2,
385 number2=1, spacing1=L_beam-b_edge, spacing2=1.0)
386
387 # Flange parts array
388 global_model.rootAssembly.translate(instanceList=('flange', ),
389 vector=(b_edge, 0.0, 0.0))
390 global_model.rootAssembly.LinearInstancePattern(direction1=(0.0,
391 0.0, 1.0), direction2=(1.0, 0.0, 0.0), instanceList=('flange', ), number1=2,
392 number2=num_wavelengths, spacing1=h_w_global, spacing2=l_wavelength)
393
394 # Stiffener parts array
395 global_model.rootAssembly.rotate(angle=90.0, axisDirection=(0.0,
396 1.0, 0.0), axisPoint=(0.0, 0.0, 0.0), instanceList=('stiffener', ))
397 global_model.rootAssembly.rotate(angle=90.0, axisDirection=(1.0,
398 0.0, 0.0), axisPoint=(0.0, 0.0, 0.0), instanceList=('stiffener', ))
399 global_model.rootAssembly.LinearInstancePattern(direction1=(1.0,
400 0.0, 0.0), direction2=(0.0, 1.0, 0.0), instanceList=('stiffener', ), number1=2,
401 number2=1, spacing1=L_beam, spacing2=1.0)
402
403 # Flange edge parts array
404 global_model.rootAssembly.LinearInstancePattern(direction1=(0.0,
405 0.0, 1.0), direction2=(1.0, 0.0, 0.0), instanceList=('flange_edge', ), number1=2,
406 number2=2, spacing1=h_w_global, spacing2=L_beam-b_edge)
407
408 # Merge instances into a CWG
409 all_instances = global_model.rootAssembly.instances
410
411 global_model.rootAssembly.InstanceFromBooleanMerge(domain=GEOMETRY,
412 instances=all_instances.values(),
413 keepIntersections=ON, name='global_model_cwg', originalInstances=DELETE)
414
415 # Create the initial load step
416 global_model.StaticStep(name='load_step', previous='Initial')
417
418 # Create pratition of the corrugated web's vertical shell edges
419 # The middle point becomes the master node
420 global_model.parts['global_model_cwg'].PartitionEdgeByParam(edges=global_model.
      parts['global_model_cwg'].edges.findAt(((L_beam, 0.0, h_w_global/2), )),
      parameter=0.5)
421 global_model.parts['global_model_cwg'].PartitionEdgeByParam(edges=global_model.
      parts['global_model_cwg'].edges.findAt(((0.0, 0.0, h_w_global/2), )), parameter
      =0.5)
422
423 # Create ties
424
425 # Ties at one end of the beam
426 global_model.rootAssembly.Set(name='m_Set-1', vertices=global_model.rootAssembly.
      instances['global_model_cwg-1'].vertices.findAt(((L_beam, 0.0, h_w_global/2),))
      )
427 global_model.rootAssembly.Set(edges=global_model.rootAssembly.instances['
      global_model_cwg-1'].edges.findAt(((L_beam, b_f/8, 0.0), ), ((L_beam, b_f/8,
      h_w_global), ), ((L_beam, 0.0, h_w_global/8),), ((L_beam, 0.0, 5*h_w_global/8),
       ), ((L_beam, -b_f/8, h_w_global), ), ((L_beam, -b_f/8,0.0), ), ), name='s_Set
      -1')
428 global_model.Coupling(controlPoint= global_model.rootAssembly.sets['m_Set-1'],
      couplingType=KINEMATIC, influenceRadius=WHOLE_SURFACE, localCsys=None, name='
      Constraint-1', surface=global_model.rootAssembly.sets['s_Set-1'], u1=ON, u2=ON,
       u3= ON, ur1=ON, ur2=ON, ur3=ON)
429
```

```
# Ties at the other end of the beam
global_model.rootAssembly.Set(name='m_Set-2', vertices=global_model.rootAssembly.instances['global_model_cwg-1'].vertices.findAt(((0.0, 0.0, h_w_global/2), )))
global_model.rootAssembly.Set(edges=global_model.rootAssembly.instances['global_model_cwg-1'].edges.findAt(((0.0, b_f/8, 0.0), ), ((0.0, b_f/8, h_w_global), ), ((0.0, 0.0, h_w_global/8),), ((0.0, 0.0, 5*h_w_global/8), ), ((0.0, -b_f/8, h_w_global), ), ((0.0, -b_f/8,0.0), ), ), name='s_Set-2')
global_model.Coupling(controlPoint=global_model.rootAssembly.sets['m_Set-2'], couplingType=KINEMATIC, influenceRadius=WHOLE_SURFACE, localCsys=None, name='Constraint-2', surface=global_model.rootAssembly.sets['s_Set-2'], u1=ON, u2=ON, u3=ON, ur1=ON, ur2=ON, ur3=ON)

# Create boundary conditions

# Boundary condition at one end of the beam
global_model.DisplacementBC(amplitude=UNSET, createStepName='Initial', distributionType=UNIFORM, fieldName='', localCsys=None, name='BC-1', region=Region(vertices=global_model.rootAssembly.instances['global_model_cwg-1'].vertices.findAt(((L_beam, 0.0, h_w_global/2), ), )), u1=UNSET, u2=SET, u3=SET, ur1=SET, ur2=UNSET, ur3=SET)

# Boundary condition at the other end of the beam
global_model.DisplacementBC(amplitude=UNSET, createStepName='Initial', distributionType=UNIFORM, fieldName='', localCsys=None, name='BC-2', region=Region(vertices=global_model.rootAssembly.instances['global_model_cwg-1'].vertices.findAt(((0.0, 0.0, h_w_global/2), ), )), u1=SET, u2=SET, u3=SET, ur1=SET, ur2=UNSET,ur3=SET)

# Create loading condition

# Moment at one end of the beam
global_model.Moment(cm2=-moment, createStepName='load_step', distributionType=UNIFORM, field='', localCsys=None, name='Load-1', region=Region(vertices=global_model.rootAssembly.instances['global_model_cwg-1'].vertices.findAt(((L_beam, 0.0, h_w_global/2), ), )))

# Moment at the other end of the beam
global_model.Moment(cm2=moment, createStepName='load_step', distributionType=UNIFORM, field='', localCsys=None, name='Load-2', region=Region(vertices=global_model.rootAssembly.instances['global_model_cwg-1'].vertices.findAt(((0, 0.0, h_w_global/2), ), )))

# Generate the Mesh
global_model.parts['global_model_cwg'].seedPart(deviationFactor=0.1,minSizeFactor=0.1, size=global_element_size)
global_model.parts['global_model_cwg'].setMeshControls(elemShape=QUAD,regions=global_model.parts['global_model_cwg'].faces, technique=STRUCTURED)
global_model.parts['global_model_cwg'].setElementType(elemTypes=(ElemType(elemCode=S8R, elemLibrary=STANDARD), ElemType(elemCode=STRI65,elemLibrary=STANDARD)), regions=(global_model.parts['global_model_cwg'].faces,))
global_model.parts['global_model_cwg'].generateMesh()


# Create global job - linear
linear_analysis = mdb.Job(atTime=None, contactPrint=OFF, description='', echoPrint= OFF,explicitPrecision=SINGLE, getMemoryFromAnalysis=True, historyPrint=OFF,memory=90, memoryUnits=PERCENTAGE, model=Model_Name_Global, modelPrint=OFF,multiprocessingMode=DEFAULT, name='linear_analysis', nodalOutputPrecision=SINGLE, numCpus=1, numGPUs=0, queue=None, resultsFormat=ODB, scratch='',type=ANALYSIS, userSubroutine='', waitHours=0, waitMinutes=0)

# Submit global job
if debug == 0:
  linear_analysis.submit(consistencyChecking=OFF)



#--------------------------LINEAR BUCKLING ANALYSIS---------------------------
Model_Name_Buckling = 'Buckling model-' + str(ID)  # Name of buckling model
Job_Name_Buckling = 'Buckling-Job-' + str(ID)  # Name of buckling job
```

```
470
471 # Copy linear model and change the name
472 mdb.Model(name=Model_Name_Buckling, objectToCopy=mdb.models[Model_Name_Global])
473 mdb.models[Model_Name_Buckling].rootAssembly.regenerate()
474
475 # Create linear buckling load step
476 mdb.models[Model_Name_Buckling].BuckleStep(blockSize=DEFAULT, description='Buckle
      ', eigensolver=LANCZOS, maintainAttributes=True, maxBlocks=DEFAULT, minEigen=0,
       name='load_step', numEigen=Modes, previous='Initial')
477
478
479 # Adding keywords to save the eigenmode
480 mdb.models[Model_Name_Buckling].keywordBlock.synchVersions(storeNodesAndElements=
      False)
481 keyword = '\n*node file, global=yes, last mode=' + str(1) + '\nU,'
482
483 blocks = []
484 for block in mdb.models[Model_Name_Buckling].keywordBlock.sieBlocks:
485   blocks.append(block)
486
487 mdb.models[Model_Name_Buckling].keywordBlock.insert(len(blocks)-2, keyword)
488
489 # Creating job for linear buckling analysis
490 mdb.Job(atTime=None, contactPrint=OFF, description='', echoPrint=OFF,
      explicitPrecision=SINGLE, getMemoryFromAnalysis=True, historyPrint=OFF, memory
      =90, memoryUnits=PERCENTAGE, model=Model_Name_Buckling, modelPrint=OFF,
      multiprocessingMode=DEFAULT, name=Job_Name_Buckling, nodalOutputPrecision=
      SINGLE, numCpus=1, numGPUs=0, queue=None, resultsFormat=ODB, scratch='', type=
      ANALYSIS, userSubroutine='', waitHours=0, waitMinutes=0)
491
492 # Job Submittal
493 mdb.jobs[Job_Name_Buckling].submit(consistencyChecking=OFF)
494 mdb.jobs[Job_Name_Buckling].waitForCompletion()
495
496
497 #----------------------------NONLINEAR ANALYSIS----------------------------
498 print ('processing ID' + str(ID))
499
500 Model_Name = 'Non-linear Model-' + str(ID)  # Name of nonlinear model
501 Job_Name = 'Non-linear-Job-' + str(ID)  # Name of nonlinear job
502
503 # Copy buckling model and change the name
504 mdb.Model(name=Model_Name, objectToCopy=mdb.models[Model_Name_Buckling])
505
506 # Create nonlinear load step
507 mdb.models[Model_Name].StaticRiksStep(maintainAttributes=True, name='load_step',
      nlgeom=ON, previous='Initial')
508 mdb.models[Model_Name].steps.changeKey(fromName='load_step', toName='nonlinear')
509 mdb.models[Model_Name].keywordBlock.synchVersions(storeNodesAndElements=False)
510 mdb.models[Model_Name].keywordBlock.setValues(edited=0)
511 mdb.models[Model_Name].keywordBlock.synchVersions(storeNodesAndElements=False)
512
513 # Increments - arc lengths
514 mdb.models[Model_Name].steps['nonlinear'].setValues(initialArcInc=0.4, maxArcInc
      =2, maxNumInc=Increments, minArcInc=1e-15)
515
516 # Defining Initial geometric imperfection
517
518 # Adding Keyword
519 text_to_find = '*Step, name=nonlinear, nlgeom=YES'     #Copy the full line of the
      text to find, only one line
520 blocks = []
521 for block in mdb.models[Model_Name].keywordBlock.sieBlocks:
522   blocks.append(block)
523 position = blocks.index(text_to_find) -1
524 mdb.models[Model_Name].keywordBlock.synchVersions()  # IMPORTANT STRINGS TO MAKE
      IT WORK
525 mdb.models[Model_Name].keywordBlock.setValues(edited = 0)  # IMPORTANT STRINGS TO
      MAKE IT WORK
526 mdb.models[Model_Name].keywordBlock.synchVersions()  # IMPORTANT STRINGS TO MAKE
```

```
    IT WORK
527
528 imperfection = '\n*imperfection, file=Buckling-Job-' + str(ID) + ', step=1\n' +
      str(1) + ',' +str(Initial_imperfection)  # ADD YOUR Keyword Here
529 mdb.models[Model_Name].keywordBlock.insert(position, imperfection)  # Inserting
      the keyword in the desired row
530
531 # Job Submittal
532 mdb.Job(atTime=None, contactPrint=OFF, description='', echoPrint=OFF,
      explicitPrecision=SINGLE, getMemoryFromAnalysis=True, historyPrint=OFF,memory
      =90, memoryUnits=PERCENTAGE, model=Model_Name, modelPrint=OFF,
      multiprocessingMode=DEFAULT, name=Job_Name,nodalOutputPrecision=SINGLE, numCpus
      =1, numGPUs=0, queue=None, resultsFormat=ODB, scratch='', type=ANALYSIS,
      userSubroutine='', waitHours=0, waitMinutes=0)
533
534 mdb.jobs[Job_Name].setValues(multiprocessingMode=THREADS, numCpus=6, # Increase
      Processing Power
535   numDomains=6, numGPUs=6)
536 mdb.jobs[Job_Name].submit(consistencyChecking=OFF)
537 mdb.jobs[Job_Name].waitForCompletion()
538
539
540
541 #-----------------------------EXPORT RESULTS-----------------------------
542 odbpath = cwd + '/odbs/' + Job_Name + '.odb'
543 odb = openOdb(path=odbpath)
544
545 # Load Factor
546 print('Exporting Results to Excel')
547 LoadFactor = session.XYDataFromHistory(name='LoadFactor',odb=odb,
      outputVariableName='Load proportionality factor: LPF for Whole Model',steps=('
      nonlinear',))
548
549 LPFs = []  #List with LPF's
550 for i in LoadFactor:
551   LPFs.append(i[1])
552
553 # Displacement For The Midspan - U3 (vertical dir)
554 Mid_Span_Displacements = []
555 midspan = mdb.models[Model_Name_Global].rootAssembly.instances['global_model_cwg
      -1'].vertices.findAt(((L_beam/2,0,0),))[0].index
556
557 for x in range(0,Increments-1):
558   U_Values= odb.steps['nonlinear'].frames[x].fieldOutputs['U'].values
559   for v in U_Values:
560     if v.nodeLabel == midspan:
561       Mid_Span_Displacements.append([x,v.data[2]])
562
563 # Merging and Exporting
564 Merge = zip (Mid_Span_Displacements,LPFs)
565 File_Name = 'Results-ID-' + str(ID) +'.csv' # Name of current ID .csv
566 CSV_file = open(File_Name,'w')
567 # Writing columns with "Increment - Mid-span disp - Disp - M":
568 CSV_file.write('Results of ID %s \n \n Increment; Mid-Span Displacement (mm);LPF;
      M (kNm) \n' %(ID,))
569
570 moments = []  # Empty list for storage of moments
571
572 # Loop of each row of Merge-file
573 for y in Merge:
574   Increment = y[0][0]
575   U3 = y[0][1]
576   LPF = y[1]
577
578   M = LPF*moment/1e6  # Convert to kNm
579   moments.append(M)
580
581   # Writing data for current increment row
582   CSV_file.write('%.0f;%.4f;%.4f;%.3f \n'%(Increment, U3, LPF, M))
583
```

```
584 Max_moment = max(moments)  # maximum moment
585 Max_moment = round(Max_moment,2)  # Rounding the maximum moment to 2 decimal
586
587 # Writing what the max moment is in the last row
588 CSV_file.write('\n Max moment is: %s (kNm) \n' %(Max_moment,))
589 CSV_file.close()
```

B

Appendix: Data of girders

B.1 Data of girders undergoing normal stress flange buckling as 1st eigenmode

Table B.1: Geometric parameters and results from the numerical analyses for girders ID-1 to ID-127.

ID	a_1 [mm]	a_3 [mm]	α [deg]	b_f [mm]	t_f [mm]	t_f/t_w	R	$M_{cr.num}$ [kNm]	$\kappa_{\sigma.num}$	$M_{ult.num}$ [kNm]	ρ_{num}
1	200	100	30	400	25	6,25	0,171	5676	0,598	2130	0,898
4	300	150	30	600	25	6,25	0,171	4211	0,666	2518	0,707
7	600	300	30	600	25	6,25	0,342	1927	0,439	1453	0,408
10	400	200	30	800	25	6,25	0,171	3426	0,722	2464	0,519
13	300	150	30	1000	25	6,25	0,102	4464	0,995	3659	0,617
16	600	300	30	1000	25	6,25	0,205	2440	0,695	1928	0,325
19	600	200	30	400	25	6,25	0,366	2545	0,386	1680	0,708
22	600	200	30	600	25	6,25	0,244	3069	0,552	2182	0,613
25	300	100	30	800	25	6,25	0,092	5199	0,888	3487	0,735
28	750	250	30	800	25	6,25	0,229	2456	0,571	1869	0,394
31	600	200	30	1000	25	6,25	0,146	3485	0,846	2704	0,456
34	400	100	30	400	25	6,25	0,192	4799	0,506	2181	0,919
37	400	100	30	600	25	6,25	0,128	5266	0,725	2951	0,829
40	1000	250	30	600	25	6,25	0,320	2241	0,455	1669	0,469
43	600	150	30	800	25	6,25	0,144	4136	0,787	2984	0,629
46	1200	300	30	800	25	6,25	0,288	2074	0,529	1624	0,342
49	1000	250	30	1000	25	6,25	0,192	2673	0,704	2122	0,358
52	300	150	30	400	25	4,17	0,256	3835	0,489	1953	0,823
55	400	200	30	600	25	4,17	0,228	3376	0,607	2263	0,636
58	200	100	30	800	25	4,17	0,085	6001	1,024	3618	0,762
61	500	250	30	800	25	4,17	0,213	3081	0,716	2324	0,490
64	400	200	30	1000	25	4,17	0,137	3997	0,970	2994	0,505
67	300	100	30	400	25	4,17	0,183	5592	0,589	2227	0,939
70	300	100	30	600	25	4,17	0,122	6172	0,850	3047	0,856
73	750	250	30	600	25	4,17	0,305	2490	0,506	1823	0,512
76	450	150	30	800	25	4,17	0,137	4659	0,886	3168	0,668
79	900	300	30	800	25	4,17	0,275	2337	0,596	1830	0,386
82	750	250	30	1000	25	4,17	0,183	2928	0,771	2328	0,392
85	600	150	30	400	25	4,17	0,288	4121	0,525	2152	0,907
88	600	150	30	600	25	4,17	0,192	4557	0,720	2860	0,803
91	1200	300	30	600	25	4,17	0,384	2173	0,494	1665	0,468
94	800	200	30	800	25	4,17	0,192	3398	0,716	2556	0,538
97	600	150	30	1000	25	4,17	0,115	4157	0,927	3594	0,606
100	1200	300	30	1000	25	4,17	0,230	2558	0,729	2124	0,358
103	200	100	30	600	25	2,50	0,114	7554	1,040	3194	0,897
106	500	250	30	600	25	2,50	0,285	3665	0,744	2452	0,689
109	300	150	30	800	25	2,50	0,128	5676	1,080	3488	0,735
112	600	300	30	800	25	2,50	0,256	3272	0,834	2472	0,521
115	500	250	30	1000	25	2,50	0,171	3925	1,034	3033	0,511
118	450	150	30	400	25	2,50	0,275	5282	0,673	2299	0,969
121	450	150	30	600	25	2,50	0,183	5580	0,882	3053	0,858
124	900	300	30	600	25	2,50	0,366	2952	0,672	2105	0,591
127	600	200	30	800	25	2,50	0,183	4612	0,972	3284	0,692

Table B.2: Geometric parameters and results from the numerical analyses for girders ID-130 to ID-280.

ID	a_1 [mm]	a_3 [mm]	α [deg]	b_f [mm]	t_f [mm]	t_f/t_w	R	$M_{cr.num}$ [kNm]	$\kappa_{\sigma.num}$	$M_{ult.num}$ [kNm]	ρ_{num}
130	450	150	30	1000	25	2,50	0,110	4802	1,071	3818	0,644
133	900	300	30	1000	25	2,50	0,220	3192	0,909	2575	0,434
136	800	200	30	400	25	2,50	0,384	3906	0,593	2158	0,909
139	800	200	30	600	25	2,50	0,256	4240	0,762	2772	0,779
142	400	100	30	800	25	2,50	0,096	5690	0,971	3648	0,769
145	1000	250	30	800	25	2,50	0,240	3690	0,857	2864	0,603
148	800	200	30	1000	25	2,50	0,154	3919	0,952	3334	0,562
151	200	100	45	400	25	6,25	0,188	8297	0,874	2240	0,944
154	300	150	45	600	25	6,25	0,188	6373	1,007	2847	0,800
157	600	300	45	600	25	6,25	0,375	3026	0,689	1998	0,561
160	400	200	45	800	25	6,25	0,188	5260	1,108	3079	0,649
163	300	150	45	1000	25	6,25	0,113	5644	1,258	3986	0,672
166	600	300	45	1000	25	6,25	0,225	3798	1,082	2713	0,457
169	600	200	45	400	25	6,25	0,400	3710	0,563	1951	0,822
172	600	200	45	600	25	6,25	0,267	4418	0,795	2617	0,735
175	300	100	45	800	25	6,25	0,100	6166	1,052	3665	0,772
178	750	250	45	800	25	6,25	0,250	3657	0,850	2541	0,535
181	600	200	45	1000	25	6,25	0,160	4725	1,147	3459	0,583
187	400	100	45	600	25	6,25	0,139	6636	0,914	3134	0,880
190	1000	250	45	600	25	6,25	0,347	3223	0,654	2237	0,629
193	600	150	45	800	25	6,25	0,156	5235	0,996	3339	0,704
196	1200	300	45	800	25	6,25	0,313	2917	0,744	2255	0,475
199	1000	250	45	1000	25	6,25	0,208	3611	0,951	2975	0,502
202	300	150	45	400	25	4,17	0,281	5787	0,738	2116	0,892
205	400	200	45	600	25	4,17	0,250	5134	0,923	2664	0,748
208	200	100	45	800	25	4,17	0,094	7324	1,250	3802	0,801
211	500	250	45	800	25	4,17	0,234	4648	1,080	2944	0,620
214	400	200	45	1000	25	4,17	0,150	5472	1,328	3746	0,632
217	300	100	45	400	25	4,17	0,200	7607	0,802	2309	0,973
220	300	100	45	600	25	4,17	0,133	7600	1,046	3181	0,894
223	750	250	45	600	25	4,17	0,333	3561	0,723	2325	0,653
226	450	150	45	800	25	4,17	0,150	6000	1,141	3495	0,736
229	900	300	45	800	25	4,17	0,300	3293	0,840	2436	0,513
232	750	250	45	1000	25	4,17	0,200	4129	1,088	3046	0,513
235	600	150	45	400	25	4,17	0,313	5465	0,697	2265	0,955
238	600	150	45	600	25	4,17	0,208	5888	0,931	3022	0,849
241	1200	300	45	600	25	4,17	0,417	2878	0,655	2120	0,595
244	800	200	45	800	25	4,17	0,208	4493	0,947	3061	0,645
247	600	150	45	1000	25	4,17	0,125	4979	1,110	3847	0,648
250	1200	300	45	1000	25	4,17	0,250	3288	0,937	2900	0,489
253	200	100	45	600	25	2,50	0,125	9161	1,261	3256	0,915
256	500	250	45	600	25	2,50	0,313	4894	0,994	2711	0,762
259	300	150	45	800	25	2,50	0,141	7119	1,354	3676	0,775
262	600	300	45	800	25	2,50	0,281	4367	1,114	2919	0,615
265	500	250	45	1000	25	2,50	0,188	5373	1,415	3598	0,607
268	450	150	45	400	25	2,50	0,300	6560	0,836	2317	0,976
271	450	150	45	600	25	2,50	0,200	7060	1,116	3143	0,883
274	900	300	45	600	25	2,50	0,400	3479	0,792	2380	0,669
277	600	200	45	800	25	2,50	0,200	5650	1,191	3467	0,731
280	450	150	45	1000	25	2,50	0,120	5709	1,273	4041	0,681

Table B.3: Geometric parameters and results from the numerical analyses for girders ID-283 to ID-436.

ID	a_1 [mm]	a_3 [mm]	α [deg]	b_f [mm]	t_f [mm]	t_f/t_w	R	$M_{cr.num}$ [kNm]	$\kappa_{\sigma.num}$	$M_{ult.num}$ [kNm]	ρ_{num}
283	900	300	45	1000	25	2,50	0,240	3948	1,125	3184	0,537
286	800	200	45	400	25	2,50	0,417	4524	0,686	2217	0,934
289	800	200	45	600	25	2,50	0,278	5004	0,900	2995	0,841
292	400	100	45	800	25	2,50	0,104	6502	1,110	3776	0,796
295	1000	250	45	800	25	2,50	0,260	4185	0,972	3316	0,699
298	800	200	45	1000	25	2,50	0,167	4448	1,080	3954	0,666
301	200	100	60	400	25	6,25	0,204	10663	1,124	2381	1,003
304	300	150	60	600	25	6,25	0,204	8470	1,339	3158	0,887
307	600	300	60	600	25	6,25	0,408	4253	0,968	2364	0,664
310	400	200	60	800	25	6,25	0,204	7045	1,485	3580	0,754
313	300	150	60	1000	25	6,25	0,123	6630	1,478	4229	0,713
316	600	300	60	1000	25	6,25	0,245	5202	1,482	3277	0,552
322	600	200	60	600	25	6,25	0,287	5727	1,030	2843	0,799
325	300	100	60	800	25	6,25	0,108	6947	1,186	3794	0,799
328	750	250	60	800	25	6,25	0,269	4783	1,111	2984	0,629
331	600	200	60	1000	25	6,25	0,172	5594	1,358	3988	0,672
337	400	100	60	600	25	6,25	0,148	7454	1,026	3161	0,888
340	1000	250	60	600	25	6,25	0,370	3960	0,804	2525	0,709
343	600	150	60	800	25	6,25	0,166	5879	1,118	3544	0,747
346	1200	300	60	800	25	6,25	0,333	3528	0,900	2659	0,560
349	1000	250	60	1000	25	6,25	0,222	3923	1,033	3687	0,622
352	300	150	60	400	25	4,17	0,306	7967	1,016	2233	0,941
355	400	200	60	600	25	4,17	0,272	7095	1,276	2894	0,813
358	200	100	60	800	25	4,17	0,102	8443	1,441	3939	0,830
361	500	250	60	800	25	4,17	0,255	6332	1,471	3309	0,697
364	400	200	60	1000	25	4,17	0,163	6569	1,595	4047	0,682
367	300	100	60	400	25	4,17	0,215	9548	1,006	2376	1,001
370	300	100	60	600	25	4,17	0,144	8578	1,181	3246	0,912
373	750	250	60	600	25	4,17	0,359	4599	0,934	2606	0,732
376	450	150	60	800	25	4,17	0,161	6969	1,325	3659	0,771
379	900	300	60	800	25	4,17	0,323	4153	1,059	2802	0,590
382	750	250	60	1000	25	4,17	0,215	4880	1,286	3826	0,645
385	600	150	60	400	25	4,17	0,333	6467	0,824	2298	0,968
388	600	150	60	600	25	4,17	0,222	6508	1,029	3097	0,870
391	1200	300	60	600	25	4,17	0,444	3382	0,770	2401	0,674
394	800	200	60	800	25	4,17	0,222	4916	1,036	3406	0,718
397	600	150	60	1000	25	4,17	0,133	5527	1,232	4140	0,698
400	1200	300	60	1000	25	4,17	0,266	3519	1,003	3525	0,594
403	200	100	60	600	25	2,50	0,136	10579	1,457	3360	0,944
406	500	250	60	600	25	2,50	0,340	6416	1,303	2862	0,804
409	300	150	60	800	25	2,50	0,153	8301	1,579	3860	0,813
412	600	300	60	800	25	2,50	0,306	5684	1,449	3172	0,668
415	500	250	60	1000	25	2,50	0,204	6713	1,768	4315	0,727
418	450	150	60	400	25	2,50	0,323	7991	1,019	2346	0,989
421	450	150	60	600	25	2,50	0,215	8164	1,290	3153	0,886
424	900	300	60	600	25	2,50	0,431	4065	0,925	2536	0,712
427	600	200	60	800	25	2,50	0,215	6266	1,321	3610	0,761
430	450	150	60	1000	25	2,50	0,129	6441	1,436	4214	0,710
433	900	300	60	1000	25	2,50	0,258	4377	1,247	3670	0,619
436	800	200	60	400	25	2,50	0,444	5142	0,780	2256	0,951

Table B.4: Geometric parameters and results from the numerical analyses for girders ID-439 to ID-589.

ID	a_1 [mm]	a_3 [mm]	α [deg]	b_f [mm]	t_f [mm]	t_f/t_w	R	$M_{cr.num}$ [kNm]	$\kappa_{\sigma.num}$	$M_{ult.num}$ [kNm]	ρ_{num}
439	800	200	60	600	25	2,50	0,296	5490	0,987	2998	0,842
442	400	100	60	800	25	2,50	0,111	7179	1,226	3884	0,818
445	1000	250	60	800	25	2,50	0,277	4397	1,022	3303	0,696
448	800	200	60	1000	25	2,50	0,178	4778	1,160	4006	0,675
451	200	100	30	400	35	8,75	0,171	13938	0,525	3294	0,973
454	300	150	30	600	35	8,75	0,171	10249	0,579	4354	0,857
457	600	300	30	600	35	8,75	0,342	4195	0,341	2848	0,561
460	400	200	30	800	35	8,75	0,171	8271	0,623	4839	0,715
463	300	150	30	1000	35	8,75	0,102	11547	0,921	6612	0,781
466	600	300	30	1000	35	8,75	0,205	5655	0,576	4007	0,473
469	600	200	30	400	35	8,75	0,366	5245	0,285	2779	0,821
472	600	200	30	600	35	8,75	0,244	6595	0,424	3877	0,763
475	300	100	30	800	35	8,75	0,092	13244	0,809	6039	0,892
478	750	250	30	800	35	8,75	0,229	5652	0,470	3805	0,562
481	600	200	30	1000	35	8,75	0,146	8044	0,698	5360	0,633
487	400	100	30	600	35	8,75	0,128	11836	0,583	4709	0,927
490	1000	250	30	600	35	8,75	0,320	4857	0,353	3203	0,631
493	600	150	30	800	35	8,75	0,144	9198	0,626	5362	0,792
496	1200	300	30	800	35	8,75	0,288	4578	0,418	3196	0,472
499	1000	250	30	1000	35	8,75	0,192	6100	0,575	4238	0,501
502	300	150	30	400	35	5,83	0,256	8555	0,390	3100	0,916
505	400	200	30	600	35	5,83	0,228	7601	0,489	4020	0,792
508	200	100	30	800	35	5,83	0,085	15421	0,941	6099	0,901
511	500	250	30	800	35	5,83	0,213	6876	0,571	4455	0,658
514	400	200	30	1000	35	5,83	0,137	9708	0,843	5868	0,693
517	300	100	30	400	35	5,83	0,183	12256	0,462	3357	0,992
520	300	100	30	600	35	5,83	0,122	14504	0,714	4835	0,952
523	750	250	30	600	35	5,83	0,305	5380	0,391	3450	0,679
526	450	150	30	800	35	5,83	0,137	10704	0,728	5607	0,828
529	900	300	30	800	35	5,83	0,275	5098	0,465	3642	0,538
532	750	250	30	1000	35	5,83	0,183	6734	0,634	4788	0,566
535	600	150	30	400	35	5,83	0,288	8200	0,374	3250	0,960
538	600	150	30	600	35	5,83	0,192	9559	0,540	4594	0,905
541	1200	300	30	600	35	5,83	0,384	4388	0,357	3046	0,600
544	800	200	30	800	35	5,83	0,192	7614	0,574	4903	0,724
547	600	150	30	1000	35	5,83	0,115	10191	0,813	6523	0,771
550	1200	300	30	1000	35	5,83	0,230	5614	0,572	4209	0,497
553	200	100	30	600	35	3,50	0,114	18458	0,909	5013	0,987
556	500	250	30	600	35	3,50	0,285	7213	0,524	4041	0,796
559	300	150	30	800	35	3,50	0,128	13688	0,931	5879	0,868
562	600	300	30	800	35	3,50	0,256	6643	0,606	4404	0,650
565	500	250	30	1000	35	3,50	0,171	8689	0,819	5607	0,663
568	450	150	30	400	35	3,50	0,275	10081	0,460	3383	0,999
571	450	150	30	600	35	3,50	0,183	11553	0,653	4760	0,937
574	900	300	30	600	35	3,50	0,366	5540	0,451	3565	0,702
577	600	200	30	800	35	3,50	0,183	9734	0,734	5541	0,818
580	450	150	30	1000	35	3,50	0,110	11731	0,935	6754	0,798
583	900	300	30	1000	35	3,50	0,220	6716	0,684	4808	0,568
586	800	200	30	400	35	3,50	0,384	7100	0,385	3157	0,933
589	800	200	30	600	35	3,50	0,256	8468	0,545	4416	0,870

Table B.5: Geometric parameters and results from the numerical analyses for girders ID-592 to ID-751.

ID	a_1 [mm]	a_3 [mm]	α [deg]	b_f [mm]	t_f [mm]	t_f/t_w	R	$M_{cr.num}$ [kNm]	$\kappa_{\sigma.num}$	$M_{ult.num}$ [kNm]	ρ_{num}
592	400	100	30	800	35	3,50	0,096	13908	0,849	6192	0,915
595	1000	250	30	800	35	3,50	0,240	7658	0,636	5007	0,740
598	800	200	30	1000	35	3,50	0,154	9322	0,809	6101	0,721
601	200	100	45	400	35	8,75	0,188	19558	0,737	3419	1,010
604	300	150	45	600	35	8,75	0,188	15054	0,851	4601	0,906
607	600	300	45	600	35	8,75	0,375	6767	0,551	3621	0,713
610	400	200	45	800	35	8,75	0,188	12467	0,940	5430	0,802
613	300	150	45	1000	35	8,75	0,113	14104	1,125	6923	0,818
616	600	300	45	1000	35	8,75	0,225	8869	0,904	5198	0,614
625	300	100	45	800	35	8,75	0,100	15170	0,926	6140	0,907
628	750	250	45	800	35	8,75	0,250	8415	0,699	4733	0,699
631	600	200	45	1000	35	8,75	0,160	11218	0,974	6177	0,730
640	1000	250	45	600	35	8,75	0,347	7249	0,526	3937	0,775
643	600	150	45	800	35	8,75	0,156	12072	0,821	5729	0,846
646	1200	300	45	800	35	8,75	0,313	6783	0,619	4300	0,635
649	1000	250	45	1000	35	8,75	0,208	8641	0,814	5346	0,632
652	300	150	45	400	35	5,83	0,281	12839	0,585	3273	0,967
655	400	200	45	600	35	5,83	0,250	11654	0,750	4402	0,867
658	200	100	45	800	35	5,83	0,094	18406	1,124	6220	0,919
661	500	250	45	800	35	5,83	0,234	10648	0,885	5212	0,770
664	400	200	45	1000	35	5,83	0,150	13583	1,179	6761	0,799
667	300	100	45	400	35	5,83	0,200	16359	0,616	3467	1,024
670	300	100	45	600	35	5,83	0,133	18157	0,894	5009	0,986
673	750	250	45	600	35	5,83	0,333	8097	0,588	4101	0,807
676	450	150	45	800	35	5,83	0,150	14469	0,984	6084	0,899
679	900	300	45	800	35	5,83	0,300	7640	0,697	4656	0,688
682	750	250	45	1000	35	5,83	0,200	9772	0,921	5839	0,690
685	600	150	45	400	35	5,83	0,313	11348	0,517	3403	1,005
688	600	150	45	600	35	5,83	0,208	12845	0,726	4834	0,952
691	1200	300	45	600	35	5,83	0,417	6469	0,527	3862	0,760
694	800	200	45	800	35	5,83	0,208	10601	0,799	5552	0,820
697	600	150	45	1000	35	5,83	0,125	12278	0,979	6760	0,799
700	1200	300	45	1000	35	5,83	0,250	7942	0,809	5425	0,641
703	200	100	45	600	35	3,50	0,125	22090	1,088	5100	1,004
706	500	250	45	600	35	3,50	0,313	10658	0,774	4413	0,869
709	300	150	45	800	35	3,50	0,141	17514	1,191	6179	0,913
712	600	300	45	800	35	3,50	0,281	9825	0,896	5124	0,757
715	500	250	45	1000	35	3,50	0,188	12749	1,201	6411	0,758
718	450	150	45	400	35	3,50	0,300	13656	0,623	3488	1,030
721	450	150	45	600	35	3,50	0,200	15521	0,877	4914	0,968
724	900	300	45	600	35	3,50	0,400	7594	0,618	4091	0,806
727	600	200	45	800	35	3,50	0,200	13181	0,993	5888	0,870
730	450	150	45	1000	35	3,50	0,120	14124	1,126	6998	0,827
733	900	300	45	1000	35	3,50	0,240	9286	0,946	5783	0,683
736	800	200	45	400	35	3,50	0,417	9518	0,516	3317	0,980
739	800	200	45	600	35	3,50	0,278	11250	0,724	4717	0,929
742	400	100	45	800	35	3,50	0,104	15899	0,971	6269	0,926
745	1000	250	45	800	35	3,50	0,260	10069	0,837	5586	0,825
748	800	200	45	1000	35	3,50	0,167	11560	1,004	6446	0,762
751	200	100	60	400	35	8,75	0,204	23743	0,895	3638	1,075

Table B.6: Geometric parameters and results from the numerical analyses for girders ID-763 to ID-949.

ID	a_1 [mm]	a_3 [mm]	α [deg]	b_f [mm]	t_f [mm]	t_f/t_w	R	$M_{cr.num}$ [kNm]	$\kappa_{\sigma.num}$	$M_{ult.num}$ [kNm]	ρ_{num}
763	300	150	60	1000	35	8,75	0,123	16251	1,296	7143	0,844
766	600	300	60	1000	35	8,75	0,245	12229	1,246	5903	0,697
775	300	100	60	800	35	8,75	0,108	16691	1,019	6217	0,918
781	600	200	60	1000	35	8,75	0,172	13684	1,188	6663	0,787
796	1200	300	60	800	35	8,75	0,333	8581	0,783	4934	0,729
799	1000	250	60	1000	35	8,75	0,222	10483	0,988	6367	0,752
802	300	150	60	400	35	5,83	0,306	17329	0,790	3403	1,005
805	400	200	60	600	35	5,83	0,272	15990	1,028	4665	0,919
808	200	100	60	800	35	5,83	0,102	20985	1,281	6310	0,932
811	500	250	60	800	35	5,83	0,255	14666	1,219	5633	0,832
814	400	200	60	1000	35	5,83	0,163	16326	1,417	7029	0,830
817	300	100	60	400	35	5,83	0,215	20112	0,758	3568	1,054
820	300	100	60	600	35	5,83	0,144	20421	1,006	5091	1,003
823	750	250	60	600	35	5,83	0,359	10765	0,782	4449	0,876
826	450	150	60	800	35	5,83	0,161	16868	1,147	6162	0,910
829	900	300	60	800	35	5,83	0,323	10042	0,916	5202	0,768
832	750	250	60	1000	35	5,83	0,215	12540	1,181	6410	0,757
838	600	150	60	600	35	5,83	0,222	15598	0,882	4961	0,977
841	1200	300	60	600	35	5,83	0,444	8202	0,668	4300	0,847
844	800	200	60	800	35	5,83	0,222	12963	0,977	5811	0,858
847	600	150	60	1000	35	5,83	0,133	13691	1,092	6945	0,821
850	1200	300	60	1000	35	5,83	0,266	9482	0,966	5878	0,695
853	200	100	60	600	35	3,50	0,136	25183	1,240	5184	1,021
856	500	250	60	600	35	3,50	0,340	14679	1,066	4664	0,918
859	300	150	60	800	35	3,50	0,153	20533	1,397	6312	0,932
862	600	300	60	800	35	3,50	0,306	13468	1,228	5526	0,816
865	500	250	60	1000	35	3,50	0,204	16713	1,575	6970	0,823
868	450	150	60	400	35	3,50	0,323	17263	0,787	3582	1,058
871	450	150	60	600	35	3,50	0,215	19257	1,089	5029	0,990
874	900	300	60	600	35	3,50	0,431	9681	0,788	4404	0,867
877	600	200	60	800	35	3,50	0,215	16455	1,240	6215	0,918
880	450	150	60	1000	35	3,50	0,129	15906	1,268	7198	0,850
883	900	300	60	1000	35	3,50	0,258	11660	1,188	6271	0,741
886	800	200	60	400	35	3,50	0,444	11773	0,639	3423	1,011
889	800	200	60	600	35	3,50	0,296	13691	0,881	4879	0,961
892	400	100	60	800	35	3,50	0,111	17335	1,058	6339	0,936
895	1000	250	60	800	35	3,50	0,277	11648	0,968	5675	0,838
898	800	200	60	1000	35	3,50	0,178	12815	1,113	6853	0,810
901	200	100	30	400	50	12,50	0,171	36471	0,459	5167	1,039
904	300	150	30	600	50	12,50	0,171	27179	0,513	7082	0,950
907	600	300	30	600	50	12,50	0,342	10079	0,274	5514	0,739
910	400	200	30	800	50	12,50	0,171	21763	0,547	8599	0,865
913	300	150	30	1000	50	12,50	0,102	31531	0,839	11523	0,927
916	600	300	30	1000	50	12,50	0,205	14332	0,487	8430	0,678
925	300	100	30	800	50	12,50	0,092	35946	0,732	9827	0,988
928	750	250	30	800	50	12,50	0,229	13596	0,377	7337	0,738
931	600	200	30	1000	50	12,50	0,146	19976	0,579	10049	0,808
940	1000	250	30	600	50	12,50	0,320	11219	0,272	5940	0,796
946	1200	300	30	800	50	12,50	0,288	10842	0,330	6242	0,628
949	1000	250	30	1000	50	12,50	0,192	14537	0,457	8422	0,678

Table B.7: Geometric parameters and results from the numerical analyses for girders ID-952 to ID-1150.

ID	a_1 [mm]	a_3 [mm]	α [deg]	b_f [mm]	t_f [mm]	t_f/t_w	R	$M_{cr.num}$ [kNm]	$\kappa_{\sigma.num}$	$M_{ult.num}$ [kNm]	ρ_{num}
952	300	150	30	400	50	8,33	0,256	21245	0,323	4866	0,979
955	400	200	30	600	50	8,33	0,228	18919	0,406	6746	0,904
958	200	100	30	800	50	8,33	0,085	42220	0,860	9947	1,000
961	500	250	30	800	50	8,33	0,213	16992	0,471	8163	0,821
964	400	200	30	1000	50	8,33	0,137	25682	0,744	10703	0,861
967	300	100	30	400	50	8,33	0,183	29646	0,373	5154	1,037
970	300	100	30	600	50	8,33	0,122	37090	0,609	7565	1,014
973	750	250	30	600	50	8,33	0,305	12628	0,306	6238	0,836
976	450	150	30	800	50	8,33	0,137	26627	0,604	9290	0,934
979	900	300	30	800	50	8,33	0,275	12144	0,370	7248	0,729
982	750	250	30	1000	50	8,33	0,183	16557	0,520	9503	0,765
985	600	150	30	400	50	8,33	0,288	17359	0,264	4929	0,991
988	600	150	30	600	50	8,33	0,192	21229	0,400	7229	0,969
991	1200	300	30	600	50	8,33	0,384	9964	0,271	5680	0,762
994	800	200	30	800	50	8,33	0,192	17911	0,450	8675	0,872
997	600	150	30	1000	50	8,33	0,115	25287	0,673	11192	0,900
1000	1200	300	30	1000	50	8,33	0,230	13350	0,454	8574	0,690
1003	200	100	30	600	50	5,00	0,114	48629	0,799	8021	1,075
1006	500	250	30	600	50	5,00	0,285	16068	0,389	6642	0,891
1009	300	150	30	800	50	5,00	0,128	35245	0,800	9591	0,964
1012	600	300	30	800	50	5,00	0,256	15118	0,460	7929	0,797
1015	500	250	30	1000	50	5,00	0,171	21221	0,667	10227	0,823
1018	450	150	30	400	50	5,00	0,275	21330	0,325	5092	1,024
1021	450	150	30	600	50	5,00	0,183	26159	0,493	7386	0,990
1024	900	300	30	600	50	5,00	0,366	11890	0,323	6128	0,822
1027	600	200	30	800	50	5,00	0,183	22144	0,557	9130	0,918
1030	450	150	30	1000	50	5,00	0,110	30790	0,819	11672	0,939
1033	900	300	30	1000	50	5,00	0,220	15551	0,529	9312	0,749
1036	800	200	30	400	50	5,00	0,384	14753	0,267	4811	0,968
1039	800	200	30	600	50	5,00	0,256	18572	0,399	7052	0,946
1042	400	100	30	800	50	5,00	0,096	36264	0,739	9986	1,004
1045	1000	250	30	800	50	5,00	0,240	17048	0,473	8610	0,866
1048	800	200	30	1000	50	5,00	0,154	21978	0,637	10860	0,874
1063	300	150	45	1000	50	12,50	0,113	37112	0,987	11690	0,940
1066	600	300	45	1000	50	12,50	0,225	21760	0,740	9552	0,768
1102	300	150	45	400	50	8,33	0,281	30751	0,468	5049	1,016
1105	400	200	45	600	50	8,33	0,250	28081	0,603	7074	0,949
1108	200	100	45	800	50	8,33	0,094	49564	1,010	10057	1,011
1111	500	250	45	800	50	8,33	0,234	25708	0,713	8783	0,883
1114	400	200	45	1000	50	8,33	0,150	35275	1,022	11580	0,932
1120	300	100	45	600	50	8,33	0,133	45816	0,753	7988	1,071
1123	750	250	45	600	50	8,33	0,333	18680	0,453	6792	0,911
1126	450	150	45	800	50	8,33	0,150	35249	0,800	9571	0,962
1129	900	300	45	800	50	8,33	0,300	18159	0,553	8322	0,837
1132	750	250	45	1000	50	8,33	0,200	23478	0,738	10408	0,837
1138	600	150	45	600	50	8,33	0,208	27383	0,516	7387	0,990
1141	1200	300	45	600	50	8,33	0,417	15081	0,410	6566	0,880
1144	800	200	45	800	50	8,33	0,208	24152	0,607	9148	0,920
1147	600	150	45	1000	50	8,33	0,125	31328	0,833	11726	0,943
1150	1200	300	45	1000	50	8,33	0,250	19129	0,650	10043	0,808

Table B.8: Geometric parameters and results from the numerical analyses for girders ID-1153 to ID-1348.

ID	a_1 [mm]	a_3 [mm]	α [deg]	b_f [mm]	t_f [mm]	t_f/t_w	R	$M_{cr.num}$ [kNm]	$\kappa_{\sigma.num}$	$M_{ult.num}$ [kNm]	ρ_{num}
1153	200	100	45	600	50	5,00	0,125	56395	0,927	8091	1,085
1156	500	250	45	600	50	5,00	0,313	24488	0,593	7092	0,951
1159	300	150	45	800	50	5,00	0,141	44985	1,021	10002	1,006
1162	600	300	45	800	50	5,00	0,281	23244	0,707	8701	0,875
1165	500	250	45	1000	50	5,00	0,188	31636	0,994	10993	0,884
1168	450	150	45	400	50	5,00	0,300	29069	0,442	5301	1,066
1171	450	150	45	600	50	5,00	0,200	35079	0,662	7619	1,022
1174	900	300	45	600	50	5,00	0,400	17661	0,480	6777	0,909
1177	600	200	45	800	50	5,00	0,200	30504	0,767	9532	0,959
1180	450	150	45	1000	50	5,00	0,120	36662	0,975	11851	0,953
1183	900	300	45	1000	50	5,00	0,240	22501	0,765	10426	0,839
1186	800	200	45	400	50	5,00	0,417	20919	0,379	5016	1,009
1189	800	200	45	600	50	5,00	0,278	25544	0,548	7406	0,993
1192	400	100	45	800	50	5,00	0,104	40719	0,829	10119	1,018
1195	1000	250	45	800	50	5,00	0,260	23755	0,659	9284	0,934
1198	800	200	45	1000	50	5,00	0,167	29070	0,842	11408	0,918
1213	300	150	60	1000	50	12,50	0,123	41919	1,115	11809	0,950
1258	200	100	60	800	50	8,33	0,102	56105	1,143	10509	1,057
1261	500	250	60	800	50	8,33	0,255	34652	0,961	9171	0,922
1264	400	200	60	1000	50	8,33	0,163	41404	1,199	11792	0,949
1270	300	100	60	600	50	8,33	0,144	50014	0,822	8065	1,081
1276	450	150	60	800	50	8,33	0,161	41355	0,939	9962	1,002
1279	900	300	60	800	50	8,33	0,323	23808	0,724	8837	0,889
1282	750	250	60	1000	50	8,33	0,215	29702	0,934	10854	0,873
1291	1200	300	60	600	50	8,33	0,444	19601	0,532	7078	0,949
1297	600	150	60	1000	50	8,33	0,133	34892	0,928	11827	0,951
1300	1200	300	60	1000	50	8,33	0,266	23927	0,813	10725	0,863
1303	200	100	60	600	50	5,00	0,136	63107	1,037	8150	1,093
1306	500	250	60	600	50	5,00	0,340	33693	0,816	7409	0,993
1309	300	150	60	800	50	5,00	0,153	51836	1,176	10171	1,023
1312	600	300	60	800	50	5,00	0,306	32147	0,978	9234	0,929
1315	500	250	60	1000	50	5,00	0,204	42069	1,322	11622	0,935
1318	450	150	60	400	50	5,00	0,323	36294	0,552	5443	1,095
1321	450	150	60	600	50	5,00	0,215	43152	0,814	7829	1,050
1324	900	300	60	600	50	5,00	0,431	23437	0,636	7193	0,964
1327	600	200	60	800	50	5,00	0,215	38181	0,960	9797	0,985
1330	450	150	60	1000	50	5,00	0,129	41289	1,098	11990	0,965
1333	900	300	60	1000	50	5,00	0,258	29003	0,986	11011	0,886
1336	800	200	60	400	50	5,00	0,444	26510	0,480	5189	1,044
1339	800	200	60	600	50	5,00	0,296	31606	0,678	7658	1,027
1342	400	100	60	800	50	5,00	0,111	44126	0,899	10218	1,028
1345	1000	250	60	800	50	5,00	0,277	29396	0,815	9637	0,969
1348	800	200	60	1000	50	5,00	0,178	34784	1,008	11649	0,937

B.2 Data of girders undergoing normal stress web buckling as 1st eigenmode

Table B.9: Geometric parameters and critical moments $M_{cr.num}$ from the numerical analyses for girders in the range ID-184 to ID-1090.

ID	a_1 [mm]	a_3 [mm]	α [deg]	b_f [mm]	t_f [mm]	t_f/t_w	R	$M_{cr.num}$ [kNm]
184	400	100	45	400	25	6,25	0,208	5848
319	600	200	60	400	25	6,25	0,431	4589
334	400	100	60	400	25	6,25	0,222	5909
484	400	100	30	400	35	8,75	0,192	8453
619	600	200	45	400	35	8,75	0,400	6321
622	600	200	45	600	35	8,75	0,267	9339
634	400	100	45	400	35	8,75	0,208	8315
637	400	100	45	600	35	8,75	0,139	12413
754	300	150	60	600	35	8,75	0,204	18367
757	600	300	60	600	35	8,75	0,408	9386
760	400	200	60	800	35	8,75	0,204	16560
769	600	200	60	400	35	8,75	0,431	6316
772	600	200	60	600	35	8,75	0,287	9334
778	750	250	60	800	35	8,75	0,269	9558
784	400	100	60	400	35	8,75	0,222	8340
787	400	100	60	600	35	8,75	0,148	12458
790	1000	250	60	600	35	8,75	0,370	8084
793	600	150	60	800	35	8,75	0,166	12368
835	600	150	60	400	35	5,83	0,333	13487
919	600	200	30	400	50	12,50	0,366	8973
922	600	200	30	600	50	12,50	0,244	13315
934	400	100	30	400	50	12,50	0,192	12323
937	400	100	30	600	50	12,50	0,128	18420
943	600	150	30	800	50	12,50	0,144	17503
1051	200	100	45	400	50	12,50	0,188	39680
1054	300	150	45	600	50	12,50	0,188	28429
1057	600	300	45	600	50	12,50	0,375	13388
1060	400	200	45	800	50	12,50	0,188	25220
1069	600	200	45	400	50	12,50	0,400	8924
1072	600	200	45	600	50	12,50	0,267	13264
1075	300	100	45	800	50	12,50	0,100	36950
1078	750	250	45	800	50	12,50	0,250	13572
1081	600	200	45	1000	50	12,50	0,160	21873
1084	400	100	45	400	50	12,50	0,208	12118
1087	400	100	45	600	50	12,50	0,139	18121
1090	1000	250	45	600	50	12,50	0,347	11262

Table B.10: Geometric parameters and critical moments $M_{cr.num}$ from the numerical analyses for girders in the range ID-1093 to ID-1294.

ID	a_1 [mm]	a_3 [mm]	α [deg]	b_f [mm]	t_f [mm]	t_f/t_w	R	$M_{cr.num}$ [kNm]
1093	600	150	45	800	50	12,50	0,156	17544
1096	1200	300	45	800	50	12,50	0,313	13264
1099	1000	250	45	1000	50	12,50	0,208	18601
1117	300	100	45	400	50	8,33	0,200	37687
1135	600	150	45	400	50	8,33	0,313	19198
1201	200	100	60	400	50	12,50	0,204	39350
1204	300	150	60	600	50	12,50	0,204	27153
1207	600	300	60	600	50	12,50	0,408	13253
1210	400	200	60	800	50	12,50	0,204	24209
1216	600	300	60	1000	50	12,50	0,245	21927
1219	600	200	60	400	50	12,50	0,431	8901
1222	600	200	60	600	50	12,50	0,287	13214
1225	300	100	60	800	50	12,50	0,108	38469
1228	750	250	60	800	50	12,50	0,269	13393
1231	600	200	60	1000	50	12,50	0,172	21880
1234	400	100	60	400	50	12,50	0,222	12159
1237	400	100	60	600	50	12,50	0,148	18180
1240	1000	250	60	600	50	12,50	0,370	11229
1243	600	150	60	800	50	12,50	0,166	17580
1246	1200	300	60	800	50	12,50	0,333	13253
1249	1000	250	60	1000	50	12,50	0,222	18558
1252	300	150	60	400	50	8,33	0,306	37939
1255	400	200	60	600	50	8,33	0,272	36578
1267	300	100	60	400	50	8,33	0,215	39727
1273	750	250	60	600	50	8,33	0,359	21023
1285	600	150	60	400	50	8,33	0,333	19265
1288	600	150	60	600	50	8,33	0,222	28581
1294	800	200	60	800	50	8,33	0,222	27295

C

Appendix: Comparisons

C.1 Comparisons with Eurocode 3

Table C.1: Comparisons of results from numerical analyses with suggestions of the Eurocode for girders ID-1 to ID-253.

ID	$\kappa_{\sigma.EC}/\kappa_{\sigma.num}$	$M_{ult.EC}/M_{ult.num}$		ID	$\kappa_{\sigma.EC}/\kappa_{\sigma.num}$	$M_{ult.EC}/M_{ult.num}$	
		$\bar{\lambda}_p(\kappa_{\sigma.EC})$	$\bar{\lambda}_p(\sigma_{cr.num})$			$\bar{\lambda}_p(\kappa_{\sigma.EC})$	$\bar{\lambda}_p(\sigma_{cr.num})$
1	1,00	1,11	1,11	127	0,60	0,94	1,16
4	0,90	1,18	1,22	130	0,56	0,91	1,16
7	1,15	1,65	1,55	133	0,60	1,36	1,46
10	0,83	1,27	1,38	136	0,79	1,10	1,07
13	0,60	0,95	1,18	139	0,66	1,12	1,11
16	0,84	1,61	1,73	142	0,62	0,94	1,13
19	1,25	1,28	1,18	145	0,59	1,17	1,22
22	0,95	1,23	1,25	148	0,62	1,13	1,23
25	0,68	0,98	1,14	151	0,69	1,06	1,06
28	0,94	1,80	1,58	154	0,60	1,04	1,25
31	0,71	1,24	1,44	157	0,83	1,26	1,36
34	1,07	1,09	1,09	160	0,54	1,02	1,30
37	0,83	1,06	1,13	163	0,48	0,87	1,19
40	1,06	1,78	1,44	166	0,55	1,16	1,49
43	0,76	1,10	1,22	169	0,92	1,13	1,16
46	0,93	1,99	1,69	172	0,74	1,07	1,20
49	0,77	1,71	1,64	175	0,57	0,93	1,16
52	1,11	1,22	1,18	178	0,71	1,32	1,37
55	0,93	1,22	1,25	181	0,52	0,97	1,27
58	0,59	0,95	1,16	187	0,66	0,99	1,14
61	0,81	1,28	1,40	190	0,78	1,33	1,24
64	0,62	1,12	1,38	193	0,60	0,98	1,20
67	0,98	1,07	1,07	196	0,70	1,43	1,41
70	0,71	1,02	1,16	199	0,63	1,22	1,33
73	0,99	1,63	1,38	202	0,81	1,12	1,12
76	0,68	1,03	1,21	205	0,65	1,06	1,24
79	0,86	1,77	1,58	208	0,48	0,90	1,19
82	0,75	1,56	1,55	211	0,56	1,02	1,30
85	0,93	1,07	1,09	214	0,45	0,90	1,25
88	0,75	1,00	1,11	217	0,75	1,03	1,03
91	0,95	1,71	1,42	220	0,57	0,98	1,12
94	0,76	1,37	1,32	223	0,75	1,28	1,24
97	0,65	0,97	1,16	226	0,53	0,94	1,20
100	0,71	1,65	1,61	229	0,67	1,33	1,37
103	0,58	0,98	1,11	232	0,55	1,19	1,37
106	0,71	1,04	1,19	235	0,75	1,04	1,05
109	0,56	0,94	1,18	238	0,64	0,98	1,15
112	0,65	1,12	1,35	241	0,75	1,34	1,25
115	0,58	1,07	1,35	244	0,63	1,14	1,23
118	0,76	1,01	1,03	247	0,54	0,91	1,17
121	0,66	0,96	1,12	250	0,60	1,21	1,31
124	0,72	1,35	1,28	253	0,48	0,96	1,09

Table C.2: Comparisons of results from numerical analyses with suggestions of the Eurocode for girders ID-256 to ID-544.

ID	$\kappa_{\sigma.EC}/\kappa_{\sigma.num}$	$M_{ult.EC}/M_{ult.num}$		ID	$\kappa_{\sigma.EC}/\kappa_{\sigma.num}$	$M_{ult.EC}/M_{ult.num}$	
		$\lambda_p(\kappa_{\sigma.EC})$	$\lambda_p(\sigma_{cr.num})$			$\lambda_p(\kappa_{\sigma.EC})$	$\lambda_p(\sigma_{cr.num})$
256	0,60	0,99	1,20	403	0,41	1,06	1,06
259	0,44	0,89	1,22	406	0,46	1,20	1,24
262	0,54	0,99	1,28	409	0,38	1,12	1,22
265	0,42	0,90	1,29	412	0,41	1,31	1,30
268	0,67	1,02	1,02	415	0,34	1,13	1,17
271	0,54	0,94	1,13	418	0,59	1,01	1,01
274	0,66	1,20	1,20	421	0,46	1,12	1,13
277	0,50	0,91	1,19	424	0,61	1,12	1,20
280	0,47	0,86	1,17	427	0,45	1,18	1,18
283	0,53	1,10	1,29	430	0,42	1,19	1,18
286	0,72	1,07	1,07	433	0,48	0,96	1,16
289	0,60	1,04	1,10	436	0,66	1,05	1,05
292	0,54	0,91	1,15	439	0,59	1,04	1,13
295	0,57	1,01	1,11	442	0,49	1,13	1,16
298	0,56	0,95	1,09	445	0,58	1,02	1,13
301	0,53	-	-	448	0,52	0,94	1,10
304	0,45	1,11	1,13	451	1,14	1,03	1,03
307	0,62	1,44	1,31	454	1,04	1,17	1,17
310	0,40	1,18	1,25	457	1,48	1,78	1,34
313	0,41	1,19	1,19	460	0,96	1,40	1,23
316	0,40	1,47	1,40	463	0,65	1,23	1,17
322	0,58	1,24	1,21	466	1,02	1,94	1,46
325	0,51	1,16	1,17	469	1,70	1,22	1,16
328	0,54	1,13	1,30	472	1,24	1,31	1,17
331	0,44	1,24	1,18	475	0,74	1,12	1,12
337	0,58	1,13	1,13	478	1,14	1,63	1,35
340	0,67	1,18	1,19	481	0,86	1,49	1,26
343	0,54	1,22	1,18	487	1,03	1,08	1,08
346	0,62	1,22	1,29	490	1,37	1,59	1,27
349	0,58	0,99	1,11	493	0,96	1,26	1,15
352	0,59	1,06	1,06	496	1,17	1,88	1,47
355	0,47	1,20	1,23	499	0,94	1,61	1,42
358	0,42	1,12	1,20	502	1,39	1,09	1,09
361	0,41	1,27	1,30	505	1,15	1,26	1,19
364	0,38	1,22	1,24	508	0,64	1,11	1,11
367	0,60	-	-	511	1,01	1,50	1,24
370	0,51	1,10	1,10	514	0,71	1,36	1,23
373	0,64	1,14	1,22	517	1,25	1,01	1,01
376	0,45	1,18	1,21	520	0,84	1,05	1,05
379	0,57	1,15	1,31	523	1,28	1,47	1,22
382	0,47	0,95	1,17	526	0,82	1,21	1,16
385	0,67	1,03	1,03	529	1,10	1,65	1,35
388	0,58	1,15	1,15	532	0,91	1,42	1,31
391	0,67	1,19	1,18	535	1,31	1,04	1,04
394	0,58	1,03	1,15	538	1,00	1,11	1,11
397	0,49	1,22	1,13	541	1,32	1,67	1,28
400	0,60	1,00	1,11	544	0,94	1,31	1,17

Table C.3: Comparisons of results from numerical analyses with suggestions of the Eurocode for girders ID-547 to ID-871.

ID	$\kappa_{\sigma.EC}/\kappa_{\sigma.num}$	$M_{ult.EC}/M_{ult.num}$		ID	$\kappa_{\sigma.EC}/\kappa_{\sigma.num}$	$M_{ult.EC}/M_{ult.num}$	
		$\lambda_p(\kappa_{\sigma.EC})$	$\lambda_p(\sigma_{cr.num})$			$\lambda_p(\kappa_{\sigma.EC})$	$\lambda_p(\sigma_{cr.num})$
547	0,74	1,24	1,13	700	0,69	1,22	1,24
550	0,90	1,57	1,39	703	0,55	-	-
553	0,66	1,01	1,01	706	0,78	1,15	1,15
556	1,01	1,26	1,16	709	0,50	1,10	1,10
559	0,64	1,15	1,15	712	0,67	1,29	1,23
562	0,90	1,50	1,24	715	0,50	1,23	1,25
565	0,73	1,40	1,24	718	0,91	-	-
568	1,11	1,00	1,00	721	0,68	1,03	1,03
571	0,89	1,07	1,07	724	0,84	1,24	1,17
574	1,07	1,42	1,20	727	0,60	1,15	1,15
577	0,79	1,22	1,13	730	0,53	1,16	1,18
580	0,64	1,20	1,15	733	0,63	1,14	1,23
583	0,79	1,37	1,31	736	0,95	1,02	1,02
586	1,22	1,07	1,07	739	0,75	1,08	1,08
589	0,92	1,15	1,12	742	0,62	1,08	1,08
592	0,71	1,09	1,09	745	0,66	1,11	1,14
595	0,80	1,24	1,15	748	0,60	1,09	1,20
598	0,73	1,15	1,17	751	0,67	-	-
601	0,81	-	-	763	0,46	1,14	1,18
604	0,71	1,10	1,10	766	0,48	1,32	1,33
607	1,04	1,40	1,27	775	0,59	1,09	1,09
610	0,64	1,25	1,25	781	0,51	1,20	1,23
613	0,53	1,17	1,20	796	0,71	1,22	1,22
616	0,66	1,49	1,35	799	0,61	1,07	1,17
625	0,65	1,10	1,10	802	0,76	-	-
628	0,86	1,31	1,26	805	0,58	1,09	1,09
631	0,62	1,29	1,24	808	0,47	1,07	1,07
640	0,97	1,29	1,19	811	0,49	1,20	1,20
643	0,73	1,18	1,18	814	0,42	1,14	1,20
646	0,85	1,40	1,28	817	0,79	-	-
649	0,74	1,27	1,30	820	0,60	-	-
652	1,02	1,03	1,03	823	0,76	1,14	1,14
655	0,80	1,15	1,15	826	0,52	1,10	1,10
658	0,53	1,09	1,09	829	0,66	1,15	1,22
661	0,68	1,28	1,25	832	0,51	1,06	1,24
664	0,51	1,18	1,21	838	0,68	1,02	1,02
667	0,97	-	-	841	0,77	1,18	1,14
670	0,67	1,01	1,01	844	0,61	1,11	1,17
673	0,93	1,24	1,19	847	0,55	1,17	1,18
676	0,61	1,11	1,11	850	0,62	1,12	1,22
679	0,81	1,29	1,24	853	0,48	-	-
682	0,65	1,17	1,24	856	0,56	1,09	1,09
685	1,01	-	-	859	0,43	1,07	1,07
688	0,83	1,05	1,05	862	0,49	1,21	1,23
691	0,94	1,32	1,17	865	0,38	1,13	1,21
694	0,75	1,16	1,17	868	0,76	-	-
697	0,61	1,20	1,17	871	0,55	1,01	1,01

Table C.4: Comparisons of results from numerical analyses with suggestions of the Eurocode for girders ID-874 to ID-1279.

ID	$\kappa_{\sigma.EC}/\kappa_{\sigma.num}$	$M_{ult.EC}/M_{ult.num}$		ID	$\kappa_{\sigma.EC}/\kappa_{\sigma.num}$	$M_{ult.EC}/M_{ult.num}$	
		$\lambda_p(\kappa_{\sigma.EC})$	$\lambda_p(\sigma_{cr.num})$			$\lambda_p(\kappa_{\sigma.EC})$	$\lambda_p(\sigma_{cr.num})$
874	0,71	1,15	1,15	1030	0,73	1,06	1,06
877	0,48	1,09	1,09	1033	1,03	1,33	1,18
880	0,47	1,13	1,18	1036	1,76	1,03	1,03
883	0,50	1,05	1,23	1039	1,26	1,06	1,06
886	0,81	-	-	1042	0,81	-	-
889	0,66	1,04	1,04	1045	1,08	1,15	1,14
892	0,57	1,07	1,07	1048	0,93	1,14	1,14
895	0,62	1,09	1,18	1063	0,61	1,06	1,06
898	0,54	1,03	1,17	1066	0,81	1,30	1,29
901	1,31	-	-	1102	1,28	-	-
904	1,17	1,05	1,05	1105	1,00	1,05	1,05
907	1,85	1,35	1,23	1108	0,59	-	-
910	1,10	1,16	1,16	1111	0,84	1,13	1,13
913	0,72	1,08	1,08	1114	0,59	1,07	1,07
916	1,21	1,47	1,26	1120	0,80	-	-
925	0,82	1,01	1,01	1123	1,21	1,10	1,10
928	1,42	1,36	1,24	1126	0,75	1,04	1,04
931	1,04	1,24	1,19	1129	1,02	1,19	1,19
940	1,77	1,26	1,18	1132	0,81	1,19	1,19
946	1,49	1,59	1,34	1138	1,16	1,01	1,01
949	1,19	1,48	1,27	1141	1,20	1,14	1,14
952	1,68	1,02	1,02	1144	0,99	1,09	1,09
955	1,39	1,11	1,11	1147	0,72	1,06	1,06
958	0,70	-	-	1150	0,86	1,24	1,18
961	1,23	1,22	1,20	1153	0,65	-	-
964	0,81	1,16	1,16	1156	1,01	1,05	1,05
967	1,55	-	-	1159	0,59	-	-
970	0,98	-	-	1162	0,85	1,14	1,14
973	1,63	1,20	1,18	1165	0,60	1,13	1,13
976	0,99	1,07	1,07	1168	1,28	-	-
979	1,38	1,37	1,20	1171	0,91	-	-
982	1,11	1,31	1,18	1174	1,08	1,10	1,10
985	1,86	1,01	1,01	1177	0,78	1,04	1,04
988	1,35	1,03	1,03	1180	0,62	1,05	1,05
991	1,74	1,31	1,31	1183	0,78	1,19	1,19
994	1,20	1,15	1,15	1186	1,30	-	-
997	0,89	1,11	1,11	1189	0,99	1,01	1,01
1000	1,13	1,45	1,21	1192	0,72	-	-
1003	0,75	-	-	1195	0,84	1,07	1,07
1006	1,35	1,12	1,12	1198	0,71	1,09	1,09
1009	0,75	1,04	1,04	1213	0,54	1,05	1,05
1012	1,18	1,25	1,19	1258	0,53	-	-
1015	0,90	1,22	1,20	1261	0,62	1,08	1,08
1018	1,57	-	-	1264	0,50	1,05	1,05
1021	1,17	1,01	1,01	1270	0,73	-	-
1024	1,50	1,22	1,17	1276	0,64	-	-
1027	1,04	1,09	1,09	1279	0,83	1,13	1,13

Table C.5: Comparisons of results from numerical analyses with suggestions of the Eurocode for girders ID-1282 to ID-1348.

ID	$\kappa_{\sigma.EC}/\kappa_{\sigma.num}$	$M_{ult.EC}/M_{ult.num}$	
		$\lambda_p(\kappa_{\sigma.EC})$	$\lambda_p(\sigma_{cr.num})$
1282	0,64	1,15	1,15
1291	0,97	1,05	1,05
1297	0,65	1,05	1,05
1300	0,74	1,16	1,16
1303	0,58	-	-
1306	0,74	1,01	1,01
1309	0,51	-	-
1312	0,61	1,08	1,08
1315	0,45	1,07	1,07
1318	1,09	-	-
1321	0,74	-	-
1324	0,88	1,04	1,04
1327	0,62	1,02	1,02
1330	0,55	1,04	1,04
1333	0,61	1,13	1,13
1336	1,07	-	-
1339	0,86	-	-
1342	0,67	-	-
1345	0,73	1,03	1,03
1348	0,60	1,07	1,07

C.2 Comparisons with the models of Jáger et al.

Table C.6: Comparisons of results from numerical analyses with suggested models of Jáger et al. for girders ID-1 to ID-109.

ID	$\kappa_{\sigma.Jag}/\kappa_{\sigma.num}$	$M_{ult.Jag}/M_{ult.num}$			
		$\rho = (10\epsilon_{ss.f} \cdot c_f/t_f)^\beta$		$\rho = (14\epsilon_{ss.f} \cdot c_f/t_f)^\beta$	
		ρ on b_f	ρ on c_f	ρ on b_f	ρ on c_f
1	0,70	0,78	0,91	1,10	1,10
4	0,63	0,66	0,94	0,93	1,11
7	0,59	0,96	1,33	1,34	1,62
10	0,58	0,68	1,15	0,95	1,32
13	0,72	0,74	1,11	0,92	1,22
16	0,52	0,83	1,62	1,17	1,83
19	0,60	0,83	0,97	1,16	1,22
22	0,53	0,72	1,02	1,00	1,21
25	0,80	0,78	1,03	0,95	1,13
28	0,54	0,85	1,43	1,19	1,66
31	0,51	0,68	1,29	0,94	1,44
34	0,63	0,77	0,89	1,07	1,08
37	0,61	0,68	0,90	0,90	1,03
40	0,52	0,88	1,25	1,24	1,50
43	0,51	0,63	1,02	0,86	1,16
46	0,47	0,93	1,56	1,31	1,81
49	0,45	0,79	1,54	1,10	1,74
52	0,80	0,78	0,91	1,09	1,13
55	0,68	0,69	0,99	0,97	1,17
58	0,96	0,82	1,04	0,97	1,12
61	0,60	0,68	1,15	0,96	1,33
64	0,61	0,84	1,29	1,06	1,43
67	0,74	0,77	0,88	1,05	1,06
70	0,69	0,76	0,93	0,94	1,03
73	0,67	0,81	1,14	1,13	1,37
76	0,60	0,74	1,05	0,94	1,17
79	0,60	0,83	1,38	1,16	1,61
82	0,57	0,77	1,44	1,06	1,62
85	0,63	0,71	0,83	0,99	1,02
88	0,55	0,59	0,84	0,82	0,98
91	0,61	0,84	1,16	1,17	1,41
94	0,56	0,66	1,11	0,92	1,27
97	0,61	0,82	1,17	1,00	1,28
100	0,50	0,76	1,47	1,06	1,67
103	0,81	0,79	0,93	0,93	1,01
106	0,71	0,60	0,85	0,84	1,02
109	0,71	0,80	1,03	0,96	1,12

Table C.7: Comparisons of results from numerical analyses with suggested models of Jáger et al. for girders ID-112 to ID-232.

ID	$\kappa_{\sigma.Jag}/\kappa_{\sigma.num}$	$M_{ult.Jag}/M_{ult.num}$			
		$\rho = (10\epsilon_{ss.f} \cdot c_f/t_f)^\beta$		$\rho = (14\epsilon_{ss.f} \cdot c_f/t_f)^\beta$	
		ρ on b_f	ρ on c_f	ρ on b_f	ρ on c_f
112	0,65	0,61	1,02	0,86	1,19
115	0,62	0,79	1,23	1,01	1,36
118	0,76	0,66	0,78	0,92	0,96
121	0,66	0,65	0,85	0,85	0,97
124	0,72	0,66	0,92	0,93	1,12
127	0,60	0,65	0,95	0,84	1,07
130	0,73	0,86	1,15	1,02	1,25
133	0,60	0,70	1,26	0,95	1,42
136	0,79	0,64	0,76	0,90	0,95
139	0,66	0,56	0,80	0,79	0,95
142	0,82	0,81	1,03	0,96	1,11
145	0,59	0,56	0,93	0,78	1,08
148	0,62	0,81	1,20	1,01	1,32
151	0,69	0,81	0,90	1,05	1,05
154	0,60	0,70	0,90	0,90	1,03
157	0,46	0,70	0,97	0,98	1,18
160	0,54	0,69	1,01	0,89	1,14
163	0,91	0,82	1,11	0,97	1,19
166	0,46	0,65	1,19	0,89	1,34
169	0,47	0,71	0,84	1,00	1,05
172	0,45	0,60	0,85	0,84	1,01
175	0,98	0,81	1,02	0,96	1,11
178	0,44	0,63	1,05	0,88	1,22
181	0,50	0,76	1,14	0,95	1,26
187	0,61	0,77	0,92	0,93	1,02
190	0,40	0,66	0,93	0,92	1,12
193	0,50	0,75	1,02	0,93	1,13
196	0,38	0,67	1,12	0,94	1,31
199	0,40	0,67	1,17	0,90	1,31
202	0,66	0,72	0,85	1,01	1,04
205	0,57	0,65	0,88	0,87	1,03
208	1,04	0,78	0,99	0,92	1,07
211	0,52	0,66	0,99	0,87	1,12
214	0,64	0,83	1,13	0,99	1,23
217	0,67	0,80	0,89	1,02	1,02
220	0,75	0,79	0,93	0,94	1,01
223	0,53	0,63	0,90	0,89	1,07
226	0,61	0,81	1,03	0,96	1,12
229	0,48	0,62	1,04	0,87	1,21
232	0,49	0,80	1,23	1,02	1,36

Table C.8: Comparisons of results from numerical analyses with suggested models of Jáger et al. for girders ID-235 to ID-358.

ID	$\kappa_{\sigma.Jag}/\kappa_{\sigma.num}$	$M_{ult.Jag}/M_{ult.num}$			
		$\rho = (10\epsilon_{ss.f} \cdot c_f/t_f)^\beta$		$\rho = (14\epsilon_{ss.f} \cdot c_f/t_f)^\beta$	
		ρ on b_f	ρ on c_f	ρ on b_f	ρ on c_f
235	0,52	0,67	0,79	0,94	0,97
238	0,49	0,68	0,87	0,87	0,98
241	0,49	0,66	0,91	0,92	1,11
244	0,48	0,72	1,03	0,93	1,16
247	0,64	0,85	1,15	1,01	1,24
250	0,44	0,65	1,14	0,87	1,28
253	0,95	0,78	0,91	0,92	0,99
256	0,61	0,57	0,79	0,79	0,94
259	0,78	0,79	0,99	0,93	1,08
262	0,57	0,62	0,94	0,83	1,08
265	0,58	0,81	1,12	0,98	1,23
268	0,67	0,69	0,79	0,93	0,96
271	0,61	0,72	0,87	0,88	0,97
274	0,66	0,58	0,81	0,82	0,99
277	0,57	0,73	0,97	0,90	1,07
280	0,80	0,81	1,09	0,96	1,18
283	0,55	0,73	1,12	0,93	1,25
286	0,72	0,63	0,74	0,88	0,93
289	0,60	0,60	0,80	0,79	0,93
292	0,89	0,79	0,99	0,93	1,07
295	0,57	0,61	0,89	0,79	1,01
298	0,63	0,81	1,09	0,96	1,18
301	0,74	-	-	-	-
304	0,62	0,75	0,89	0,90	0,99
307	0,41	0,59	0,82	0,82	0,99
310	0,56	0,76	0,97	0,91	1,06
313	0,88	0,78	1,04	0,92	1,12
316	0,45	0,78	1,14	0,97	1,26
322	0,41	0,67	0,87	0,87	1,00
325	1,10	0,78	0,99	0,93	1,07
328	0,40	0,74	1,03	0,93	1,16
331	0,54	0,81	1,08	0,95	1,17
337	0,66	0,80	0,93	0,94	1,02
340	0,36	0,60	0,84	0,83	1,00
343	0,53	0,81	1,03	0,96	1,12
346	0,34	0,66	1,01	0,89	1,17
349	0,42	0,77	1,08	0,94	1,19
352	0,60	0,77	0,86	0,98	1,01
355	0,53	0,72	0,89	0,90	1,01
358	0,90	0,75	0,95	0,89	1,03

Table C.9: Comparisons of results from numerical analyses with suggested models of Jáger et al. for girders ID-361 to ID-478.

ID	$\kappa_{\sigma.Jag}/\kappa_{\sigma.num}$	$M_{ult.Jag}/M_{ult.num}$			
		$\rho = (10\epsilon_{ss.f} \cdot c_f/t_f)^\beta$		$\rho = (14\epsilon_{ss.f} \cdot c_f/t_f)^\beta$	
		ρ on b_f	ρ on c_f	ρ on b_f	ρ on c_f
361	0,49	0,74	0,98	0,90	1,09
364	0,75	0,79	1,06	0,94	1,15
367	0,64	-	-	-	-
370	0,85	0,78	0,91	0,92	0,99
373	0,46	0,64	0,85	0,86	1,01
376	0,66	0,79	1,00	0,93	1,08
379	0,44	0,70	1,01	0,91	1,16
382	0,50	0,81	1,09	0,96	1,18
385	0,48	0,72	0,82	0,95	0,97
388	0,50	0,77	0,91	0,92	1,01
391	0,44	0,58	0,81	0,81	0,98
394	0,50	0,80	1,02	0,96	1,12
397	0,69	0,79	1,06	0,94	1,15
400	0,45	0,73	1,07	0,91	1,18
403	0,89	0,75	0,88	0,89	0,96
406	0,55	0,65	0,82	0,83	0,95
409	0,82	0,75	0,94	0,89	1,03
412	0,53	0,70	0,95	0,88	1,07
415	0,60	0,73	0,97	0,86	1,06
418	0,61	0,74	0,83	0,94	0,96
421	0,61	0,77	0,91	0,91	1,00
424	0,61	0,59	0,79	0,80	0,95
427	0,60	0,78	0,98	0,92	1,07
430	0,89	0,78	1,05	0,92	1,13
433	0,56	0,78	1,07	0,94	1,18
436	0,66	0,63	0,74	0,87	0,92
439	0,59	0,70	0,86	0,87	0,98
442	0,97	0,76	0,96	0,90	1,04
445	0,58	0,75	0,98	0,91	1,09
448	0,66	0,80	1,07	0,95	1,16
451	0,71	1,01	1,02	1,03	1,03
454	0,64	0,77	0,92	1,07	1,11
457	0,61	0,98	1,18	1,37	1,47
460	0,60	0,69	0,96	0,96	1,13
463	0,73	0,62	0,90	0,83	1,02
466	0,55	0,80	1,26	1,12	1,47
469	0,64	1,00	1,05	1,22	1,22
472	0,58	0,81	0,97	1,13	1,19
475	0,82	0,71	0,89	0,92	1,01
478	0,55	0,83	1,16	1,17	1,38

Table C.10: Comparisons of results from numerical analyses with suggested models of Jáger et al. for girders ID-481 to ID-601.

ID	$\kappa_{\sigma.Jag}/\kappa_{\sigma.num}$	$M_{ult.Jag}/M_{ult.num}$			
		$\rho = (10\epsilon_{ss.f} \cdot c_f/t_f)^\beta$		$\rho = (14\epsilon_{ss.f} \cdot c_f/t_f)^\beta$	
		ρ on b_f	ρ on c_f	ρ on b_f	ρ on c_f
481	0,55	0,65	1,02	0,91	1,18
487	0,67	0,76	0,89	1,06	1,07
490	0,53	0,92	1,11	1,29	1,37
493	0,56	0,65	0,90	0,92	1,06
496	0,48	0,95	1,31	1,33	1,57
499	0,47	0,79	1,24	1,10	1,44
502	0,82	0,98	1,01	1,09	1,09
505	0,71	0,78	0,94	1,09	1,15
508	0,98	0,81	0,94	0,96	1,03
511	0,64	0,71	0,99	1,00	1,18
514	0,63	0,68	0,98	0,90	1,12
517	0,80	0,99	1,00	1,01	1,01
520	0,74	0,80	0,91	1,04	1,04
523	0,69	0,85	1,03	1,19	1,28
526	0,65	0,69	0,90	0,92	1,04
529	0,61	0,83	1,15	1,17	1,38
532	0,58	0,70	1,10	0,98	1,27
535	0,70	0,93	0,97	1,04	1,04
538	0,61	0,73	0,87	1,02	1,05
541	0,64	0,91	1,10	1,28	1,38
544	0,58	0,68	0,94	0,95	1,11
547	0,61	0,71	0,96	0,90	1,07
550	0,52	0,76	1,20	1,07	1,40
553	0,82	0,84	0,91	1,00	1,01
556	0,79	0,73	0,88	1,02	1,09
559	0,72	0,77	0,93	0,95	1,03
562	0,72	0,69	0,95	0,96	1,14
565	0,66	0,71	1,01	0,93	1,15
568	0,87	0,90	0,93	1,00	1,00
571	0,73	0,74	0,86	0,99	1,02
574	0,81	0,78	0,94	1,09	1,17
577	0,65	0,66	0,87	0,89	1,01
580	0,74	0,81	1,00	0,96	1,08
583	0,64	0,67	1,05	0,93	1,22
586	0,91	0,88	0,93	1,07	1,07
589	0,72	0,71	0,86	0,99	1,04
592	0,83	0,81	0,93	0,96	1,02
595	0,63	0,63	0,88	0,89	1,05
598	0,61	0,73	0,99	0,93	1,11
601	0,75	-	-	-	-

Table C.11: Comparisons of results from numerical analyses with suggested models of Jáger et al. for girders ID-604 to ID-733.

ID	$\kappa_{\sigma.Jag}/\kappa_{\sigma.num}$	$M_{ult.Jag}/M_{ult.num}$			
		$\rho = (10\epsilon_{ss.f} \cdot c_f/t_f)^\beta$		$\rho = (14\epsilon_{ss.f} \cdot c_f/t_f)^\beta$	
		ρ on b_f	ρ on c_f	ρ on b_f	ρ on c_f
604	0,65	0,75	0,88	1,02	1,05
607	0,49	0,77	0,93	1,07	1,16
610	0,59	0,65	0,88	0,89	1,02
613	0,97	0,77	0,96	0,92	1,05
616	0,49	0,62	0,97	0,86	1,13
625	1,07	0,82	0,94	0,97	1,03
628	0,46	0,67	0,93	0,94	1,11
631	0,54	0,68	0,96	0,89	1,08
640	0,40	0,75	0,91	1,05	1,12
643	0,54	0,72	0,91	0,93	1,03
646	0,37	0,71	0,98	0,99	1,17
649	0,41	0,62	0,98	0,87	1,14
652	0,71	0,93	0,96	1,03	1,03
655	0,61	0,71	0,86	0,99	1,05
658	1,16	0,81	0,93	0,95	1,01
661	0,55	0,64	0,87	0,88	1,02
664	0,67	0,73	0,94	0,90	1,04
667	0,76	-	-	-	-
670	0,81	0,84	0,91	1,01	1,01
673	0,53	0,72	0,87	1,00	1,07
676	0,64	0,75	0,90	0,92	1,00
679	0,48	0,65	0,90	0,91	1,08
682	0,51	0,69	0,97	0,90	1,11
685	0,56	-	-	-	-
688	0,54	0,74	0,86	0,98	1,01
691	0,46	0,72	0,87	1,01	1,08
694	0,49	0,68	0,88	0,89	1,02
697	0,65	0,82	1,00	0,97	1,09
700	0,42	0,59	0,93	0,83	1,08
703	1,01	-	-	-	-
706	0,64	0,67	0,81	0,93	1,00
709	0,81	0,79	0,91	0,93	1,00
712	0,59	0,63	0,84	0,86	1,00
715	0,60	0,74	0,96	0,91	1,07
718	0,73	-	-	-	-
721	0,66	0,78	0,88	0,98	1,00
724	0,64	0,68	0,82	0,95	1,02
727	0,58	0,72	0,88	0,90	0,99
730	0,82	0,79	0,97	0,94	1,05
733	0,54	0,68	0,95	0,89	1,09

Table C.12: Comparisons of results from numerical analyses with suggested models of Jáger et al. for girders ID-736 to ID-886.

ID	$\kappa_{\sigma.Jag}/\kappa_{\sigma.num}$	$M_{ult.Jag}/M_{ult.num}$			
		$\rho = (10\epsilon_{ss.f} \cdot c_f/t_f)^\beta$		$\rho = (14\epsilon_{ss.f} \cdot c_f/t_f)^\beta$	
		ρ on b_f	ρ on c_f	ρ on b_f	ρ on c_f
736	0,71	0,84	0,88	1,02	1,02
739	0,60	0,69	0,82	0,94	0,99
742	0,93	0,80	0,92	0,95	1,00
745	0,53	0,63	0,83	0,84	0,97
748	0,58	0,80	1,01	0,97	1,11
751	0,88	-	-	-	-
763	1,00	0,78	0,95	0,92	1,03
766	0,50	0,73	0,97	0,92	1,10
775	1,28	0,81	0,93	0,95	1,01
781	0,58	0,81	1,00	0,96	1,09
796	0,33	0,64	0,87	0,88	1,03
799	0,39	0,74	0,96	0,91	1,07
802	0,68	-	-	-	-
805	0,59	0,77	0,88	0,98	1,02
808	1,01	0,79	0,92	0,94	1,00
811	0,53	0,73	0,89	0,91	1,01
814	0,80	0,77	0,94	0,91	1,03
817	0,76	-	-	-	-
820	0,93	-	-	-	-
823	0,46	0,69	0,82	0,94	1,00
826	0,70	0,79	0,92	0,94	1,00
829	0,43	0,67	0,87	0,88	1,01
832	0,49	0,79	0,99	0,95	1,09
838	0,51	0,80	0,89	0,98	0,99
841	0,39	0,65	0,78	0,90	0,97
844	0,46	0,78	0,92	0,94	1,03
847	0,72	0,80	0,98	0,94	1,06
850	0,40	0,74	0,98	0,93	1,11
853	1,05	-	-	-	-
856	0,57	0,71	0,82	0,92	0,97
859	0,93	0,77	0,89	0,91	0,98
862	0,53	0,70	0,86	0,88	0,99
865	0,61	0,76	0,93	0,90	1,02
868	0,65	-	-	-	-
871	0,63	0,82	0,89	0,97	0,98
874	0,55	0,64	0,76	0,89	0,95
877	0,56	0,76	0,89	0,90	0,97
880	0,94	0,77	0,94	0,91	1,02
883	0,50	0,76	0,97	0,93	1,07
886	0,61	-	-	-	-

Table C.13: Comparisons of results from numerical analyses with suggested models of Jáger et al. for girders ID-889 to ID-1021.

ID	$\kappa_{\sigma.Jag}/\kappa_{\sigma.num}$	$M_{ult.Jag}/M_{ult.num}$			
		$\rho = (10\epsilon_{ss.f} \cdot c_f/t_f)^\beta$		$\rho = (14\epsilon_{ss.f} \cdot c_f/t_f)^\beta$	
		ρ on b_f	ρ on c_f	ρ on b_f	ρ on c_f
889	0,53	0,75	0,85	0,94	0,97
892	1,04	0,79	0,91	0,93	0,99
895	0,50	0,74	0,89	0,91	1,01
898	0,60	0,79	0,97	0,94	1,06
901	0,73	-	-	-	-
904	0,65	0,99	1,01	1,05	1,05
907	0,62	1,06	1,13	1,35	1,35
910	0,61	0,81	0,94	1,14	1,15
913	0,75	0,66	0,84	0,92	0,99
916	0,56	0,80	1,03	1,12	1,24
925	0,85	0,79	0,89	1,01	1,01
928	0,58	0,91	1,06	1,27	1,30
931	0,60	0,73	0,93	1,02	1,10
940	0,55	1,04	1,10	1,26	1,26
946	0,50	1,02	1,20	1,43	1,48
949	0,51	0,83	1,07	1,16	1,28
952	0,82	1,02	1,02	1,02	1,02
955	0,72	0,97	1,02	1,11	1,11
958	1,01	-	-	-	-
961	0,66	0,82	0,95	1,14	1,17
964	0,64	0,68	0,87	0,95	1,04
967	0,85	-	-	-	-
970	0,78	-	-	-	-
973	0,70	0,99	1,05	1,20	1,20
976	0,69	0,79	0,91	1,07	1,07
979	0,62	0,88	1,03	1,23	1,27
982	0,61	0,74	0,95	1,03	1,13
985	0,79	1,01	1,01	1,01	1,01
988	0,69	0,97	0,99	1,03	1,03
991	0,64	1,03	1,10	1,31	1,31
994	0,62	0,81	0,93	1,13	1,14
997	0,66	0,71	0,88	0,96	1,03
1000	0,53	0,78	1,02	1,10	1,22
1003	0,84	-	-	-	-
1006	0,85	0,93	0,99	1,12	1,12
1009	0,74	0,83	0,92	1,04	1,04
1012	0,76	0,80	0,94	1,12	1,16
1015	0,69	0,70	0,89	0,97	1,06
1018	0,97	-	-	-	-
1021	0,81	0,95	0,97	1,01	1,01

Table C.14: Comparisons of results from numerical analyses with suggested models of Jáger et al. for girders ID-1024 to ID-1192.

ID	$\kappa_{\sigma.Jag}/\kappa_{\sigma.num}$	$M_{ult.Jag}/M_{ult.num}$			
		$\rho = (10\epsilon_{ss.f} \cdot c_f/t_f)^\beta$		$\rho = (14\epsilon_{ss.f} \cdot c_f/t_f)^\beta$	
		ρ on b_f	ρ on c_f	ρ on b_f	ρ on c_f
1024	0,85	0,95	1,02	1,22	1,22
1027	0,72	0,77	0,89	1,07	1,08
1030	0,75	0,78	0,90	0,97	1,01
1033	0,67	0,72	0,94	1,01	1,12
1036	0,97	1,03	1,03	1,03	1,03
1039	0,78	0,93	0,97	1,06	1,06
1042	0,85	-	-	-	-
1045	0,68	0,77	0,90	1,08	1,11
1048	0,65	0,72	0,89	0,96	1,04
1063	1,07	0,76	0,89	0,96	1,00
1066	0,55	0,70	0,91	0,99	1,10
1102	0,77	-	-	-	-
1105	0,67	0,93	0,97	1,05	1,05
1108	1,29	-	-	-	-
1111	0,61	0,76	0,89	1,06	1,09
1114	0,72	0,73	0,87	0,93	0,99
1120	0,89	-	-	-	-
1123	0,56	0,91	0,96	1,10	1,10
1126	0,72	0,84	0,92	1,04	1,04
1129	0,51	0,76	0,90	1,07	1,11
1132	0,56	0,69	0,88	0,95	1,04
1138	0,65	0,95	0,97	1,01	1,01
1141	0,46	0,89	0,95	1,14	1,14
1144	0,55	0,77	0,89	1,07	1,08
1147	0,71	0,79	0,91	0,97	1,01
1150	0,44	0,67	0,87	0,94	1,04
1153	1,11	-	-	-	-
1156	0,69	0,87	0,92	1,05	1,05
1159	0,87	-	-	-	-
1162	0,63	0,73	0,86	1,02	1,06
1165	0,64	0,75	0,90	0,96	1,02
1168	0,83	-	-	-	-
1171	0,75	-	-	-	-
1174	0,64	0,86	0,92	1,10	1,10
1177	0,65	0,80	0,89	1,03	1,04
1180	0,87	0,82	0,92	0,97	1,00
1183	0,56	0,69	0,86	0,93	1,02
1186	0,73	-	-	-	-
1189	0,63	0,89	0,93	1,01	1,01
1192	1,00	-	-	-	-

Table C.15: Comparisons of results from numerical analyses with suggested models of Jáger et al. for girders ID-1195 to ID-1348.

ID	$\kappa_{\sigma.Jag}/\kappa_{\sigma.num}$	$M_{ult.Jag}/M_{ult.num}$			
		$\rho = (10\epsilon_{ss.f} \cdot c_f/t_f)^\beta$		$\rho = (14\epsilon_{ss.f} \cdot c_f/t_f)^\beta$	
		ρ on b_f	ρ on c_f	ρ on b_f	ρ on c_f
1195	0,55	0,72	0,84	1,01	1,03
1198	0,60	0,78	0,90	0,96	1,01
1213	1,17	0,82	0,92	0,97	1,01
1258	1,14	-	-	-	-
1261	0,62	0,81	0,91	1,04	1,05
1264	0,90	0,81	0,91	0,96	0,99
1270	1,08	-	-	-	-
1276	0,80	-	-	-	-
1279	0,46	0,75	0,87	1,02	1,05
1282	0,56	0,81	0,93	0,99	1,05
1291	0,39	0,82	0,88	1,05	1,05
1297	0,79	0,82	0,92	0,97	1,01
1300	0,40	0,73	0,88	0,94	1,02
1303	1,25	-	-	-	-
1306	0,63	0,86	0,90	1,01	1,01
1309	1,07	-	-	-	-
1312	0,58	0,77	0,86	0,99	1,02
1315	0,66	0,80	0,90	0,95	0,99
1318	0,76	-	-	-	-
1321	0,75	-	-	-	-
1324	0,54	0,81	0,87	1,04	1,04
1327	0,63	0,84	0,91	1,01	1,01
1330	1,01	0,81	0,91	0,96	0,99
1333	0,52	0,76	0,89	0,94	1,01
1336	0,61	-	-	-	-
1339	0,56	-	-	-	-
1342	1,14	-	-	-	-
1345	0,49	0,78	0,87	0,99	1,00
1348	0,59	0,82	0,92	0,97	1,01

C.3 Comparisons with the model of the DASt Richtlinie 015

Table C.16: Comparisons of results from numerical analyses with the suggested model of the DASt Richtlinie 015 for girders ID-1 to ID-373.

ID	$M_{ult.DASt}/M_{ult.num}$	ID	$M_{ult.DASt}/M_{ult.num}$	ID	$M_{ult.DASt}/M_{ult.num}$
1	1,11	121	1,09	244	1,08
4	1,32	124	1,58	247	0,86
7	2,28	127	1,01	250	1,14
10	1,35	130	0,87	253	1,02
13	0,91	133	1,29	256	1,22
16	1,72	136	1,10	259	0,90
19	1,41	139	1,20	262	1,14
22	1,52	142	0,91	265	0,92
25	0,95	145	1,16	268	1,02
28	1,78	148	1,00	271	1,06
31	1,23	151	1,06	274	1,39
34	1,09	154	1,17	277	0,96
37	1,12	157	1,66	280	0,82
40	1,99	160	1,08	283	1,04
43	1,11	163	0,83	286	1,07
46	2,04	166	1,22	289	1,11
49	1,56	169	1,22	292	0,88
52	1,22	172	1,27	295	1,00
55	1,47	175	0,91	298	0,84
58	0,92	178	1,31	304	1,05
61	1,43	181	0,96	307	1,40
64	1,11	187	1,06	310	0,93
67	1,07	190	1,48	313	0,78
70	1,09	193	0,99	316	1,01
73	1,82	196	1,47	322	1,17
76	1,05	199	1,12	325	0,87
79	1,81	202	1,12	328	1,11
82	1,43	205	1,25	331	0,83
85	1,10	208	0,87	337	1,05
88	1,16	211	1,13	340	1,31
91	1,99	214	0,89	343	0,94
94	1,30	217	1,03	346	1,25
97	0,92	220	1,04	349	0,90
100	1,56	223	1,43	352	1,06
103	1,04	226	0,95	355	1,15
106	1,35	229	1,36	358	0,84
109	0,95	232	1,09	361	1,00
112	1,34	235	1,05	364	0,82
115	1,09	238	1,10	370	1,02
118	1,03	241	1,57	373	1,27

Table C.17: Comparisons of results from numerical analyses with the suggested model of the DASt Richtlinie 015 for girders ID-376 to ID-832.

ID	$M_{ult.DASt}/M_{ult.num}$	ID	$M_{ult.DASt}/M_{ult.num}$	ID	$M_{ult.DASt}/M_{ult.num}$
376	0,91	508	1,09	652	1,03
379	1,18	511	1,49	655	1,15
382	0,87	514	1,13	658	1,07
385	1,03	517	1,01	661	1,27
388	1,07	520	1,05	664	0,98
391	1,38	523	1,47	670	1,01
394	0,97	526	1,18	673	1,24
397	0,80	529	1,82	676	1,09
400	0,94	532	1,38	679	1,42
403	0,99	535	1,04	682	1,13
406	1,16	538	1,11	688	1,05
409	0,86	541	1,67	691	1,32
412	1,05	544	1,35	694	1,19
415	0,77	547	1,02	697	0,98
418	1,01	550	1,57	700	1,22
421	1,05	553	1,01	706	1,15
424	1,31	556	1,26	709	1,07
427	0,92	559	1,13	712	1,29
430	0,79	562	1,50	715	1,03
433	0,90	565	1,18	721	1,03
436	1,05	568	1,00	724	1,24
439	1,11	571	1,07	727	1,13
442	0,85	574	1,42	730	0,95
445	1,00	577	1,20	733	1,15
448	0,83	580	0,98	736	1,02
451	1,03	583	1,38	739	1,08
454	1,17	586	1,07	742	1,06
457	1,78	589	1,15	745	1,19
460	1,37	592	1,07	748	1,03
463	1,00	595	1,32	763	0,93
466	1,65	598	1,09	766	1,12
469	1,22	604	1,10	775	1,07
472	1,31	607	1,40	781	0,99
475	1,10	610	1,22	796	1,34
478	1,74	613	0,96	799	1,04
481	1,24	616	1,27	805	1,09
487	1,08	625	1,08	808	1,05
490	1,59	628	1,40	811	1,18
493	1,24	631	1,07	814	0,94
496	2,07	640	1,29	823	1,14
499	1,56	643	1,16	826	1,08
502	1,09	646	1,54	829	1,27
505	1,26	649	1,24	832	1,03

Table C.18: Comparisons of results from numerical analyses with the suggested model of the DASt Richtlinie 015 for girders ID-838 to ID-1348.

ID	$M_{ult.DASt}/M_{ult.num}$	ID	$M_{ult.DASt}/M_{ult.num}$	ID	$M_{ult.DASt}/M_{ult.num}$
838	1,02	973	1,20	1141	1,14
841	1,18	976	1,07	1144	1,09
844	1,14	979	1,37	1147	1,06
847	0,95	982	1,31	1150	1,24
850	1,13	985	1,01	1156	1,05
856	1,09	988	1,03	1162	1,14
859	1,05	991	1,31	1165	1,13
862	1,20	994	1,15	1174	1,10
865	0,95	997	1,11	1177	1,04
871	1,01	1000	1,45	1180	1,05
874	1,15	1006	1,12	1183	1,19
877	1,07	1009	1,04	1189	1,01
880	0,92	1012	1,25	1195	1,07
883	1,06	1015	1,22	1198	1,09
889	1,04	1021	1,01	1213	1,05
892	1,05	1024	1,22	1261	1,08
895	1,17	1027	1,09	1264	1,05
898	0,97	1030	1,06	1279	1,13
904	1,05	1033	1,33	1282	1,15
907	1,35	1036	1,03	1291	1,05
910	1,16	1039	1,06	1297	1,05
913	1,08	1045	1,15	1300	1,16
916	1,47	1048	1,14	1306	1,01
925	1,01	1063	1,06	1312	1,08
928	1,36	1066	1,30	1315	1,07
931	1,24	1105	1,05	1324	1,04
940	1,26	1111	1,13	1327	1,02
946	1,59	1114	1,07	1330	1,04
949	1,48	1123	1,10	1333	1,13
952	1,02	1126	1,04	1345	1,03
955	1,11	1129	1,19	1348	1,07
961	1,22	1132	1,19		
964	1,16	1138	1,01		

C.4 Comparisons with the developed model of this thesis

Table C.19: Comparisons of results from numerical analyses with the developed models of this thesis for girders ID-1 to ID-265.

ID	$\kappa_{\sigma.approx}/\kappa_{\sigma.num}$	$M_{ult.approx}/M_{ult.num}$	ID	$\kappa_{\sigma.approx}/\kappa_{\sigma.num}$	$M_{ult.approx}/M_{ult.num}$
1	1,08	0,92	133	1,07	0,73
4	1,13	0,91	136	1,03	0,79
7	1,37	1,06	139	0,89	0,73
10	1,20	0,95	142	1,07	0,82
13	1,12	0,77	145	0,93	0,70
16	1,28	0,85	148	0,97	0,64
19	1,15	0,87	151	1,07	0,96
22	1,01	0,81	154	1,04	0,93
25	1,11	0,83	157	1,18	0,98
28	1,21	0,91	160	1,04	0,92
31	1,11	0,80	163	1,01	0,79
34	0,96	0,82	166	1,06	0,86
37	0,94	0,79	169	1,08	0,87
40	1,13	0,88	172	0,93	0,81
43	0,90	0,71	175	1,07	0,84
46	1,19	0,79	178	1,03	0,86
49	1,16	0,76	181	1,07	0,82
52	1,09	0,88	187	1,02	0,84
55	1,12	0,89	190	0,98	0,80
58	1,06	0,84	193	1,01	0,82
61	1,14	0,88	196	1,02	0,76
64	1,17	0,89	199	1,02	0,71
67	1,03	0,86	202	1,04	0,92
70	1,02	0,85	205	1,00	0,89
73	1,20	0,94	208	0,97	0,84
76	1,05	0,82	211	0,99	0,86
79	1,22	0,88	214	1,04	0,83
82	1,22	0,86	217	1,02	0,90
85	0,85	0,74	220	1,04	0,88
88	0,90	0,74	223	1,07	0,87
91	1,25	0,95	226	1,04	0,86
94	1,06	0,82	229	1,07	0,84
97	1,07	0,70	232	1,05	0,83
100	1,12	0,66	235	0,83	0,78
103	1,01	0,86	238	0,87	0,79
106	1,01	0,82	241	1,15	0,87
109	1,05	0,84	244	0,97	0,80
112	1,05	0,81	247	1,08	0,78
115	1,09	0,82	250	1,03	0,64
118	0,87	0,78	253	0,98	0,89
121	0,92	0,78	256	0,99	0,85
124	1,13	0,88	259	1,01	0,88
127	0,95	0,75	262	1,00	0,84
130	1,10	0,77	265	1,00	0,84

Table C.20: Comparisons of results from numerical analyses with the developed models of this thesis for girders ID-268 to ID-574.

ID	$\kappa_{\sigma.approx}/\kappa_{\sigma.num}$	$M_{ult.approx}/M_{ult.num}$	ID	$\kappa_{\sigma.approx}/\kappa_{\sigma.num}$	$M_{ult.approx}/M_{ult.num}$
268	0,91	0,84	424	1,16	0,90
271	0,92	0,83	427	1,00	0,84
274	1,17	0,89	430	1,02	0,82
277	0,95	0,81	433	1,07	0,74
280	1,07	0,81	436	1,10	0,85
283	1,03	0,74	439	0,95	0,80
286	1,08	0,82	442	1,05	0,85
289	0,91	0,75	445	1,04	0,77
292	1,08	0,84	448	1,22	0,80
295	0,97	0,70	451	1,04	0,96
298	1,17	0,74	454	1,08	0,91
301	1,09	-	457	1,32	1,03
304	1,00	0,91	460	1,13	0,92
307	1,06	0,95	463	1,02	0,84
310	0,97	0,89	466	1,19	0,97
313	0,92	0,77	469	1,16	0,89
316	0,95	0,87	472	0,99	0,83
322	0,87	0,83	475	1,04	0,85
325	1,01	0,84	478	1,11	0,92
328	0,93	0,83	481	1,07	0,86
331	1,09	0,83	487	0,96	0,85
337	1,04	0,88	490	1,05	0,87
340	0,94	0,79	493	0,88	0,76
343	1,04	0,84	496	1,08	0,90
346	0,97	0,75	499	1,08	0,91
349	1,06	0,66	502	1,06	0,91
352	0,99	0,93	505	1,08	0,89
355	0,92	0,91	508	1,00	0,88
358	0,89	0,83	511	1,11	0,90
361	0,90	0,88	514	1,12	0,90
364	0,95	0,82	517	1,08	0,92
367	0,99	-	520	1,03	0,89
370	1,02	0,89	523	1,14	0,90
373	0,99	0,86	526	1,05	0,85
376	1,01	0,87	529	1,15	0,92
379	0,99	0,84	532	1,16	0,91
382	1,03	0,75	535	0,87	0,81
385	0,84	0,82	538	0,94	0,81
388	0,91	0,82	541	1,26	0,96
391	1,12	0,84	544	1,03	0,82
394	1,01	0,78	547	0,99	0,78
397	1,07	0,77	550	1,06	0,82
400	1,08	0,62	553	1,00	0,91
403	0,93	0,89	556	1,09	0,87
406	0,93	0,89	559	1,03	0,88
409	0,95	0,87	562	1,10	0,88
412	0,94	0,88	565	1,10	0,89
415	0,97	0,80	568	0,97	0,85
418	0,91	0,87	571	1,00	0,85
421	0,94	0,88	574	1,24	0,92

Table C.21: Comparisons of results from numerical analyses with the developed models of this thesis for girders ID-577 to ID-925.

ID	$\kappa_{\sigma.approx}/\kappa_{\sigma.num}$	$M_{ult.approx}/M_{ult.num}$	ID	$\kappa_{\sigma.approx}/\kappa_{\sigma.num}$	$M_{ult.approx}/M_{ult.num}$
577	1,00	0,81	739	0,89	0,81
580	1,05	0,84	742	1,07	0,88
583	1,08	0,86	745	0,88	0,77
586	1,16	0,87	748	1,04	0,87
589	0,92	0,79	751	1,26	-
592	1,04	0,85	763	0,91	0,85
595	0,93	0,77	766	0,97	0,95
598	0,88	0,73	775	1,03	0,89
601	1,14	-	781	1,08	0,92
604	1,08	0,96	796	0,89	0,81
607	1,21	0,98	799	0,92	0,79
610	1,06	0,94	802	1,12	-
613	0,98	0,86	805	1,00	0,94
616	1,05	0,95	808	0,88	0,89
625	1,05	0,88	811	0,94	0,92
628	1,01	0,89	814	0,93	0,88
631	1,06	0,90	817	1,17	-
640	0,95	0,84	820	1,07	-
643	1,03	0,87	823	0,98	0,88
646	0,95	0,83	826	1,01	0,90
649	0,96	0,85	829	0,94	0,86
652	1,11	0,96	832	0,95	0,87
655	1,04	0,93	838	0,90	0,86
658	0,94	0,89	841	1,03	0,84
661	1,01	0,90	844	0,89	0,84
664	1,01	0,87	847	1,03	0,86
667	1,14	-	850	0,90	0,79
670	1,07	0,92	853	0,97	-
673	1,04	0,88	856	0,96	0,92
676	1,04	0,87	859	0,94	0,91
679	1,02	0,86	862	0,93	0,91
682	1,02	0,88	865	0,94	0,90
685	0,89	-	868	0,98	-
688	0,92	0,84	871	0,96	0,91
691	1,10	0,87	874	1,11	0,89
694	0,93	0,82	877	0,91	0,86
697	1,04	0,85	880	1,00	0,87
700	0,93	0,77	883	0,92	0,85
703	1,01	-	886	1,08	-
706	1,03	0,90	889	0,86	0,83
709	1,00	0,90	892	1,06	0,89
712	1,01	0,89	895	0,88	0,82
715	0,99	0,90	898	1,07	0,87
718	0,99	-	901	1,03	-
721	0,98	0,89	904	1,02	0,95
724	1,17	0,90	907	1,23	0,96
727	0,94	0,85	910	1,06	0,92
730	1,04	0,87	913	0,96	0,87
733	0,98	0,84	916	1,10	0,93
736	1,12	0,89	925	0,99	0,90

Table C.22: Comparisons of results from numerical analyses with the developed models of this thesis for girders ID-928 to ID-1348.

ID	$\kappa_{\sigma.approx}/\kappa_{\sigma.num}$	$M_{ult.approx}/M_{ult.num}$	ID	$\kappa_{\sigma.approx}/\kappa_{\sigma.num}$	$M_{ult.approx}/M_{ult.num}$
928	1,04	0,90	1132	1,06	0,91
931	1,03	0,87	1138	1,07	0,92
940	0,95	0,84	1141	1,11	0,90
946	0,96	0,90	1144	1,00	0,88
949	1,04	0,91	1147	1,04	0,87
952	1,00	0,95	1150	0,90	0,81
955	1,02	0,91	1153	1,06	-
958	0,95	-	1156	1,11	0,94
961	1,05	0,89	1159	1,02	-
964	1,06	0,90	1162	1,05	0,93
967	1,11	-	1165	1,02	0,93
970	1,03	-	1168	1,14	-
973	1,06	0,88	1171	1,11	-
976	1,04	0,90	1174	1,19	0,93
979	1,06	0,87	1177	1,03	0,91
982	1,11	0,88	1180	1,04	0,90
985	0,88	0,87	1183	0,97	0,87
988	1,00	0,87	1186	1,20	-
991	1,20	0,92	1189	0,92	0,87
994	1,01	0,84	1192	1,09	-
997	0,98	0,84	1195	0,88	0,83
1000	0,98	0,82	1198	1,04	0,88
1003	0,99	-	1213	0,93	0,91
1006	1,11	0,90	1258	0,88	-
1009	1,03	0,93	1261	1,05	0,97
1012	1,10	0,89	1264	0,97	0,92
1015	1,09	0,90	1270	1,17	-
1018	1,02	-	1276	1,09	-
1021	1,07	0,91	1279	0,99	0,90
1024	1,27	0,93	1282	1,04	0,93
1027	1,04	0,87	1291	1,06	0,89
1030	1,01	0,87	1297	1,05	0,89
1033	1,05	0,86	1300	0,87	0,82
1036	1,21	0,93	1303	1,05	-
1039	0,92	0,84	1306	1,08	0,96
1042	1,01	-	1309	0,99	-
1045	0,92	0,80	1312	1,00	0,94
1048	0,85	0,77	1315	0,99	0,94
1063	0,97	0,90	1318	1,19	-
1066	1,08	0,97	1321	1,13	-
1102	1,19	-	1324	1,13	0,93
1105	1,10	0,97	1327	1,01	0,93
1108	0,93	-	1330	1,01	0,91
1111	1,05	0,95	1333	0,93	0,88
1114	1,01	0,91	1336	1,17	-
1120	1,12	-	1339	0,92	-
1123	1,09	0,92	1342	1,10	-
1126	1,11	0,95	1345	0,85	0,84
1129	1,02	0,89	1348	1,02	0,90